DEVELOPMENT OF PHYSICAL TECHNIQUES FOR HYDRATE MONITORING AND EARLY WARNING SYSTEMS

Ivan Valko

Submitted for the degree of Doctor of Philosophy

Heriot-Watt University

Institute of Petroleum Engineering

April 2011

ABSTRACT

One of the challenges that the petroleum industry faces is to ensure unimpeded flow of hydrocarbons. During production, transportation and processing, there can be free water in the produced fluid, and/or changes in temperature and pressure can lead to water condensation causing ice and/or hydrates formation. Gas hydrates pose serious flow assurance, economic and safety concerns. Chemical inhibitors are widely used to reduce the risks associated with hydrates. However, the upstream injection of hydrate inhibitors is generally based on thermodynamic model predictions and estimations of the worst conditions without much downstream measurements.

This thesis presents a research work in which a number of techniques were investigated with the ultimate aim to mitigate hydrate risks during hydrocarbon recovery.

Hydrate Monitoring Techniques are where the hydrate stability zone (HSZ) could be determined by testing downstream samples. Spectroscopy, dielectric permittivity, and freezing point depression methods were experimentally examined. A novel pseudo concentration approach was created as a result of this research work. This approach is more reliable and robust than the historically developed correlation, since it takes into account the pressure, hydrate structure and inhibitor type effects. Spectroscopy, dialectic permittivity set-ups and a freezing point prototype device based on Peltier heat pumps have been designed, built and tested.

Hydrate Early Warning Techniques are where the hydrate formation could be detected based on water memory phenomenon. This phenomenon suggests that sampled fluid under specific conditions can carry remnant molecular structure related to hydrate formation if it had taken place. Spectroscopy, onset of ice formation and onset of hydrate formation were investigated. During this work, a multiple probe freezing apparatus and hydrate mini-rig prototypes have been designed, built, and tested.

These techniques can provide technical measures for hydrate monitoring and early warning, helping to lessen the risk of pipeline blockages as well as to minimise the amount of chemicals required to inhibit any hydrate formation, hence improve the production economics and reduce the impact on the environment. Moreover, the investigated techniques show a potential to be deployed in Supervisory Control And Data Acquisition (SCADA) systems widely used in the petroleum industry for reservoir/production monitoring and management.

To all members of my family

For their Trust and Encouragement

ACKNOWLEDGEMENTS

I deeply thank Professor Bahman Tohidi for providing me this great opportunity to work in the professional research team on a very interesting topic that I wanted to investigate. I especially thank Bahman for his effort in initiating this study and spending his valuable time for supervision of the project in spite of his busy schedule. In many ways, I appreciate Dr. Jinhai Yang for his instruction, encouragement and patience. I thank Dr. Antonin Chapoy for his professionalism, unlimited help and inspiration during my entire PhD study.

I truly appreciate all the support and help from the teachers, assistants, technicians and students from Centre for Gas Hydrate Research whose I was lucky enough to build a collegial and friendship relations with. I thank Ross Anderson, Rod Burgass, Prof. Adrian Todd, Dr. Joanna Lachwa-Langa, Dr. Jeerachada Tanchawanich for their generous help and kindness. I express appreciation to Mr. Saeid Mazloum, Ms. Roghieh Azarinezhad, Ms. Suzannah Toulmin, Mr. Jebraeel Gholinezhad, Mr Hooman Haghighi, Mr. Hossein Moradpour and Mr. Manoochehr Salehabadi for their friendship and assistance. I value the punctuality, professionalism and gentleness of Mr Colin Flockhart and Mr Thomas McGravie who were in charge of manufacturing and maintenance of the equipment.

I thank Professor Patrick Corbett for his sincere care, thoughtfulness and time he dedicated to work on issues of research students within the Institute. I thank all the staff of Institute of Petroleum Engineering for being open and supportive. My heartfelt gratitude goes to you all.

I also thank my wife for her support and inspiration during the entire period of the research. Recently, our family have grown - a baby girl who I would like to thank for giving enough sleeping time during these nights and a lot of refreshing joy during a free time.

This thesis was prepared during a Joint Industry Project funded by a consortium of companies including TOTAL, BP, Chevron, National Iranian Gas Company, PETRONAS and Statoil which is gratefully acknowledged. I would also like to thank Institute of Petroleum Engineering for providing a full scholarship during this research towards PhD.

DECLARATION STATEMENT

ACADEMIC REGISTRY
Research Thesis Submission

Name*:*	Ivan Valko		
School/PGI:	Institute of Petroleum Engineering		
Version: *(i.e. First, Resubmission, Final)*	Final	Degree Sought (Award **and** Subject area)	PhD in Petroleum Engineering

Declaration

In accordance with the appropriate regulations I hereby submit my thesis and I declare that:

1) the thesis embodies the results of my own work and has been composed by myself
2) where appropriate, I have made acknowledgement of the work of others and have made reference to work carried out in collaboration with other persons
3) the thesis is the correct version of the thesis for submission and is the same version as any electronic versions submitted*.
4) my thesis for the award referred to, deposited in the Heriot-Watt University Library, should be made available for loan or photocopying and be available via the Institutional Repository, subject to such conditions as the Librarian may require
5) I understand that as a student of the University I am required to abide by the Regulations of the University and to conform to its discipline.

* *Please note that it is the responsibility of the candidate to ensure that the correct version of the thesis is submitted.*

Signature of Candidate*:*		Date:	

Submission

Submitted By *(name in capitals):*	IVAN VALKO
Signature of Individual Submitting:	
Date Submitted:	

For Completion in the Student Service Centre (SSC)

Received in the SSC by *(name in capitals):*			
Method of Submission *(Handed in to SSC; posted through internal/external mail):*			
E-thesis Submitted (*mandatory for final theses)*			
Signature:		Date:	

TABLE OF CONTENTS

ABSTRACT **II**

ACKNOWLEDGEMENTS **IV**

TABLE OF CONTENTS **VI**

LIST OF SYMBOLS **IX**

LIST OF FIGURES **X**

LIST OF TABLES **XVII**

CHAPTER 1 INTRODUCTION **1**

1.1 CONCEPT OF HYDRATE MONITORING AND EARLY WARNING 1

1.2 HYDRATE MONITORING SYSTEMS 9
1.2.1 Freezing Point Depression Method 11
1.2.2 Spectroscopy Method 11
1.2.3 Dielectric Permittivity Method 12

1.3 HYDRATE EARLY WARNING SYSTEMS 12
1.3.1 Onset of Ice Formation 13
1.3.2 Onset of Hydrate Formation 13
1.3.3 Electromagnetic Methods 14

1.4 THESIS AS PART OF JOINT INDUSTRIAL PROJECT 14

1.5 STRUCTURE OF THE THESIS 16

CHAPTER 2 UV/VIS/NIR SPECTROSCOPY **17**

2.1 INTRODUCTION 17
2.1.1 Theory of Light Absorption 19
2.1.2 Spectroscopy 21
2.1.3 Components of Molecular Spectrophotometer 21

2.2 EXPERIMENTAL BACKGROUND 25
2.2.1 Experimental Set-up 26
2.2.2 Materials 27
2.2.3 Procedures 28

2.3 HYDRATE FORMATION 28
2.3.1 Detection of Hydrate Formation (Stage One) 28
2.3.2 Detection of Hydrate Formation (Stage Two) 31

2.4 CONCLUSIONS 38

CHAPTER 3 INHIBITORS MONITORING TECHNIQUE **39**

3.1 INTRODUCTION 39

3.2 SPECTROSCOPY 40

3.3 EXPERIMENTAL SET-UP AND PROCEDURES 40
3.3.1 Experimental Set-up 40
3.3.2 Materials 41
3.3.3 Procedures 41

3.4 THERMODYNAMIC INHIBITORS 41

3.5 EFFECT OF SALT 47

3.6 LOW DOSAGE HYDRATE INHIBITORS 51
3.6.1 Fluid Systems in the Presence of LDHI 52

3.7 EFFECT OF CONTAMINATIONS 60
3.7.1 Synthetic Solution with Single Hydrocarbon 61
3.7.2 Solution with 5 mass% Oil 62
3.7.3 Solution with Solids (Fine Sand Particles) 63
3.7.4 BP Produced Water with Various MeOH Content 63
3.7.5 Total Produced Water with Various MeOH Contents 65

3.8 DIELECTRIC PERMITTIVITY 68
3.8.1 Introduction 68
3.8.2 Experimental Set-up and Procedures 69
3.8.3 Key Findings 70

3.9 CONCLUSIONS 77

CHAPTER 4 FREEZING POINT DEPRESSION 79

4.1 INTRODUCTION 79

4.2 DEVELOPMENT OF CORRELATION 81

4.3 DEVELOPMENT OF FREEZING POINT PROTOTYPE DEVICES 84
4.3.1 Comparison of Cooling Systems 85
4.3.2 Design of Prototype with Water Cooling System 89
4.3.3 Specifications of the Final Prototype 93

4.4 MEASUREMENT RESULTS 95
4.4.1 Experimental Set-up 95
4.4.2 Materials 95
4.4.3 Procedures 95
4.4.4 Results of Freezing Point Depression Measurements 98
4.4.5 Determination of Hydrate Dissociation Temperature Using the Measured Freezing Point Depression 101

4.5 PSEUDO CONCENTRATION METHOD 105
4.5.1 Feasibility 106
4.5.2 Effect of Hydrate Structure 108
4.5.3 Comparison with the Correlation 111

4.6 CONCLUSIONS 113

CHAPTER 5 ONSET OF ICE FORMATION 115

5.1 INTRODUCTION 115

5.2 ONSET OF ICE FORMATION METHOD 116
5.2.1 Experimental Set-up and Procedures 116
5.2.2 Nucleation Probability Distribution 121
5.2.3 Results and Discussion 122

5.3 CONCLUSIONS 129

CHAPTER 6 ONSET OF HYDRATE FORMATION 131

6.1 INTRODUCTION 131

6.2 EXPERIMENTAL SET-UP AND PROCEDURES 132
6.2.1 Experimental Set-up 132
6.2.2 Materials 133
6.2.3 Procedures 133
6.2.4 Definitions 134

6.3 RESULTS 135
6.3.1 Natural Gas - Deionised Water Systems 135
6.3.2 Natural Gas - Deionised Water Systems with 3 mass% Salt 139
6.3.3 Natural Gas - Deionised Water Systems with 5 mass% Salt 140
6.3.4 Natural Gas - Deionised Water Systems with 10 mass% Salt 141
6.3.5 Natural Gas - Deionised Water Systems with 15 mass% Methanol 142
6.3.6 Natural Gas - Deionised Water Systems with 3 mass% Salt and 15 mass% Methanol 143
6.3.7 Natural Gas - Deionised Water Systems with 30 mass% Methanol 144
6.3.8 Natural Gas - Deionised Water Systems with 15 mass% Ethylene Glycol 145
6.3.9 Natural Gas - Deionised Water Systems with 3 mass% Salt and 15 mass% Ethylene Glycol 146
6.3.10 Natural Gas - Deionised Water Systems with 30 mass% Ethylene Glycol 147
6.3.11 Produced Water 148

6.4 SUMMARY 149

6.5 HYDRATE MINI RIGS 152
6.5.1 Tall-Narrow Design 152
6.5.2 Short-Wide Design 153

6.6 CONCLUSIONS 155

CHAPTER 7 CONCLUSIONS AND RECOMMENDATIONS 157

7.1 CONCLUSIONS 157

7.2 RECOMMENDATIONS FOR FUTURE WORK 161

REFERENCES 163

APPENDIX A 175

APPENDIX B 178

APPENDIX C 190

APPENDIX D 192

LIST OF SYMBOLS

Abbreviations

AA	Anti-agglomerates
AAD	Average absolute deviation
ABS	Absolute value
AC	Alternating current
d	Molecular diameter
DC	Direct current
EG	Ethylene glycol
EM	Electromagnetic
EoS	Equation of state
FIR	Far infrared
FP	Freezing point
GHD	Gas hydrate deposit
GUI	Graphical user interface
HMI	Human-machine interface
HSB	Hydrate stability boundary
HSZ	Hydrate stability zone
HWHYD	Heriot-Watt hydrate prediction software
HYDRAFLASH	Hydrate and PVT Prediction Commercial Software
IR	Infrared
KI	Kinetic inhibitor
LDHI	Low dosage hydrate inhibitor
MW	Micro wave
NIR	Near infrared
PE	Peltier element
ppm	Part per million
PRT	Platinum resistance temperature probe
PTFE	Poly(tetrafluoroethylene)
PVCap	Polyvinylcaprolactam
PVT	Pressure-volume-temperature
PVTX	Pressure-volume-temperature and concentration
RTD	Resistance thermometer device
SCADA	Supervisory control and data acquisition systems
sH	Structure H gas hydrate
sI	Structure I gas hydrate
sII	Structure II gas hydrate
TE	Thermoelectric module
UV	Ultraviolet
VIS	Visible

LIST OF FIGURES

Figure 1.1 World consumption of primary energy by fuel type 2

Figure 1.2 Crude oil prices 1861-2009 in US dollars per barrel (Source: BP Statistical Review of World Energy 2010) 2

Figure 1.3 Clathrate hydrate structures 4

Figure 1.4 Example of structure I hydrate stability boundary for simple methane-water mixture 5

Figure 1.5 Map of discovered gas-hydrate deposits (Makogon et al., 2004). 5

Figure 1.6 Autocatalytic reaction mechanisms for hydrate formation (Lederhos et al., 1996) 6

Figure 1.7 Integrated Subsurface Information System (Foot at al., 2006) 8

Figure 1.8 Stand-alone monitoring and early warning systems 9

Figure 1.9 Hydrate monitoring systems diagram 10

Figure 1.10 Early warning systems diagram 13

Figure 1.11 JIP research workflow diagram 15

Figure 2.1 The regions of the electromagnetic spectrum (Skoog et al., 2008) 18

Figure 2.2 Attenuation of a beam of radiation by an absorbing solution of length *l* and concentration *c* (Beer-Lambert Law) 19

Figure 2.3 Vibrating diatomic molecule A-B 20

Figure 2.4 Normal modes of vibration in water and carbon dioxide 20

Figure 2.5 Generalised diagram of a molecular spectrometer 21

Figure 2.6 Czerney-Turner grating monochromator 23

Figure 2.7 A multiple reflection ATR system 24

Figure 2.8 Cross section of a photomultiplier tube 25

Figure 2.9 Schematic diagram of the Hydrate Visual Rig (left) and its equilibrium cell (right) 27

Figure 2.10 Pictures of Experimental Set-Up 27

Figure 2.11 Sample preparation pressure-temperature profile for stage one study of hydrate formation 28

Figure 2.12 Light spectrums over the hydrate formation-dissociation process (on all graphs, blue line indicates the spectrum of pressurised water before hydrate formation) 30

Figure 2.13 Sample pressure-temperature profile for further study of hydrate formation 32

Figure 2.14 Spectral attenuation at different temperatures (T/ °C) and pressures (P / bar) for water – natural gas fluid system 32

Figure 2.15 Attenuation at different temperatures for 350 nm and 750 nm wavelengths 33

Figure 2.16 Attenuation coefficient against amount of hydrate formed indicating the linear relationship 34

Figure 2.17 Test with distilled water under atmospheric pressure which followed the same temperature path as hydrate forming pressurised system 35

Figure 2.18 Temperature-Pressure profile for distilled water pressurised with hydrogen 35

Figure 2.19 Spectral attenuation at different temperatures and pressures for distilled water pressurised with hydrogen (T is temperature in ^{o}C, P is pressure in bar) 36

Figure 2.20 Intensity change showing the memory effect disappearing in 24 hours 37

Figure 2.21 Attenuation coefficient showing the memory effect disappearing in 24 hours 37

Figure 3.1 Schematic diagram of the sample cell holder 41

Figure 3.2 Spectra for methanol aqueous solutions indicating the highest effect in the NIR spectrum of light (940-1040nm) 43

Figure 3.3 Spectra for methanol aqueous solutions indicating the highest effect in the NIR spectrum of light (zoomed 940-1040nm) 43

Figure 3.4 Intensity change in NIR spectrum of light at 950nm wavelength linearly increases with the methanol concentration 44

Figure 3.5 Spectra for ethylene glycol aqueous solutions indicating the highest effect in the NIR spectrum of light (940-1040nm) 45

Figure 3.6 Spectra for ethylene glycol aqueous solutions indicating the highest effect in the NIR spectrum of light (zoomed 940-1040nm) 45

Figure 3.7 Intensity change of the NIR spectrum of light at 950 nm wavelength is also linearly increases with the ethylene glycol aqueous concentration 46

Figure 3.8 Degree of ionisation of NaCl and $CaCl_2$ at 293.15 K as a function of concentration (Ostergaard et al., 2005) 47

Figure 3.9 Effect of water salinity on methane concentration (Tohidi et al., 1997) 48

Figure 3.10 Spectra for deionised water, EG, NaCl systems indicating insensitivity of spectroscopy technique to salt component 49

Figure 3.11 Spectra for deionised water, EG, NaCl systems indicating insensitivity of spectroscopy technique to salt component (zoomed 940-1040 nm) 49

Figure 3.12 Intensity change for water with various NaCl concentrations 50

Figure 3.13 Intensity change for water with ethylene glycol and various NaCl concentrations 50

Figure 3.14 Spectra for EG-PVCap solutions showing no effect in the 580-1100 nm frequency range and a strong effect in the range of 300-580 nm 53

Figure 3.15 Spectra for EG-PVCap solutions (zoomed 300-400 nm) 53

Figure 3.16 Intensity of EG-PVCap solutions at 350 nm indicating exponential dependency 55

Figure 3.17 Intensity of EG-PVCap solutions at 950 nm indicating no dependency rather stochastic fluctuations or noise 56

Figure 3.18 Spectra for EG-PVCap-salt solutions showing negligible effect of salt in 300-1100 nm frequency range 57

Figure 3.19 Intensity of EG-PVCap-NaCl solutions at 350 nm indicating match of previously developed exponential dependency for solutions without salt 57

Figure 3.20 Spectra for EG-PVCap-water solutions showing typical trend of EG-water mixture in NIR frequency range and EG-PVCap mixture in UV range 58

Figure 3.21 Spectra for EG-PVCap-water solutions (zoomed 300-400 nm) 59

Figure 3.22 Intensity of EG-PVCap-water solutions at 350 nm indicating no effect of water and match of previously developed exponential dependency 59

Figure 3.23 Intensity change of EG-PVCap-water solutions at 950 nm indicating typical EG dependency with the slope of 0.376 and no effect of PVCap 60

Figure 3.24 Spectra for synthetic solution indicating no influence of heavy hydrocarbon component alone (Decane) 61

Figure 3.25 Spectra for methanol aqueous solution with and without oil indicating the highest influence of oil in the UV region and no effect in NIR region 62

Figure 3.26 Spectra for methanol aqueous solutions with and without sand indicating stochastic influence of sand on the spectrum 63

Figure 3.27 Spectra for BP produced water with various MeOH concentrations 64

Figure 3.28 Intensity change against methanol concentration at 950 nm wavelength showing that BP water trend is similar to what was measured for laboratory water 64

Figure 3.29 Spectra for Total produced water with various MeOH concentrations 65

Figure 3.30 Absorption (optical density) spectra of hydrocarbons, water and CO_2 between 400 and 2000 nm (Betancourt et al., 2006) 66

Figure 3.31 Absorption spectra of original and separated produced water 67

Figure 3.32 Absorption (optical density) spectra of hydrocarbons and CO_2 between 1600 and 1800 nm (Halim et al., 2007) 67

Figure 3.33 Schematic of dielectric permittivity measurement set-up 69

Figure 3.34 Set-up for dielectric permittivity measurements 70

Figure 3.35 Dielectric permittivity against frequency for ethylene glycol aqueous solutions 71

Figure 3.36 Dielectric permittivity against EG concentrations at 4 GHz and 11 GHz 71

Figure 3.37 Dielectric permittivity against frequency for methanol aqueous systems 72

Figure 3.38 Dielectric permittivity against MeOH concentrations at 4 GHz and 11 GHz 72

Figure 3.39 Dielectric permittivity against frequency for aqueous solution with 20 mass% methanol and various NaCl concentrations 73

Figure 3.40 Dielectric permittivity against NaCl concentrations in 20 mass% methanol aqueous solution at 4 GHz and 11 GHz frequencies 74

Figure 3.41 Illustration of the real and imaginary parts of the permittivity as a function of frequency for various dielectric mechanisms (Application Note 1217-1, 1992) 74

Figure 3.42 Dielectric permittivity against frequency for contaminated solutions 76

Figure 3.43 Dielectric permittivity against sample type at 4 GHz and 11 GHz frequencies showing no effect of contamination 76

Figure 4.1 Hydrate suppression temperature for methane hydrates vs. freezing point depression temperature in the presence of aqueous solutions of salts and/or organic inhibitors 83

Figure 4.2 HWHYD model prediction, new and previous correlations for methane hydrate dissociation conditions in the presence of 25 mass% of aqueous EG and 5 mass% NaCl 84

Figure 4.3 Model of the freezing point measurement device. 86

Figure 4.4 Performance graphs for C1-1.4-127-1.14-WPN1 cooling modules (Tellurex Corp., 2007) 87

Figure 4.5 Schematic of the conceptual design of Peltier device 90

Figure 4.6 Prototype structure: left – previous device, right – modified device with three-stage Peltier elements 90

Figure 4.7 Picture of the prototype set-up: left – one-stage Peltier device, right – three-stage Peltier device 91

Figure 4.8 Cells of the prototype device: left – sample cell, right – reference cell 91

Figure 4.9 The performance of the Peltier device with three-stage Peltier elements 92

Figure 4.10 Schematic design 93

Figure 4.11 Schematics of onset of ice formation during the cooling stage 97

Figure 4.12 Melting during the heating stage of measurement cycle 97

Figure 4.13 Delta temperature plotted against sample temperature used to identify freezing point. Delta temperature is the difference between reference and sample temperatures. Freezing point is the sample temperature at which measured data starts descending linear trend. In this example, the measured freezing point is -8.9 ^{o}C for 21.5 mass% aqueous methanol solutions. 98

Figure 4.14 Comparison of the measured freezing point depression with the predicted for the aqueous ethylene glycol and methanol solutions without salts 99

Figure 4.15 Comparison of the measured freezing point depression with the predicted for the aqueous ethylene glycol and methanol solutions in the presence of salt 100

Figure 4.16 Correlated and predicted methane hydrate phase boundary for the aqueous ethylene glycol solutions without salts 101

Figure 4.17 Correlated and predicted methane hydrate phase boundary for the aqueous methanol solutions without salts 102

Figure 4.18 Correlated and predicted methane hydrate phase boundary for the 20 mass% aqueous methanol solutions with various sodium chloride contents 103

Figure 4.19 Correlated and predicted methane hydrate phase boundary for 25 mass% aqueous ethylene glycol solutions with various sodium chloride contents 103

Figure 4.20 GUI of the FPD executable programme for determining pseudo inhibitor concentration using the measured freezing point depression 105

Figure 4.21 HSZs for different fluid systems having the same FP 107

Figure 4.22 (Enlarged picture) HSZ for different fluid systems having the same FP 107

Figure 4.23 Structure I gas hydrate stability zone for fluid systems having the same FP 108

Figure 4.24 (Enlarged picture) Structure I gas hydrate stability zone for fluid systems having the same FP 109

Figure 4.25 Structure II gas hydrate stability zone for fluid systems having the same FP 110

Figure 4.26 (Enlarged picture) Structure II gas hydrate stability zone for fluid systems having the same FP 110

Figure 4.27 Comparison of correlation method with PCM for aqueous solutions with low MeOH-NaCl content which have the same -6.47 ^{o}C freezing point 111

Figure 4.28 Comparison of correlation method with PCM for aqueous solutions with high EG-NaCl content which have the same -16.32 ^{o}C freezing point 112

Figure 4.29 Comparison of correlation method with PCM for aqueous solutions high MeOH-NaCl content which have the same -23.25 ^{o}C freezing point 112

Figure 4.30 Comparison of correlation method with PCM for aqueous solutions with high methanol and ±2 mass% variation in NaCl content showing the PCM methodology robustness and reliability. Solutions have the same -23.25 ^{o}C freezing point. 113

Figure 5.1 Schematic diagram of the high pressure hydrate kinetic rig 117

Figure 5.2 Freezing point depression apparatus (overall view) 117

Figure 5.3 Freezing point depression apparatus (sample probe) 118

Figure 5.4 Preparation of hydrate water and saturated water samples along the paths inside the hydrate phase boundary 119

Figure 5.5 Sample preparation paths inside hydrate phase boundary 122

Figure 5.6 Onset of ice formation for sample preparation paths inside hydrate phase boundary 123

Figure 5.7 Sample preparation paths outside hydrate phase boundary 123

Figure 5.8 Onset of ice formation for sample preparation paths outside hydrate phase boundary 124

Figure 5.9 Sample preparation path for BP produced water 127

Figure 5.10 Onset of ice formations for BP produced water 127

Figure 5.11 Sample preparation path for TOTAL produced water 128

Figure 5.12 Onset of ice formations for TOTAL produced water 129

Figure 6.1 Schematic diagram of the high pressure hydrate kinetic rig 133

Figure 6.2 Pressure-Temperature diagram for a typical gas hydrate (Natural gas and water) to illustrate main definitions used throughout Chapter 6 134

Figure 6.3 Cooling/heating cycles repeated for the distilled water-natural gas system 135

Figure 6.4 Evolution of subcooling temperature for distilled water-natural gas system 137

Figure 6.5 Initial and secondary hydrate formation without mixing 138

Figure 6.6 Evolution of subcooling temperature for 3 mass% aqueous NaCl solution 139

Figure 6.7 Evolution of subcooling temperature for 5 mass% aqueous NaCl solution 140

Figure 6.8 Evolution of subcooling temperature for 10 mass% aqueous NaCl solution 141

Figure 6.9 Evolution of subcooling temperature for 15 mass% aqueous MeOH solution 142

Figure 6.10 Evolution of subcooling temperature for aqueous solution containing 3 mass% NaCl and 15 mass% MeOH 143

Figure 6.11 Evolution of the onset of hydrate formation temperature for 30 mass% aqueous MeOH solution 144

Figure 6.12 Evolution of subcooling temperature for 15 mass% aqueous EG solution 145

Figure 6.13 Evolution of subcooling temperature for aqueous solution containing 3 mass% NaCl and 15 mass% EG 146

Figure 6.14 Evolution of subcooling temperature for 30 mass% aqueous EG solution 147

Figure 6.15 Evolution of subcooling temperature for water with 15 mass% EG systems 148

Figure 6.16 Summary of various aqueous solutions tests with 1 hour dissociation 150

Figure 6.17 Summary of various aqueous solutions tests with 12 hours dissociation 150

Figure 6.18 Picture of the tall-narrow hydrate mini-rig set-up 152

Figure 6.19 Sample temperature-pressure path showing no sign of hydrate formation 153

Figure 6.20 Picture of the short-wide hydrate mini-rig set-up 154

Figure 6.21 Sample temperature-pressure path showing notable hydrate quantities formed 154

LIST OF TABLES

Table 2.1 Natural gas composition 27

Table 2.2 Summary of UV/VIS spectroscopy results for the main stages of hydrate formation and dissociation processes. Attenuation parameter (at 350 nm and 750 nm) will be related to the amount of hydrate formed in the next (stage two) experiment. 30

Table 2.3 Relation between attenuation coefficient and amount of hydrate formed 33

Table 3.1 Light intensities for MeOH aqueous solutions at 450 nm, 670 nm and 950 nm 44

Table 3.2 Light intensities for EG aqueous solutions at 450 nm, 670 nm and 950 nm 46

Table 3.3 Oil composition (from North Sea Brent reservoir) 62

Table 3.4 Typical dielectric permittivities at room temperature (Uematsu et al., 1980; Akerlof, 1932) 69

Table 4.1 The K values for some gas hydrate inhibitors 80

Table 4.2 Maximum concentration (based on water) of salts and/or organic inhibitors in the aqueous phase systems used in the development of the correlation 82

Table 4.3 Main prototype components 86

Table 4.4 Specifications of Peltier element 86

Table 4.5 Temperature at Peltier element sides for different cooling systems 88

Table 4.6 Constants used in heat transfer calculations 88

Table 4.7 Specification of the main elements for the final freezing prototype 94

Table 4.8 Freezing point of aqueous methanol and ethylene glycol solutions (Weast et al., 1989) 96

Table 4.9 Measured and predicted freezing point depression 99

Table 4.10 Measured and predicted freezing point depression 100

Table 4.11 Gas composition 106

Table 4.12 Freezing points for various aqueous phase compositions 106

Table 4.13 Composition of gas forming structure I gas hydrate 108

Table 4.14 Gas composition forming structure II gas hydrate 109

Table 5.1 Types of samples prepared to investigate the memory phenomenon 119

Table 5.2 Nucleation rates for various water samples 124

Table 5.3 Mean freezing temperatures, divergence area, nucleation rates and t-, f-, ks-tests for 4 tests on deionised water 125

Table 5.4 Freezing points and nucleation rates for BP produced water samples 128

Table 5.5 Freezing points and nucleation rates for TOTAL produced water samples 129

Table 6.1 Subcooling temperature of hydrate formation measured in the repeated cooling- heating cycles for distilled water-natural gas system 136

Table 6.2 Subcooling temperature of hydrate formation after heating to various temperatures in the depressurisation tests 137

Table 6.3 Subcooling temperature of hydrate formation measured in the repeated cooling- heating cycles for 3 mass% aqueous NaCl solution 139

Table 6.4 Subcooling temperature of hydrate formation measured in the repeated cooling- heating cycles for 5 mass% aqueous NaCl solution 140

Table 6.5 Subcooling temperature of hydrate formation measured in the repeated cooling- heating cycles for 10 mass% aqueous NaCl solution 141

Table 6.6 Subcooling temperature of hydrate formation measured in the repeated cooling- heating cycles for 15 mass% aqueous MeOH solution 142

Table 6.7 Subcooling temperature of hydrate formation measured in the repeated cooling- heating cycles for solution containing 3 mass% NaCl and 15 mass% MeOH143

Table 6.8 Subcooling temperature of hydrate formation measured in the repeated cooling- heating cycles for 30 mass% aqueous MeOH solution 144

Table 6.9 Onset of hydrate formation temperature measured in the repeated cooling-heating cycles for 15 mass% aqueous EG solution 145

Table 6.10 Subcooling temperature of hydrate formation measured in the repeated cooling- heating cycles for aqueous solution containing 3 mass% NaCl and 15 mass% EG 146

Table 6.11 Subcooling temperature of hydrate formation measured in the repeated cooling- heating cycles for 30 mass% aqueous EG solution 147

Table 6.12 Onset of hydrate formation temperature measured in the repeated cooling-heating cycles for water with 15 mass% EG systems 148

Table 6.13 Summary of various aqueous solutions tests 151

Table 7.1 Techniques categorised by their applicability in laboratory and industrial conditions 157

CHAPTER 1 INTRODUCTION

1.1 CONCEPT OF HYDRATE MONITORING AND EARLY WARNING

Increasing demand for the world energy resources leads the petroleum industry to extend the development of oil and gas fields further into the deepwater driving the innovations in offshore technologies and flow assurance. World primary energy consumption (Figure 1.1) fell by 1.1% in 2009, the first decline since 1982, followed the consecutive year of growth (BP Statistical Review of World Energy, June 2010). As a result of misbalance between energy supply and demand, oil price (Figure 1.2) has subsequently dropped. Energy developments in 2009 were dominated by a global recession. Currently, prices have an upward trend following the economic recovery. The prices are slowly returning to 2000-2010 decade tendency. Fundamentally, the growth in oil price can make it economically feasible to develop petroleum provinces located at high water depths and long distances from a shore. Production at those extremes requires the application of advanced flow assurance techniques which can effectively tackle hydrate, wax, asphaltenes, inorganic scale deposition, solids, corrosion, and erosion problems.

In a survey of 110 energy companies, flow assurance was listed as the major technical problem in offshore energy development (Welling at al., 2000). Flow assurance is extremely diverse, encompassing many discrete and specialized subjects and bridging across the full range of engineering disciplines. Among all of the severe aspects addressed by flow assurance engineers, hydrates are the leading problem, by an order of magnitude. Hydrate can damage or block hydrocarbon transportation lines and the surface processing facilities (Tohidi, 1995). The financial loss from production interruption or asset damage due to flow assurance mishap can be astronomical. Major health, safety and environmental concerns can be caused by hydrates formation.

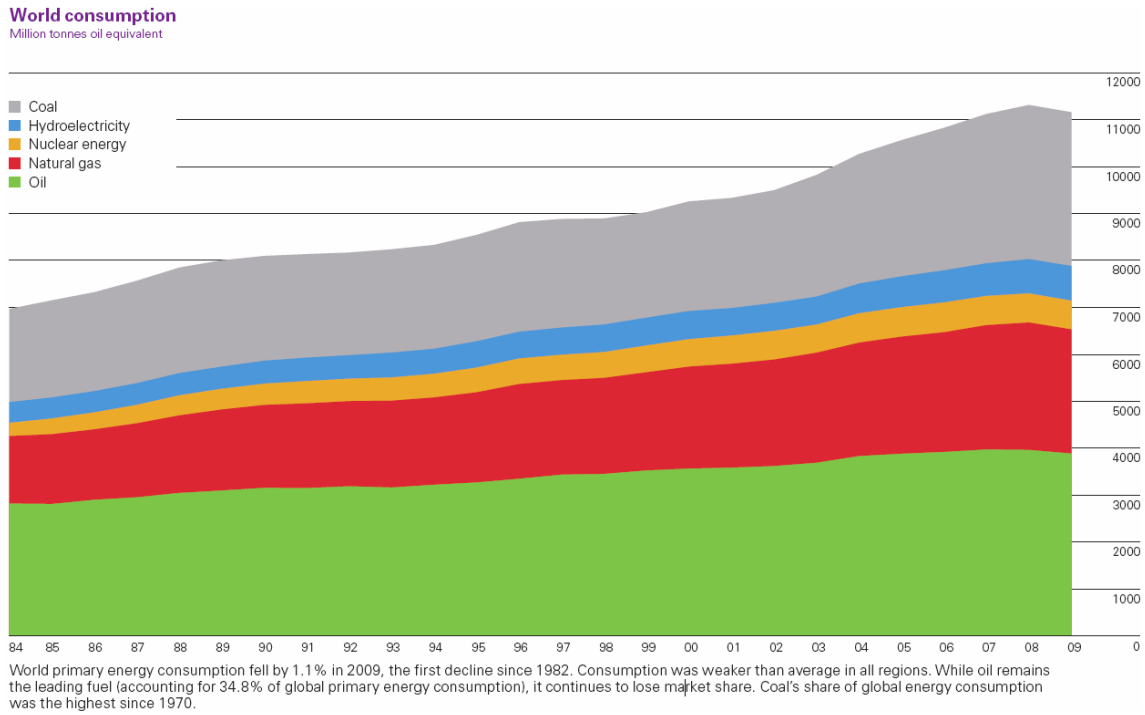

Figure 1.1 World consumption of primary energy by fuel type

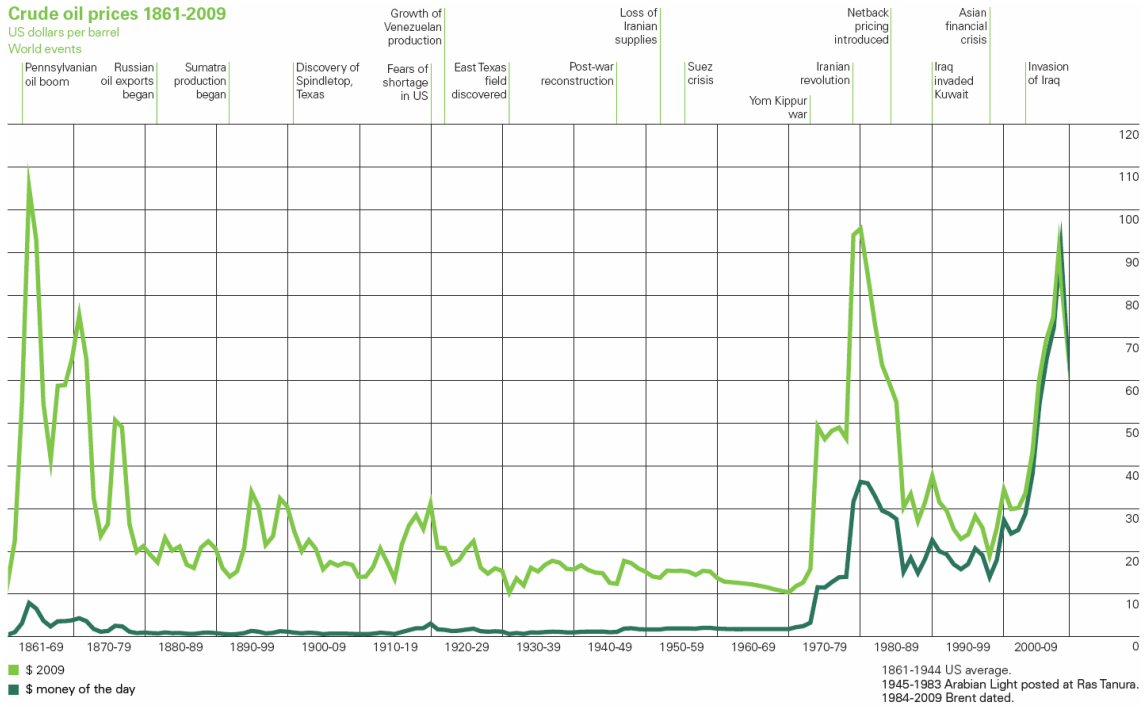

Figure 1.2 Crude oil prices 1861-2009 in US dollars per barrel (Source: BP Statistical Review of World Energy 2010)

Gas hydrates are non-stoichiometric crystalline compounds that belong to the inclusion chemical group called clathrates. Physically resembling ice, gas hydrates are crystalline

water based solids forming when non-polar or slightly polar molecules (guest) of suitable size are trapped inside "cages" of hydrogen bonded water molecules (host) under favourable high-pressure and low-temperature conditions. Hydrates were first obtained by the great English philosopher and naturalist Priestly in Birmingham, U.K. in 1778, under laboratory conditions by bubbling SO_2 through 0 °C water at atmospheric pressure (Priestly, 1790; Makogon et al., 2007). However, they were not massively recognised until 1934, after American chemist Hammerschmidt discovered that hydrates were a cause of plugging natural gas transmission lines in the United States (Hammerschmidt, 1934). This led to significant research efforts focusing on chemistry and physics of hydrate formation.

The three most common types of hydrate structures that form naturally in gas/water mixtures are structure I, structure II and structure H. The determination of two hydrate crystal structures (sI and sII) happened in the late 1940s and early 1950s (von Stackelberg et al., 1949; von Stackelberg et al., 1954). The existence of sH was discovered in 1987 (Ripmeester et al., 1987). Hydrate structure H was discovered to form in the laboratory conditions as well as in the nature, e.g. Gulf of Mexico continental slope (Sassen et al., 1994). The importance of structure H hydrates in oil and gas production has not been clarified yet. However, sH forms from both small molecules such as methane and larger molecules commonly found in condensate or oil (Sloan et al., 2008). Exploring new and less common hydrate structures is becoming of increasing interest. A new hydrate structure T has been recently discovered (Udachin et al., 2001) in which all the large cages are occupied by dimethyl ether guest molecules. In addition, two new structures MH-II and MH-III were found which can describe formation of methane hydrate in space, e.g. in the primordial core of Titan, at high pressures up to 10 GPa and low temperatures around 150 K (Loveday et al., 2001). It is likely that more hydrate structure types will be discovered in the future.

Hydrate structures consist of repetitive crystal units called “cages”, as shown in Figure 1.3, formed by hydrogen-bonded water molecules. Cages are asymmetric and spherical-like. Each hydrate structure is composed of a certain number of large and small cavities. The minimum fraction of structure cavities has to be filled with the guest molecules to stabilize a hydrate crystal. At usual pressures, each cage can accommodate at most one guest molecule, held within the cage by dispersion forces. However, at very high pressures, nitrogen, hydrogen, methane, and argon can multiply occupy the large cavity of structure II (Sloan et al., 2008).

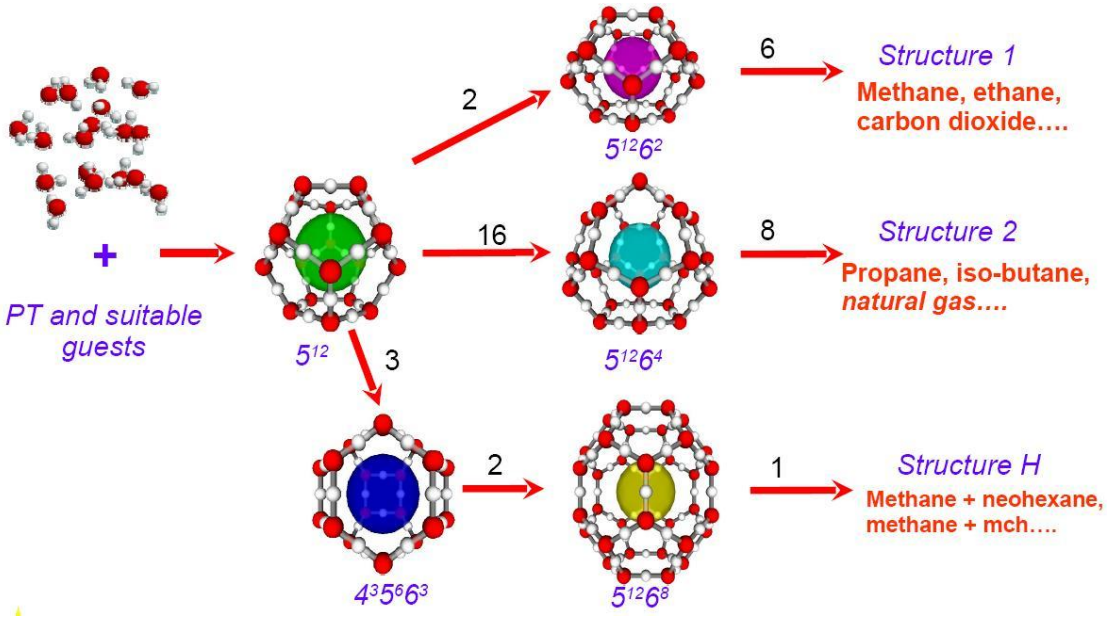

Figure 1.3 Clathrate hydrate structures

46 water molecules form the unit cell of structure I which is a 12 Å cube consisting of two types of cavities: two small cavities are pentagonal dodecahedra (5^{12}); six large cavities are tetradecanhedra ($5^{12}6^2$). This structure is formed with molecules smaller than 6 Å, such as methane, ethane, carbon dioxide, and hydrogen sulphide. Nitrogen and smaller molecules (d<4.2 Å) are exceptions and form structure II as single guests.

136 water molecules form the unit cell of structure II which is a 17.3 Å cube containing two types of cavities: 16 smaller cavities are distorted pentagonal dodecahedra; 8 larger cavities are hexadecahedra ($5^{12}6^4$). Larger (6 Å<d<7 Å) single guest molecules such as propane or iso-butane can form structure II.

34 water molecules form a hexagonal lattice of structure H with parameters a = 12.26 Å and c = 10.17 Å consisting of three different types of cavities: three cavities are pentagonal dodecahedra; two new 12 faces $4^35^66^3$ cavities; one new large $5^{12}6^8$ cavity. Larger molecules (7 Å<d<9 Å) such as iso-pentane or neohexane can form structure H provided they are accompanied by smaller molecules such as methane, hydrogen sulphide, or nitrogen (Sloan et al., 2008).

Gas hydrates can form in conditions where water and suitably sized gas molecules exist under favourable pressure and temperature. The set of pressures-temperatures at which hydrate can form is called hydrate stability zone (Figure 1.4). The boundary of hydrate stability zone (HSB) depends upon composition of aqueous and hydrocarbon phases.

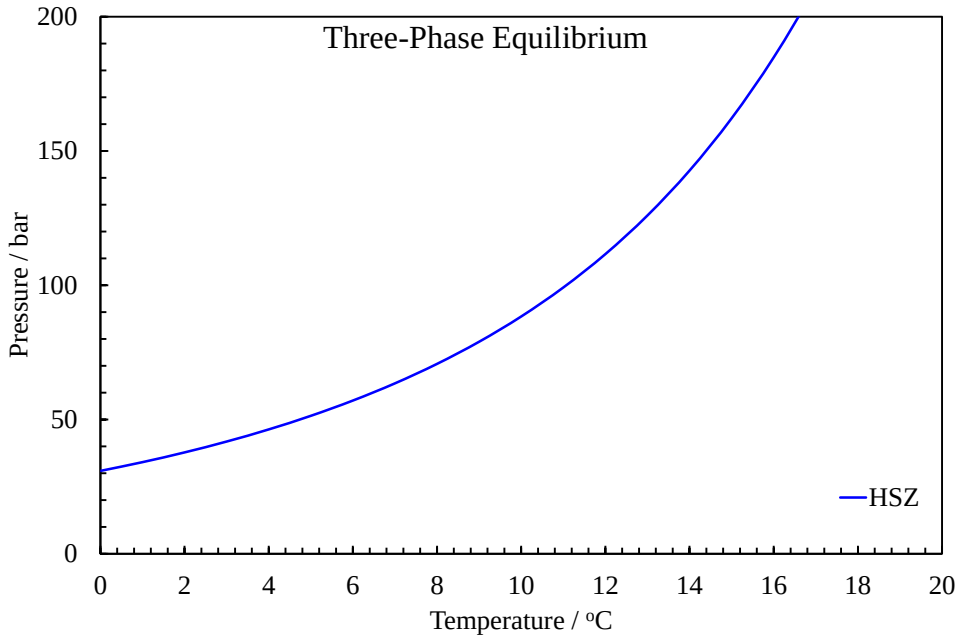

Figure 1.4 Example of structure I hydrate stability boundary for simple methane-water mixture

Two major areas of hydrate appearance are technogenic (due to an industrial activity) and natural gas hydrates (Tohidi et al., 1993). Natural gas-hydrates received a high attention over last decades and are considered as an unconventional source of energy (Makogon et al., 2007). Over 220 gas-hydrate deposits (Figure 1.5) have been found in the world to date.

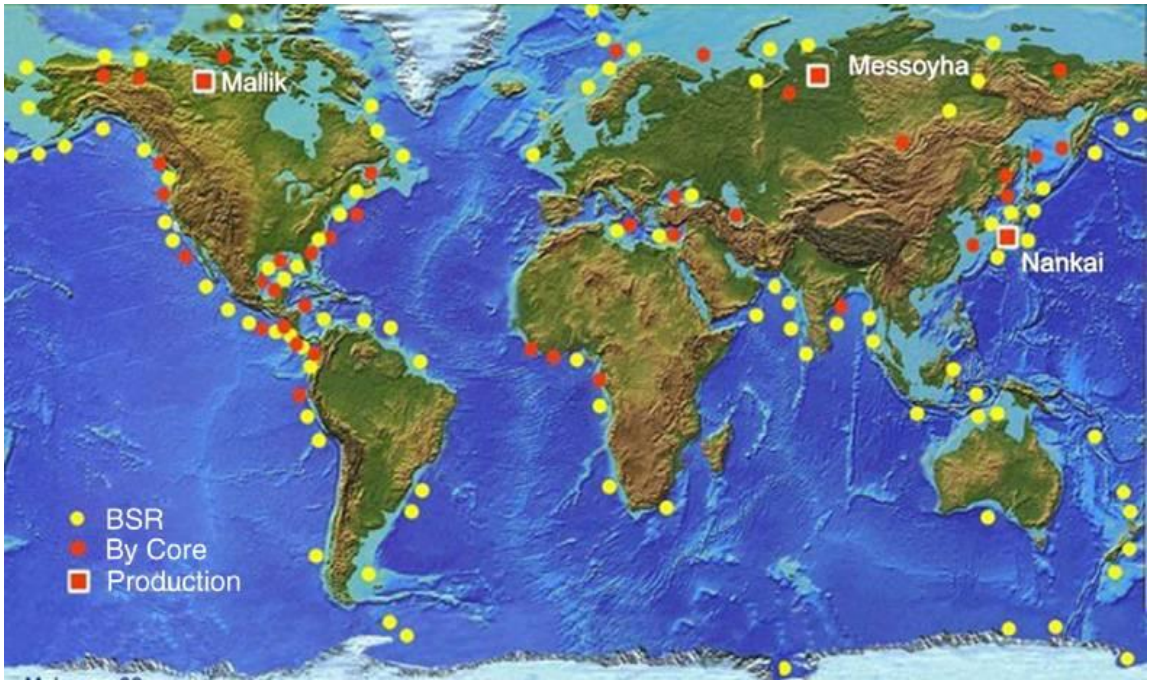

Figure 1.5 Map of discovered gas-hydrate deposits (Makogon et al., 2004).

Technogenic formation of gas hydrates is mostly associated with damage, blockage and shutdown of gas and oil subsea pipelines, valves or processing instrumentation. Conditions for technogenic hydrate formation depend on composition of aqueous and hydrocarbon phases. In the petroleum pipeline, the gas which is similar to natural gas by composition can be produced from reservoirs or come out of solution then fluid flowing pressure drops below bubble point. The main component of natural gas is methane with the remainder composed of other hydrocarbon gases (ethane, propane, etc.) and non-hydrocarbon gases (carbon dioxide, nitrogen, etc.). Because of its composition, natural gas in conjunction with free water present in the transmission line is a good former of structure II hydrates. Free water can be present in the produced fluid as formation water, injected water, and/or condensed water (due to changes in the pipeline temperature and pressure conditions).

Having all necessary components in place and favourable pressure-temperature conditions, gas hydrate can start to form. Several theories have been developed explaining the mechanisms of hydrate formation. Lederhos proposed that gas hydrates form in an autocatalytic reaction mechanism (Lederhos et al., 1996), when water molecules cluster around natural gas molecules in structures (Figure 1.6). Recent research describing the trend in water structure during the hydrate formation and decomposition by using neutron diffraction showed that hydrate crystal begins to form at several places within the sample, in such a way as to trap or "confine" the remaining gas-water liquid in small pores (Buchanan et al., 2006).

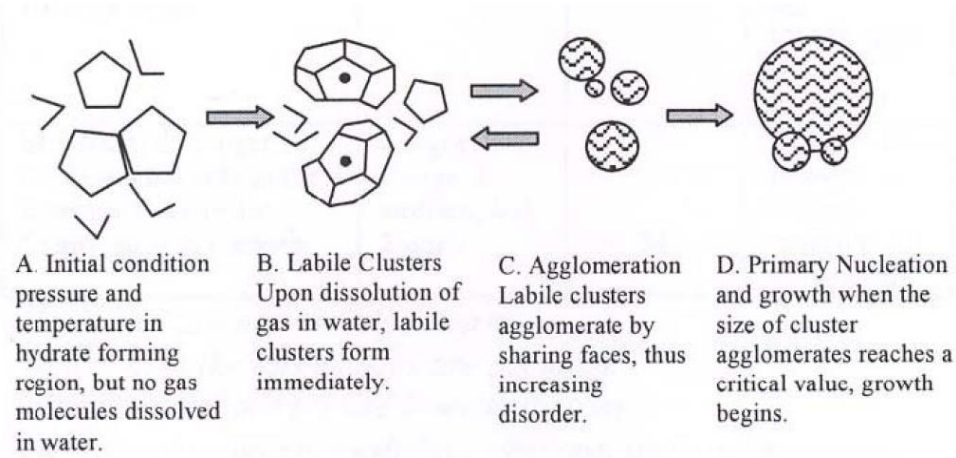

Figure 1.6 Autocatalytic reaction mechanisms for hydrate formation (Lederhos et al., 1996)

Since the formation of hydrate is associated with the high risk of plugging and damaging transporting pipelines, several mechanisms have been developed to avoid those problems:

- Preventing hydrates by controlling one of their formation parameters including flowline pressure (well choking/pumps operation) and temperature (heating and/or insulating).

- Inhibiting hydrate formation by adding chemical inhibitors to the produced fluids.

- Allowing hydrate formation with a control of crystals size by the means of polymeric chemicals called anti-agglomerates (AA). Avoiding agglomeration of hydrate crystals and hence avoiding pipeline blockage can lead to additional benefits of gas transportation as hydrate slurry.

Based on economic aspects and availability of resources, a common method practiced in the industry to avoid hydrate risks is the injection of thermodynamic inhibitors to prevent hydrate formation or the use of kinetic hydrate inhibitors to sufficiently delay hydrate nucleation or growth (Sloan et al., 2005). Currently, the amount of inhibitor required is either calculated and/or determined based on lab experiments. Despite the usual safety precautions, gas hydrates are formed in the transmission line which could result in serious operational, economic and environmental concerns. One of the examples can be "1991 Gulf Oil Incident". On 10 January 1991, the Rimbey gas plant was in the start-up mode. A hydrate or ice plug formed in the overhead line from the amine contactor. The line had been depressurised to the flare system, downstream of the plug. The ambient temperature, which had been –1.1 ^{o}C, rose rapidly owing to warming winds around midnight. At 2 a.m. the overhead line came apart, killing the chief operator. In addition, the plant suffered approximately U.S. $6 million in damages. Pre-existing cracks in the pipeline contributed to this failure. While these cracks did not impair the piping's pressure-containing ability under steady-state conditions, they reduced the piping strength under the transient (impact) conditions when the plug broke free (Sloan et al., 2000).

In some cases, the amount of injected inhibitor is more than what is necessary for hydrate prevention being not adjusted with seasonal changes which can lead to increase in CAPEX and OPEX, and the unnecessary pollution of the environment. These

happen, because hydrate prevention techniques are applied without much downstream measurements.

This Thesis presents a research in the development of downstream online measurements for:

1. Monitoring the hydrate safety margin to optimize the inhibitor injection rates and/or operational conditions. The systems investigated determine the amount of inhibitor in the aqueous phase and/or directly the hydrate phase boundary given that the gas/oil composition is known.

2. Early warning system against hydrate blockage based on the detection of the initial hydrate formation. The systems investigated detect changes in physical properties of pipeline fluid due to hydrate formation with the aim of giving the operator enough time to prevent a blockage.

Hydrate Monitoring and Early Warning Systems represent a real-time monitoring and controlling technologies which can be installed as a part of the industrial SCADA systems, e.g. ISIS developed by BP (Figure 1.7). This additional functionality will extend the informational system capabilities to pipeline flow assurance.

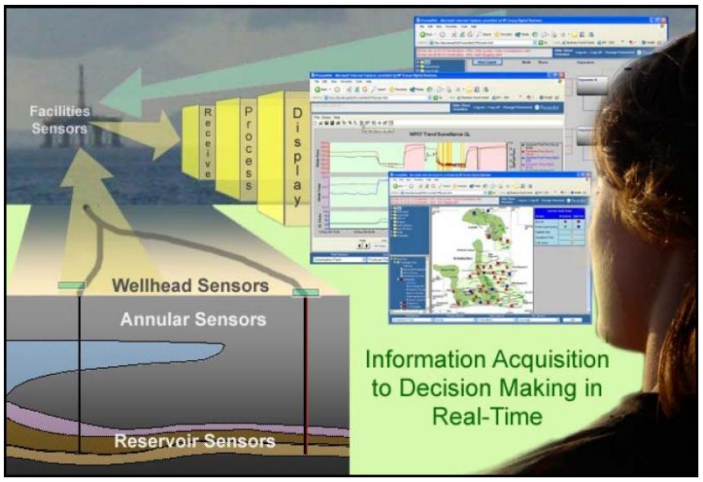

Figure 1.7 Integrated Subsurface Information System (Foot at al., 2006)

Alternatively, the monitoring and early warning systems can be operated on a stand-alone basis (Figure 1.8) where the informational environment is governed by a web server and consists of three parts: User, Pipeline, and Surface Facilities. Each part has its own working algorithm while User part is unique by the presence of human-machine interface (see Appendix A). To be used efficiently, the developed systems should meet

the following requirements: to operate under standardized protocols to flexibly add/remove measuring devices, and to be easily expanded or fixed after failures; to possess to date analytical toolbox for processing the gathered data.

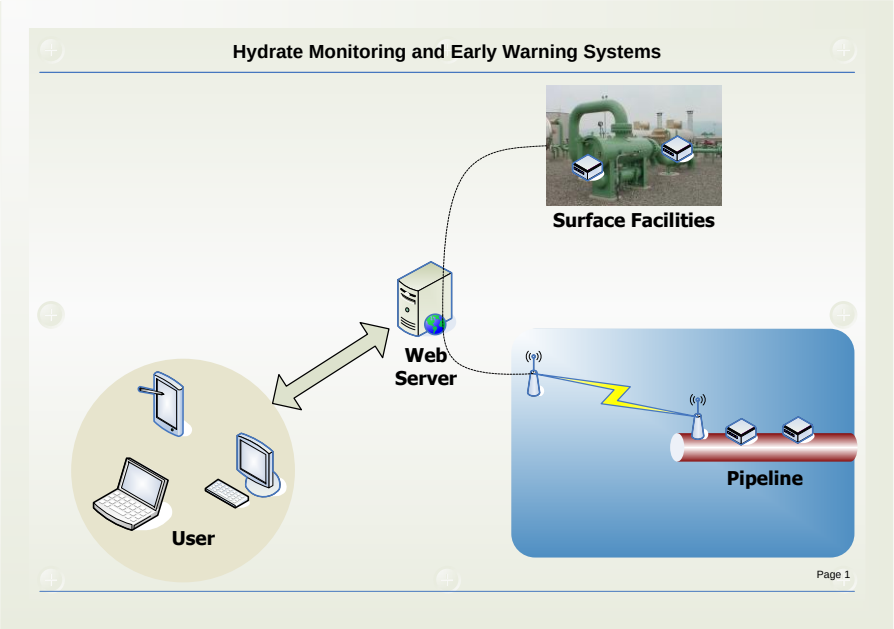

Figure 1.8 Stand-alone monitoring and early warning systems

1.2 HYDRATE MONITORING SYSTEMS

The aim of hydrate monitoring techniques is to provide an accurate and timely data of the degree of hydrate inhibition in the pipeline or processing facilities. The methods perform measurements of physical parameters of produced fluids which are then used to either directly calculate hydrate phase boundary or indirectly through inhibitors concentrations. The determined phase behaviour of produced fluids is compared with the operational conditions of the production unit in which the measurements take place. If the operational pressure and temperature are inside the hydrate stability zone than the unit is under the risk of hydrate formation and blockage, and, therefore, warning is generated to operator to take precautions actions. Alternatively, if the operating point is outside the phase boundary than the system can be over inhibited indicating to operator that the inhibitors injection rate can be optimized to minimize their environmental impact and improve the economic aspects of field operation. The method diagram is presented in Figure 1.9.

Several techniques have been investigated for hydrate monitoring purposes. These are:

1. Freezing point depression method;
2. Concentration monitoring by Spectroscopy method;
3. Concentration monitoring by Dielectric Permittivity Method.

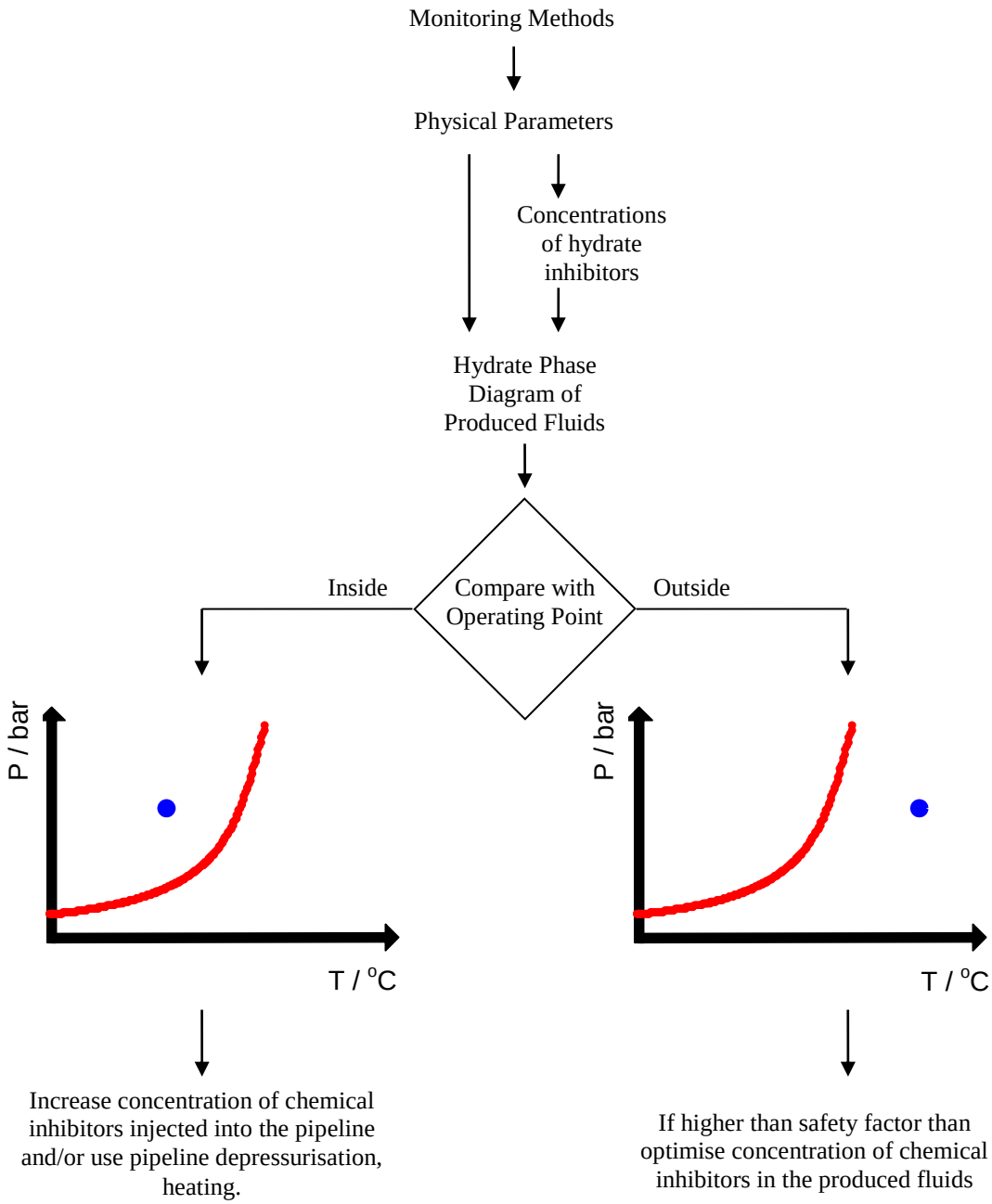

Figure 1.9 Hydrate monitoring systems diagram

1.2.1 Freezing Point Depression Method

One of the hydrate monitoring systems can be based on simple techniques such as freezing point depression measurement for aqueous phase. Previously several investigators have correlated the degree of hydrate inhibition in terms of the amount and nature of the inhibitor present in the system. In the 1930s Hammerschmidt presented a semi-empirical equation (Hammerschmidt, 1939) for predicting hydrate depression of typical natural gases in contact with dilute aqueous solutions of antifreeze agents such as methanol or ethylene glycol.

In this work, the device prototype was developed to physically measure the freezing point of the aqueous solution. The measured freezing point is then used either to correlate distilled water to the aqueous solution hydrate phase boundary or to find pseudo concentrations of the hydrate inhibitors which are thereafter used for calculation of the phase boundary. In the first method, degree of hydrate inhibition was directly correlated to the freezing point depression due to the presence of salt and/or organic inhibitors in the aqueous phase, regardless of the type and amount of the salts and/or inhibitors present in the system, eliminating the need for compositional analysis of the aqueous phase. In the second method, concentration of pseudo (or supposed) inhibitor(s) is matched against the measured freezing point of the aqueous solution. These concentrations can be imprecise, but rather can be used to calculate hydrate stability zone by means of thermodynamic models, e.g. HydraFLASH® (Hydrafact Ltd., 2010).

1.2.2 Spectroscopy Method

Light is electromagnetic wave radiated within a wavelength range from 100 nm to 1 mm. There are three major wavelength ranges in the light: ultraviolet (UV) from 100 nm to 400 nm, visible (VIS) from 400 nm to 750 nm, and infrared (IR) from 750 nm to 1 mm. UV/VIS/NIR spectroscopy technique is used in petroleum industry for concentration analysis and monitoring of treating chemicals (Brost et al., 1991; Schake et al., 2001). Beer-Lambert Law is used to determine concentrations in the fluid systems. The spectroscopy method was recently successfully applied to measure the alcohol and other additives concentration in spirit drinks (Dirk et al., 2007), as well as to distinguish various chemical mixtures in synthetic and water samples (Hasani et al., 2007).

In this work, the spectroscopy technique was applied to monitor the concentration of hydrate inhibitors in the aqueous solutions which is then considered as input parameters for thermodynamic models for predicting the hydrate phase boundary. Various aqueous solutions containing alcohols (Methanol and Ethylene Glycol), KHI (PVCap) and/or salt (Sodium Chloride) were tested to identify spectral ranges affected by the presence of specific hydrate inhibitor.

1.2.3 Dielectric Permittivity Method

Permittivity is a physical quantity that describes how an electric field affects and is affected by a dielectric medium. Dielectric permittivity is determined by the ability of a material to polarize in response to the field, and thereby reduce the total electric field inside it. Thus, permittivity relates to a material's ability to transmit (or "permit") an electric field. With application to the petroleum industry, some of the researchers comprehensively studied the different types of ionic and nonionic micro-emulsions with their static and dynamic dielectric properties as a function of temperature, frequency and concentration of water, oil, surfactant and co-surfactant (Feldman et al., 1997). This physics can be applied to the hydrogen bonding of alcohols in aqueous solutions so that alcohol dipole relaxation can be studied by measuring the complex permittivity (Smith et al., 1998). In this work, a simple hydrate inhibitor concentration measurement technique based on dielectric permittivity was investigated with the aim of being applied in the monitoring systems.

1.3 HYDRATE EARLY WARNING SYSTEMS

The aim of hydrate early warning techniques is to provide timely signals of initial hydrate formation in the pipeline and/or processing facilities. The methods provide measurements of physical parameters of fluids flow and/or fluids samples which are then used to determine whether the initial hydrate formation took place in the system. The provided measurements can detect either minute hydrate particles and/or changes in the water structure referred as hydrate water memory (Buchanan et al., 2005; Thompson et al., 2006). The signals are designed to give the operator adequate time to initiate remedial steps prior to massive hydrate formation/build up which could result in pipeline/facilities blockage. The method diagram is presented in Figure 1.10.

To meet the above objectives, several techniques were investigated:

1. Onset of Ice Formation

2. Onset of Hydrate Formation

3. Electromagnetic methods

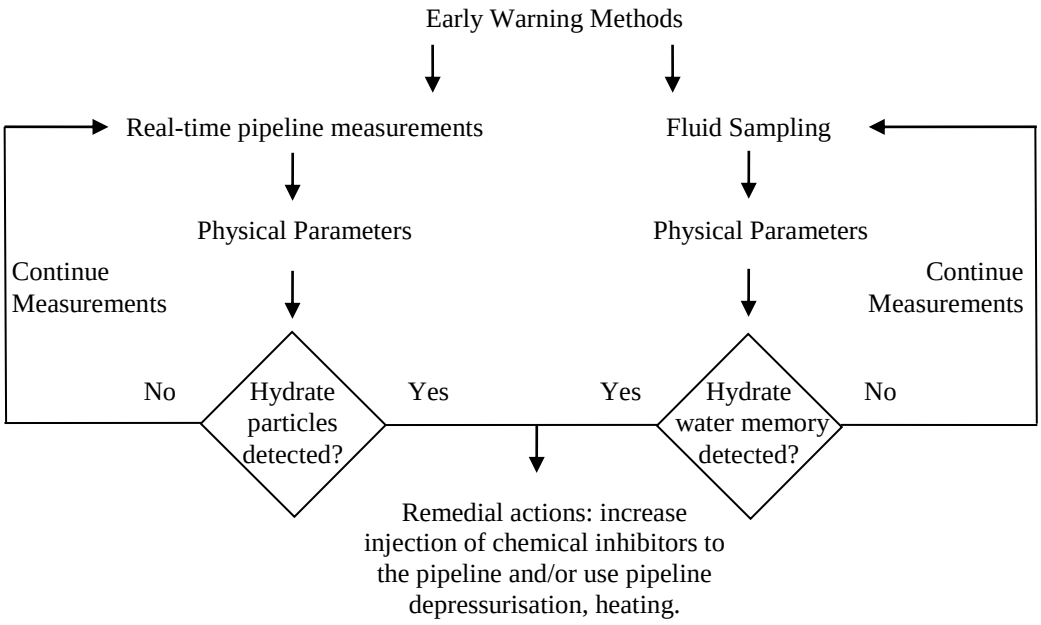

Figure 1.10 Early warning systems diagram

1.3.1 Onset of Ice Formation

The onset of ice formation by freezing method is considered as one of the potential techniques for hydrate early warning systems. The theoretical principle of the method is based on detection of the hydrate memory in water (Toschev et al., 1972; Takeya et al., 2000; Ohmura et al., 2003). In the production pipeline, labile hydrate clusters can form and disintegrate (Figure 1.6, stage C) under favourable pressure-temperature conditions. The produced water can keep the memory of those hydrate nuclei fluctuations. The objective is to detect this memory at the sampling point. In the work presented here, the onset of ice formation by freezing method is investigated for detecting the hydrate water memory.

1.3.2 Onset of Hydrate Formation

As an alternative to the stochastic ice formation method, a new technique was proposed which is based on hydrate formation. The principal of the technique is that hydrate forms more easily from a solution with hydrate memory than from a freshly prepared gas-water mixture. Nevertheless, some researchers measuring crystallinity by using

neutron diffraction before hydrate formation and after dissociation doubt about hydrate water memory (Buchanan et al., 2005), others are heavily investigating this phenomenon (Thompson et al., 2006; Zeng et al., 2006). In this work, the hydrate water memory by hydrate formation method was investigated for various aqueous solutions under various temperature, timing and mixing conditions.

1.3.3 Electromagnetic Methods

There are several evidences to support the fact that physical phenomenon called water memory is sensitive to and can be studied by electromagnetic (EM) methods. Water molecules are dipoles which interact with the external and internal EM field. Due to polarity of the water molecules, they can coordinate into an instantaneous hydrogen bonded network (Eisenberg et al., 1969; Franks, 1972), studied by different EM experimental techniques (Palese et al., 1996; Ratajska-Gadomska et al., 2006) and molecular dynamics simulations (Bursulaya et al., 1996; Guardiaa et al., 2002), which is responsible for all specific features of this liquid. Being cooled, water molecule electrons can increase local density of states close to $3a_1$ orbital altering water electromagnetic properties (Nordlund et al., 2008). Therefore, the memory effect itself can be related to preservation of orientation of EM field in the solution after experiencing a specific treatment. In this work, dielectric permittivity, magnetic susceptibility and spectroscopy techniques were applied to investigate the memory effect of water experienced formation of hydrate solid state. Research was also carried out to investigate the impact of hydrate formation on the light spectrum in order to see if light properties can be used for fast detection of early hydrate formation.

1.4 THESIS AS PART OF JOINT INDUSTRIAL PROJECT

Hydrate monitoring and early warning systems are aiming to reduce the risk of gas hydrate deposition in oil and gas pipelines and processing facilities. Several physical hypotheses were generated and examined for this purpose. Some of them showed a high potential to be employed in the industry. The thesis represents a part of a joint industrial project investigating and developing 3 methods for monitoring and 3 methods for early warning systems. JIP workflow (Figure 1.11) consists of the following main steps:

1. Generate a bank of physical methods to be applied for both systems;

2. Develop one or two methods for hydrate monitoring systems;

3. Develop one or two methods for hydrate early warning systems;

4. Design and build a working hydrate monitoring prototype;

5. Design and construct a working early warning system prototype.

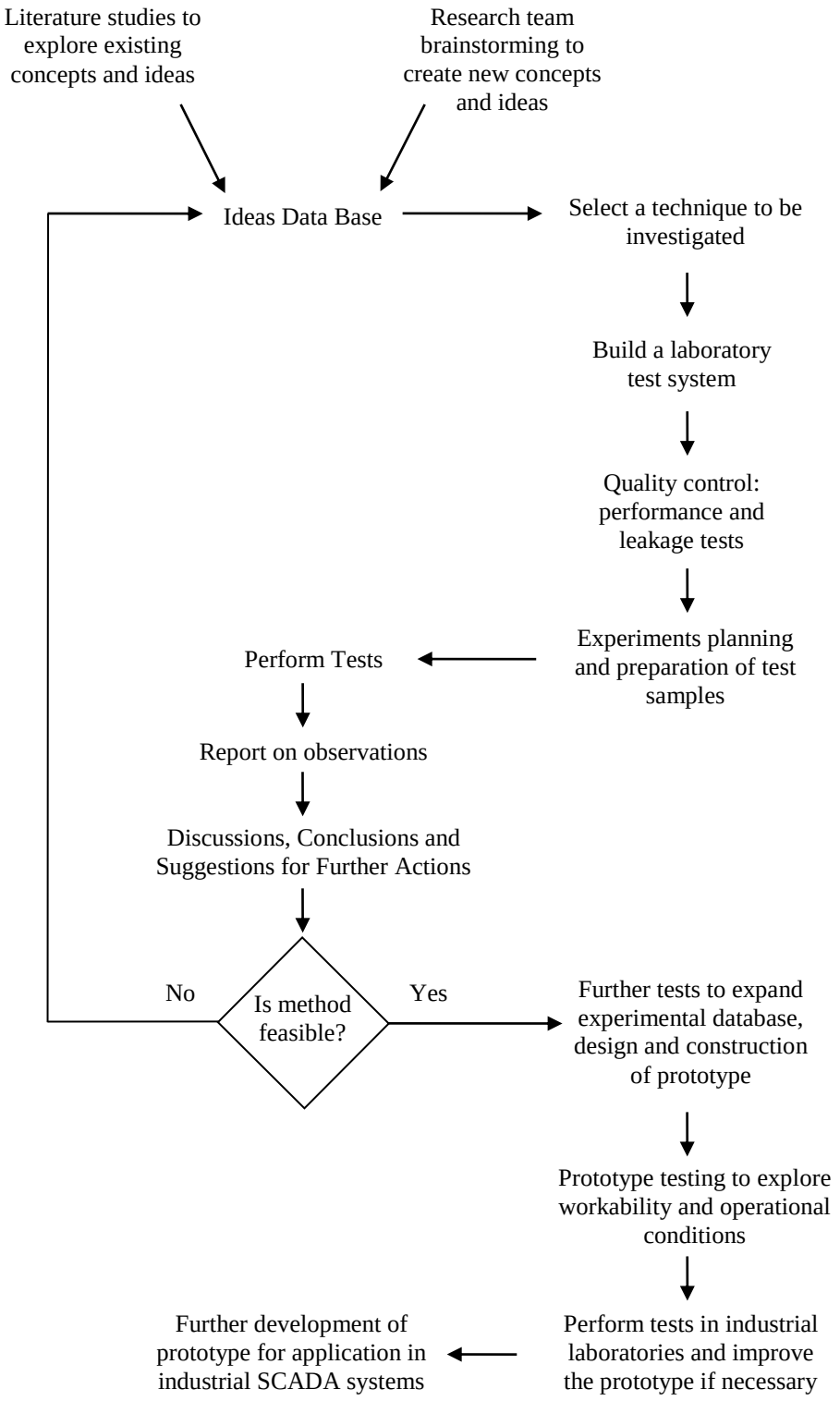

Figure 1.11 JIP research workflow diagram

1.5 STRUCTURE OF THE THESIS

The thesis contains 7 chapters. The present chapter introduces the concept of hydrate monitoring and early warning systems, presenting the main definitions and sets the aims and methodological foundation of the research.

Chapter 2 is dedicated to the application of spectroscopy method commonly used in analytical chemistry and physics to the thesis topic. The spectroscopy technique was investigated to figure out if hydrates formation and dissociation can influence light properties. Applicability of the technique is proposed for hydrate nuclei detection, hydrate water history detection in water samples, inhibitor concentration monitoring.

Chapter 3 details on hydrate monitoring techniques based on dielectric permittivity and spectroscopy measurement to determine the concentrations of chemical inhibitors in the production system. The determined concentrations of hydrate inhibitors then can be used to predict hydrate stability zone for industrial application.

Chapter 4 describes one of the monitoring techniques based on freezing point of aqueous solution. The scientific approach and development of prototype device are presented.

Chapter 5 reports on the onset of ice formation by freezing method. The method is considered as one of the potential techniques for hydrate early warning systems based on detection of the hydrate memory in water.

Chapter 6 is concentrated on an alternative to the stochastic ice formation method, a new technique which is based on hydrate formation. The principal of the technique is that hydrate forms more easily from a solution which experienced hydrate solid state in the past than from a freshly prepared gas-water mixture. In this work, the hydrate water memory by hydrate formation method was investigated for various aqueous solutions under various temperature, timing and mixing conditions.

Finally, in Chapter 7, the main conclusions drawn from all the sections of this thesis are reported. Novelty of this work, new challenges and opportunities that hydrate monitoring and early warning systems can bring in the area of flow assurance for the petroleum industry are summarised.

CHAPTER 2 UV/VIS/NIR SPECTROSCOPY

2.1 INTRODUCTION

The industry is facing rising flow assurance challenges due to deepwater exploration and production and increased risk of hydrate deposition in pipelines at inaccessible locations. Any blockage in a transfer line due to hydrate is a serious concern to the economics of field development, cost effective strategy of remediation and personnel safety. One of the problems other than blockages is the movement of the hydrate plugs in the pipeline causing rupture in the pipeline. The current industry practice for hydrate prevention is injecting hydrate inhibitors at the upstream end of pipelines based on the calculated or measured hydrate phase boundary, water cut, worst pressure and temperature conditions, the amount of inhibitor lost to non-aqueous phases, and a safety factor. Generally, systematic approach of controlling and monitoring the degree of inhibition along the pipeline and downstream is limited. In this section of the thesis, the spectroscopy technique which is used as an important instrument in analytical chemistry and physics was investigated for the application in hydrate monitoring and early warning systems.

The Electromagnetic spectrum is a continuous range of radiation encompassing γ-rays, X-rays, light, microwaves and radiowave (Figure 2.1). Light is electromagnetic wave radiated within a wavelength range from 100 nm to 1 mm further subdivided into three major ranges: ultraviolet (UV) from 100 nm to 400 nm, visible (VIS) from 400 nm to 750 nm, and infrared (IR) from 750 nm to 1 mm. Phenomenon of light absorption by matter is used to analyse samples in UV/VIS/IR regions of electromagnetic spectrum, in laboratories throughout the world. UV/VIS/IR spectroscopy technique is generally used in petroleum industry for concentration analysis and monitoring of treating chemicals (Brost et al., 1991; Schake et al., 2001). Moreover, spectroscopy is used to obtain

physical information on produced fluids, more specifically for monitoring of asphaltene and calcium naphthenate precipitations in oil (Evdokimov et al., 2004; Havre, 2004).

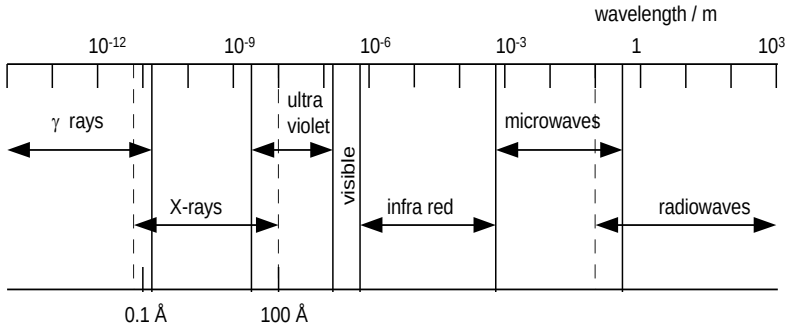

Figure 2.1 The regions of the electromagnetic spectrum (Skoog et al., 2008)

The nature of the types of radiation has been interpreted by Maxwell's classical theory of electro- and magneto - dynamics. This theory describes the radiation as two mutually perpendicular electric and magnetic fields, oscillating in single planes at right angles to each other. The distance between the peaks of the waveform is known as the wavelength, λ. However, the wave model does not describe phenomena of emission and absorption of radiant energy. The concept of wave-particle duality has been originated stating that light and matter both exhibit properties of waves and of particles. Absorption and emission of radiation is only explained by considering radiation as a stream of photons. The energy of those photons is given by the Bohr Equation:

$$E = \frac{hc}{\lambda} \qquad 2.1$$

where h is the Planck constant (h = 6.626 x 10^{-34} J.s), c is light velocity in vacuum (c = 3.0 x 10^{8} m.s^{-1}).

Many molecules absorb electromagnetic radiation in the ultra-violet, visible and infrared region. The absorbance of a solution increases as the intensity of the beam decreases. Lambert's Law states that the absorbance is directly proportional to the path length, l, and Beer's Law that the absorbance, A, is proportional to the concentration, c, of the absorbing species. When combined, The Beer-Lambert law (Figure 2.2) relates the absorption of light to the properties of the media the light is travelling through. As a fundamental background, Beer-Lambert Law is used to determine concentrations in the fluid systems. Importantly, to use the Beer-Lambert Law for concentration determination, it is necessary to know absorption coefficient or how quickly the

absorbance changes with concentration. This is represented by molar extinction coefficients, which can be taken from reference tables, or determined from experimental calibration curve.

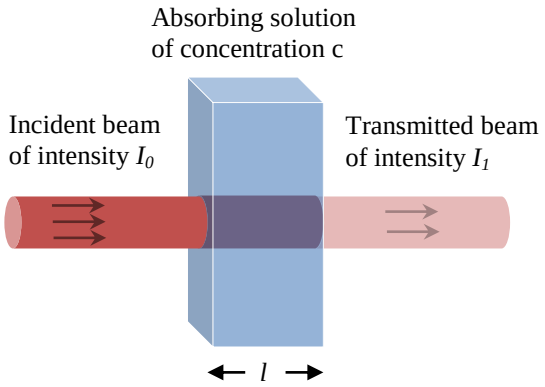

$$A = -\log_{10}\frac{I_1}{I_0} = \alpha\, l = \varepsilon\, l\, c \qquad 2.2$$

Figure 2.2 Attenuation of a beam of radiation by an absorbing solution of length l and concentration c (Beer-Lambert Law)

Where A is absorption or attenuation (dimensionless), I_0 states for the intensity of the incident light ($W.m^{-2}$), I_1 means the intensity after passing through the medium ($W.m^{-2}$), l is the distance that the light travels through the material (the path length) (cm), c implies the concentration of absorbing species in the material (mol/L), ε is absorptivity or the molar absorption coefficient of the absorber (L/mol/cm) , and α is absorption coefficient of the substance (cm^{-1}).

In this Chapter, the spectroscopy technique has been investigated to determine if hydrates formation and dissociation can influence light properties. Possible applications of the technique were:

- Hydrate nuclei detection;
- Hydrate water history detection in water samples;
- Inhibitor concentration monitoring.

2.1.1 Theory of Light Absorption

The absorption of UV or visible radiation corresponds to the excitation of bonding electrons in molecules. When a molecule absorbs energy, electrons are promoted from

their ground state to an excited state. In a molecule, the atoms can rotate and vibrate with respect to each other. These vibrations have also discrete energy levels, which can be considered as being packed on top of each electronic level (Thomas et al., 1996).

Infrared radiation is not energetic enough to bring about the kinds of electronic transitions, which are achieved for UV/VIS radiation. The interaction of infrared radiation with matter can induce changes in molecule dipoles associated with natural vibrations of bonds (Skoog et al., 2008).

The classical theory of a diatomic molecule considers the two atoms joined together by a bond, which behaves like a spring (Figure 2.3). Molecules which consist of different atoms will have a permanent dipole moment. The alternating electrical field of the radiation interacts with fluctuations in the dipole moment of the molecule. If the frequency of the radiation matches the vibration frequency of the molecule then radiation will be absorbed (Skoog et al., 2008).

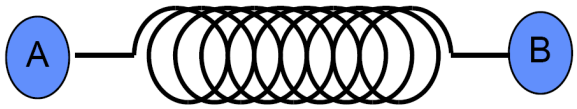

Figure 2.3 Vibrating diatomic molecule A-B

Most molecules are polyatomic. Each atom in the molecule can take the position in 3D space (coordinates x, y and z). Thus, each atom is said to have 3 degrees of freedom, i.e. it can move relative to each of those coordinate axes. An example of such motions is presented in Figure 2.4.

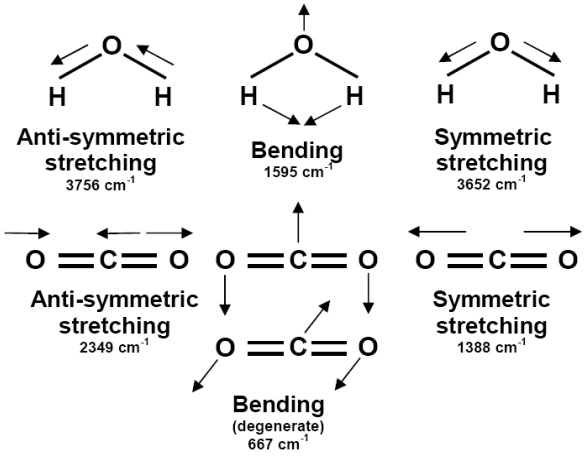

Figure 2.4 Normal modes of vibration in water and carbon dioxide

2.1.2 Spectroscopy

Spectroscopic methods are a large group of analytical methods based on atomic and molecular spectroscopy and used to investigate the energy levels of atoms, molecules and quantum transition. Spectroscopy is a general term for the science that deals with the interactions of various types of radiation with matter. Historically, the interactions of interest were between electromagnetic radiation and matter. Nowadays, spectroscopy has been broadened to include interactions between matter and other forms of energy such as acoustic waves and beams of particles like ions and electrons. Spectrometry and spectrometric methods refer to the measurement of the intensity of radiation with a photoelectric transducer or other type of electronic device converting radiation intensity to some sort of signal. The most widely used spectrometric methods are based on electromagnetic radiation, which is a type of energy that takes several forms, the most readily recognizable being light and radiant heat. Less obvious manifestations include gamma rays and X-rays as well as ultraviolet, microwave, and radio-frequency radiation (Thomas et al., 1996; Skoog et al., 2008).

2.1.3 Components of Molecular Spectrophotometer

A spectrophotometer is employed to measure light absorption. The instrument operates by passing a beam of light through a sample and measuring the intensity of light reaching a detector. UV/VIS/IR spectrophotometer is typically made up of the following components:

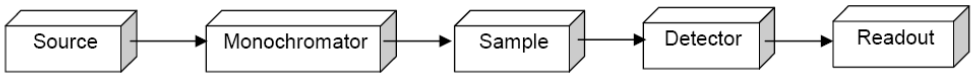

Figure 2.5 Generalised diagram of a molecular spectrometer

In practice another monochromator is also placed after the sample in infrared spectrometers in order to reduce the amount of any scattered radiation reaching the detector.

2.1.3.1 Sources of light

The function of the light source is to provide a continuous spread of wavelengths covering the region of the electromagnetic spectrum for which a spectrum or absorbance reading is required.

a) Sources of ultraviolet radiation

The electrical excitation of deuterium or hydrogen at low pressure produces a continuous UV spectrum. The mechanism for this involves formation of an excited molecular species, which breaks up to give two atomic species and an ultraviolet photon. This can be shown as:

$$D_2 + \text{electrical energy} \longrightarrow D_2^* \longrightarrow D' + D'' + h\nu$$

Both deuterium and hydrogen lamps emit radiation in the range 160 - 375 nm. It is important that the power of the radiation source does not change abruptly over its wavelength range.

b) Sources of visible radiation

A tungsten filament lamp is commonly employed as a source of visible light. This type of lamp is used in the wavelength range of 350 - 2500nm. The energy emitted by a tungsten filament lamp is proportional to the fourth power of the operating voltage. This means that for the energy output to be stable, the voltage to the lamp must be very stable indeed.

c) Source of IR radiation

All objects with an absolute temperature of over 0 K radiate infrared energy. An inert solid is electrically heated to temperature of 1500-2200K to emit infrared radiation. Infrared source can be blackbody radiators, tungsten lamps, silicon carbide and other.

2.1.3.2 Monochromator

Monochromator is a wavelength selector. Monochromator contains the following component parts (Figure 2.6): entrance slit, collimating lens, dispersing device (usually a prism or a grating), focusing lens and exit slit.

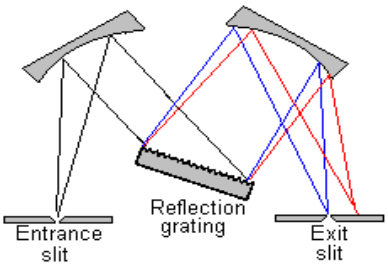

Figure 2.6 Czerney-Turner grating monochromator

Polychromatic radiation enters the monochromator through the entrance slit. The beam is collimated, and then strikes the dispersing element at an angle. The beam is split into its component wavelengths by the grating or prism. By moving the dispersing element or the exit slit, radiation of only a particular wavelength leaves the monochromator through the exit slit.

In this study, the use of monochromator was not necessary, since the spectrum was measured in the full wavelength range of the source light.

2.1.3.3 Sample Cuvette

a) UV / VIS Spectroscopy

The containers for the sample and reference solutions must be transparent to the radiation which will pass through them in order to measure the relevant optical properties. In this study, a quartz cuvette with 190-2200 nm spectral range and 1 cm pathlength was used.

b) IR Spectroscopy

Attenuated total reflectance (ATR) is typically used as a sampling technique. ATR used in conjunction with infrared spectroscopy enables samples to be examined directly in the solid or liquid state without further preparation.

An attenuated total reflection accessory operates by measuring the changes that occur in a totally internally reflected infrared beam when the beam comes into contact with a sample (Figure 2.7). An infrared beam is directed onto an optically dense crystal with a high refractive index at a certain angle. This internal reflectance creates an evanescent wave that extends beyond the surface of the crystal into the sample held in contact with the crystal. This evanescent wave protrudes only a few microns (0.5 μ - 5 μ) beyond the

crystal surface and into the sample. In regions of the infrared spectrum where the sample absorbs energy, the evanescent wave will be attenuated or altered. The attenuated energy from each evanescent wave is passed back to the IR beam, which then exits the opposite end of the crystal and is passed to the detector in the IR spectrometer.

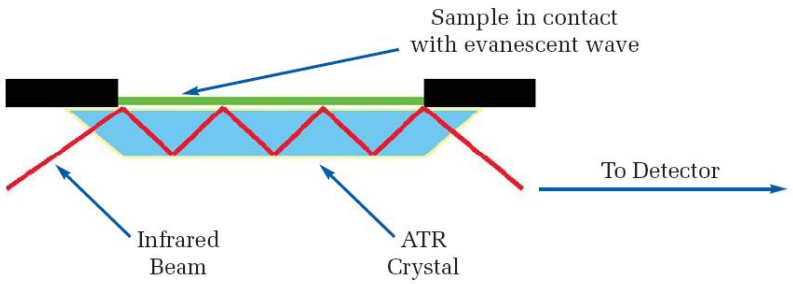

Figure 2.7 A multiple reflection ATR system

Diamond is the best ATR crystal material because of its robustness and durability. The original purchase cost is obviously higher than that of other crystal materials available, but over the instrument's lifetime replacement costs should be minimal.

In this study, transmission spectroscopy measurements were performed, as they are relatively simple and straightforward so that Beer-Lambert law can be directly applied to the measured absorption. IR spectrum properties were not measured with multiple reflection system. As the future expansion of the technique into further mid/far IR region, ATR sampling technique can be considered.

2.1.3.4 Detectors

The photomultiplier tube is a commonly used detector in UV/VIS spectroscopy (Figure 2.8). It consists of a photoemissive cathode (a cathode which emits electrons when struck by photons of radiation), several dynodes (which emit several electrons for each electron striking them) and an anode.

A photon of radiation entering the tube strikes the cathode, causing the emission of several electrons. These electrons are accelerated towards the first dynode (which is 100V more positive than the cathode). The electrons strike the first dynode, causing the emission of several electrons for each incident electron. These electrons are then accelerated towards the second dynode, to produce more electrons which are accelerated towards dynode three and so on. Eventually, the electrons are collected at the anode. By this time, each original photon has produced 10^6 - 10^7 electrons. The resulting

current is amplified and measured. Photomultipliers are very sensitive to UV and visible radiation and have fast response times.

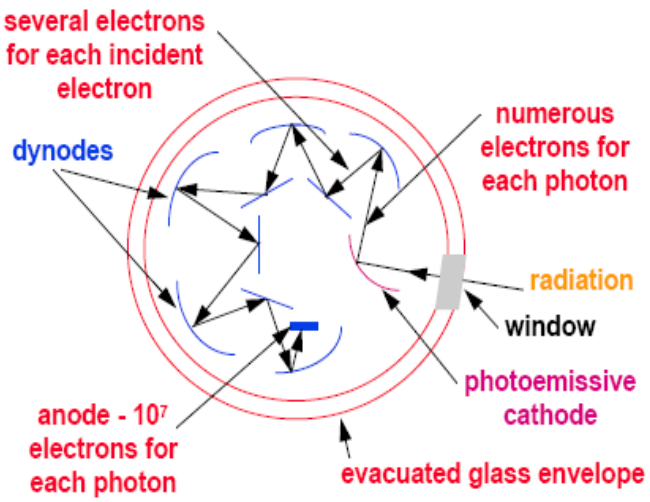

Figure 2.8 Cross section of a photomultiplier tube

Pyroelectric detector is commonly used as IR radiation detector which consists of a single crystalline wafer of pyroelectric materials. When an electromagnetic field (light) is applied across the pyroelectric material, temperature dependant polarization occurs. Being employed in a capacitor of the electric circuit, this polarisation alters the electric current by which the intensity of light can be measured. Pyroelectric detector has a fast response time (Skoog et al., 2008).

2.2 EXPERIMENTAL BACKGROUND

From the flow assurance aspect, gas hydrate formation is undoubtedly dreaded as the major risk of plugging the oil and gas production systems. Numerous studies are generally performed, to carefully select the gas hydrate inhibitor which is the best compromise between cost and associated risks. However, a chosen chemical can be inefficient or uneconomic under changing production conditions. From this point of view, unique technique has to be developed as an indispensable component of the hydrate control strategy. In this section, experimental set-up and procedures are described which were used to investigate the spectroscopy technique in the laboratory environment with further potential to be implemented on the field.

2.2.1 Experimental Set-up

Deionised water and natural gas were used in tests conducted in a rocking rig equipped with high pressure sapphire windows from two sides (Figure 2.9). The rig is comprised of a windowed equilibrium cell, cryostat, rocking/pivot mechanism, and temperature/pressure recording equipment controlled by a computer.

The equilibrium cell (maximum effective volume of 100 ml) is comprised of a steel cylindrical sample chamber with sapphire windows at each end. The cell is mounted on a pivot frame that allows a rocking motion around a horizontal axis. Rocking of the cell, controlled by a compressed air drive system, provides mixing of sample fluids. For the experiments reported here, the cell was rocked through 180° at a rate of 3 cycles per minute which has provided homogeneous temperature distribution in the cell.

The rig has a standard working temperature range of –20 to +50 °C, with a maximum operating pressure of 510 bar. The system temperature is controlled by circulating coolant from a cryostat within a jacket surrounding the cell. The cryostat is capable of maintaining cell temperature stability to within < ±0.02 °C. The cell temperature is monitored by a platinum resistance thermometer (PRT) calibrated at regular intervals using a precision thermometer (reported accuracy of ±0.025 °C for the operating range). The cell temperature can be measured reliably to within ±0.1 °C. The cell pressure is monitored by a pressure transducer with an accuracy of ±0.07 bar. Pressure and temperature are monitored and recorded by a PC through RS 232 outputs on the pressure and temperature readouts that are connected to serial ports on the PC. The cryostat is programmable, allowing temperature cycles to be carried out automatically.

UV/VIS/NIR light source and mini-spectrometer were mounted at either end of the cell, allowing light intensity to be captured during experiments. UV/VIS/NIR light source (L10290, Hamamatsu) outputs 200 – 1100 nm light through a fibre optic light guide. In the stage one experiments, a mini-spectrometer C10082MD (Hamamatsu Ltd.) was used to detect light coming out from sample cell of the set-up (Figure 2.10). It measures light intensity within the wavelength range from 200 to 800 nm with a Spectral Resolution Half Width (SRHW) of 6 nm. In the stage two experiments, a mini-spectrometer C10083CA (Hamamatsu Ltd.) with spectra sensitivity from 320 to 1000 nm, and SRHW of 8nm was used. Spectrum is monitored and recorded by the PC through USB.

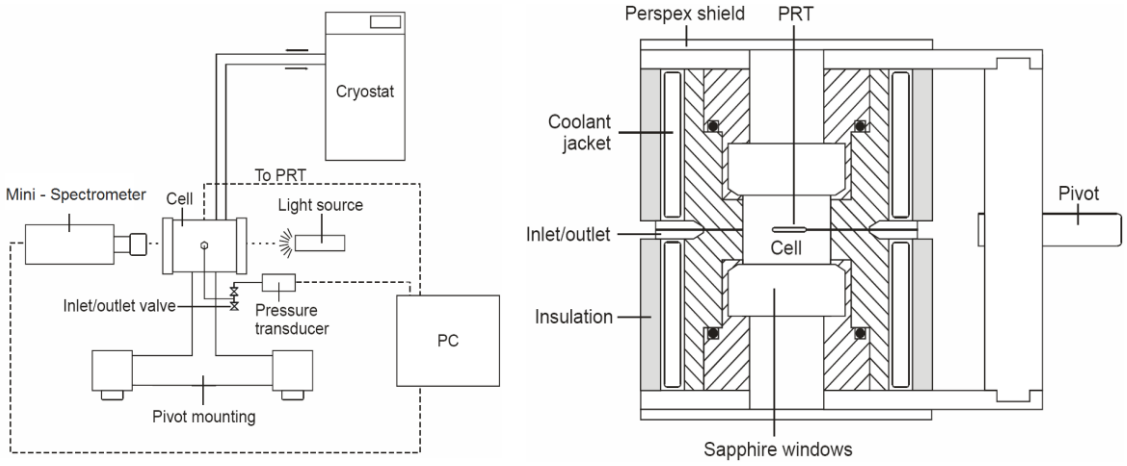

Figure 2.9 Schematic diagram of the Hydrate Visual Rig (left) and its equilibrium cell (right)

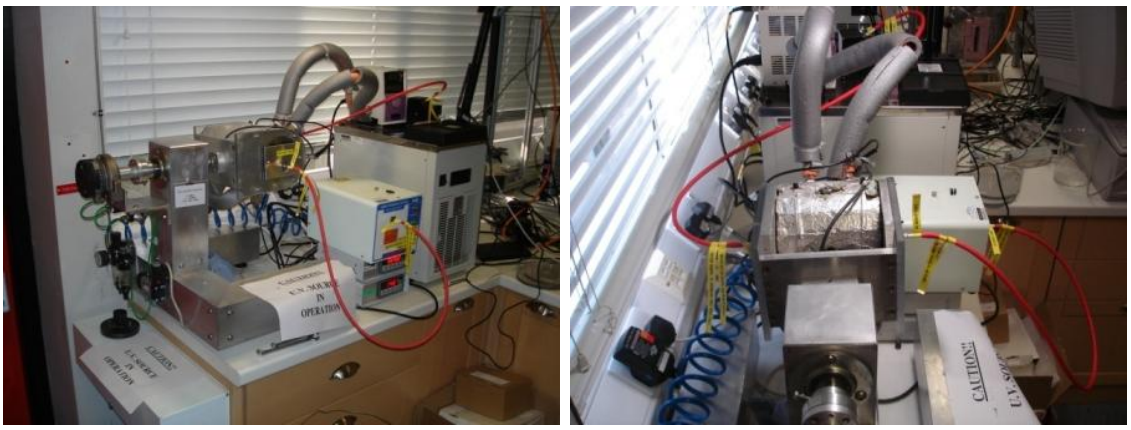

Figure 2.10 Pictures of Experimental Set-Up

2.2.2 Materials

Deionised water and a natural gas supplied by Air Products (composition listed in Table 2.1) were used in this study.

Table 2.1 Natural gas composition

Component	N_2	CO_2	C_1	C_2	C_3	iC_4	nC_4	iC_5	nC_5^+	Total
Mole (%)	2.16	1.69	89.69	4.62	1.26	0.17	0.30	0.06	0.05	100

2.2.3 Procedures

The cell was charged with 50 ml of deionised water at 20 ^{o}C and was then pressurised to near 102 bar by injecting natural gas. The system was cooled to 4 ^{o}C in the stage one tests, and to 0 ^{o}C in the stage two tests, at 0.2 ^{o}C/ min rate. Hydrate formation is detected by a sudden pressure drop on the temperature-pressure diagram. Then hydrate was dissociated by increasing the temperature back to 20 ^{o}C. UV/VIS/NIR light spectroscopy measurements were recorded every 5 minute. Rocking of the cell was switched off during the 30 seconds measurement interval.

2.3 HYDRATE FORMATION

2.3.1 Detection of Hydrate Formation (Stage One)

In these series of tests, the UV/VIS mini-spectrometer C10082MD with spectral sensitivity from 200 nm to 800 nm was used to detect the light coming out from sample cell of the set-up. The cell was charged with 50 ml deionised water, and then pressurised up to 102 bar with natural gas. The system followed the pressure-temperature path (Figure 2.11) described in section 2.2.3.

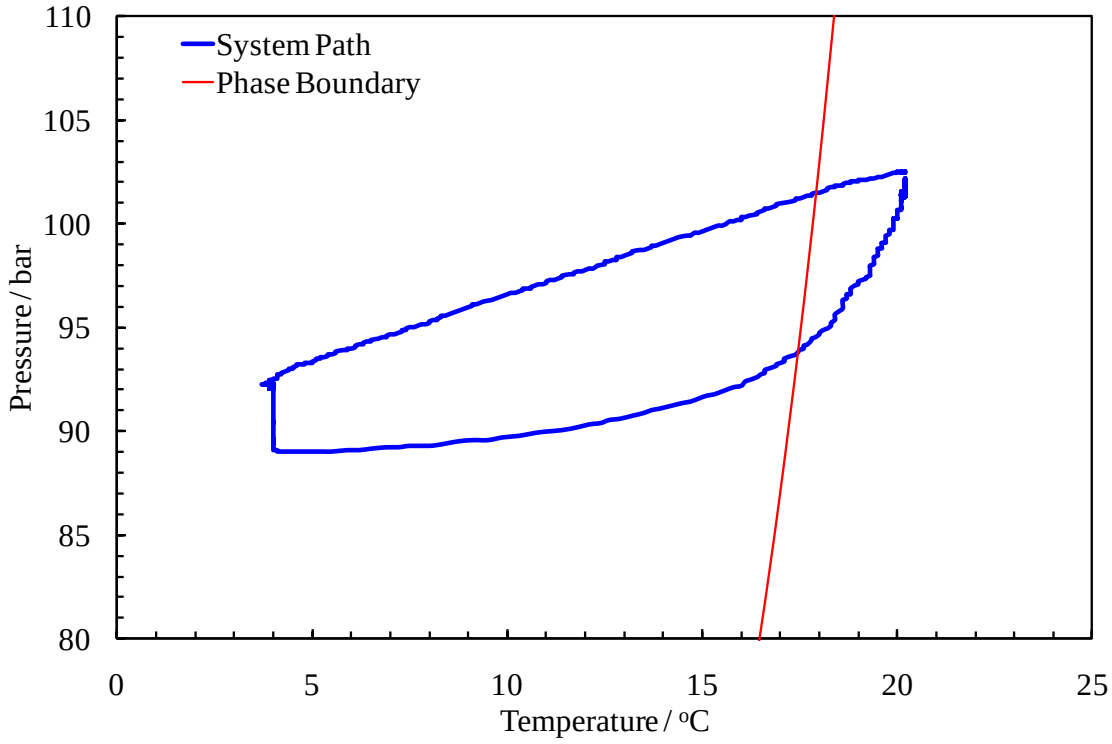

Figure 2.11 Sample preparation pressure-temperature profile for stage one study of hydrate formation

In Figure 2.11, it can also be seen that hydrate crystallization yielded a very low increase of cell temperature (lower than ~0.5 ^{o}C) which in turn means that hydrate formation was a slow process which is typical for a rocking cell rig.

Results of these measurements are presented in Figure 2.12, and summarised in Table 2.2. The key experimental stages are described as follows.

a) During hydrate formation:

1. After 30 minutes (P= 96 bar, T=9.6 °C – inside hydrate stability zone), there is a noticeable reduction in light intensity of 4% in VIS part and 9% in UV part during hydrate formation process.

2. After 1 hour (P= 92 bar, T=4 °C – inside hydrate stability zone), there is a high reduction in light intensity of 28% in visible part and 33% in UV part. At this stage, concentration of hydrate particles can be calculated from temperature-pressure data and correlated to light attenuation (section 2.3.2).

3. After 2 hours 30 minutes (P= 89 bar, T=4 °C – inside hydrate stability zone), hydrate is formed, the light is completely blocked, attenuation is 100%.

b) During hydrate dissociation:

1. After 3 hours 15 minutes (P= 100 bar, T=20 °C – outside hydrate stability zone), hydrate started to dissociate, but there is still high light attenuation of 91% in VIS part and 100% in UV part.

2. After 3 hours 45 minutes (P= 101 bar, T=20.2 °C – outside hydrate stability zone), hydrate is mostly dissociated, and the light attenuation is 30% in visible part and 50% in UV part.

3. After 4 hours 30 minutes (P= 102 bar, T=20.2 °C – outside hydrate stability zone), hydrate is completely dissociated. In the visible part, the light intensity is abnormally higher than the base line which might be related to hydrate water memory explained in more detail in Chapter 5and Chapter 6.

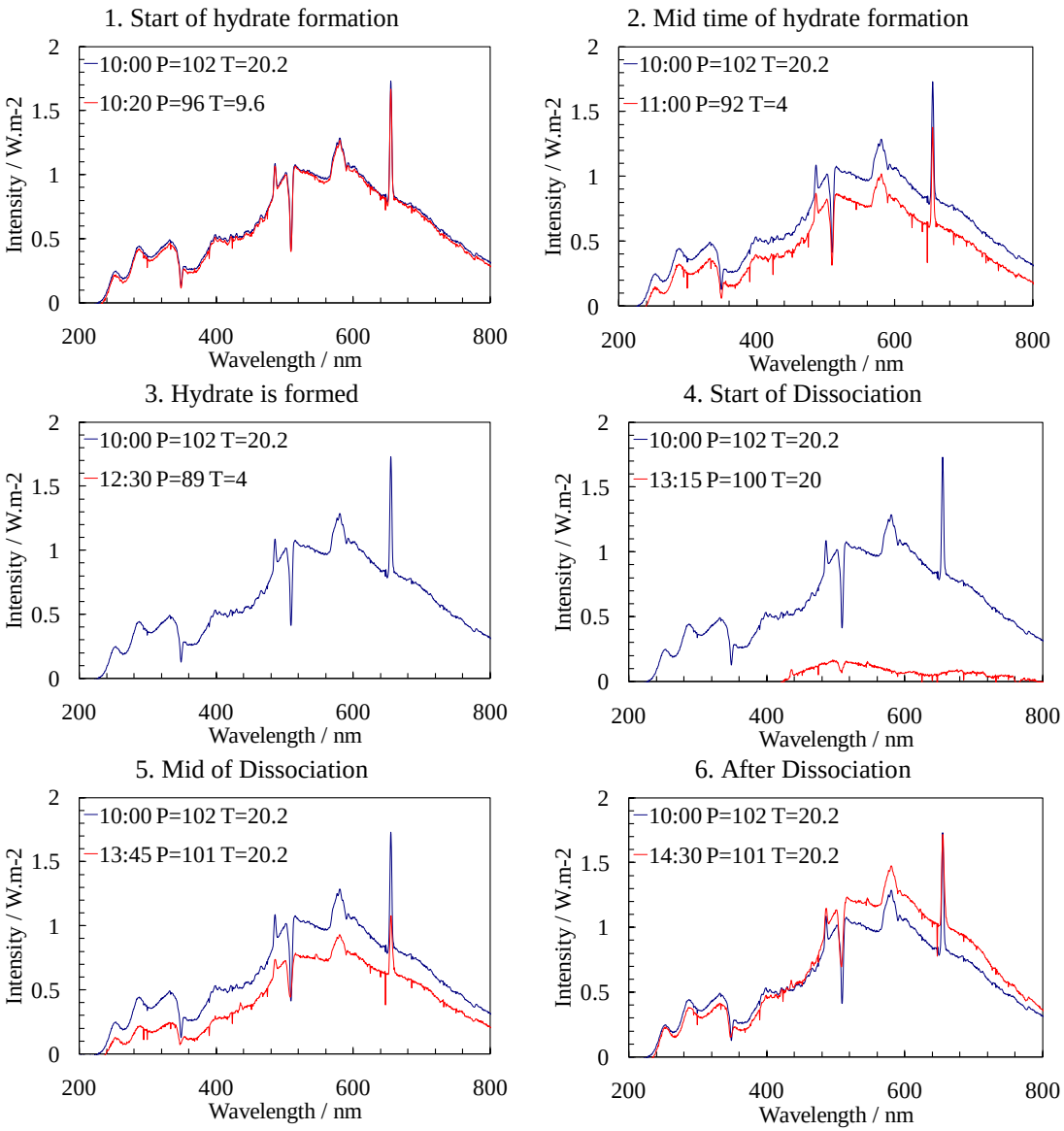

Figure 2.12 Light spectrums over the hydrate formation-dissociation process (on all graphs, blue line indicates the spectrum of pressurised water before hydrate formation)

Table 2.2 Summary of UV/VIS spectroscopy results for the main stages of hydrate formation and dissociation processes. Attenuation parameter (at 350 nm and 750 nm) will be related to the amount of hydrate formed in the next (stage two) experiment.

Stages	Time	P, bar	T, °C	Attenuation in UV part, %	Attenuation in VIS part, %
Hydrate Formation	30 min	96.3	9.6	9	4
	1 h	92.2	4	33	28
	2 h 30 min	89.6	4	100	100
Hydrate Dissociation	3 h 15 min	100.6	20	100	91
	3 h 45 min	101.4	20.2	50	30
	4 h 30 min	101.9	20.2	15	0

2.3.2 Detection of Hydrate Formation (Stage Two)

The next series of tests were conducted with the UV/VIS/NIR mini-spectrometer C10083CA with spectral sensitivity from 320 to 1000 nm. The same procedure for hydrate formation was used as described in the Experimental set-up and Procedures section 2.2. Water - natural gas system was used.

To compare the light properties at different times, the dimensionless parameter – attenuation was used:

$$A = -\log_{10}\left(\frac{I}{I_0}\right) \qquad 2.3$$

Where A is attenuation (dimensionless), I states for intensity of light at the given time ($W.m^{-2}$), I_0 means initial intensity of light at the start of experiment ($W.m^{-2}$).

From the temperature-pressure analysis (Figure 2.13), the onset of hydrate formation can be detected at 1.5 ^{o}C with the uncertainty of around ±0.3 ^{o}C. The pressure-temperature path started from a higher pressure in this experiment in order to induce higher drawdown comparing to the stage-one experiment, thus, to measure the spectral response during hydrate formation process while cooling. From fluid system light attenuation at various time steps, and, thus, various temperatures and pressures (Figure 2.14), it can be noted that the sudden increase in attenuation (yellow line) appeared at 2.2 °C which is attributed to hydrate formation. Therefore, it seems that earlier stages of hydrate formation (nucleation) can be detected with light attenuation earlier than with conventional temperature-pressure analysis. This statement is further proved by spectroscopy tests for atmospheric water and pressurised with non-hydrate forming gas water samples followed the same temperature-pressure path.

In Figure 2.14, it can be seen that attenuation is not notably changing (nearly flat line behaviour) in the whole range of spectrum, meaning that nucleation process can be equally detectable at any wavelength. Therefore, simple light diodes which emit narrow wavelength light can be used to simplify the technique for hydrate formation studies in future. This method of sample diode lighting is often used to detect the formation of micelles in water surfactant systems.

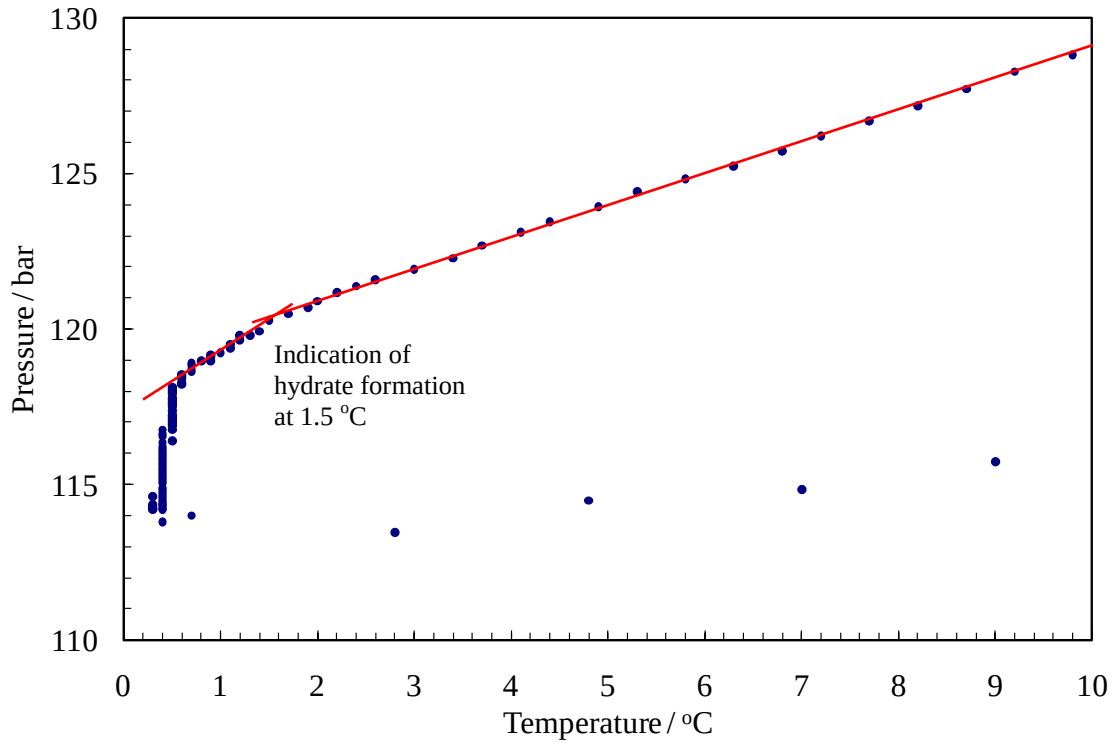

Figure 2.13 Sample pressure-temperature profile for further study of hydrate formation

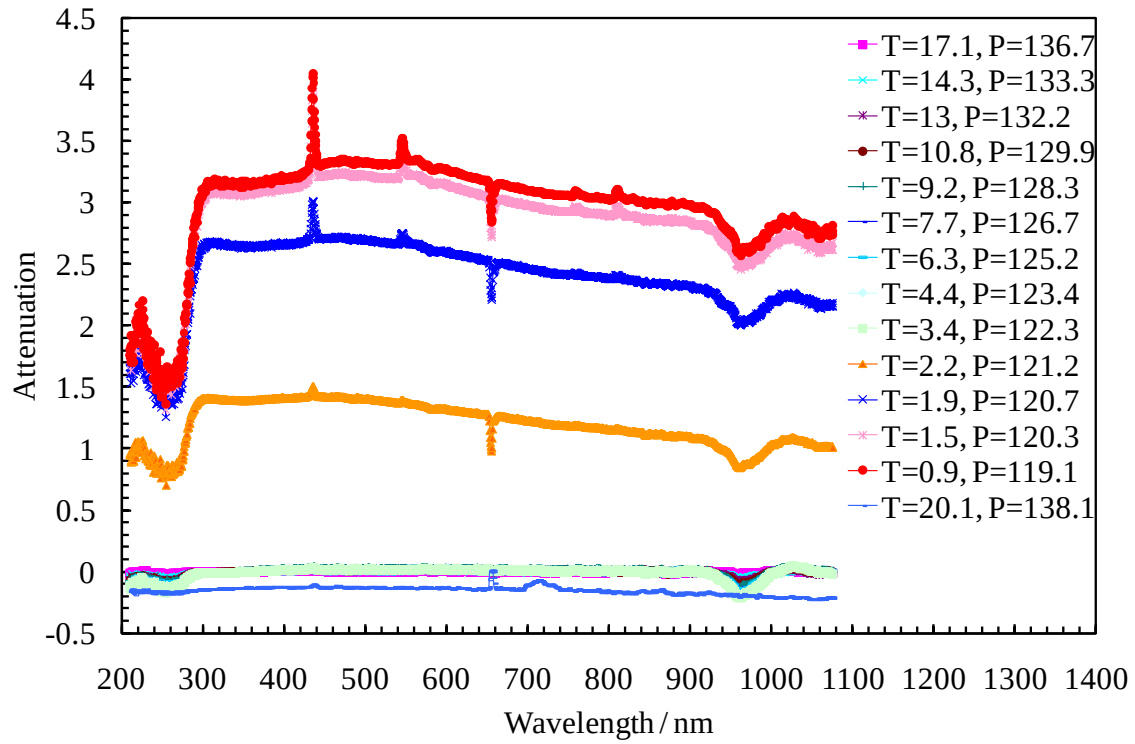

Figure 2.14 Spectral attenuation at different temperatures (T/ °C) and pressures (P / bar) for water – natural gas fluid system

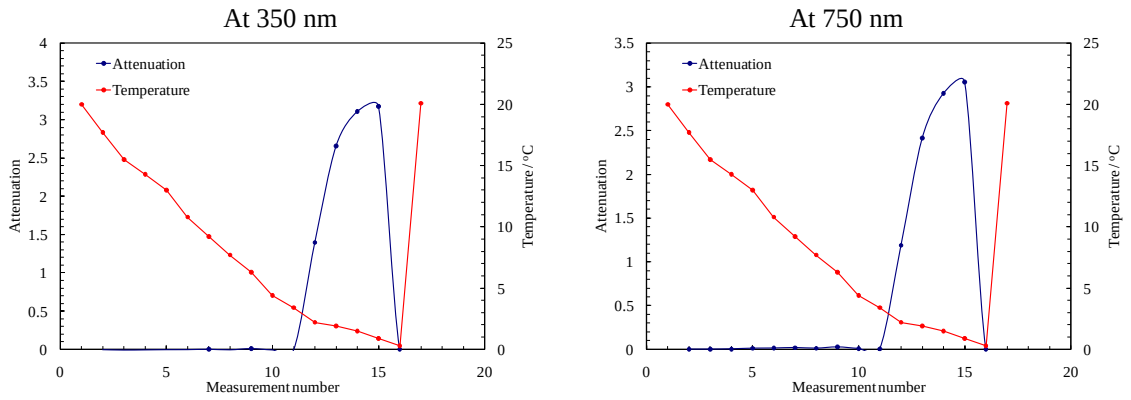

Figure 2.15 Attenuation at different temperatures for 350 nm and 750 nm wavelengths

In Figure 2.15, it can be seen that the attenuation was zero when the temperature was reduced from 20 ^{o}C to 3 ^{o}C, and there was a sharp increase in the attenuation at 2.2 ^{o}C which is related to hydrate nucleation and agglomeration stage. Then attenuation is further increasing indicating that more hydrate particles are forming and blocking the light. At this stage, the concentration of hydrate particles in the fluid system might be calculated from the temperature-pressure data. The amount of hydrate was calculated from *PVTX* relations for which equilibrium conditions at each pressure-temperature were assumed. Those values are uncertain in the approximate range of ±0.04%. The amount of hydrate was associated with the attenuation coefficient of light passing through the fluid system. The results are summarised in Table 2.3 and shown in Figure 2.16. The results show that hydrate concentration was in linear relationship with the attenuation coefficient (slow agglomeration). This technique can quantitatively detect amount of hydrate formed and can have a potential to detect its nucleation at the earliest stage. This capability can be employed in an early warning system provided the final device is installed at a reasonable distance downstream from the most risky place of the production/transport line. Therefore, hydrate formation risks against the pipeline length should be pre-evaluated by the flow assurance engineer of the operating company.

Table 2.3 Relation between attenuation coefficient and amount of hydrate formed

Time after start of cooling	P, bar	T, ^{o}C	Attenuation in UV part	Attenuation in VIS part	Attenuation in NIR part	Hydrate, mass%
10 min	122.3	3.4	0	0	0	0
26 min	121.2	2.2	1.4	1.2	1	0
32 min	120.7	1.9	2.7	2.4	2.1	0.3
34 min	120.3	1.5	3.1	2.9	2.6	0.5
42 min	119.1	0.9	3.2	3.1	9.3	0.7
1h 16 min	116.4	0.5	7.7	8.1	9.7	2.9

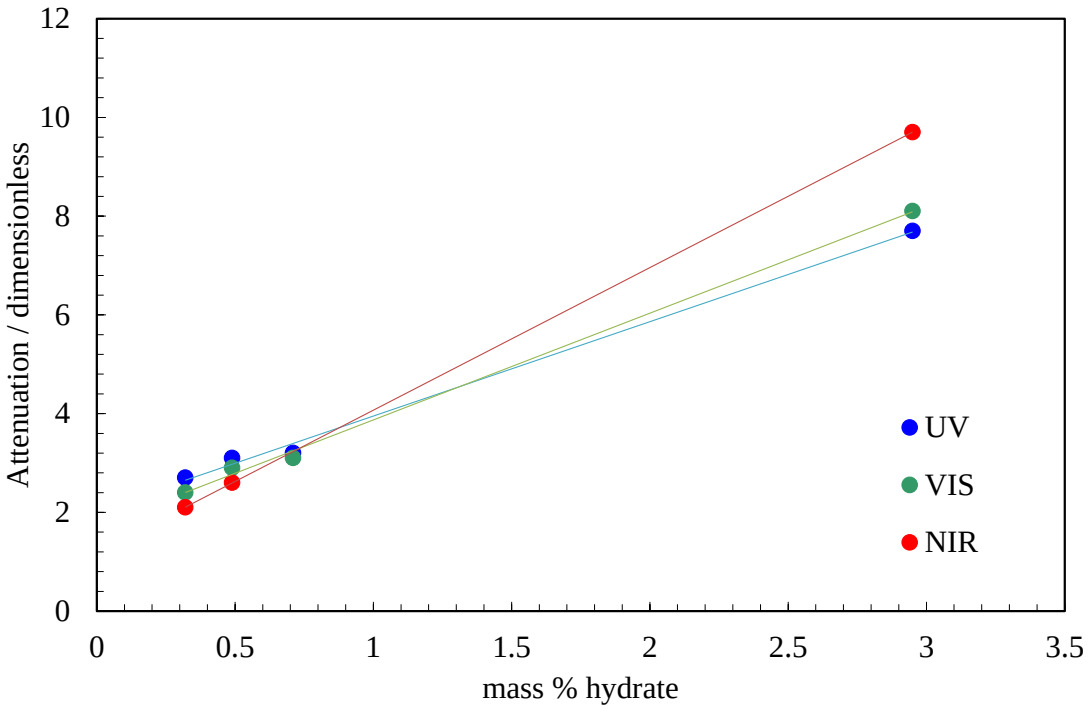

Figure 2.16 Attenuation coefficient against amount of hydrate formed indicating the linear relationship

The atmospheric and pressurised water tests were conducted to further investigate the method. The water passed the same temperature path as shown in Figure 2.13 under 1 bar pressure (Figure 2.17). Then water was pressurised to 104 bar with non-hydrate forming hydrogen gas (Figure 2.18). Attenuation for the atmospheric water (Figure 2.17) over the whole interval of experiment is low indicating that no significant changes have occurred with the water phase. To test a pressurised water system followed cooling-heating path without subsequent hydrate formation, hydrogen gas was used. This gas was selected based on the fact that hydrogen molecule diameter of 2.72 Å is smaller than the minimum diameter for guest molecule 3.8 Å that hydrate structure can accommodate (Sloan, 1990). However, under high pressures (1800 to 2200 bar at -40 to -60 ^{o}C) which were never applied in this research work hydrogen can actually form structure II hydrate with two molecules entrapped in the small cage and four in the large (Mao et al., 2002). During the cooling-heating cycle (Figure 2.18), the spectrum of light was measured in the most valuable time intervals. Results (Figure 2.19) showed that attenuation coefficient was low and did not change over the test time which implied the pressurised water cooling-heating cycle does not have an effect on light properties. This excludes the possible negative effect of condensation on the rig windows and

suggests that changes in attenuation for water-natural gas fluid system during cooling-heating process (Figure 2.14; Figure 2.15) are attributed to hydrate formation.

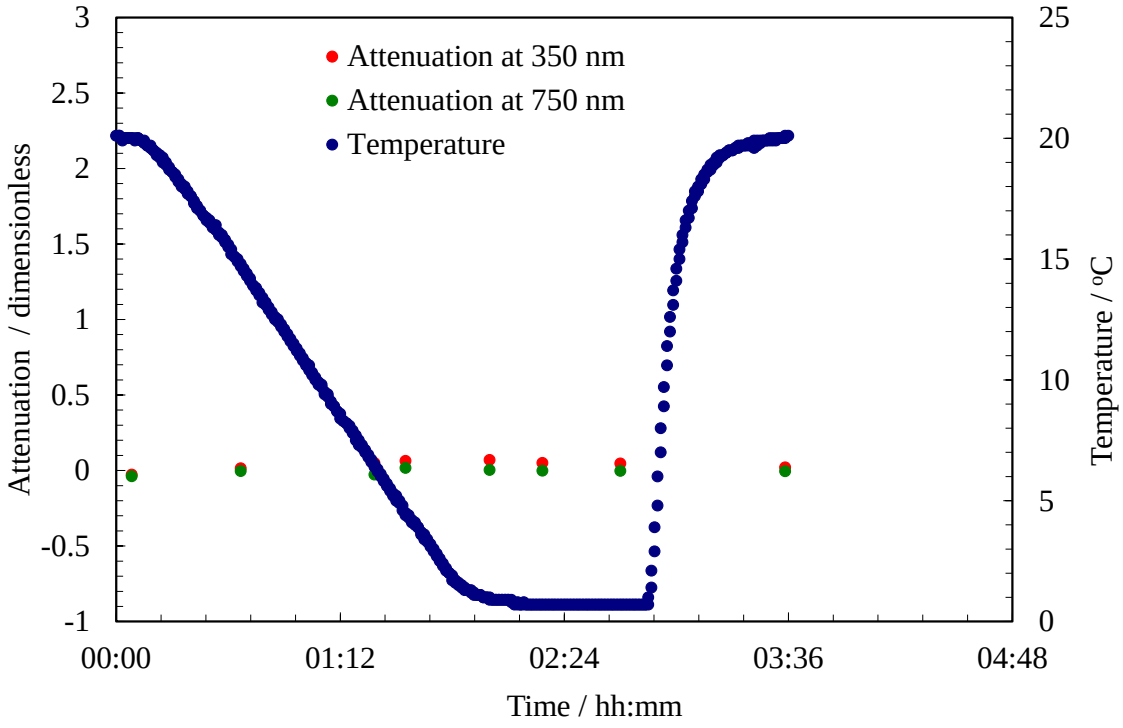

Figure 2.17 Test with distilled water under atmospheric pressure which followed the same temperature path as hydrate forming pressurised system

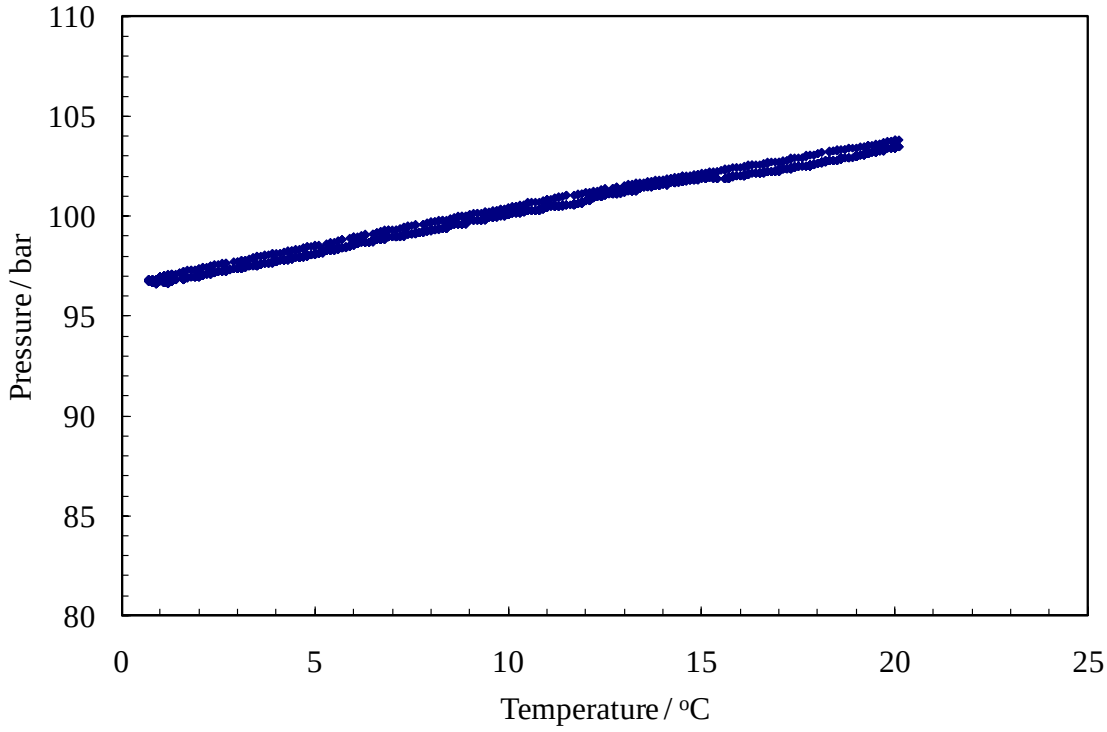

Figure 2.18 Temperature-Pressure profile for distilled water pressurised with hydrogen

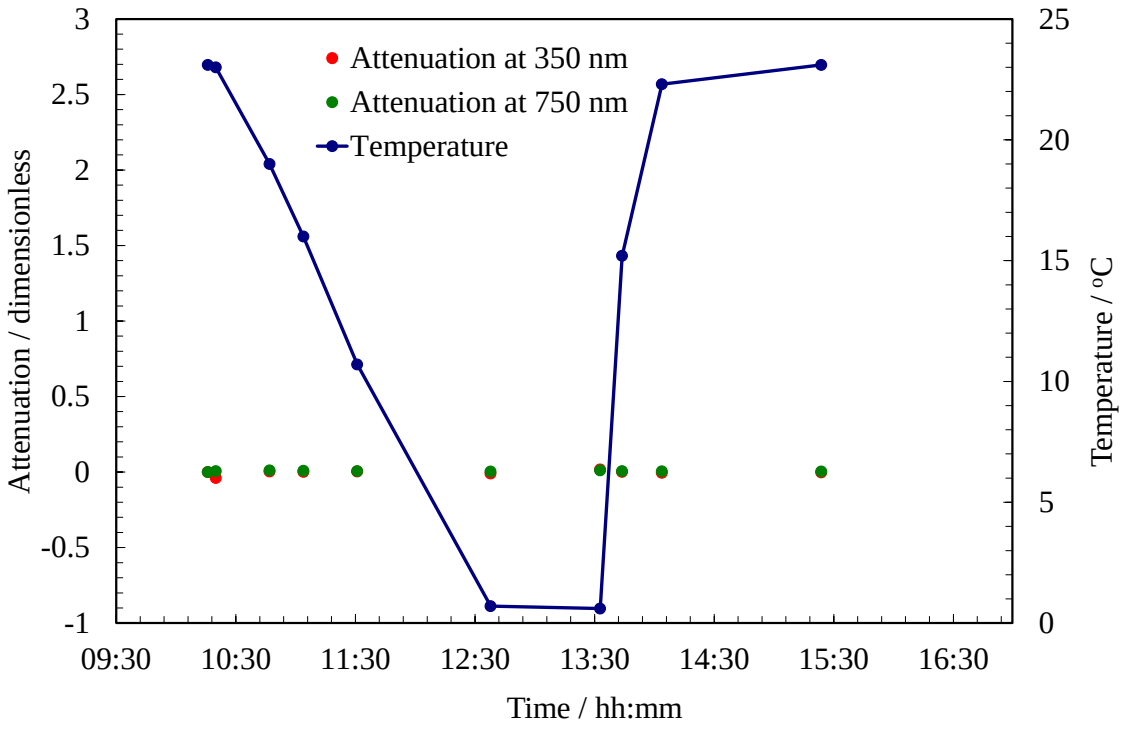

Figure 2.19 Spectral attenuation at different temperatures and pressures for distilled water pressurised with hydrogen (T is temperature in ^{o}C, P is pressure in bar)

Water memory effect explained in more details in Chapter 5 and Chapter 6 was also investigated as part of this study. After hydrate dissociation there can still be some kind of water molecular structure remaining in liquid phase. This water structure could exist as residual clusters of water molecules (Sloan et al., 1998; Ohmura et al., 2000). Other from the change of water molecular orientation/arrangement cause of the memory effect is the increased gas solubility due to gas molecules trapped over the hydrate formation stage. In this new test, the same temperature-pressure path was followed to prepare the sample as in stage one experiment (Figure 2.11). At the dissociation stage, the rocking was switched off, and light fibre cables were fixed at both ends of the rig. The measurements were conducted over 2 weeks to have a wider time interval of investigation. The results of this experiment are presented as the intensity change (Figure 2.20) and attenuation coefficient (Figure 2.21) over time. As it can be concluded from this observation, the most of the water memory effect disappears in 24 hours at 2 °C outside the HSZ. A minor drift up until ~100 hours can suggest that 360 nm wavelength is more sensitive to remaining hydrate clusters. Assuming maximum transportation pipeline length of 50 km and typical flow speed of 1-6 m/sec (Trench, 2001), the fluid travel time is calculated to be within 2-14 hours. That implies that the memory could be preserved along the entire flow path (assuming the T&P conditions

are similar to the test conditions and no other disturbing factors like chemical additives, dilution, etc.) and can therefore be detectable by hydrate early warning system downstream. This qualitative experiment was encouraging; however, only pure water with no chemical additives was investigated.

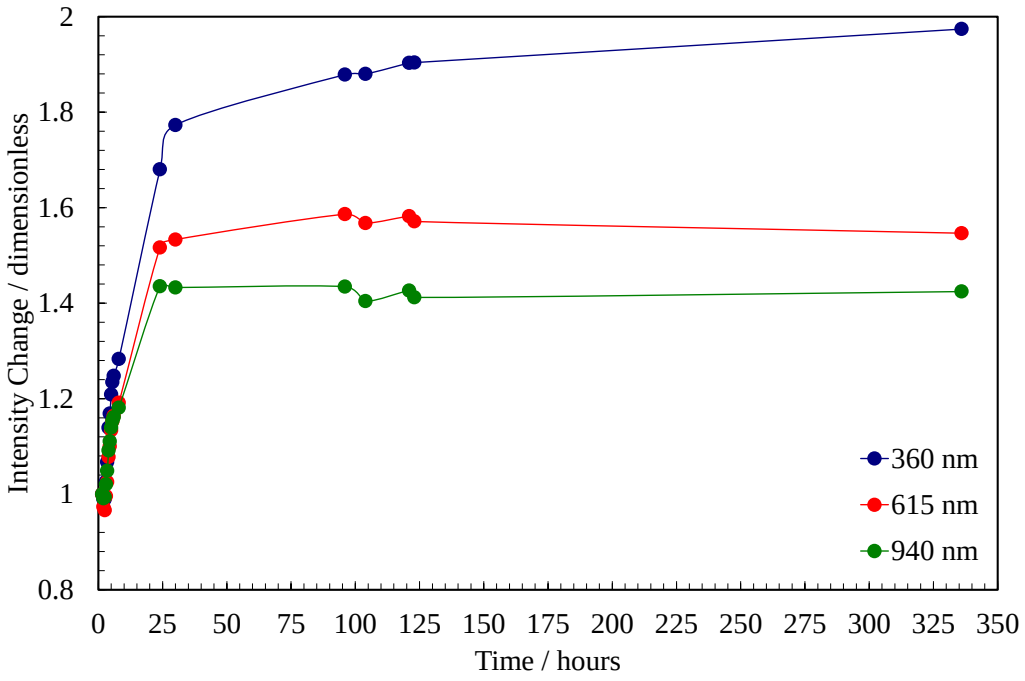

Figure 2.20 Intensity change showing the memory effect disappearing in 24 hours

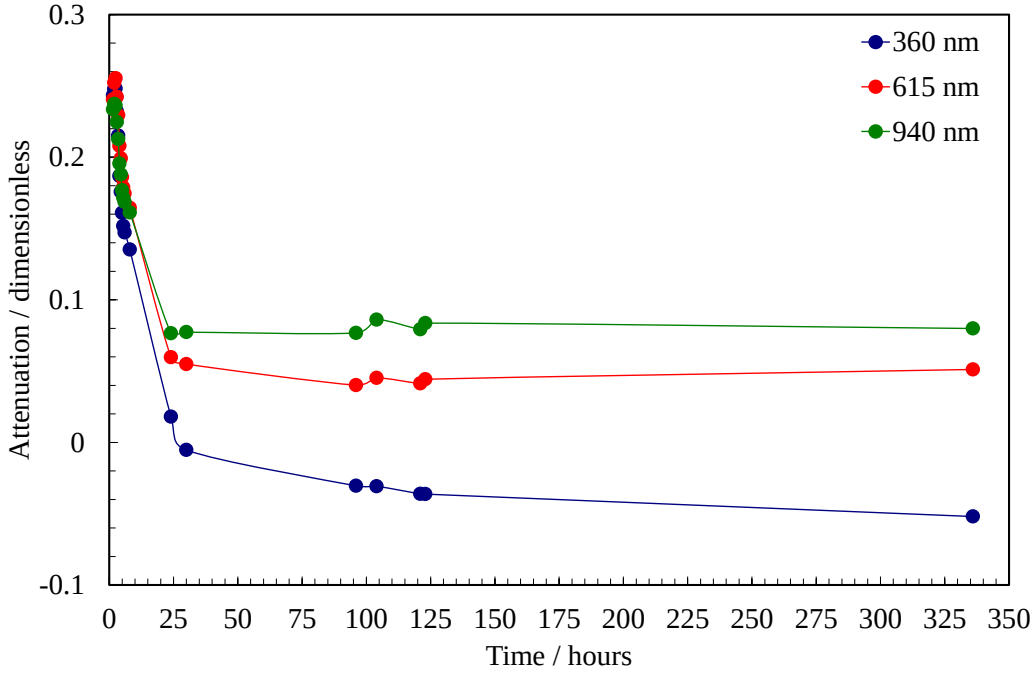

Figure 2.21 Attenuation coefficient showing the memory effect disappearing in 24 hours

2.4 CONCLUSIONS

As a part of the screening of the potential technique for hydrate monitoring and early warning systems, the spectroscopy as a fundamental tool in analytical science has been examined. The results of investigation of UV/VIS/NIR spectroscopy technique for detection of hydrate nucleation, hydrate water history and inhibitor concentration have been presented in this chapter.

The results imply that the hydrates nucleation can be detected by reduction in light intensity prior to pressure drop in conventional Pressure-Temperature profile. It was shown that attenuation is flat-like in the whole range of spectrum; therefore, light diodes might be used to simplify the technique for future nucleation studies.

The results suggest that hydrate water memory can be detected in the pure water gas system using UV/VIS/NIR spectroscopy. This can provide a simple method to identify the memory of hydrate formation in the purified produced water, hence an early warning against pipeline blockage. It was investigated under the test conditions (2 °C outside the HSZ) that water memory can exist for 24 hours after hydrate dissociation. Broader conditions were examined in the following chapters specifically dedicated to memory phenomenon.

CHAPTER 3 INHIBITORS MONITORING TECHNIQUE

3.1 INTRODUCTION

The conventional approach to prevent and reduce hydrate risks in transfer line and process facilities is to remove one of the elements favouring its formation. For example, thermal insulation and external heating methods are used to remove the low temperature element. Water can be removed by dehydration of the natural gas using glycol system and lowering the operating pressure can reduce the tendency for hydrate to form in the production system. However, these conventional ways cannot be feasible for numerous fields especially in offshore and deepwater environment due to space limitation and high insulation or heating cost. The deepwater insulation costs are reported typically US$1 million per km of flowline (Gudmundsson et al., 1998).

The alternative option is to apply thermodynamic inhibitors defined as water soluble chemical that reduces the water activity, hence shifting the hydrate phase boundary to higher pressure and/or lower temperature conditions. Among those chemicals, the most common are methanol and glycol. However, due to high dosage requirement it can result in significant increase in CAPEX and OPEX, in particular at high water cut conditions, as well as logistical and environmental problems (Wu et al., 2007).

In the recent years, the application of Low Dosage Hydrate Inhibitors (LDHIs) becomes widely practiced in the industry. The LDHIs is classified into the Kinetic Inhibitors (KIs) and Anti-Agglomerates (AAs). The KIs work by delaying nucleation and growth of crystals. AAs are designed to allow gas hydrates to form and prevent the agglomeration of hydrate crystals and thus minimize the risk of pipeline plugging (Kelland et al., 1995).

Overall, the approach practiced in the petroleum industry for hydrate prevention is to inject chemical inhibitors at the upstream end of trunkline. To reduce the risk of gas hydrate deposition in subsea facilities, monitoring of hydrate inhibitor concentrations hence the degree of hydrate inhibition along the pipeline and/or downstream is vital. Furthermore, hydrate inhibitor monitoring makes it possible to optimise the usage of the inhibitors to avoid over dosage of inhibitors and unnecessary impact on the environment. In this Chapter, the research for hydrate inhibitors monitoring technique is presented. Two electromagnetic methods were investigated for the purpose of monitoring concentration of hydrate inhibitors in the aqueous solutions:

1. Spectroscopy.

2. Dielectric permittivity.

3.2 SPECTROSCOPY

Spectroscopy method was introduced and theoretically explained in Chapter 2. One of the applications of UV/VIS/NIR spectroscopy technique is to determine and monitor concentration of treating chemicals used in the petroleum industry (Brost et al., 1991; Schake et al., 2001). In this Chapter, the technique was investigated for inhibitors monitoring.

3.3 EXPERIMENTAL SET-UP AND PROCEDURES

3.3.1 Experimental Set-up

Samples were tested in the new spectroscopy rig (Figure 3.1). The quartz cell (8 ml volume) is inserted into the sample cell holder designed with two windows on sides to pass the light through the sample. The rig has a standard working temperature range of –20 to +50 °C at atmospheric pressure. The system temperature is controlled by circulating coolant from a cryostat within a plastic jacket surrounding the sample placement. The cryostat is capable of maintaining cell temperature stability to within ±0.02 °C. The cryostat is programmable, allowing temperature cycles to be carried out automatically.

UV/VIS/NIR light source and mini-spectrometer were mounted at either end of the cell, allowing light intensity to be captured during experiments. UV/VIS/NIR light source (L10290, Hamamatsu) outputs 200-1100 nm light through a fibre optic light guide. A

mini-spectrometer C10083CA (Hamamatsu Ltd.) was used as a detector (see section 2.1.3.4) light coming out from the sample holder of the set-up (Figure 3.1). It measures light intensity within the wavelength range from 200 to 1100 nm with a Spectral Resolution Half Width (SRHW) of 8nm. Spectrum is monitored and recorded by the PC through USB.

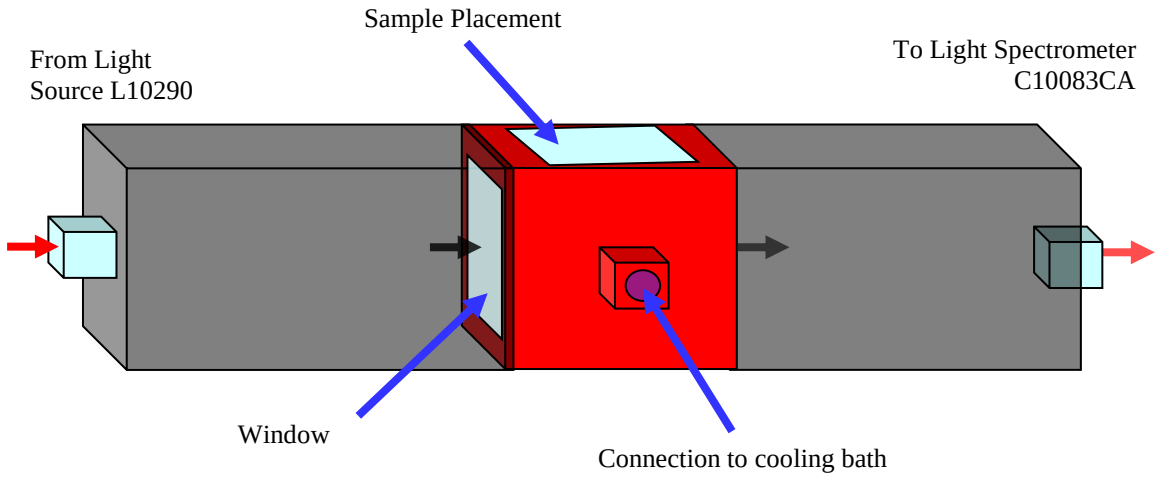

Figure 3.1 Schematic diagram of the sample cell holder

3.3.2 Materials

Methanol (99.9%), Sodium Chloride (99+%) and Decane (AR grade) supplied by Aldrich; Ethylene glycol, 99.0% supplied by Alf Aesar; North Sea Oil. Natural gas composition is provided in Table 2.1.

3.3.3 Procedures

The cell was filled up with 8 ml of various solutions (water with alcohol, salt or contaminations) at 20 ^{o}C. UV/VIS/NIR light spectrum was measured 5 times for 30 seconds (integration time) each 10 minutes for statistical purposes.

3.4 THERMODYNAMIC INHIBITORS

To prevent hydrate formation in petroleum systems, thermodynamic inhibitors are commonly used. Study on the gas hydrate thermodynamic inhibitor has become widespread (Menten et al., 1981; Ng et al., 1989; Makogon et al., 1999; Szymczak et al., 2006; Wu et al., 2007). The most extensively used thermodynamic inhibitors are methanol, mono-ethylene glycol, diethylene glycol, and some other electrolytes.

Inhibitor molecules or ions will compete with the water molecules changing the thermodynamic equilibrium of water and hydrocarbon molecules, i.e. the chemical potential of hydration, and prevent the formation of hydrate by moving the phase equilibrium curves to lower temperature and higher pressure (Wu et al., 2007).

There are a number of evidences indicating that UV/VIS/NIR spectroscopy method was recently successfully applied to measure the alcohol and other additive concentrations in spirit drinks (Dirk et al., 2007), as well as to distinguish various chemical mixtures in synthetic and water samples (Hasani et al., 2007). In this investigation, the spectroscopy technique has been analysed to monitor concentrations of alcohols (methanol and ethylene glycol) with the primary aim to depict the spectral range affected by the presence of alcohols in the aqueous solution, and the sensitivity of the method.

A variety of substances can serve as inhibitors to combat gas hydrate formation, but methanol injection is historically considered to be the best option (Hammerschmidt, 1934). Methanol is a non-corrosive fluid miscible in any proportion with water. As a hydrate inhibitor it is more effective than most other substances. It has a low enough viscosity (around 0.8 mPa*s) to be utilised for long pipelines. Methanol dissolves in water and hydrocarbon-rich liquid phases and also evaporates in the vapour phase (Avlonitis et al., 1996; Anderson et al., 1986). Its cost is low enough to permit a reasonable sacrifice of the inhibitor in the vapour phase. However, the effective use of methanol has to be accompanied by measurements of its distribution among the various phases, most importantly, in water.

The light intensity spectrum was measured for various methanol aqueous solutions (Figure 3.2). Measurements uncertainty is within ±2.2%. The results indicate that there is a significant influence of methanol in the 940-1040 nm spectral range which is NIR part of the spectrum. At the same time, there is almost no change in the UV/VIS part of the spectrum. As seen in Figure 3.4, methanol has the highest effect in the NIR spectrum (950 nm) of light. Corresponding intensities and intensity changes for UV (350 nm), VIS (670 nm) and NIR (950 nm) are summarised in Table 3.1 for various methanol concentrations. At 950 nm wavelength, the technique sensitivity for methanol content is 0.64 $mW.m^{-2}$/mass%.

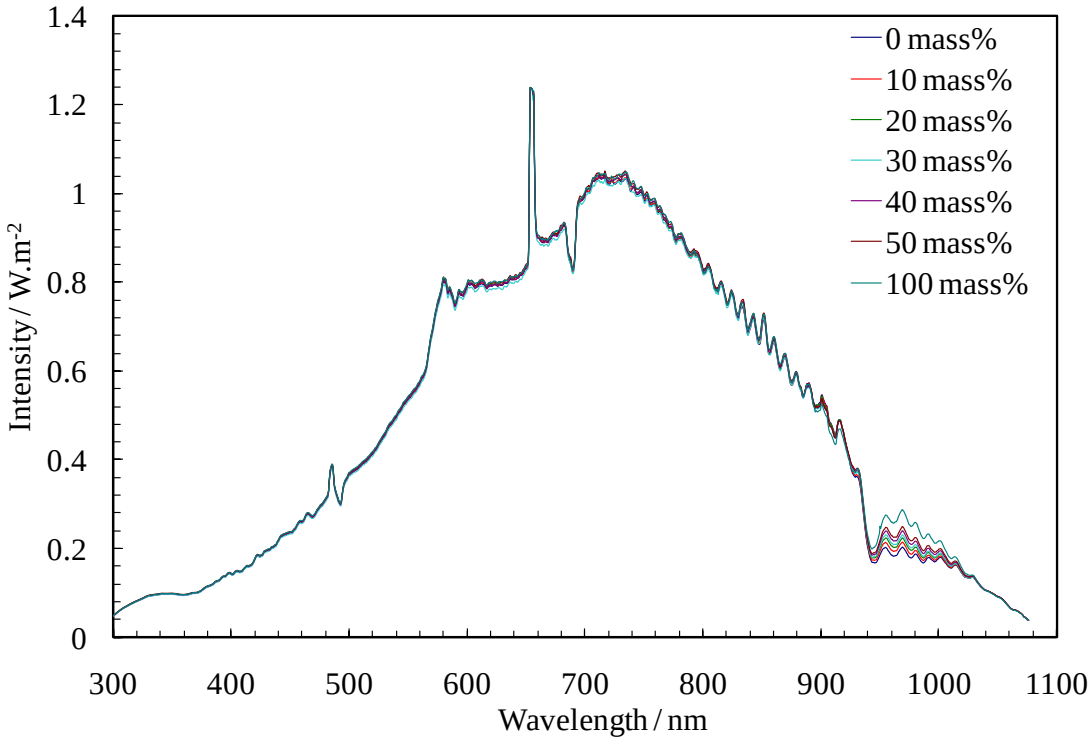

Figure 3.2 Spectra for methanol aqueous solutions indicating the highest effect in the NIR spectrum of light (940-1040nm)

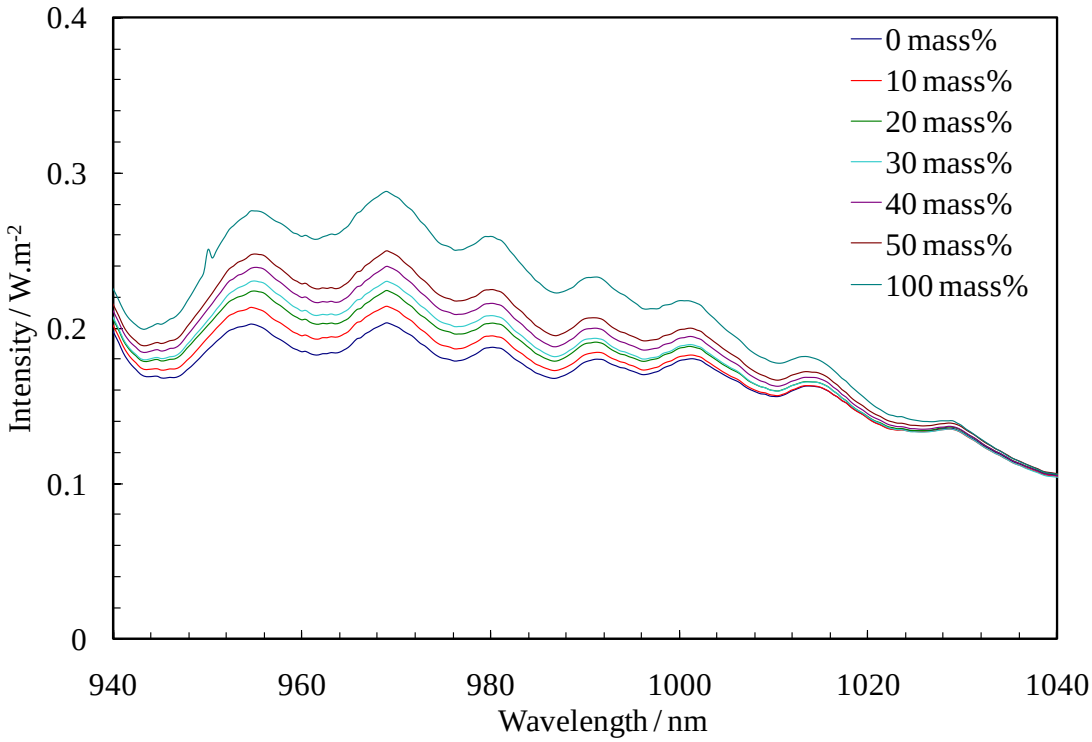

Figure 3.3 Spectra for methanol aqueous solutions indicating the highest effect in the NIR spectrum of light (zoomed 940-1040nm)

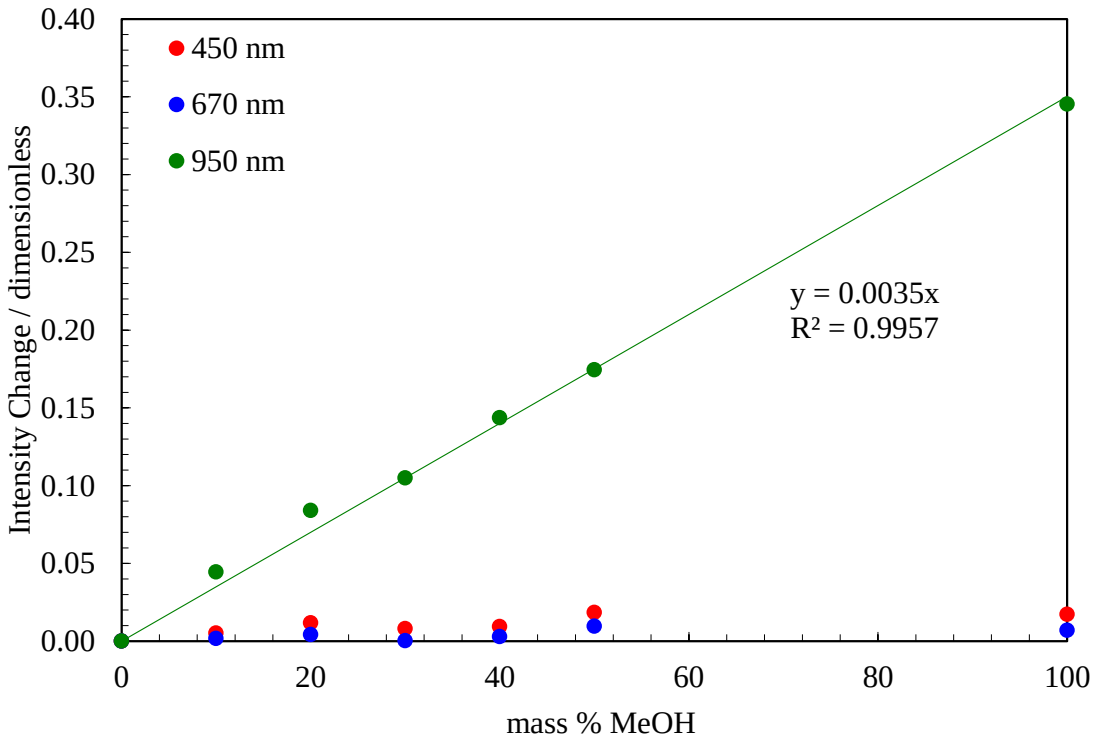

Figure 3.4 Intensity change in NIR spectrum of light at 950nm wavelength linearly increases with the methanol concentration

Table 3.1 Light intensities for MeOH aqueous solutions at 450 nm, 670 nm and 950 nm

Mass% MeOH Concentration	Intensity, $W.m^{-2}$			Intensity Change		
	450 nm	670 nm	950 nm	450 nm	670 nm	950 nm
0	0.23409	0.89455	0.18620	0.00%	0.00%	0.00%
10	0.23532	0.89612	0.19449	0.52%	0.18%	4.45%
20	0.23685	0.89837	0.20185	1.18%	0.43%	8.40%
30	0.23599	0.89482	0.20573	0.81%	0.03%	10.49%
40	0.23629	0.89716	0.21294	0.94%	0.29%	14.36%
50	0.23840	0.90308	0.21869	1.84%	0.95%	17.45%
100	0.23813	0.90073	0.25049	1.72%	0.69%	34.53%

As an alternative to methanol, ethylene glycol is widely used in the industry. It is more environmental friendly than methanol, its boiling point is much higher than methanol, and evaporation loss is negligible. Therefore, next series of experiments were conducted for various ethylene glycol solutions. The results (Figure 3.5) indicated that there was a significant influence of EG in the 940-1040 nm spectral range. Similarly to methanol results, there was almost no change in the UV/VIS part of the spectrum, intensity changes (Figure 3.7) clearly show that EG has the strongest effect in the NIR spectrum. At 950 nm wavelength, the technique sensitivity for methanol content is 0.55 $mW.m^{-2}$/mass%. The results for intensities and intensity changes for different wavelengths are summarised in Table 3.2.

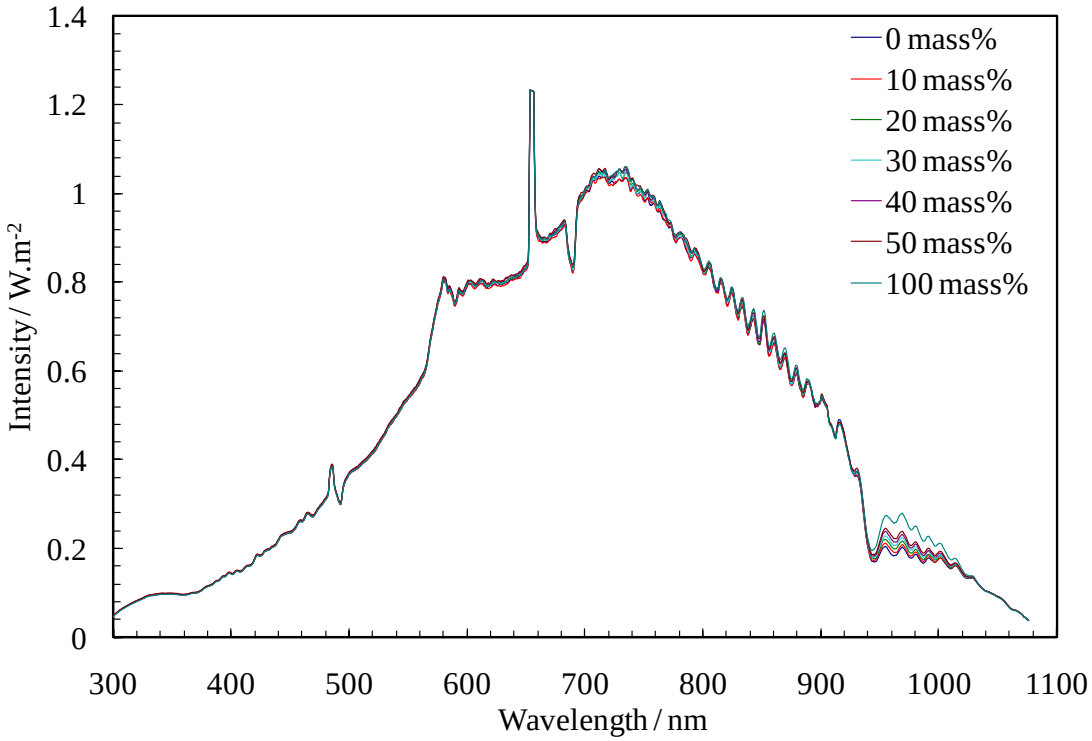

Figure 3.5 Spectra for ethylene glycol aqueous solutions indicating the highest effect in the NIR spectrum of light (940-1040nm)

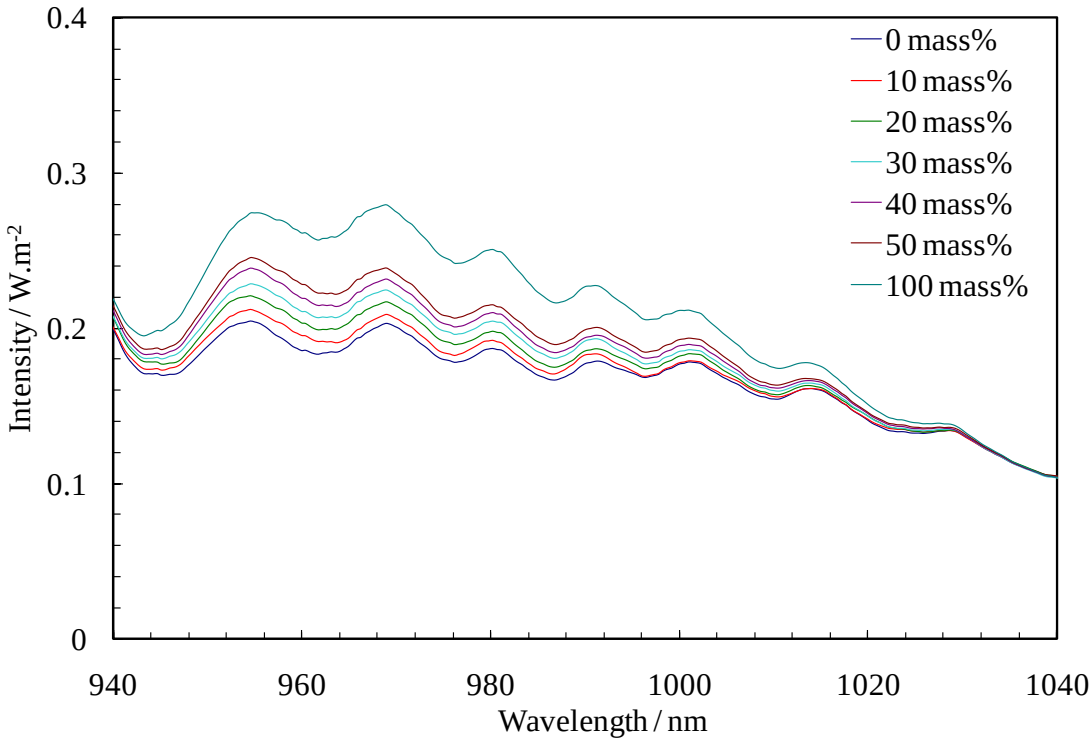

Figure 3.6 Spectra for ethylene glycol aqueous solutions indicating the highest effect in the NIR spectrum of light (zoomed 940-1040nm)

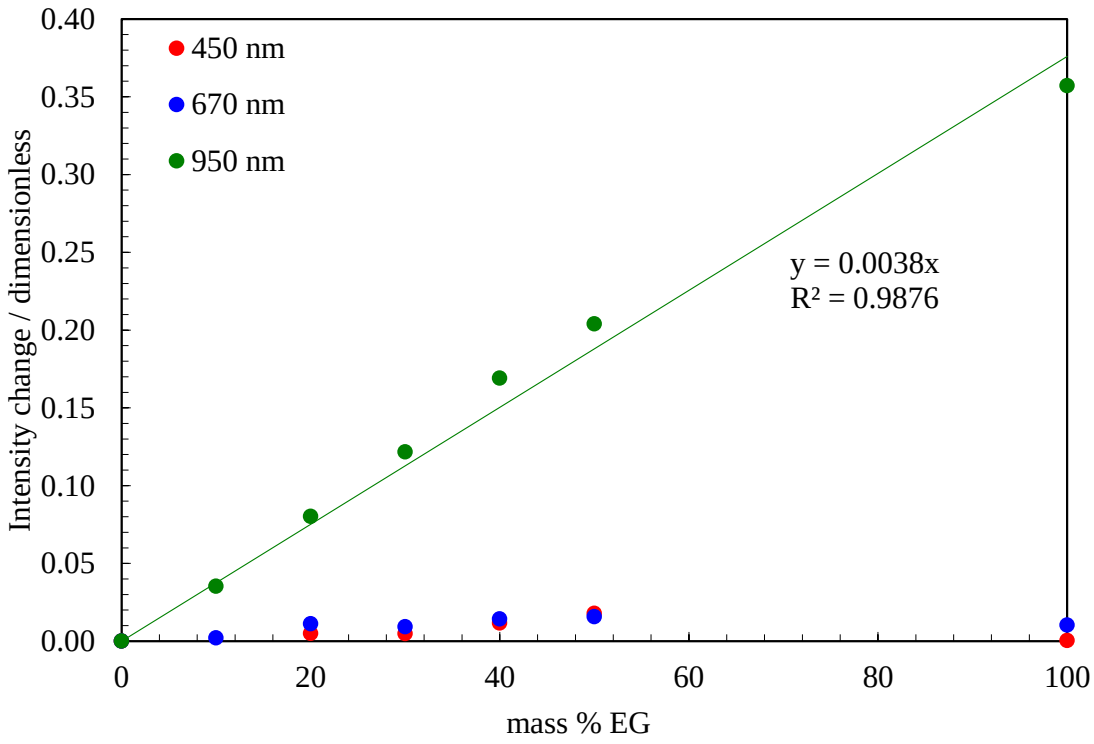

Figure 3.7 Intensity change of the NIR spectrum of light at 950 nm wavelength is also linearly increases with the ethylene glycol aqueous concentration

Table 3.2 Light intensities for EG aqueous solutions at 450 nm, 670 nm and 950 nm

Mass% EG Concentration	Intensity, $W.m^{-2}$			Intensity Change		
	450 nm	670 nm	950 nm	450 nm	670 nm	950 nm
0	0.23530	0.89485	0.20161	0.00%	0.00%	0.00%
10	0.23517	0.89669	0.20872	-0.06%	0.21%	3.53%
20	0.23648	0.90481	0.21778	0.50%	1.11%	8.02%
30	0.23643	0.90309	0.22615	0.48%	0.92%	12.17%
40	0.23804	0.90765	0.23570	1.16%	1.43%	16.91%
50	0.23950	0.90885	0.24272	1.78%	1.56%	20.39%
100	0.23539	0.90409	0.27359	0.04%	1.03%	35.71%

These results for methanol and ethylene glycol were encouraging for lab-prepared synthetic solutions. However, pipeline fluids (produced water) always contain oil, solid particles, and other chemical additives like corrosion and scale inhibitors. To understand the feasibility of the spectroscopy method for field application, the effect of impurities (such as sand, oil, and different types of inhibitors) were further investigated in Section 3.7. Expansion of the experiments in to the further infra-red range (1100-3000nm) is suggested for better alcohol concentration analysis (Felizardo et al., 2007; Gallignani et al., 2004).

3.5 EFFECT OF SALT

Hydrate inhibition effect of salt is defined by the degree of ionisation and the number of ions formed from each molecule of electrolyte (salt). The degree of ionisation is a strong function of the type and the concentration of the salt. An example of this is illustrated in Figure 3.8, which shows the degree of ionisation of NaCl and $CaCl_2$ as a function of the salt concentration at 293.15 K (Yousif and Young, 1993). Salt ions interact with water hydrogen bonding reducing water activity and the ability to form cage structures hosting guest molecules of gas. Salt is also an important component in systems containing thermodynamic inhibitors such as methanol increasing the hydrate inhibition effect (Mei et al., 1998). The effect of salt on the equilibrium concentration of gas components (e.g. methane) in the water-rich phase is demonstrated in Figure 3.9. As shown, the presence of salt(s) will reduce the methane solubility, and inhibit hydrate formation, as the hydrate-water-methane point for 3.5 mass% NaCl solution is at a lower temperature compared to pure water (Tohidi et al., 1997).

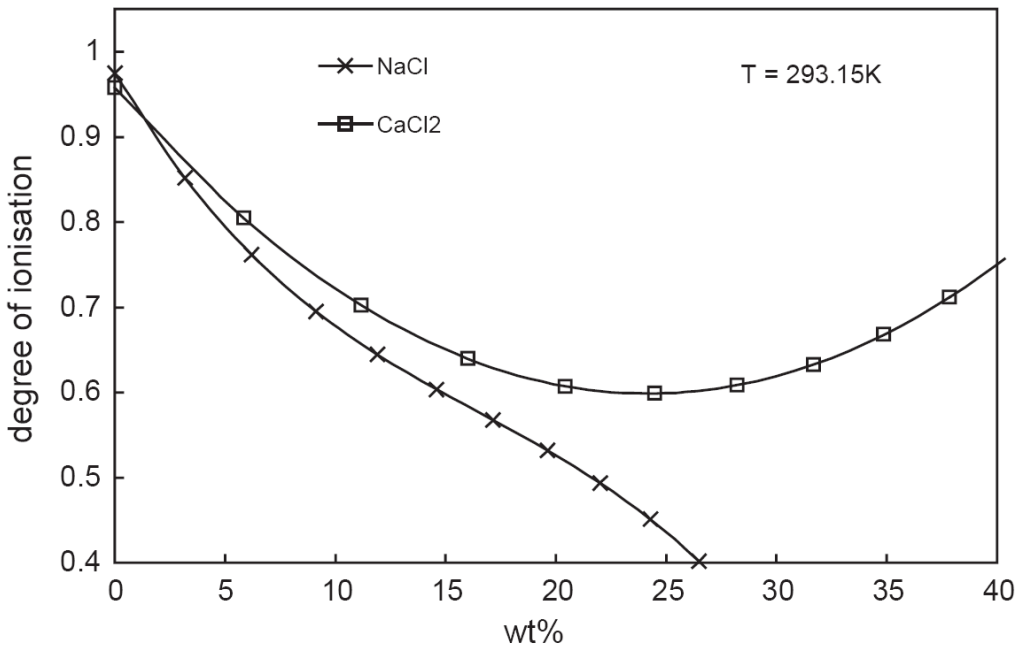

Figure 3.8 Degree of ionisation of NaCl and $CaCl_2$ at 293.15 K as a function of concentration (Ostergaard et al., 2005)

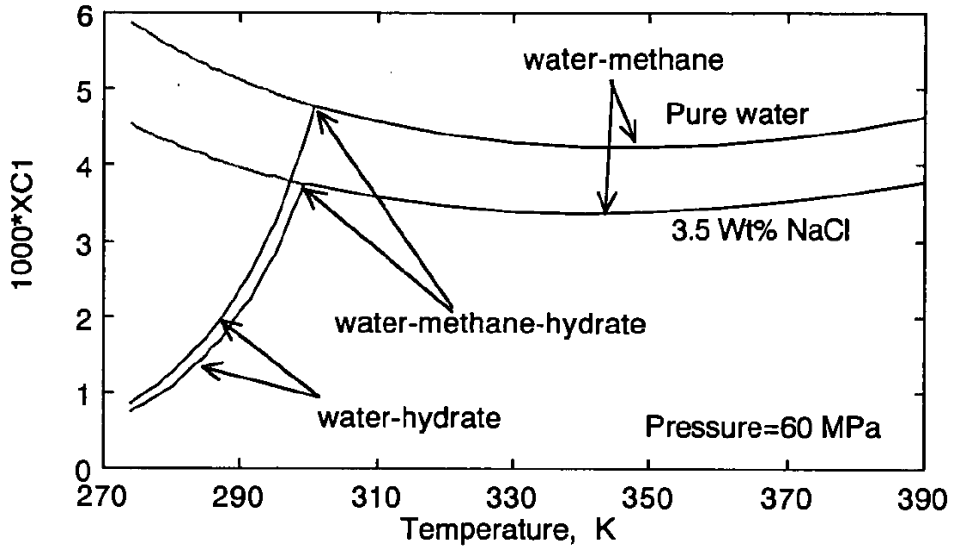

Figure 3.9 Effect of water salinity on methane concentration (Tohidi et al., 1997)

Due to hydrate formation, concentration of salt in water increases which could inhibit the further formation of hydrates. It is important to keep a close eye on concentration of salt not only because of its important role in hydrate inhibition, but also because its concentration increase can serve itself as an indicator of forming hydrate, as hydrate crystallisation involves only pure components: water and gas (Tohidi et al., 1997).

Salts, such as NaCl, KC1, $CaC1_2$, Na_2SO_4, NaF, NaBr, $MgCl_2$, $SrCl_2$, $BaCl_2$, can be encountered during the oil and gas production. To investigate the spectroscopy technique for the ability to measure salt concentrations, the most common salt, sodium chloride NaCl, was selected for these studies. The effect of salt (NaCl) on spectrum was tested at fixed ethylene glycol concentrations (0 and 50 mass%). From the intensity spectrum (Figure 3.10), it is seen that salt has a minor effect over the entire frequency range without any characteristic peaks or abnormalities. Similarly, it can be noted from the intensity change plot (Figure 3.12 and Figure 3.13).

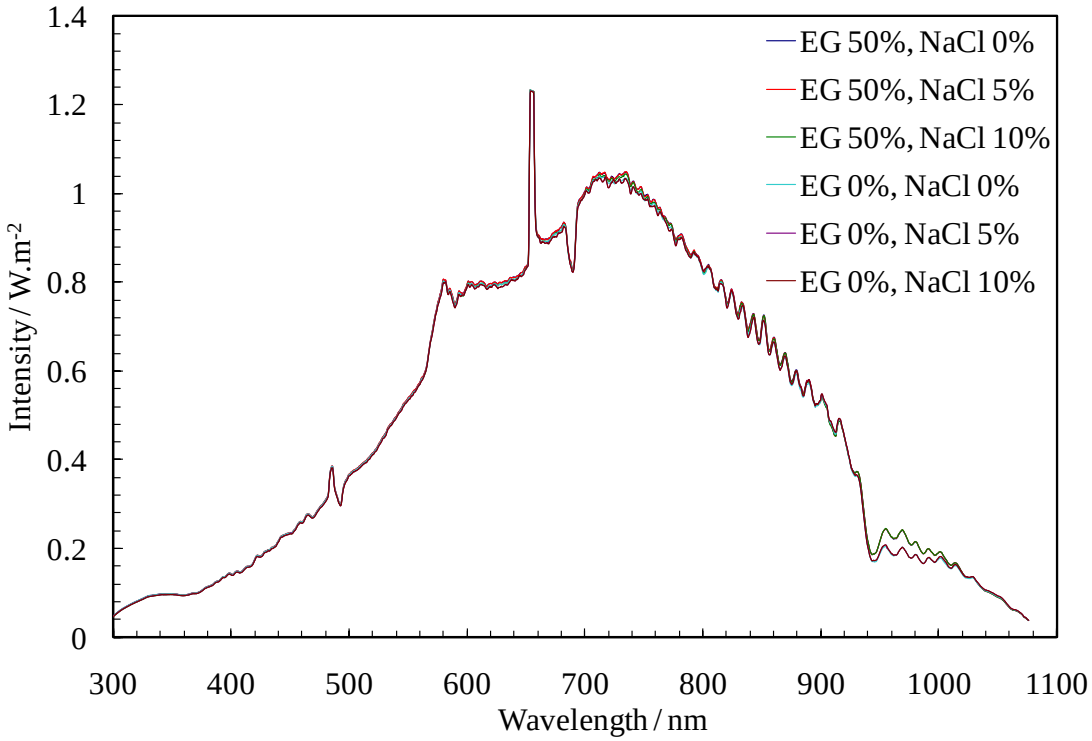

Figure 3.10 Spectra for deionised water, EG, NaCl systems indicating insensitivity of spectroscopy technique to salt component

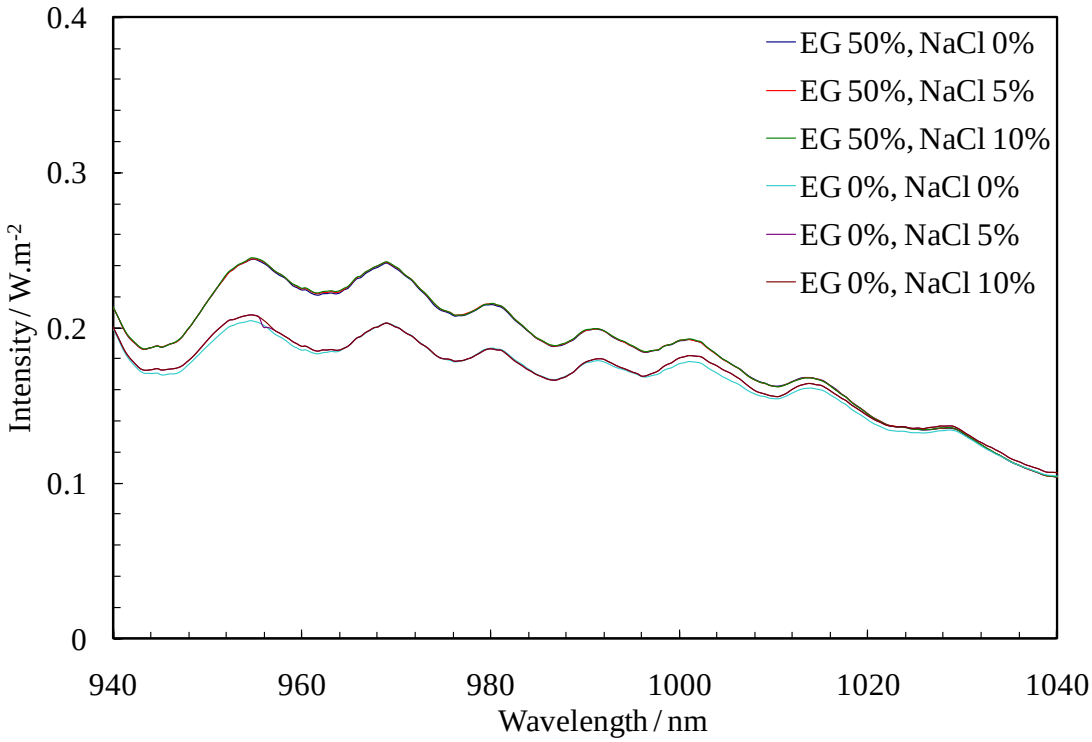

Figure 3.11 Spectra for deionised water, EG, NaCl systems indicating insensitivity of spectroscopy technique to salt component (zoomed 940-1040 nm)

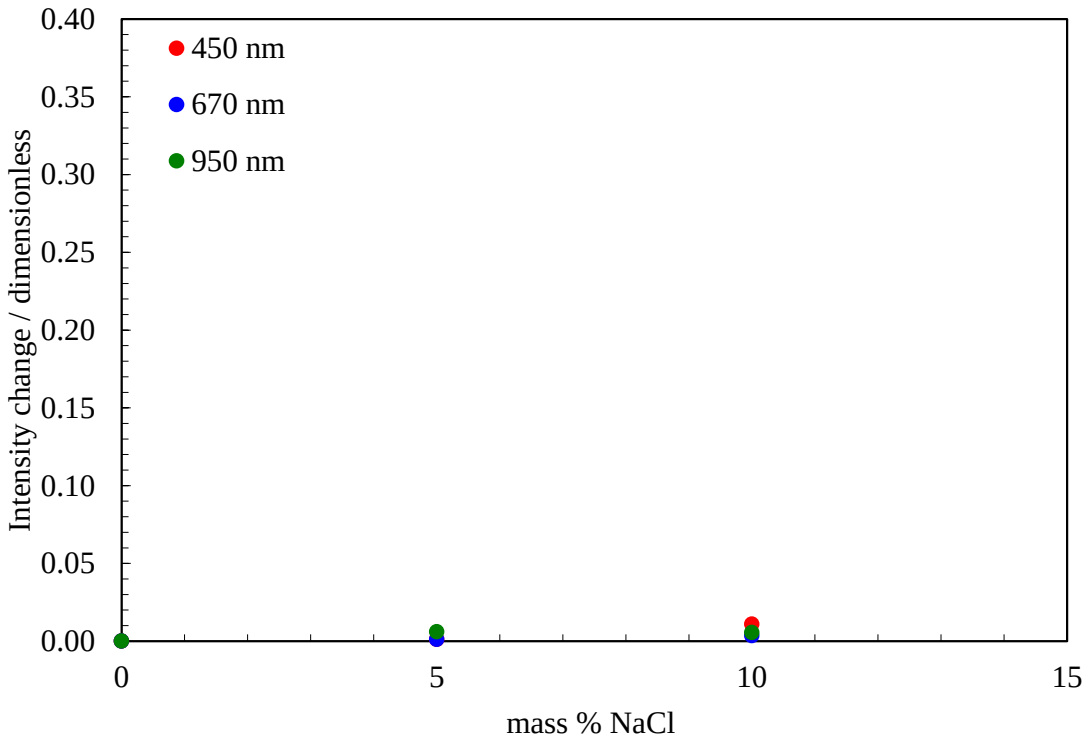

Figure 3.12 Intensity change for water with various NaCl concentrations

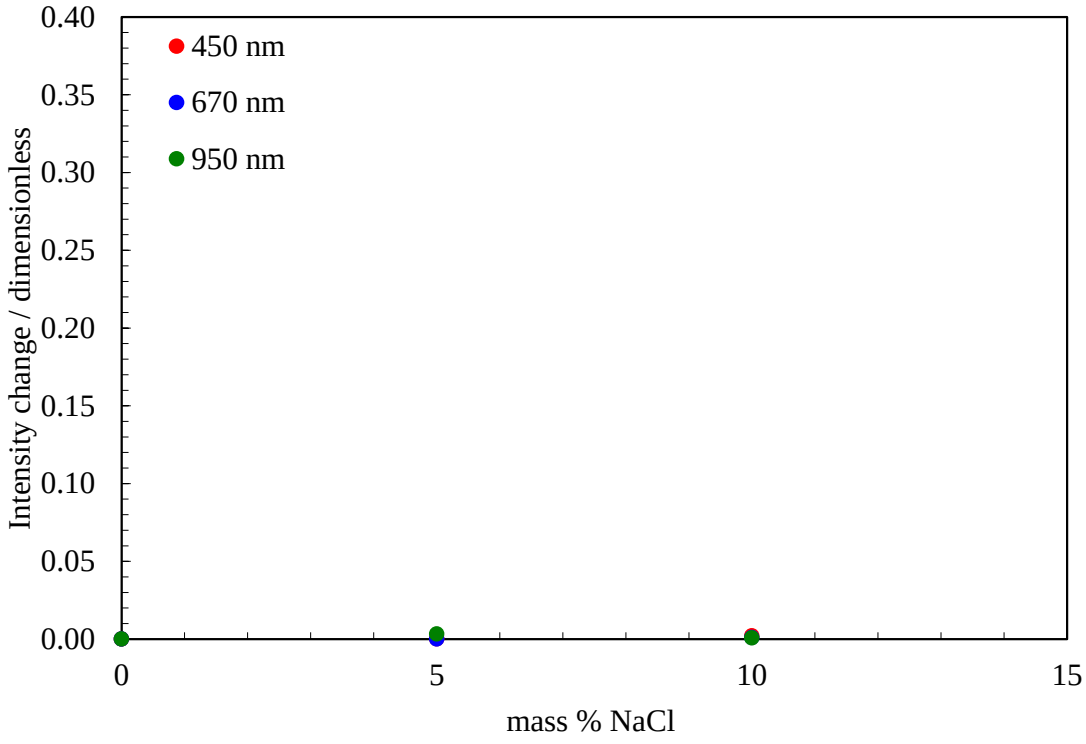

Figure 3.13 Intensity change for water with ethylene glycol and various NaCl concentrations

As it can be seen, the light intensity does not change with salt concentrations. This is in line with the fact than salts absorption spectrum leis further in infrared region.

Therefore, the spectroscopy technique in the 320-1100 nm range cannot be used to determine the salt concentration. However, expansion of the experiments in to IR range (1100-3000nm) is suggested, since the applicability of spectroscopy for salt concentration analysis has been proved for this region elsewhere (Max et al., 2000).

3.6 LOW DOSAGE HYDRATE INHIBITORS

For hydrate prevention, traditional thermodynamic inhibition approaches are beginning to be superseded by emerging technologies such as LDHIs. LDHIs have been researched and developed over the past 15 years as an alternative method to control gas hydrates. They are now established tools for the prevention of gas hydrate plugging of oil and gas pipelines and gas wells. A wide range of OPEX savings, possible extended field lifetime and multi-million dollar CAPEX savings are economic drivers for choosing LDHIs instead of other hydrate prevention methods (Kelland et al., 1995).

Low Dosage Hydrate Inhibitors can be divided into two categories; Kinetic Hydrate Inhibitors (KHIs), and Anti-Agglomerants (AAs). KHIs delay hydrate formation for a certain period of time within the hydrate region (known as induction time), depending on the system composition, degree of subcooling, and concentration of the inhibitor. AAs do not prevent or delay hydrate formation, but instead prevent gas hydrate agglomeration and thus the formation of hydrate blockages. These inhibitors, due to their low required concentrations (less than 1 mass% compared to up to 60 mass% for thermodynamic inhibitors), have a significant impact on the reliability and economics of flow assurance strategies, and environmental aspects of field development (Kelland et al., 1995).

LDHIs are so called as they can be efficiently used at dosages far lower than that of the thermodynamic inhibitors: the required concentration for these additives is currently expected in the range of 0.5-3 mass% in water. In fact, the main economic incentive of using LDHIs is in the large reduction of capital expenditures (CAPEX) via the reduction of the size of the storage, pumping and piping facilities; they are far less volatile and flammable, and relatively more environmentally friendly (Peytavy et al., 2008). These inhibitors, due to their low required concentrations, have a significant impact on the reliability and economics of flow assurance strategies for offshore/deepwater oil and gas reservoirs. Therefore, their application can improve the economic life and overall hydrocarbon recovery from these reservoirs.

As described in Chapter 2, light attenuation could identify sign of hydrate formation earlier than the conventional pressure analysis method, spectroscopy could be used to detect water memory, methanol and EG concentrations could be monitored by spectroscopy. In this part of thesis, the potential applicability for monitoring low dosage hydrate inhibitor concentration in the total fluid mixture is investigated.

3.6.1 Fluid Systems in the Presence of LDHI

When LDHI is added to the fluid system, it can alter the hydrate crystallization properties whilst its concentration is within 0.1 – 1.0 mass% (active component) based on the water phase. The question is whether those doses of chemicals measurably affect other physical properties (like passing light spectrum) of the fluid, and, as such, be detectable? The answer on this question is debated throughout this section of the thesis.

One of the usages of LDHI is to act primarily as gas hydrate anti-nucleators delaying hydrate formation although most of them also delay the growth of gas hydrate crystals (KHI). In early 90's, Colorado School of Mines successfully tested the homopolymer Poly-N-Vinyl caprolactam (PVCap) which then became a standard to which other KHIs are compared. PVCap was selected as a representative LDHI chemical for these series of experiments. No commercial chemical formulations were tested. To find the spectrum effect of this reference KHI, several solutions were examined:

1. Ethylene Glycol – PVCap systems
2. Ethylene Glycol – PVCap systems in the presence of salt (NaCl)
3. Ethylene Glycol – PVCap systems in the presence of water

3.6.1.1 Ethylene Glycol – PVCap Systems

Solutions of ethylene glycol and various PVCap mass% were used in these series of experiments. Various concentrations of PVCap were dissolved in pure EG. As it was described in procedures (Section 3.3.3), UV/VIS/NIR light spectrum was measured 5 times for 30 seconds (integration time) each 10 minutes for statistical purposes. The spectral response of the fluid systems (Figure 3.14) shows that PVCap has no effect on the spectrum in the 580-1100 nm frequency range and a strong effect in the range of 300-580 nm. At 350 nm wavelength, the technique sensitivity is 5.9 mW/m^2/mass%.

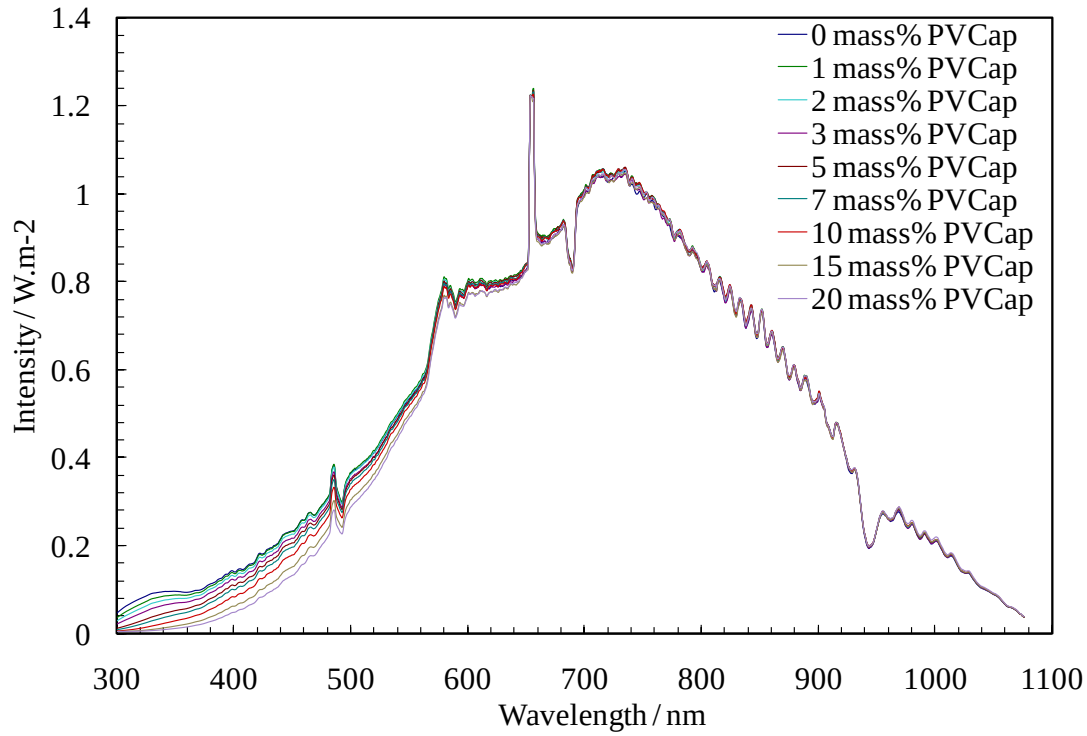

Figure 3.14 Spectra for EG-PVCap solutions showing no effect in the 580-1100 nm frequency range and a strong effect in the range of 300-580 nm

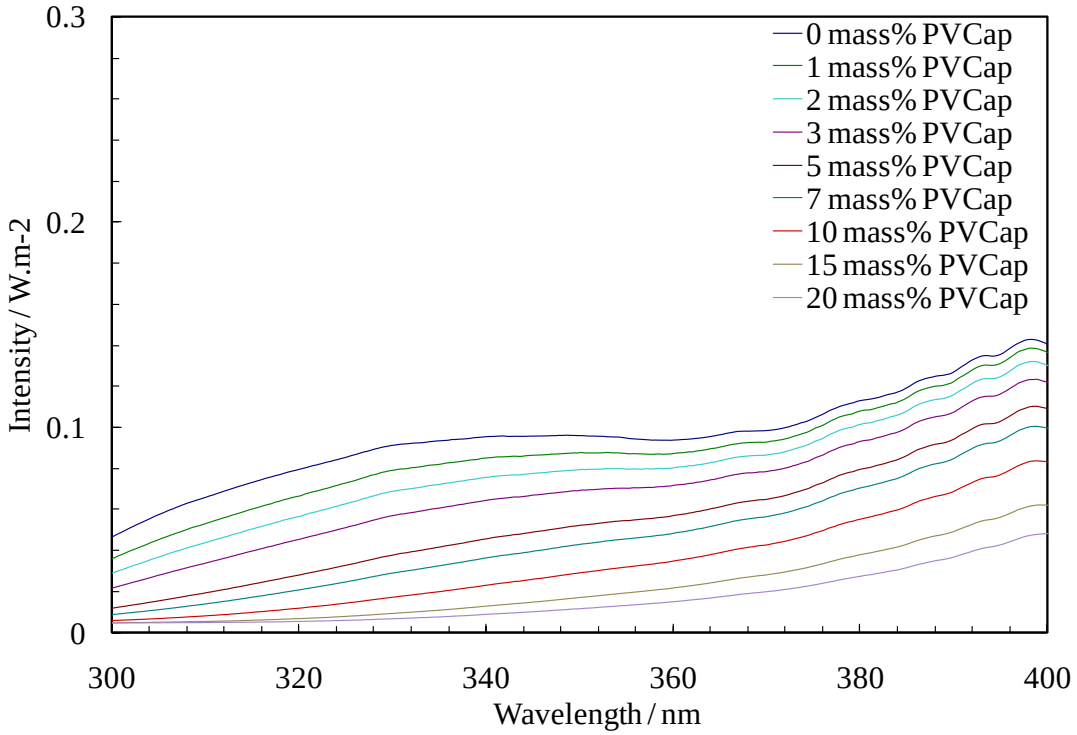

Figure 3.15 Spectra for EG-PVCap solutions (zoomed 300-400 nm)

As per Beer-Lambert Law, the intensity of passing beam exponentially depends on the concentration of absorbing species in the material the light is travelling through. For the presented Ethylene Glycol – PVCap systems with I_0 = 0.0952 W.m^{-2}, the coefficient in exponential argument is 0.11 at 350 nm (Figure 3.16). Explained in Section 2.1, Beer-Lambert Law can be applied to define direct equation for concentration of PVCap hydrate inhibitor in the EG-PVCap.

From Figure 3.16, the analytical approximation for intensity at 350 nm wavelength is

$$I = I_0 e^{-0.11c} \tag{3.1}$$

where c is concentration of PVCap (dimensionless):

$$c = -\frac{1}{0.11}\ln\left(\frac{I}{I_0}\right) = -\frac{1}{0.11}\frac{log_{10}\left(\frac{I}{I_0}\right)}{log_{10}(e)} = \frac{1}{0.11 log_{10}(e)}\left(-log_{10}\left(\frac{I}{I_0}\right)\right) \tag{3.2}$$

Stated by Beer-Lambert Law, absorption (attenuation coefficient) is:

$$A = -log_{10}(\frac{I}{I_0}) \tag{3.3}$$

the overall equation becomes:

$$c = \frac{1}{0.11 log_{10}(e)} A \tag{3.4}$$

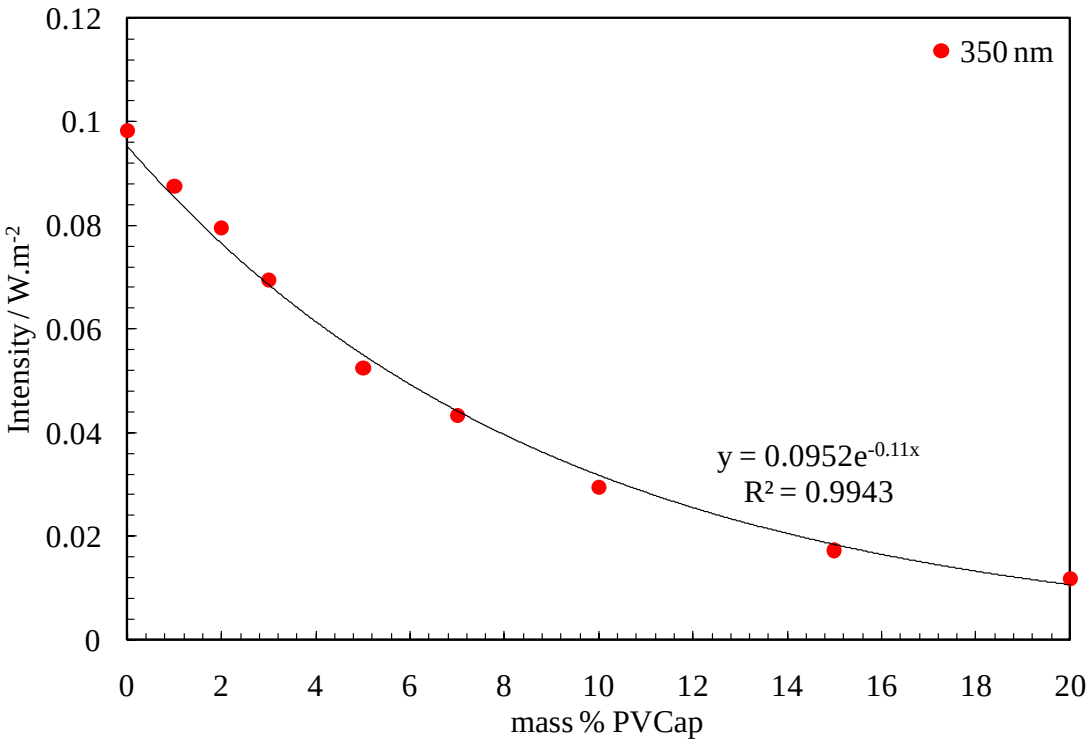

Figure 3.16 Intensity of EG-PVCap solutions at 350 nm indicating exponential dependency

PVCap showed no measurable effect in the NIR range of the spectrum (Figure 3.17). At 950 nm, the fluctuations of the intensity attribute to noise. Thus, this range cannot be applied to define PVCap content, but, in turn, can favourably be used to determine other fluid properties such as thermodynamic hydrate inhibitors concentration. As it was presented in Section 3.4 of this Chapter, hydrate inhibitors such as methanol or ethylene glycol have a distinguishable signature in NIR part of light spectrum.

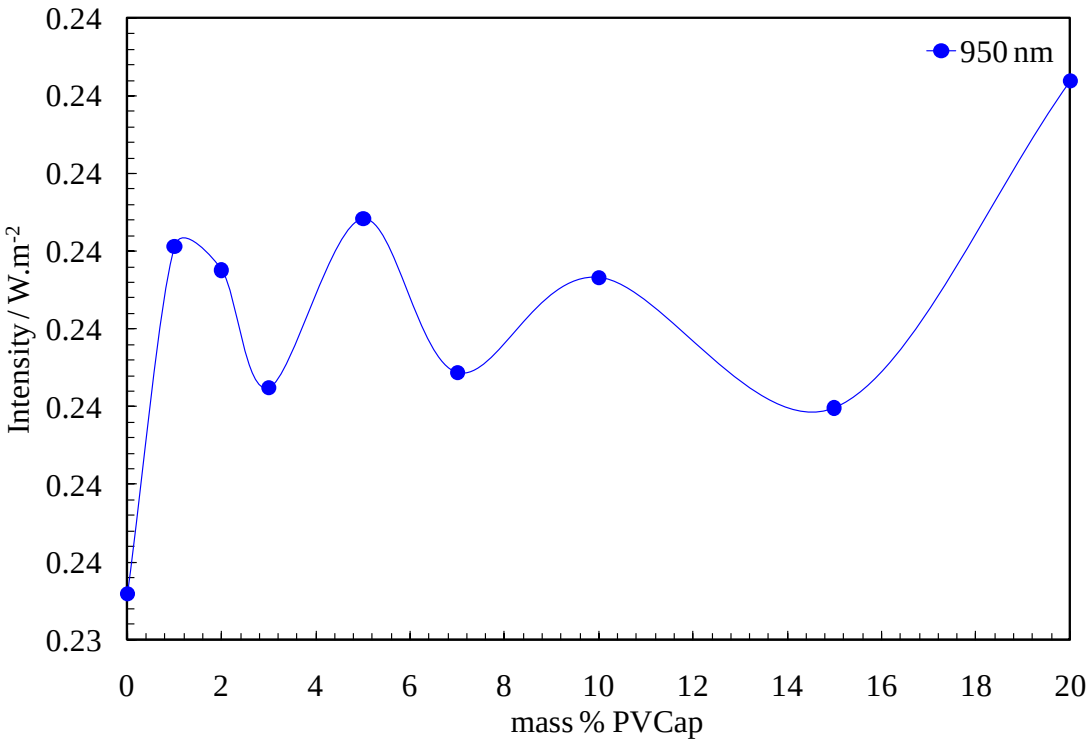

Figure 3.17 Intensity of EG-PVCap solutions at 950 nm indicating no dependency rather stochastic fluctuations or noise

3.6.1.2 Ethylene Glycol – PVCap Systems in the Presence of Salt (NaCl)

The further experiments were designed to examine the technique sensitivity for the presence of salt in LDHI fluid systems. Solutions of ethylene glycol with various PVCap and salt concentrations were prepared for these tests. As it was described in procedures (Section 3.3.3), UV/VIS/NIR light spectrum was measured 5 times for 30 seconds (integration time) each 10 minutes for statistical purposes. The signal was very repeatable with the relative standard deviation of 0.7% averaged across whole range of wavelengths, so that there was a good confidence in mini-spectrometer measurements. The spectral response of the salted fluid systems (Figure 3.18) showed similar effect of PVCap as for the systems without salt. The sensitivity of the technique at 350 nm was not changed representing the same function of total PVCap concentration. Being drawn in the same plot (Figure 3.19), the measured data showed a match with the correlation 2.1 presented above, once again highlighting the negligible salt effect. Conclusively, the conducted experiments confirmed the technique insensitivity for the presence of salt in LDHI fluid systems.

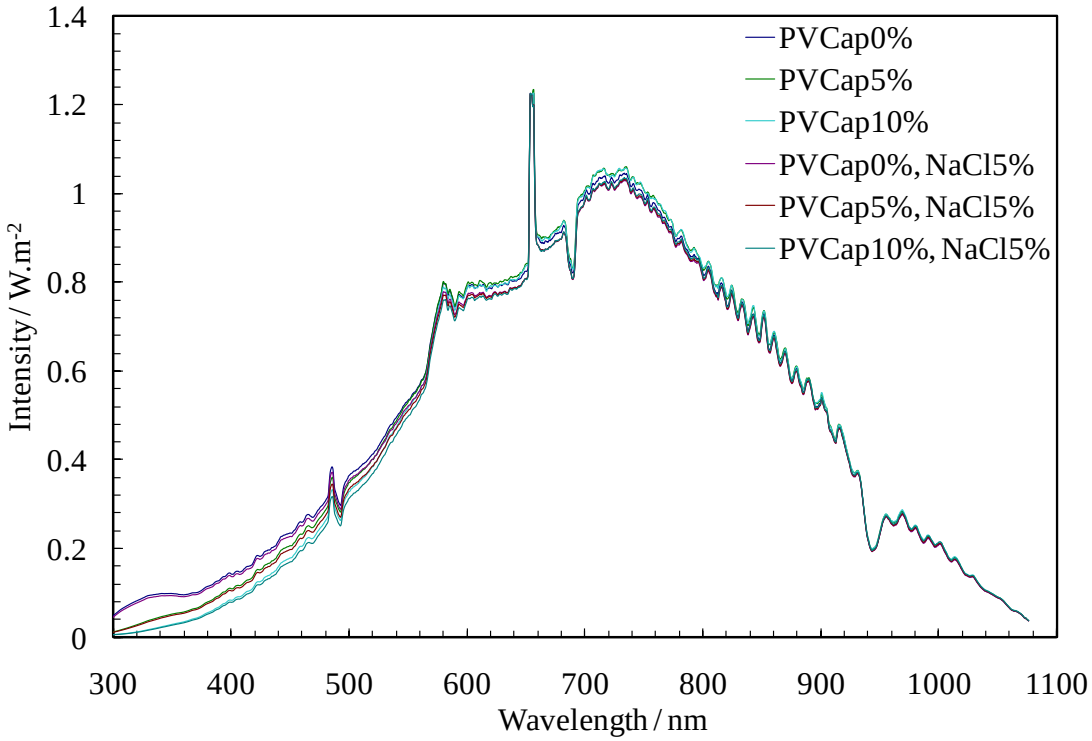

Figure 3.18 Spectra for EG-PVCap-salt solutions showing negligible effect of salt in 300-1100 nm frequency range

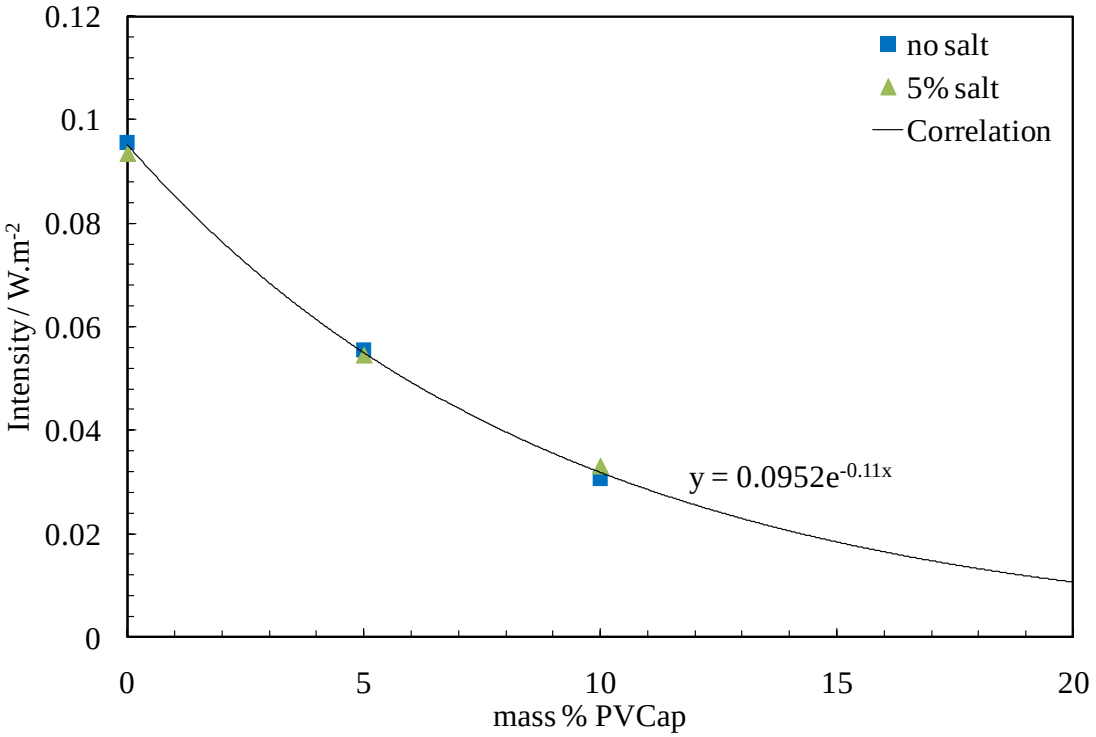

Figure 3.19 Intensity of EG-PVCap-NaCl solutions at 350 nm indicating match of previously developed exponential dependency for solutions without salt

3.6.1.3 Ethylene Glycol – PVCap Systems in the Presence of Water

Water production is generally unavoidable part of conventional hydrocarbon extraction. There can be free water in the produced fluid, or changes in temperature and pressure during production, transportation or processing can lead to water condensation. Unless properly inhibited, this water can cause gas hydrates formation. Since the presence of water is one of the main components leading to hydrate formation, more realistic fluid systems were examined in this section. PVCap detection capacity in the presence of water was investigated for systems containing 50/50 of water/EG based on mass. PVCap concentration was varied from 0 to 20 mass% based on the water phase.

As seen in Figure 3.20, there are two main regions of spectrum being affected by EG-PVCap-water fluid. From 300 to 670 nm which is UV and partly VIS region, there is a strong effect of PVCap concentration with the intensity being reduced by adding more inhibitor. The correlation developed in Section 3.6.1.1 above being plotted against measured data for 350 nm wavelength showed no effect of water present in the solution (Figure 3.22). From 940 to 1070 nm wavelength which is NIR region, there is an effect of EG/water mixture with the intensity reduction by an increase in EG content. As it was expected, no effect of PVCap was observed in this spectrum region.

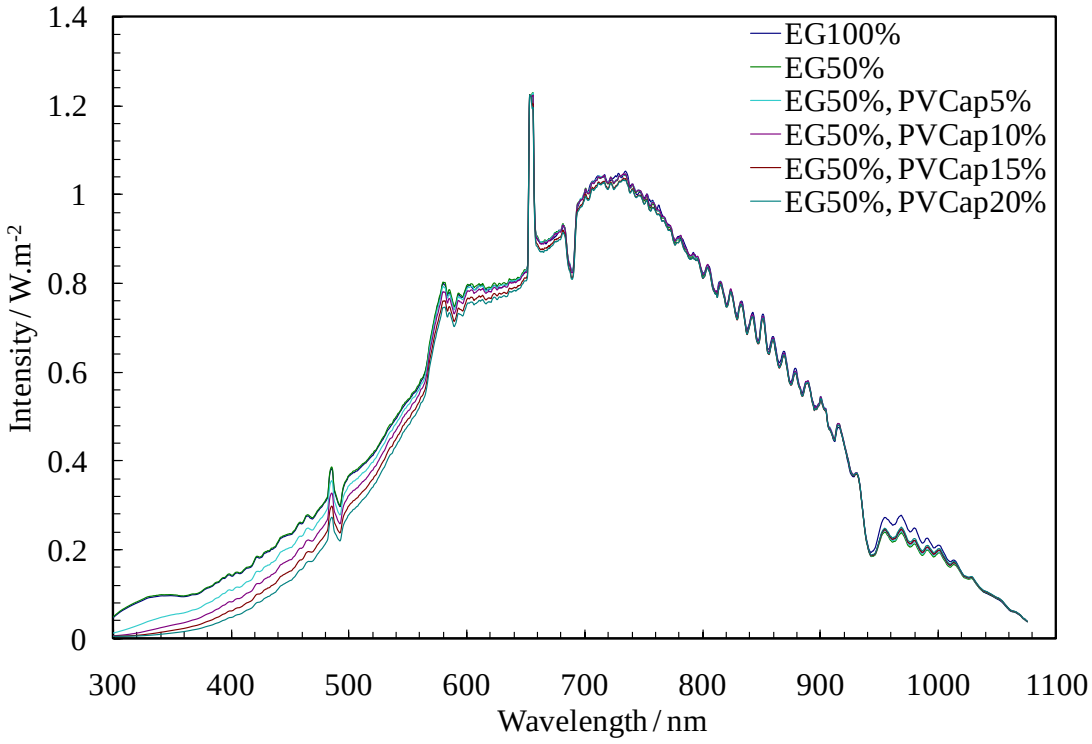

Figure 3.20 Spectra for EG-PVCap-water solutions showing typical trend of EG-water mixture in NIR frequency range and EG-PVCap mixture in UV range

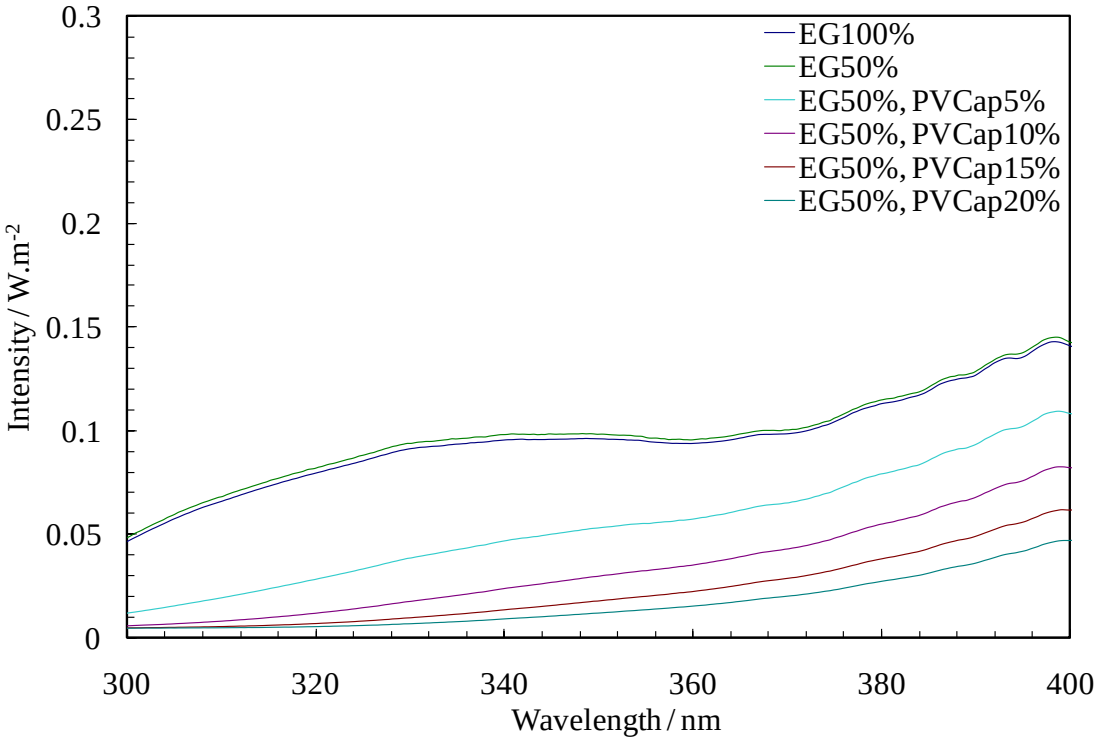

Figure 3.21 Spectra for EG-PVCap-water solutions (zoomed 300-400 nm)

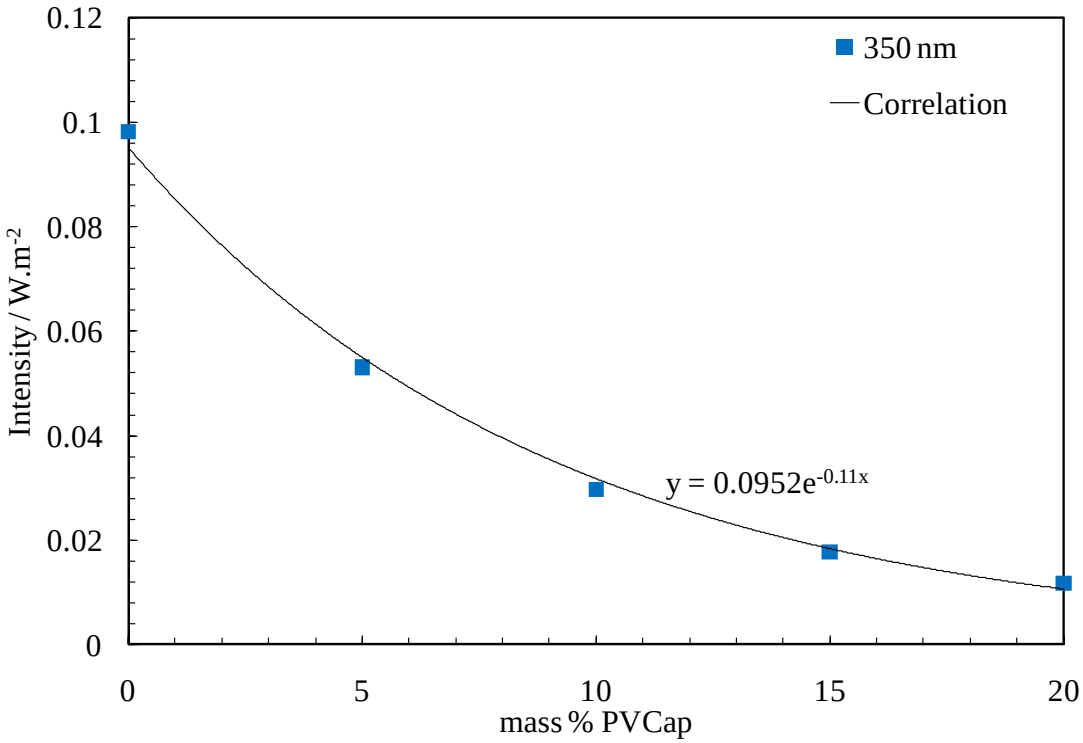

Figure 3.22 Intensity of EG-PVCap-water solutions at 350 nm indicating no effect of water and match of previously developed exponential dependency

The intensity change at 950 nm (Figure 3.23) showed the same trend as developed in Section 3.4 (Figure 3.7) with the slope of 0.0038. Therefore, the presence of PVCap had no effect on NIR region and, subsequently, EG spectrum trend.

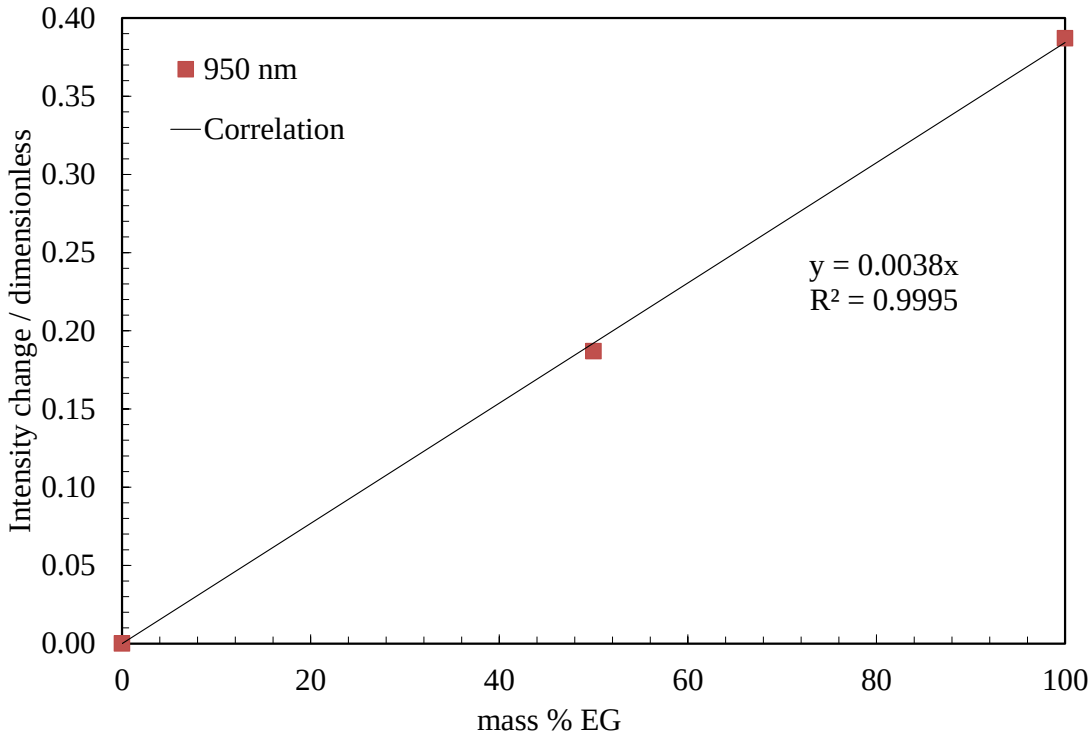

Figure 3.23 Intensity change of EG-PVCap-water solutions at 950 nm indicating typical EG dependency with the slope of 0.376 and no effect of PVCap

The technique showed two separate characteristic regions of light absorbance for PVCap and Ethylene Glycol inhibitors. This separation of spectrum regions is fundamental for the development of inhibitors monitoring technique, and, thus, suggests that the spectroscopy method has potential for determining both thermodynamic inhibitors and LDHIs in a single spectrum. However, this study was only conducted for pure PVCap solutions. The valuable signal contained in the measured spectrum can be hindered by the scattering/absorption on impurities contained in the real produced fluids. Additional investigations were conducted for various types of contamination and for produced water various thermodynamic inhibitor concentrations. The results are presented in the following Chapter.

3.7 EFFECT OF CONTAMINATIONS

This section presents a further method investigation for the effect of impurities. Impure by its origin, two types of produced water provided by BP and Total were tested. To

investigate the applicability of the technique in real production systems, several contaminated solutions with gradually increasing complexity were tested:

1. Synthetic solution with single hydrocarbon;
2. Solution with 5 mass% oil;
3. Solution with solids (fine sand particles);
4. BP Produced water with various MeOH contents;
5. Total Produced water with various MeOH contents.

3.7.1 Synthetic Solution with Single Hydrocarbon

First experiment is designed to depict the influence of hydrocarbons on water spectral response. Decane ($C_{10}H_{22}$) was selected for these tests. The spectral response (Figure 3.24) indicates that the presence of Decane in the water-methanol system does not alter the light spectrum. Decane is immiscible in water, and because the light is passing through the medium of the sample cell, the spectral response is not influenced by the presence of this pure hydrocarbon.

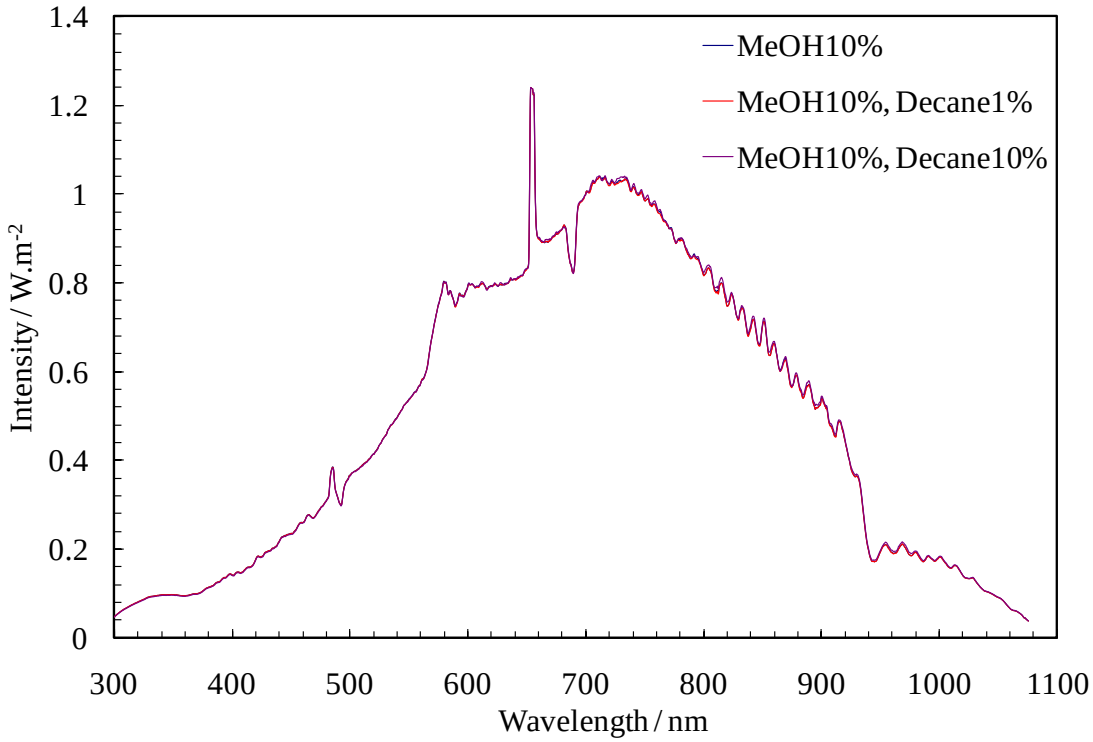

Figure 3.24 Spectra for synthetic solution indicating no influence of heavy hydrocarbon component alone (Decane)

3.7.2 Solution with 5 mass% Oil

Adding the oil to the water-methanol system significantly changes the light spectrum (Figure 3.25). This is due to the oil droplets present on the walls of test cell. The light is significantly attenuated in this fluid system. Therefore, the spectrometer integration time was increased 5 times to 50 ms to raise the electrical output of photo elements, as well as the measured spectrum was scaled by 1.45 times to fit the spectrum of pure water-methanol solution which it is compared to. Results show that spectrum of the oily system is logically attenuated in the UV region without significant change in the IR. This gives a feedback that concentration of methanol or ethylene glycol can be measured even in the presence of oil.

Table 3.3 Oil composition (from North Sea Brent reservoir)

Component	N_2	CO_2	C_1	C_2	C_3	iC_4	nC_4	iC_5	nC_5^+	Total
Mass (%)	0.26	1.86	15.16	5.68	5.34	0.90	2.72	0.99	67.09	100

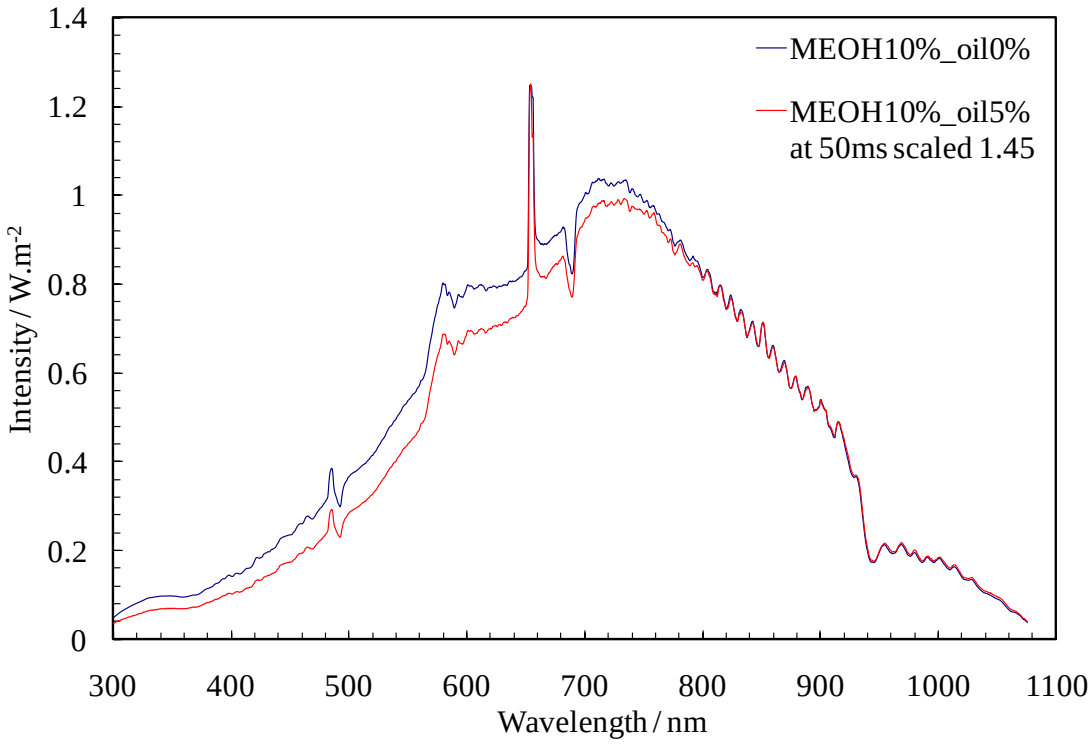

Figure 3.25 Spectra for methanol aqueous solution with and without oil indicating the highest influence of oil in the UV region and no effect in NIR region

3.7.3 Solution with Solids (Fine Sand Particles)

The presence of sand in the solution stochastically influence on the light spectrum (Figure 3.26). The intensity is reduced in UV part and increased in NIR part of the spectrum. This implies that the method is sensitive to fines such as sand, corrosion, erosion particles etc., and complicates the process of defining concentration requiring a correction of spectrum for a specific impurity.

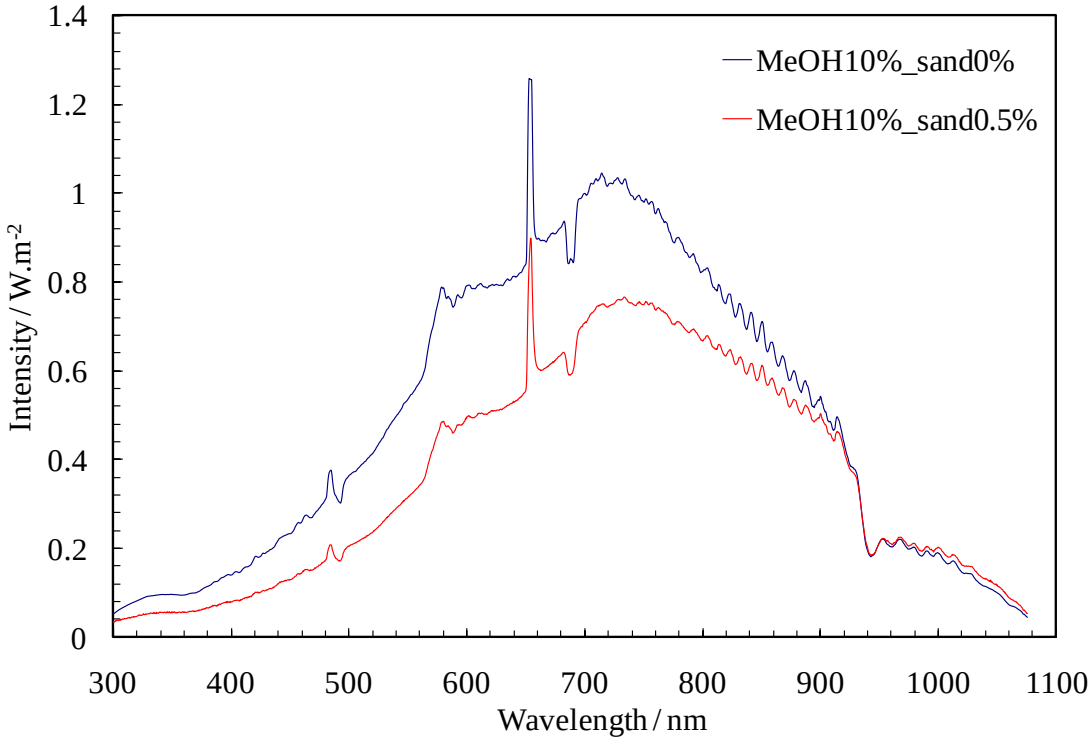

Figure 3.26 Spectra for methanol aqueous solutions with and without sand indicating stochastic influence of sand on the spectrum

3.7.4 BP Produced Water with Various MeOH Content

Industrial produced water provided by BP was tested in this series of experiments. Original produced water is alcohol free with mineralization of 5 mass% including salts like NaCl, KCl and unknown concentration of corrosion inhibitors. Methanol was then gradually added up to 50 mass%. Nevertheless BP water looks clean and clear, corrosion micro particles or reservoir clay fines could still be present causing minor fluctuations in the light spectrum. The spectra for those solutions (Figure 3.27) show that although light intensity is fluctuating in visible and UV region of spectrum, it is comparable to IR spectrum behaviour of deionised water-MeOH systems (Figure 3.2). Methanol concentration is therefore detectable in this produced water (Figure 3.28).

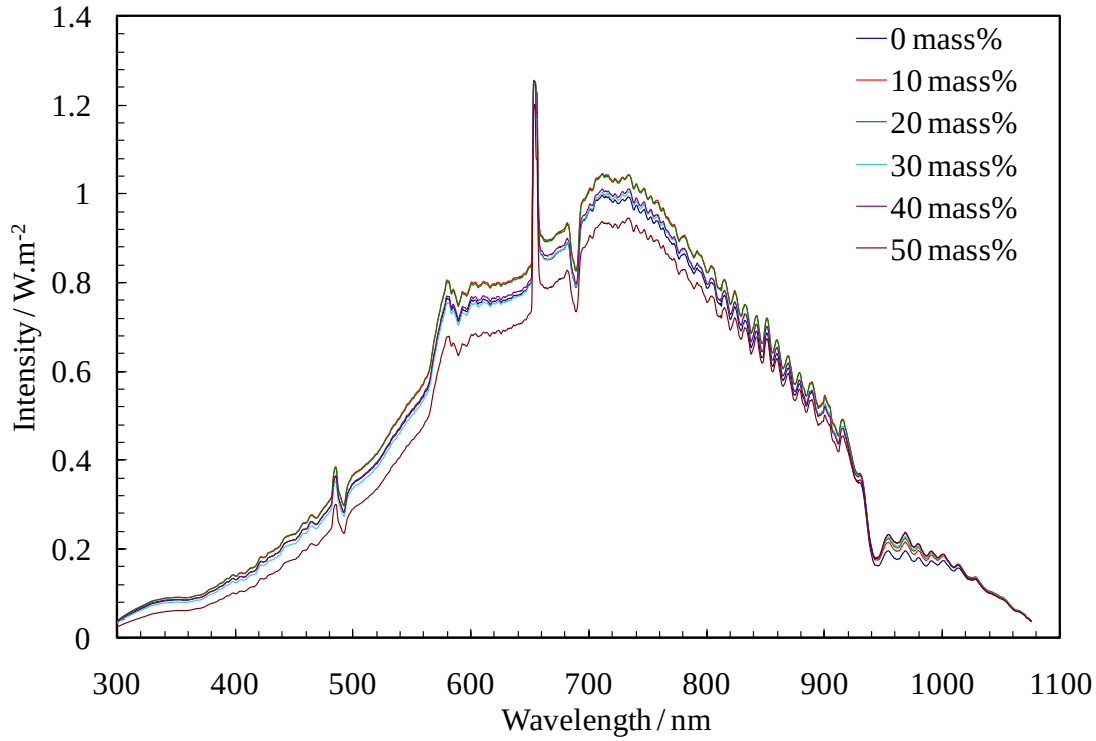

Figure 3.27 Spectra for BP produced water with various MeOH concentrations

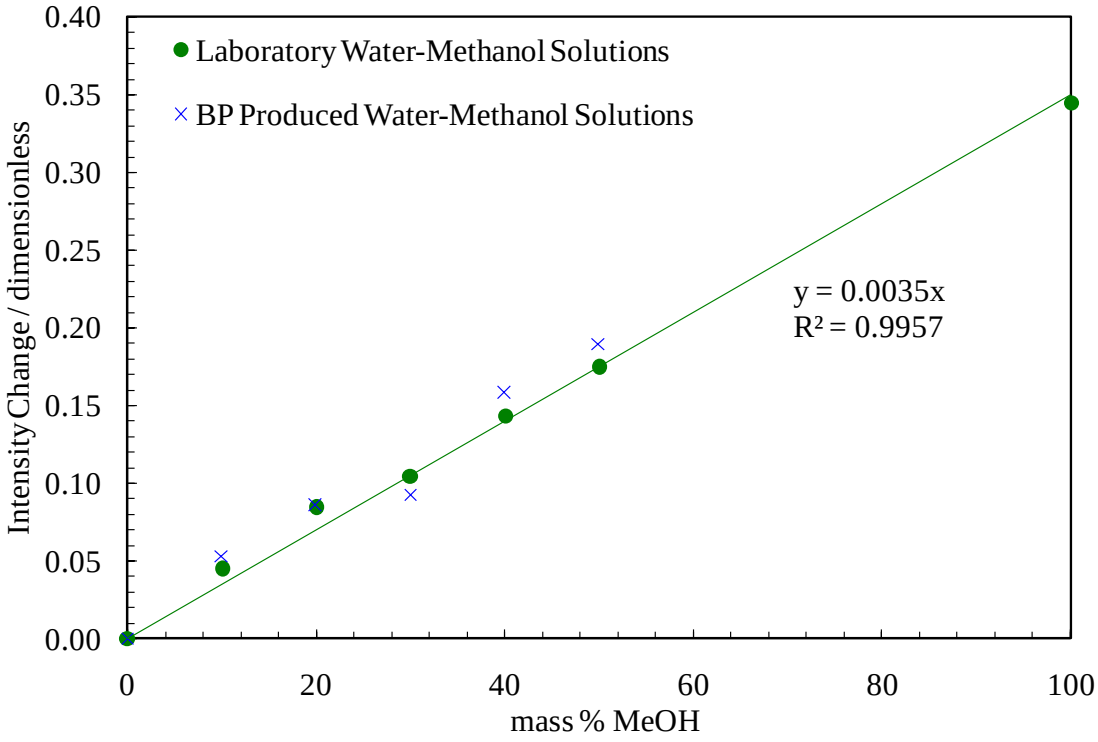

Figure 3.28 Intensity change against methanol concentration at 950 nm wavelength showing that BP water trend is similar to what was measured for laboratory water

3.7.5 Total Produced Water with Various MeOH Contents

Produced water provided by Total was also tested in this investigation. Original produced waster contains 3 mass% NaCl, 22 mass% MeOH, unknown concentration of corrosion inhibitor and oil/condensate. Methanol was then added to the solution. Because the produced water is highly contaminated (and has a milky colour), the spectrometer integration time was increased 5 times from 10 ms to 50 ms to measure intensity. The spectra for the investigated fluid systems (Figure 3.29) are highly unstable in all spectrum regions. This is because any movement of impurities in the produced water alters the refraction of light coming through the sample, and, therefore, its spectrum. Methanol concentration is not detectable in the produced water with particle/fines type of impurities.

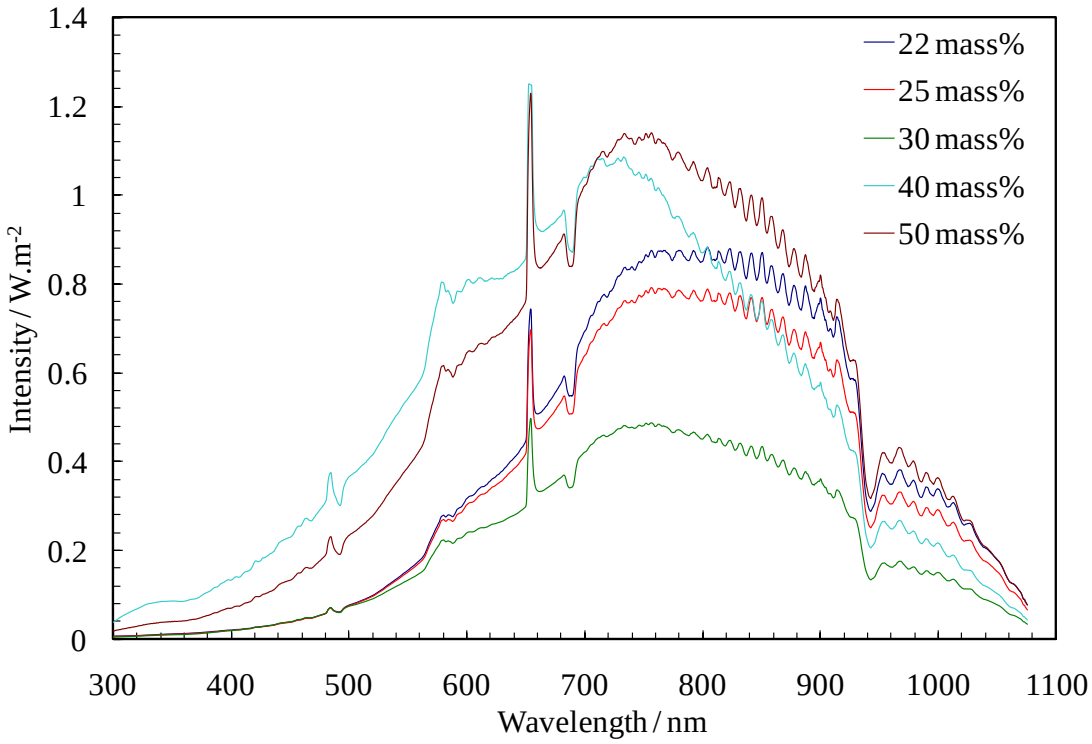

Figure 3.29 Spectra for Total produced water with various MeOH concentrations

The results can be also explained by high contamination of produced water by oil/condensate which has an absorption lines in UV, VIS and partially in NIR regions of spectrum (Figure 3.30). Another test was conducted to remove/reduce the effect of oil contamination. Fluids were centrifuged and separated under 5000 rpm for 20 minutes. After scaling, it can be noted that the spectra of original and separated produced water (Figure 3.31) have no significant difference in NIR spectrum region. The intensity slightly increased in the middle of spectrum indicating that some oil was separated from

the water. As a solution, it is suggested to measure methanol concentration in the further infrared region where the methanol has higher absorption peaks and where there is no overlap with the oil absorption line. Because methanol has the first characteristic absorption peak at 2700 nm and the second one at 7430 nm (Plyler, 1952), it is suggested to measure infrared spectrum until 3000 nm to cover the first peak. Another benefit of using the instrument with the wide spectrum range could be the measurement of a range of hydrocarbons in the produced fluids (Figure 3.32) which could be of use for another hydrate early warning system based on C_3/C_1 ratio monitoring explained elsewhere (Tohidi et al., 2008).

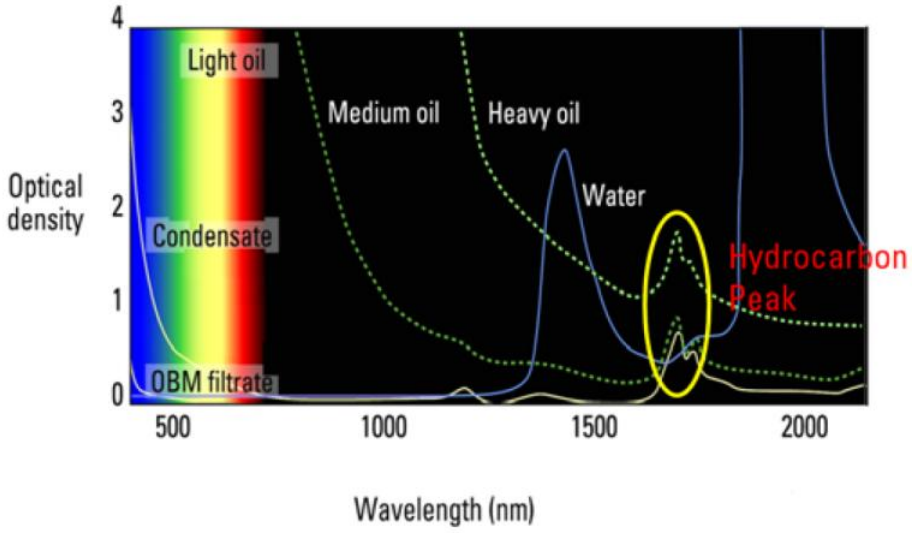

Figure 3.30 Absorption (optical density) spectra of hydrocarbons, water and CO_2 between 400 and 2000 nm (Betancourt et al., 2006)

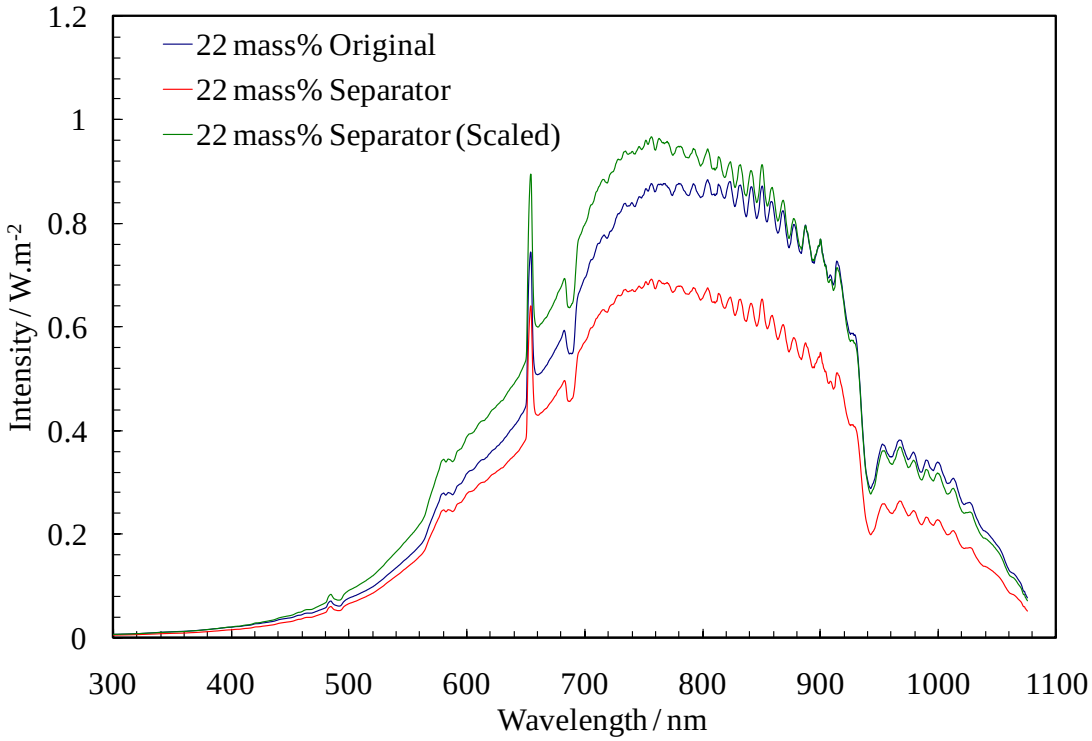

Figure 3.31 Absorption spectra of original and separated produced water

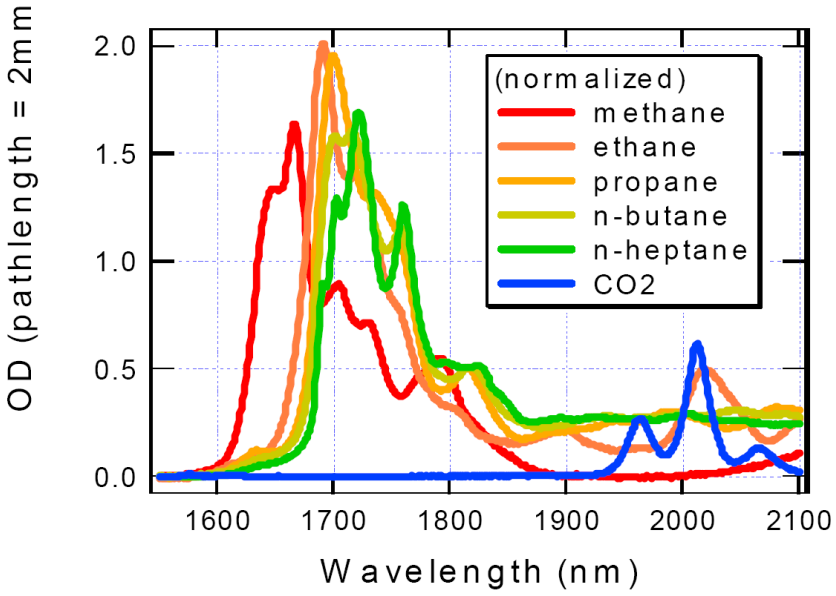

Figure 3.32 Absorption (optical density) spectra of hydrocarbons and CO_2 between 1600 and 1800 nm (Halim et al., 2007)

3.8 DIELECTRIC PERMITTIVITY

3.8.1 Introduction

Permittivity is a physical quantity that describes how an electric field affects and is affected by a dielectric medium, and is determined by the ability of a material to polarize in response to the field, and thereby reduce the total electric field inside the material. Thus, permittivity relates to a material's ability to transmit (or "permit") an electric field. The dielectric permittivity of a solvent is a relative measure of its polarity. For example, water (very polar) has a dielectric constant (or dielectric permittivity at 0 Hz frequency) of 80.10 at 20 °C while n-hexane (very non-polar) has a dielectric constant of 1.89 at 20 °C. This information is of great value when designing separation, sample preparation and chromatography techniques in analytical chemistry.

In classical electrodynamics, dielectric permittivity plays an important role as a complex function linking electric and electric displacement fields.

$$D_0 e^{-iwt} = \hat{\varepsilon}(w) E_0 e^{-iwt} \quad 3.5$$

$$\hat{\varepsilon}(w) = \varepsilon'(w) + i\varepsilon''(w) \quad 3.6$$

where E_0 is an amplitude of electric field (V.m^{-1}), D_0 is an amplitude of electric displacement field (C.m^{-2}), $\hat{\varepsilon}$ is a complex permittivity (dimensionless) which depends on frequency w (Hz), ε' and ε'' are real and imaginary part of complex dielectric permittivity (dimensionless), i is an imaginary unit (dimensionless).

The imaginary part is related to the dissipation of field energy within the medium and the real part of the permittivity relates to the stored energy within the medium. Typical zero frequency (static) dielectric permittivities for pure solutions at room temperatures are summarised in Table 3.4.

In this work, application feasibility of dielectric permittivity for monitoring of alcohol-salt concentrations in the aqueous phase was investigated. The effect of impurities on dielectric response of solutions was also studied.

Table 3.4 Typical dielectric permittivities at room temperature (Uematsu et al., 1980; Akerlof, 1932)

Material	Dielectric permittivity
Air	1.00054
Water	88 – 80.1 – 55.3 – 34.5 (0 – 20 – 100 – 200 °C)
Methanol	30
Ethylene Glycol	37
Sodium Chloride (Salt)	6.1
Oil, Petroleum	2.1

3.8.2 Experimental Set-up and Procedures

3.8.2.1 Experimental Set-up

A PNA-L Network Analyser manufactured by Agilent Technologies was used as a key instrument in the dielectric constant measurement set-up. It was equipped with a specifically designed high pressure performance probe. The frequency response of dielectric permittivity was measured in microwave range up to 20 GHz. Figure 3.33 and Figure 3.34 show the measurement set-up. The dielectric signal of the probe was transmitted through Electronic Calibration module (ECal) and then processed, displayed and recorded by the PNA_L network analyser. ECal was calibrated against standard materials including air, water, EG, MeOH, and conductive metal. The sample temperature was controlled by the bath for consistency.

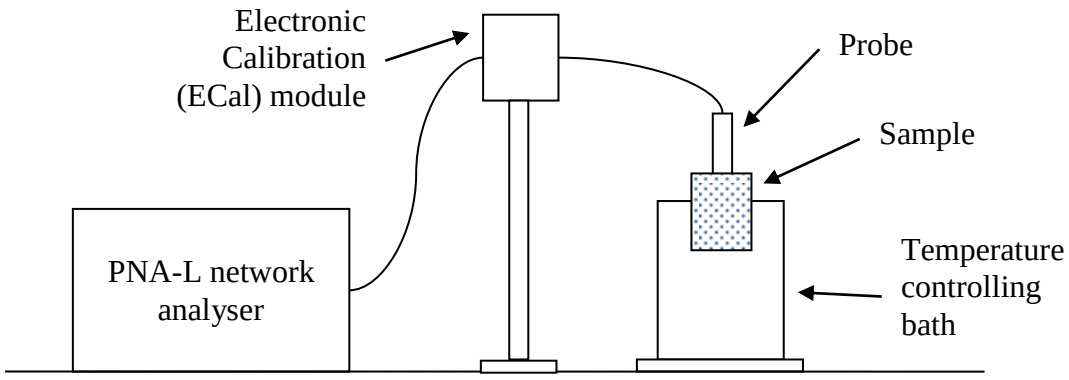

Figure 3.33 Schematic of dielectric permittivity measurement set-up

Figure 3.34 Set-up for dielectric permittivity measurements

3.8.2.2 Procedures

Aqueous solutions with methanol, ethylene glycol and sodium chloride were prepared for dielectric permittivity measurements. Measurements are conducted by submerging the measuring probe into the sample ensuring that no bubbles were attached to the tip. Dielectric permittivity is measured in 10 MHz-20 GHz frequency range.

3.8.3 Key Findings

For various ethylene glycol (EG) solutions, the measured dielectric permittivity spectrum (Figure 3.35) indicated a reduction in dielectric properties with an increase in ethylene glycol concentration. Ethylene glycol has a weaker dielectric than water as it can be seen in Table 3.4. The linearity of this reduction depends on the frequency (Figure 3.36). At 4 GHz the relation is linear whereas at 11 GHz it is quadratic.

For methanol (MeOH) solutions, the measured dielectric property (Figure 3.37) experienced similar behaviour at selected frequencies (Figure 3.38). However, the shape of the dielectric curves is not similar for different alcohols (Figure 3.35 and Figure 3.37). Such a variation in the dielectric permittivity can be explained by the mechanisms of polarisation (aligning under external electric field) which in turn depends on the character of chemical interactions. For polar dielectrics like water, the orientation polarization is the main mechanism which defines such a high static dielectric constant value 81. In polar dielectrics, groups of atoms of molecule or radicals are electric dipoles which in the absence of external electric field chaotically

oriented. When the external field is applied, assembly of those dipoles orient in line with it forming macroscopic polarization. At high frequencies, there is only electrons polarization mechanism which is less strong.

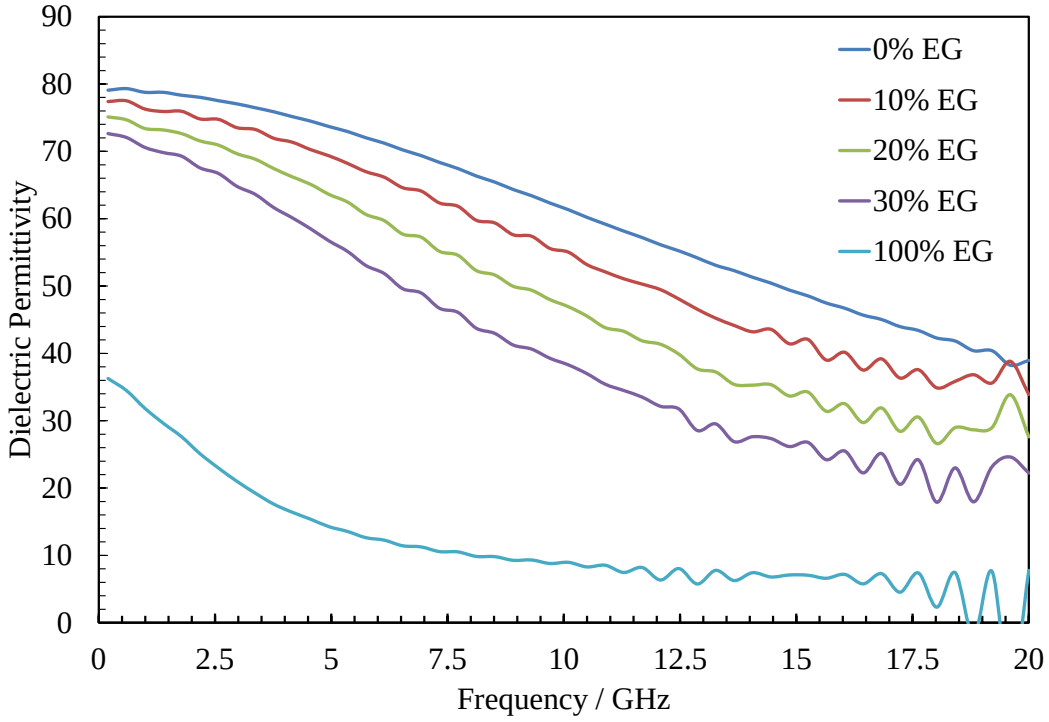

Figure 3.35 Dielectric permittivity against frequency for ethylene glycol aqueous solutions

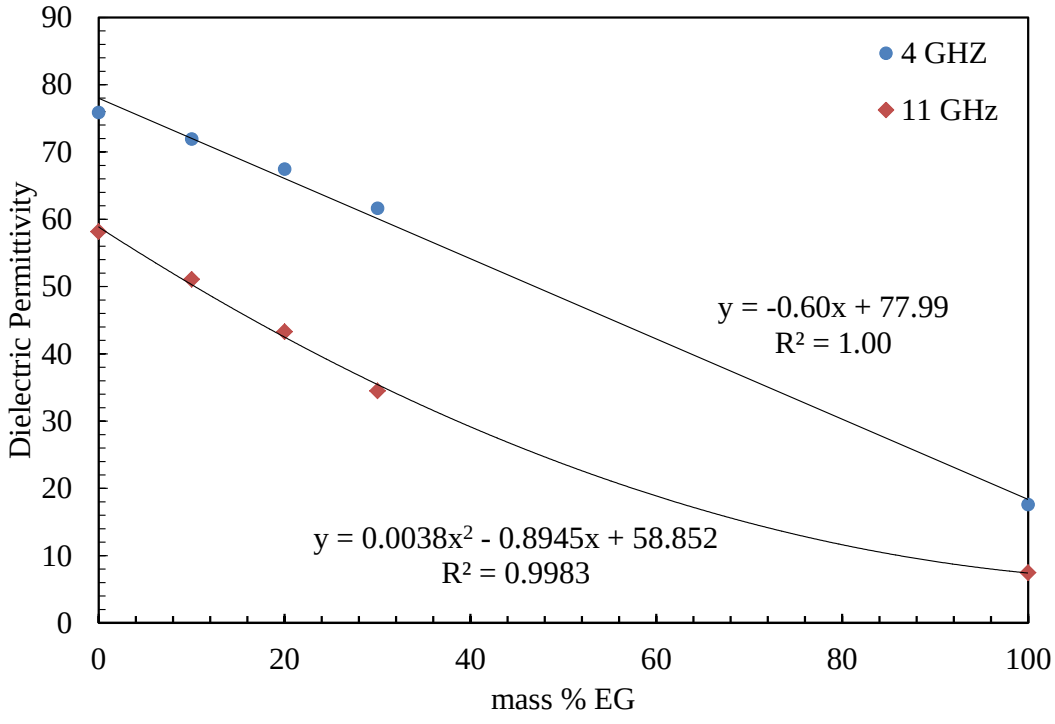

Figure 3.36 Dielectric permittivity against EG concentrations at 4 GHz and 11 GHz

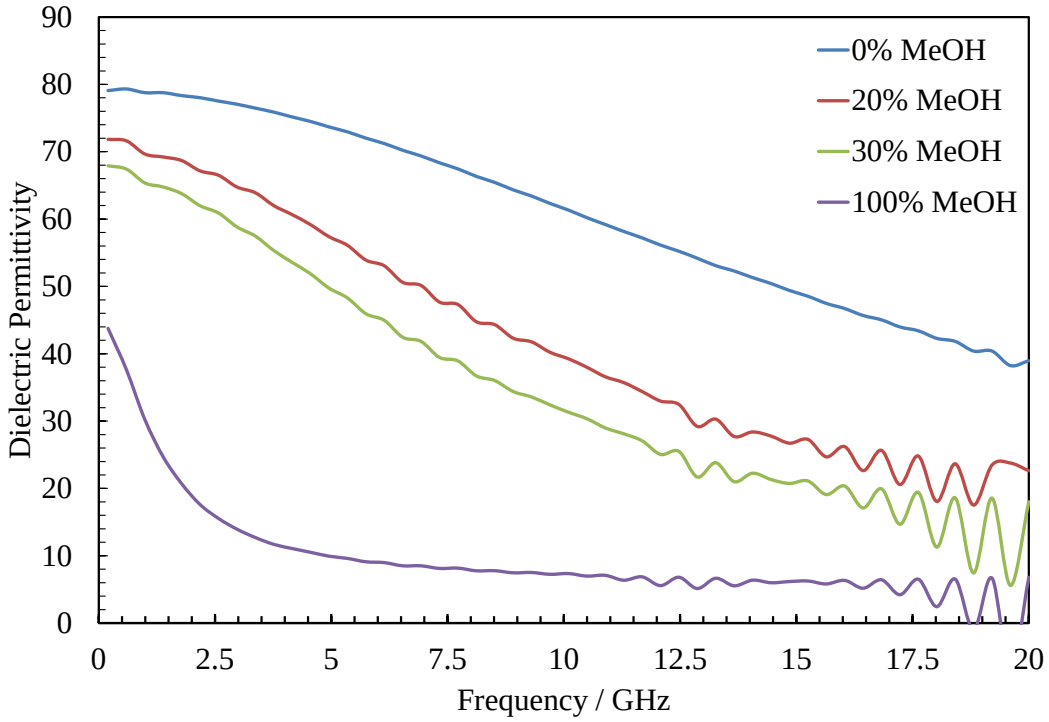

Figure 3.37 Dielectric permittivity against frequency for methanol aqueous systems

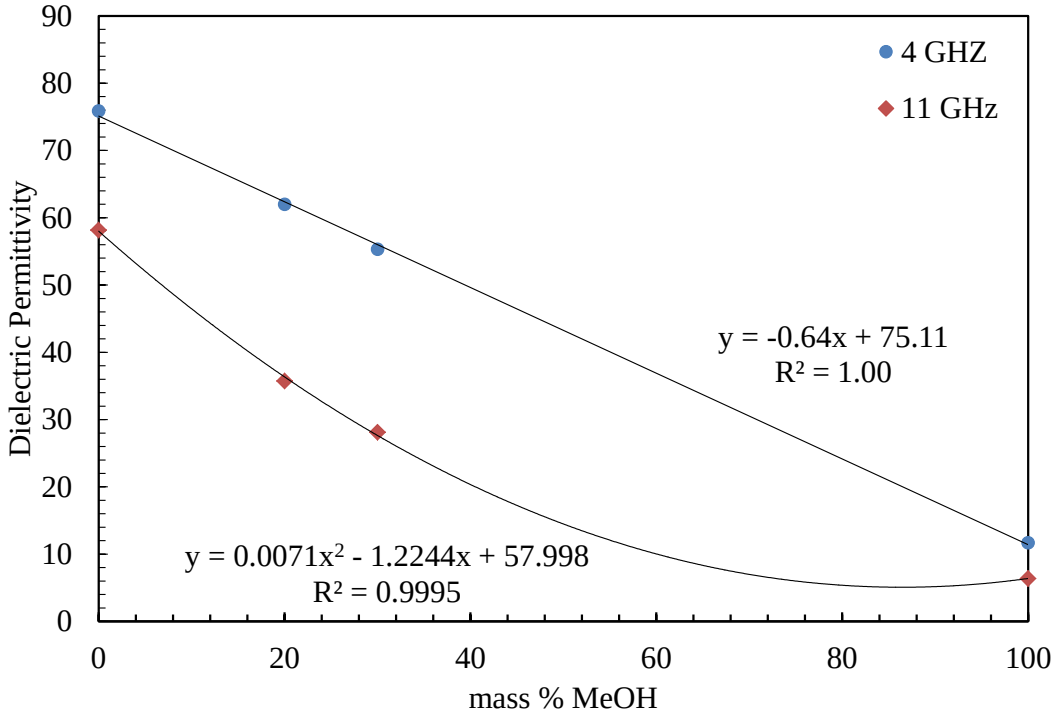

Figure 3.38 Dielectric permittivity against MeOH concentrations at 4 GHz and 11 GHz

One of the objectives for this study was to investigate the possibility of distinguishing alcohol and salt concentrations by using dielectric permittivity measurement. The

following series of tests were conducted for fixed 20 mass% MeOH solution with various NaCl concentrations. As it can be seen in Figure 3.39, salt has a significant effect on the shape of dielectric permittivity with a peak at low frequencies (10 MHz-1 GHz).

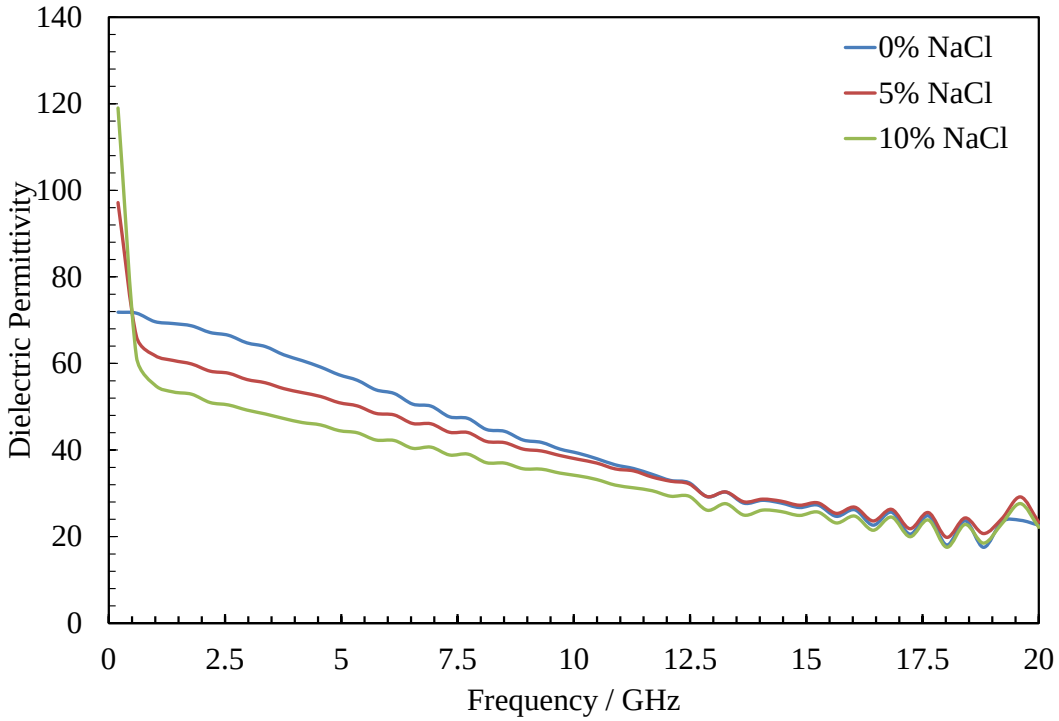

Figure 3.39 Dielectric permittivity against frequency for aqueous solution with 20 mass% methanol and various NaCl concentrations

In Figure 3.40, it can be seen that increasing salt concentration has an effect only in the lower frequency region. At 4 GHz frequency, there is a strong linear dependency, whereas, at 11 GHz, there is insignificant change. This can be served as a basis for distinction of salt and alcohol concentrations in the fluid mixture, since MeOH has a higher effect in the high frequency range.

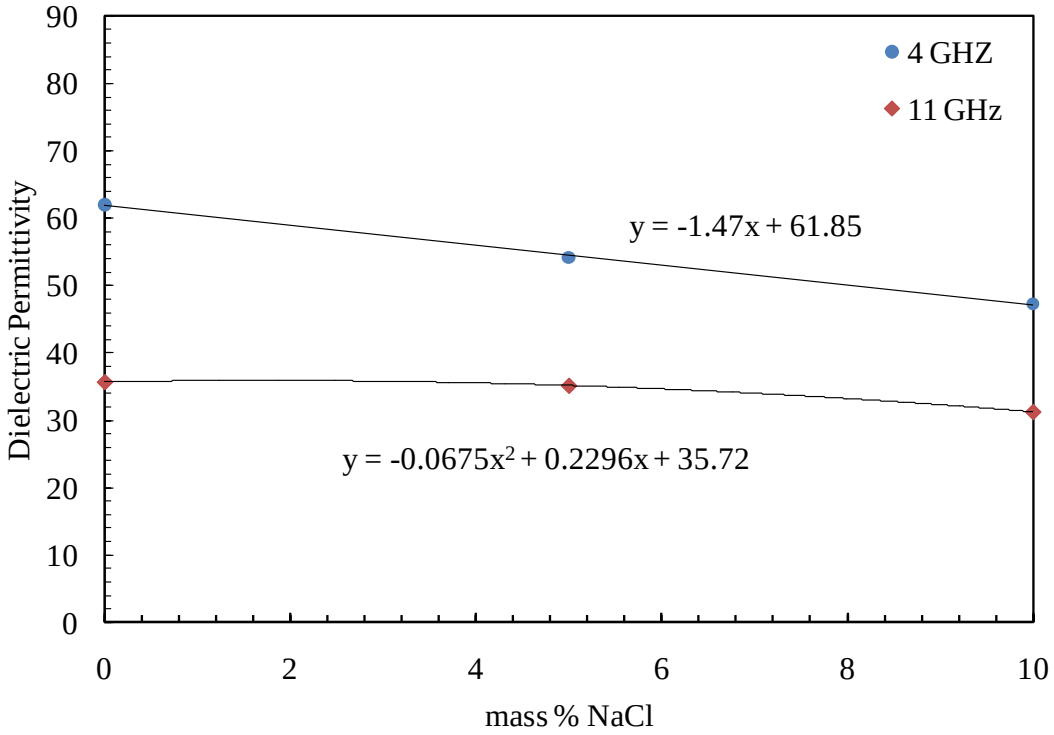

Figure 3.40 Dielectric permittivity against NaCl concentrations in 20 mass% methanol aqueous solution at 4 GHz and 11 GHz frequencies

This effect can be explained by the chemical interactions which affect polarization of the mixture. As it was explained earlier, dipolar (orientation) polarization in alcohol has an effect at high frequencies. Ionic polarization in salt affects low frequency dielectric properties. It is schematically illustrated in Figure 3.41. That is why the value of dielectric permittivity is near 1 for high frequency fields in pure ionic crystals like NaCl.

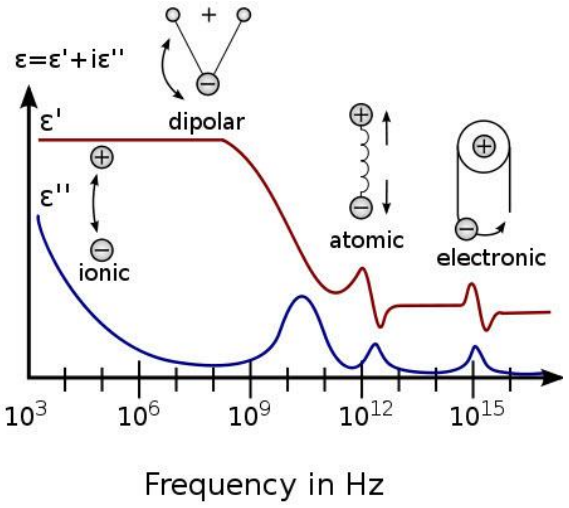

Figure 3.41 Illustration of the real and imaginary parts of the permittivity as a function of frequency for various dielectric mechanisms (Application Note 1217-1, 1992)

The industrial produced water is generally contaminated by particles/fines/sand from the reservoir, pipe cuts by erosion/corrosion, fluid formed solids like wax, asphaltenes, paraffin, added chemicals, residual oil etc. Therefore, it was important to investigate the effect of impurities on dielectric permittivity of the solutions. Three water samples were tested: pure water, water mixed with sand, and water mixed with sand and oil. The industrial produced water was not tested here. As it can be seen in Figure 3.42 and Figure 3.43, dielectric permittivity was unchanged with addition of different impurities. Small variations of curves can be explained by the difficulty of the instrument calibration. The calibration can introduce up to 6% uncertainty in measured values. Those encouraging results can however be explained by the design of the apparatus. In Table 3.4, the dielectric permittivity of oil is 2.1 at 0 Hz frequency. The fact than oil has not reduced the measured value could be explained by the design of measuring probe which had miniature sensor at the tip actually interacting with and measuring dielectric properties of the media. Most likely, during experiments, neither sand nor oil was attached to the miniature sensor. The sensor was measuring dielectric properties of pure water. As a result of this finding, the design of apparatus measuring dielectric permittivity in the entire volume can be proposed to further investigate the technique practical applicability. The entire solution has to be placed between two electrodes to form a capacitor. Properties, e.g. capacitance, conductance, resistance and reactance, of this capacitor have to be measured over the desirable frequency range, and then converted in a dielectric spectrogram. This whole set-up has to be calibrated against etalon materials of known dielectric permittivity. Additional work is recommended to be done to utilise an experience of service companies, e.g. ROXAR AS, in multiphase flow meter design which is mainly based on dielectric properties measurement of the production fluids. On the other hand, the found artefact can be considered as an advantage, since the dielectric properties were measured for the aqueous phase independently of any other large scale impurities. This in turn means that the produced aqueous samples have to be roughly/coarse separated prior to the measurements.

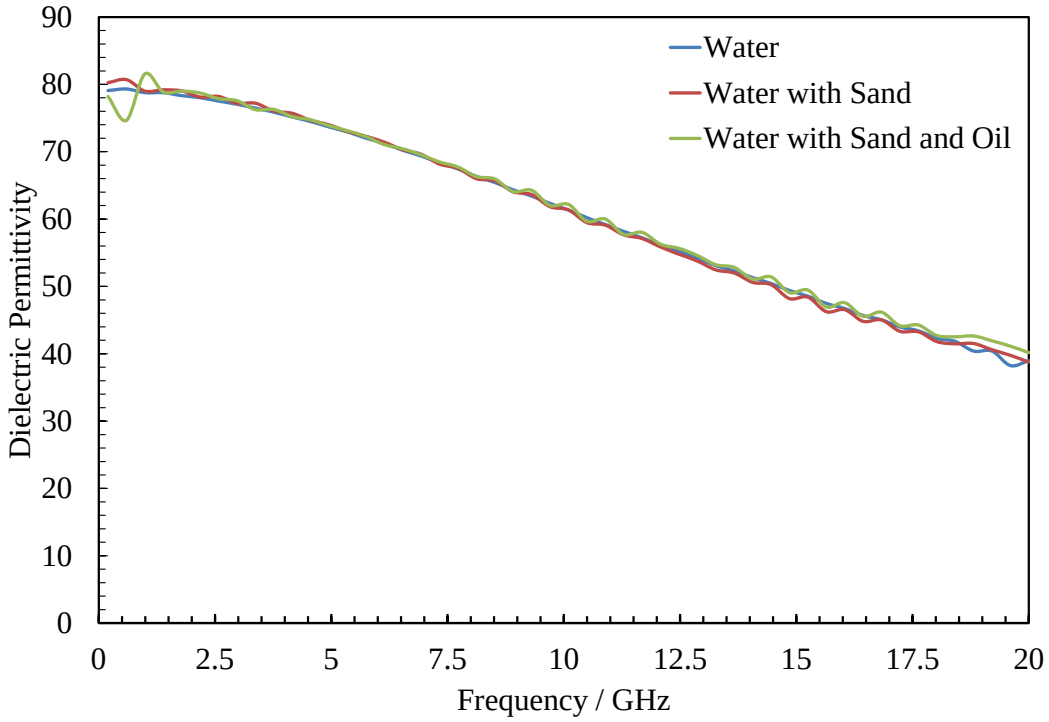

Figure 3.42 Dielectric permittivity against frequency for contaminated solutions

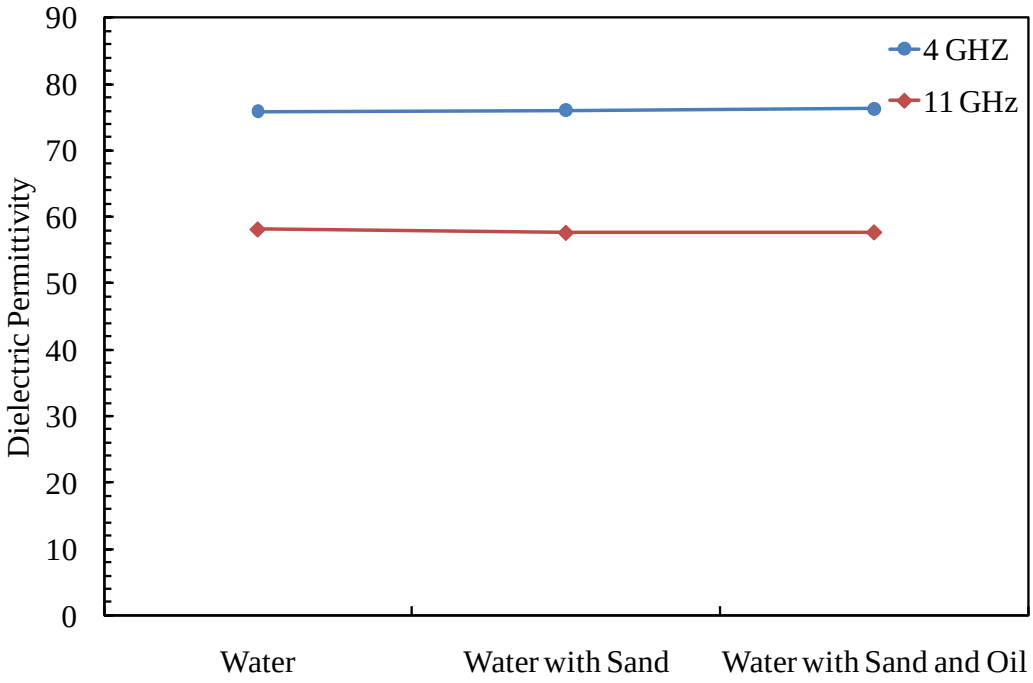

Figure 3.43 Dielectric permittivity against sample type at 4 GHz and 11 GHz frequencies showing no effect of contamination

3.9 CONCLUSIONS

In typical hydrate prevention strategy practiced in the industry, the key element is to inject chemical inhibitors at the upstream side. To calculate the safety margin for hydrate free production, thorough monitoring of those chemicals is crucial. In this Chapter, two electromagnetic methods have been investigated for the potential applicability to measure hydrate inhibitor concentrations in aqueous solutions.

UV/VIS/NIR spectroscopy technique was analysed within several main topics: thermodynamic inhibitors, effect of salt, low dosage hydrate inhibitors, contamination (oil and sand), and two produced waters with varying methanol contents. Results implied that inhibitor concentration monitoring can be based on UV/VIS/NIR spectroscopy. Results of experiments showed possibility to quantitatively measure methanol or ethylene glycol concentration from the light spectrum with acceptable sensitivity ~0.6 $mW.m^{-2}$/mass%. Results of NaCl concentration analysis indicate that salt has limited effect on light properties in 320-1100 nm spectrum region. Expansion of the experiments in to further IR range of 1100-3000 nm is suggested.

PVCap concentration in EG solution can be measured by spectroscopy in the UV range (300-550 nm) with acceptable sensitivity. The presence of salt does not affect the spectral response, and, thus, the concentration measurements. Water absorbs the light in IR spectrum (940-1040 nm) which suggests that the method can be applied to measure both water (or EG in water) and PVCap concentration from one measurement.

The effect of impurities (oil and sand) indicates that method is tolerant to the presence of oil in the fluid system. However, it is dramatically affected by the presence of particles which stochastically alters the spectrum: reducing it in UV and increasing it in NIR parts.

Two types of produced water were tested: BP water and Total water. It can be concluded that alcohol concentration is detectable in the produced water which contains salts only (BP water). However, when the produced water contains fines (Total water) the alcohol concentration is not measurable from the spectrum. If the produced water is clean (like BP water), or the sampling technique can provide sufficient purification, the technique can be viable and can provide a quick and reliable response on the inhibitor concentration change in the pipeline flow.

Applicability of dielectric permittivity technique for monitoring of alcohol-salt concentrations in the aqueous phase has been investigated and reported. The effect of impurities on dielectric response of solutions was also studied. Alcohols and salts concentrations can potentially be monitored in separate spectrum regions, since their mechanisms of polarization are different. As it was shown, alcohols (EG and MeOH) had higher effect at higher frequency range whereas salt (NaCl) had an effect at lower frequencies. The effect of contamination by sand and oil has been studied and resulted in a new set-up proposal. The screening of dielectric permittivity technique as concentration monitoring element of hydrate monitoring systems showed a potential for practical application, further experimental work is recommended.

CHAPTER 4 FREEZING POINT DEPRESSION

4.1 INTRODUCTION

The current industry practice for hydrate prevention is injecting hydrate inhibitors at the upstream end of pipelines based on the calculated/measured hydrate phase boundary, water-cut, worst pressure and temperature conditions, and the amount of inhibitor lost to non-aqueous phases. In general, systematic ways of controlling and monitoring along the pipeline and/or downstream to examine the degree of inhibition are very limited. In this Chapter, one of the potential hydrate monitoring systems is investigated. The system is based on freezing point depression measurement.

The theoretical basics for freezing point method is that any change in the alignment and arrangement order of water molecules resulted from the presence of the other chemical molecules is likely to affect the thermodynamic behaviour of gas hydrate formation as well as ice formation/melting. Thus, freezing point depression of water can reflect the presence of chemical additives, and could be correlated with gas hydrate phase boundary (Mohammadi and Tohidi, 2005). The benefit of this technique is that it could eliminate the need for compositional analysis of the aqueous phase, and could hardly be affected by the presence of other chemical additives like corrosion inhibitors.

Previously several investigators have correlated the degree of hydrate inhibition in terms of the amount and nature of the inhibitor present in the system. In the 1930s Hammerschmidt (1939) presented a semi-empirical equation (4.1) for predicting hydrate depression of typical natural gases in contact with dilute aqueous solutions of antifreeze agents such as methanol or ethylene glycol.

$$\Delta T = \frac{KW}{100M - MW} \qquad 4.1$$

where K is a constant specific to each inhibitor (Table 4.1) (K.g.mol^{-1}), M is the molecular weight of the antifreeze agent (g.mol^{-1}), W is the weight percent of the antifreeze agent in the aqueous phase (mass%) and ΔT is the hydrate depression (K).

Table 4.1 The K values for some gas hydrate inhibitors

Inhibitor	K value, K.g.mol^{-1}
Methanol, ethanol, cymene, ammonia	1228
Sodium chloride	1220
Glycol, propyl	2195
Sulphonal	2425

Following Hammerschmidt, other investigators tried to develop simple correlations to calculate the degree of inhibition based on the type and concentration of the inhibitor present in the aqueous phase. The result could show that the hydrate suppression is lower than the freezing point depression temperature (Nielsen et al., 1983; Yousif et al., 1993; Mohammadi and Tohidi, 2005).

Equation 4.1 is an empirical formula, considering no content of inhibitor in the saturated gas phase, and not applicable for the untested inhibitors. Recently, Ming Wu, Liaoning University of Petroleum and Chemical Technology, has thermodynamically derived theoretical formula (4.2) which is applicable for all inhibitor types to estimate the lowering of freezing point (Wu et al., 2007):

$$\Delta T = \frac{n\lambda'}{\lambda''}\left(\frac{T_0'}{T_0''}\right)^2 \Delta T' \qquad 4.2$$

where T_0' is the freezing point of pure water (K); λ' is the solidification heat of pure water (K.kg^{-1}); λ'' is the solidification heat of inhibitor (K.kg^{-1}); T_0'' is the freezing point of inhibitor (K).

In this Chapter, the pre-developed correlation by the hydrate research team in Heriot-Watt University was tested for various types of solutions. In Centre for Gas Hydrate Research, the degree of hydrate inhibition was correlated directly to the freezing point depression due to the presence of salt and/or organic inhibitors in the aqueous phase, regardless of the type and amount of the salts and/or inhibitors present in the system, eliminating the need for compositional analysis of the aqueous phase (Najibi et al., 2006). As part of the Joint Industrial Project, the correlation was also improved for high pressures by Dr. Antonin Chapoy. Based on the developed correlation, the hydrate stability zone in the presence of the salt and/or organic inhibitors could be determined

by combining the measured freezing point depression with the measured/predicted hydrate stability zone for the identical hydrocarbon system in the presence of distilled water.

Another method for constructing hydrate phase boundary was developed based on mathematical match of measured freezing point of the system under investigation and the analytical system with known composition. In this approach, the composition of analytical system was tuned to give the measured freezing point. The hypothesis that thermodynamic behaviour of those systems could be similar was confirmed within an acceptable error margin.

To measure freezing point, a device incorporating heat-pumps for quick cooling/heating of aqueous solutions was developed. The measurement prototype based on thermoelectric modules (Peltier elements) has been evaluated against various solutions with known freezing points. In this Chapter, the chronological development of the prototype device is also presented.

4.2 DEVELOPMENT OF CORRELATION

Centre for Gas Hydrate Research in Heriot-Watt University made a significant effort to develop a correlation which could link the freezing point of aqueous solution to its hydrate inhibition characteristics. One of the major works published by Dr. Hesam Najibi et al. (2006) details on the development of the empirical correlation used throughout this Chapter.

The required freezing point depression and hydrate phase boundaries data have been generated using a well-proven thermodynamic model (Avlonitis, 1992; Tohidi et al., 1993), for 160 different aqueous solutions (Table 4.2) containing various salts and/or organic inhibitors over a wide range of concentrations. The data generated from thermodynamic model was preferred to real experimental data, because the amount of experimental hydrate dissociation data and freezing point on multi-component mixtures, especially in the presence of electrolytes and organic inhibitors, is very limited (Amy et al., 2002; Mathews et al., 2002), and because of the limited experimental data so that any error could easily result in unreliable correlation. All of these aqueous systems were assumed to be in contact with methane and the hydrate suppression temperature for these systems at 20 MPa was used.

Table 4.2 Maximum concentration (based on water) of salts and/or organic inhibitors in the aqueous phase systems used in the development of the correlation

Inhibitor	Inhibitor mole%	Inhibitor mass%	Salt mole%	Salt mass%
NaCl	0	0	8.43	23
KCl	0	0	3.48	13
CaCl2	0	0	7.1	32
KBr	0	0	6.65	32
NaBr	0	0	10.44	40
HCOONa	0	0	10.19	30
HCOOK	0	0	8.4	30
MeOH	36	50.02	0	0
EtOH	15	31.1	0	0
EG	8	23.06	0	0
DEG	14	48.96	0	0
TEG	15	59.54	0	0
MeOH+NaCl	8.5	14.18	4.2	12.45
MeOH+KCl	6.5	11.01	2.52	9.7

For the investigated systems, the composition of the hydrocarbon system (gas phase) in contact with the aqueous phase and also the system pressure had a minor effect on the final result. The degree of hydrate inhibition was plotted against the freezing point depression for all the systems as shown in Figure 4.1. All the data points are closely fitted to a straight line, which suggests a linear relationship between hydrate suppression temperatures and freezing point depressions with a slope of 0.6825. The resulting correlation, which relates the hydrate dissociation temperature of the fluid system to the change in aqueous phase freezing point depression, (with respect to distilled water) is given by the following expression (Najibi et al., 2006):

$$T = T_0 - 0.6825\Delta T_f \qquad 4.3$$

where T is the hydrate dissociation temperature (K or ^{o}C); ΔT_f is the freezing point depression (K or ^{o}C), i.e., the change in freezing point of the aqueous solution with respect to pure water (K or ^{o}C), and T_0 is the hydrate dissociation temperature of the same fluid system in the presence of distilled water (K or ^{o}C).

Recent research conducted in China University of Geosciences showed that Najibi et al. correlation 4.3 is also suitable for estimating the hydrate safety margin of oil-based drilling fluids (OBDFs) in the presence of thermodynamic hydrate inhibitors (Ning et al., 2011).

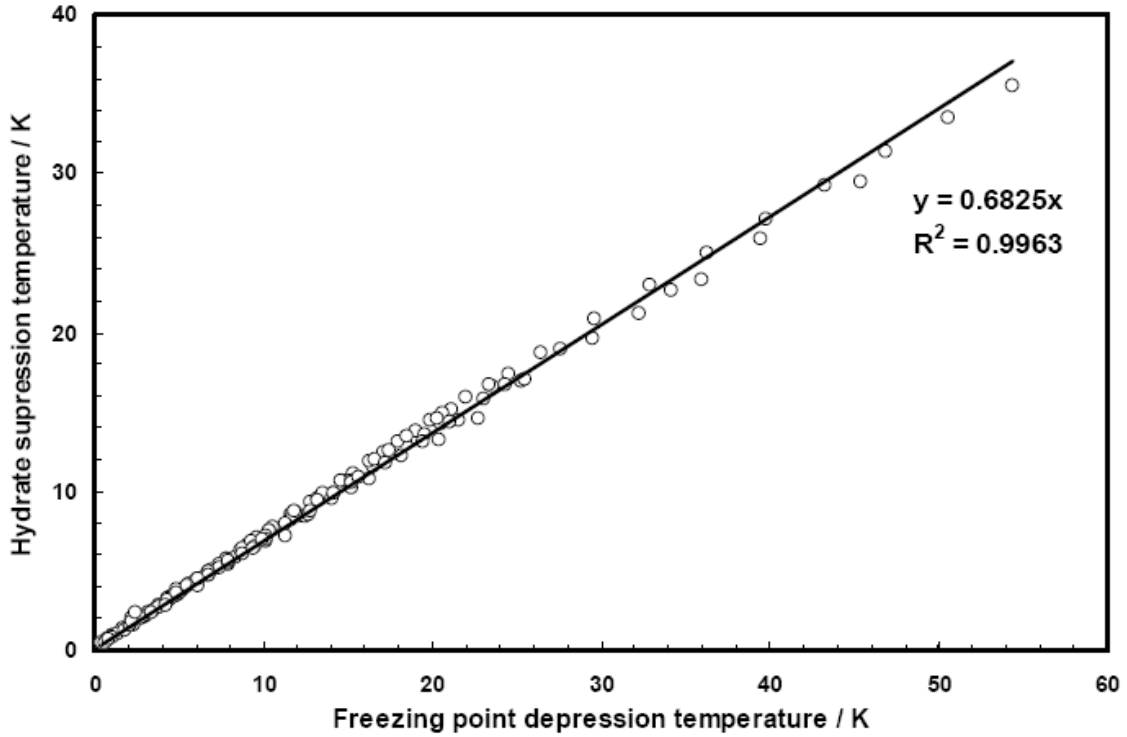

Figure 4.1 Hydrate suppression temperature for methane hydrates vs. freezing point depression temperature in the presence of aqueous solutions of salts and/or organic inhibitors

Once the freezing point is measured and the hydrate phase boundary for pure water is known, the hydrate dissociation temperature in an inhibited fluid system can be defined using the correlation (4.3). Further experiments showed that the previously developed correlation had noticeably high deviation from the phase boundary predicted by HWHYD at high pressure range for alcohol concentrations. A member of Centre for Gas Hydrate Research, Dr. Antonin Chapoy has improved the correlation by incorporating a pressure correction term. The new correlation is formulated as below:

$$T = T_0 - 0.5843\Delta T_f P_0^{0.0435} \qquad 4.4$$

where T, ΔT_f, and T_0 represent the same quantities as before (K or ^{o}C); P_0 is the hydrate dissociation pressure (bar) of the same fluid system in the presence of distilled water at the temperature T_0. Figure 4.2 demonstrates the improvement at relatively high pressure after taking into account the effect of pressure.

New correlation takes into account the pressure effect, as it can be seen in Figure 4.2 where methane hydrate dissociation conditions predicted by HWHYD are compared

with the ones computed by the new and previous correlation. The new correlation is in better agreement with the predictions of the thermodynamic model.

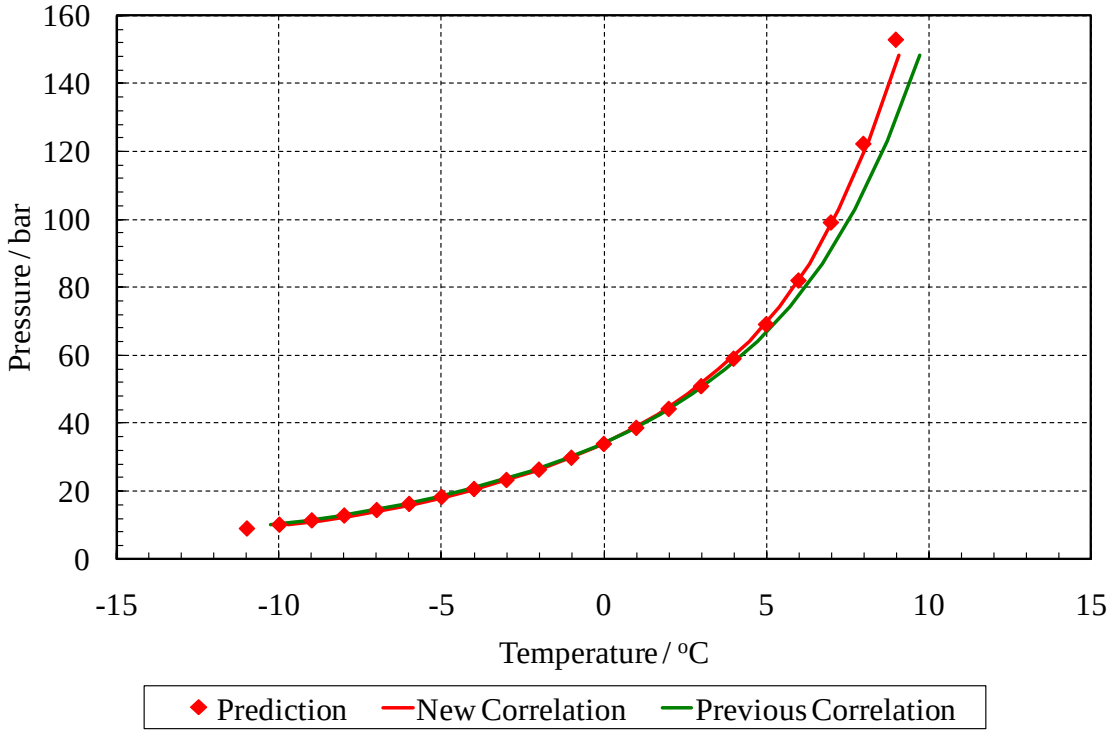

Figure 4.2 HWHYD model prediction, new and previous correlations for methane hydrate dissociation conditions in the presence of 25 mass% of aqueous EG and 5 mass% NaCl

4.3 DEVELOPMENT OF FREEZING POINT PROTOTYPE DEVICES

The idea of using Peltier elements was originally suggested to improve the speed of freezing point measurements (as well as potential field application), since then the design of the setup has evolved significantly. Peltier devices, also known as thermoelectric (TE) modules, are small solid-state devices that function as heat pumps. These units are a few millimetres thick by a few millimetres square. It is a sandwich formed by two ceramic plates with an array of small Bismuth Telluride cubes in between. When a DC current is applied heat is removed from one side of the device to the other- where it must be removed with a heat sink. The transported heat quantity, which is transported from the cold side of the Peltier element to the warm side, has to be fully led from there to avoid overheating.

The first prototype used a single-stage type of Peltier elements and an air fan as a heat sink to produce a miniaturized freezing point measurement apparatus. The results of

initial tests on this first prototype showed that it can reach -20 ^{o}C at the ambient temperature of air around 2 ^{o}C, and Peltier elements can be used for miniaturized freezing point equipment on the field for freezing point measurements.

4.3.1 Comparison of Cooling Systems

In order to freeze high inhibitor concentration solutions, the heat sink effectiveness should have been improved. The calculation of the lowest possible temperature the device could achieve with different cooling systems was based on the heat transfer equation of conduction and convection without radiation term applied to the device boundary conditions. When combined, conduction (4.5) and convection (4.6) equations form the overall equation of heat transfer (4.7) which is then used to calculate the heat fluxes for all boundaries in the freezing point measurement device model (Figure 4.3).

Conduction:

$$\dot{Q}'' = -k\frac{\partial T}{\partial n} \qquad \text{or} \qquad \dot{Q}'' = -\frac{\Delta T}{\sum_i \frac{\Delta x_i}{k_i}} \tag{4.5}$$

Convection:

$$\dot{Q}'' = h\Delta T \quad \text{or} \quad \dot{Q}'' = \frac{\Delta T}{\frac{1}{h}} \tag{4.6}$$

Overall:

$$\dot{Q}'' = \frac{\Delta T}{R} \quad \text{where } R = \sum_i \frac{\Delta x_i}{k_i} + \sum_i \frac{1}{h_i} \tag{4.7}$$

where $\dot{Q}''$ is the heat flux (W.m^{-2}); k is the thermal conductivity (W.m^{-1}.K^{-1}); T is the temperature (K); Δx_i is the thickness of i-th layer (m); R is the thermal resistance (K.m^2.W); h is the heat transfer coefficient (W.m^{-2}.K^{-1}).

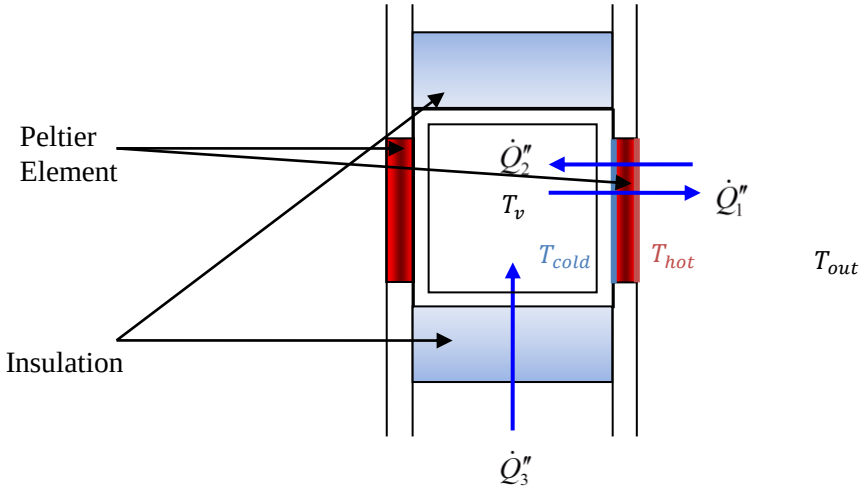

Figure 4.3 Model of the freezing point measurement device.

The components of prototype are listed Table 4.3. The Peltier elements specifications and the performance graphs are provided in Table 4.4 and Figure 4.4 respectively.

Table 4.3 Main prototype components

Component	Nomenclature
Peltier Elements	C1-1.4-127-1.14-WPN1
Air Fans	23F003
Power Supply	Thurlby 30V-2A

Table 4.4 Specifications of Peltier element

Module No.	T_{hot}, °C	I_{max}, A	V_{max}, V	Q_{max}, W	ΔT_{max}, °C
C1-1.4-127-1.14-WPN1	50	8.1	16.1	80.6	79

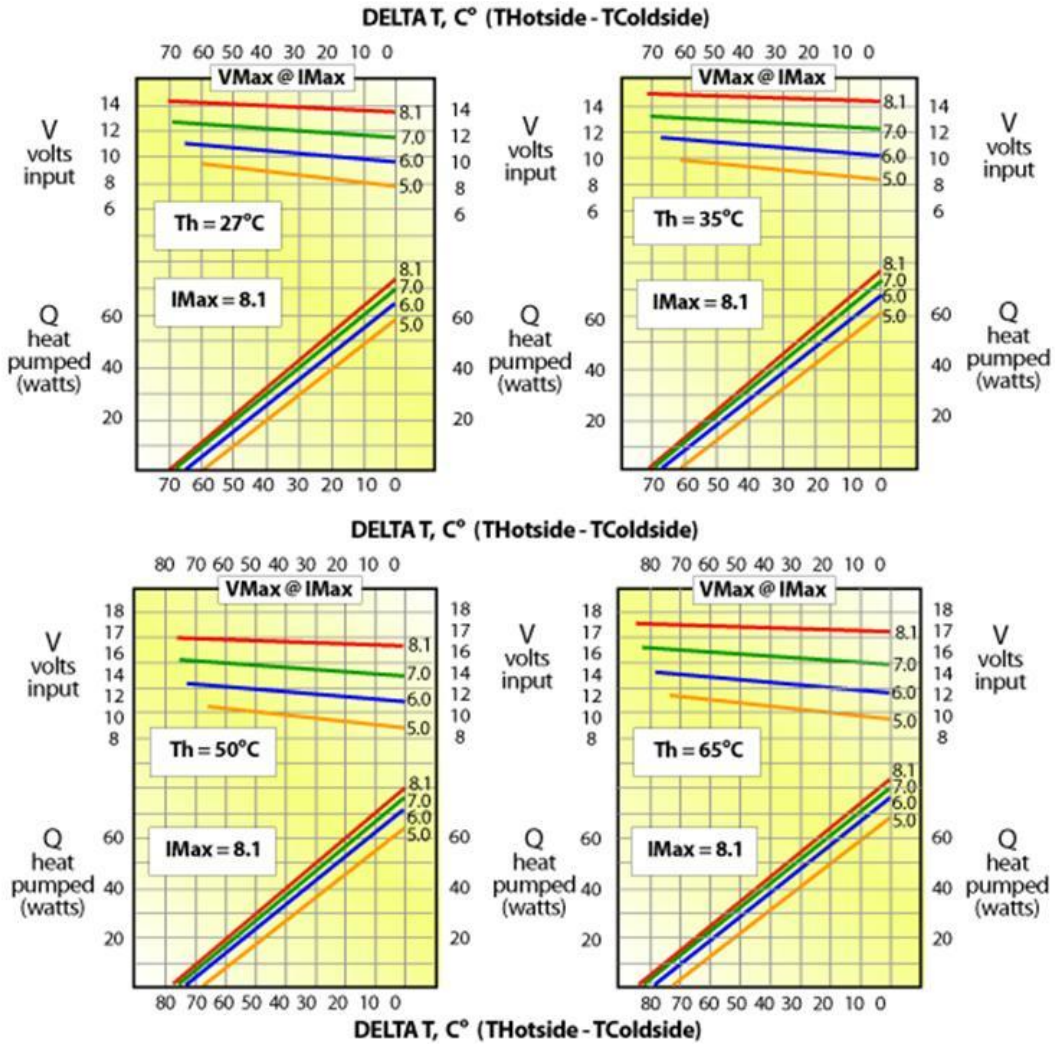

Figure 4.4 Performance graphs for C1-1.4-127-1.14-WPN1 cooling modules (Tellurex Corp., 2007)

Calculation of the minimum temperature for different cooling systems:

Internal temperature of the aqueous sample (water) was calculated at the stable conditions when heat flux caused by Peltier elements ($\dot{Q}''_{12}$) is equal to the heat flux from the surrounding (4.8).

$4\dot{Q}''_{12} = 4\dot{Q}''_2 + 2\dot{Q}''_3$, or

$$4\frac{T_v - T_{cold}}{\frac{1}{h_{waterfree}} + \frac{\Delta x_1}{k_{aluminium}}} = 4\frac{T_{hot} - T_v}{\frac{1}{h_{airfree}} + \frac{\Delta x_1}{k_{aluminium}} + \frac{1}{h_{waterfree}}} + 2\frac{T_{hot} - Tv}{\frac{1}{h_{airfree}} + \frac{\Delta x_2}{k_{insulation}} + \frac{1}{h_{waterfree}}} \qquad 4.8$$

where T_{hot} is the temperature on the hot side of Peltier element (K); T_{cold} is the temperature at the cold side of Peltier element (K); T_v is the temperature inside the

sample vessel (K); $h_{air\ free}$ and $h_{water\ free}$ are the free convection coefficients for air and water respectively ($W.m^{-2}.K^{-1}$); $k_{aluminium}$ and $k_{insulation}$ are the thermal conductivities for aluminium and insulation respectively ($W.m^{-1}.k^{-1}$); Δx_1 and Δx_2 are thicknesses of the vessel at Peltier element side and at insulation side respectively (m).

Temperature at the hot side of Peltier element is calculated by the following equation:

$$\dot{Q}''_{11} = \frac{T_{hot} - T_{out}}{\frac{1}{h_{forced}}} \qquad 4.9$$

where T_{out} is the temperature outside the device or room temperature (K); h_{forced} is the convection coefficients for air or water depending on the cooling system ($W.m^{-2}.K^{-1}$).

Taking into account that the power supply was set to 40 W to feed each Peltier element, the hot and cold side' temperatures were determined (Table 4.5) from the performance graphs (Figure 4.4).

Table 4.5 Temperature at Peltier element sides for different cooling systems

	Cooling System	
	Air	Water
T_{hot} , °C	24.6	23.02
T_{cold} , °C	-34.4	-39.98

Using the above equation 4.8 with the parameter values presented in Table 4.5 and Table 4.6, the temperature inside the sample vessel at the static conditions which is the minimum possible temperature the device can reach is equal to **-31.2°C**.

Table 4.6 Constants used in heat transfer calculations

Symbol	Value	Unit
k_{cooper}	401	$W*m^{-1}*K^{-1}$
$k_{aluminium}$	237	$W*m^{-1}*K^{-1}$
$k_{insulation}$	0.1	$W*m^{-1}*K^{-1}$
$h_{air\ free}$	2	$W*m^{-2}*K^{-1}$
$h_{air\ forced}$	25	$W*m^{-2}*K^{-1}$
$h_{water\ free}$	50	$W*m^{-2}*K^{-1}$
$h_{water\ forced}$	2000	$W*m^{-2}*K^{-1}$
Δx_1	$3.3*^{10-3}$	m
Δx_2	$2.3*^{10-3}$	m

If water cooling system is used to cool the outer side of Peltier elements then the equation 4.8 can be modified to the following:

$$4\frac{T_v - T_{cold}}{\frac{1}{h_{waterfree}} + \frac{\Delta x_1}{k_{aluminium}}} = 4\frac{T_{hot} - T_v}{\frac{1}{h_{waterfree}} + \frac{\Delta x_1}{k_{aluminium}} + \frac{1}{h_{waterfree}}} + 2\frac{T_{hot} - Tv}{\frac{1}{h_{waterfree}} + \frac{\Delta x_2}{k_{insulation}} + \frac{1}{h_{waterfree}}} \quad 4.10$$

Using the parameters listed in the Table 4.6 and, this time, the equation 4.10, the minimum possible temperature inside the vessel is equal to **-36.59 ^{o}C** that is lower than the temperature for the device with air cooling system. Therefore, water circulation makes the cooling process more efficient.

4.3.2 Design of Prototype with Water Cooling System

To achieve lower cooling temperature, a new conceptual design of Peltier device was proposed and implemented which included usage of more powerful Peltier elements, smaller cooper bath and water cooling system. The conceptual design of freezing point measurement device is shown in Figure 4.5. The modified version of Peltier element device looked like a sandwich with several layers (Figure 4.6 left). The central was a copper block being drilled two holes for housing the test sample and reference liquid. The temperature in 1 ml test sample and 1 ml reference liquid could be monitored with PRT probes (Figure 4.8). At the two sides of the central block there were two Peltier elements. Each of the Peltier elements had two sides called hot side and cool side, respectively. The cool side contacted the central block, and the hot side contacted the heat sink. Figure 4.7 left shows picture of this freezing point set-up. The modified prototype could reach lowest temperature of -24 ^{o}C when the heat sink water temperature was set to 4 ^{o}C which is a typical temperature of the North Sea water. This result was mainly limited by the one-stage Peltier element used.

To be able to freeze solutions with high alcohol concentrations, for example, 30 mass% MeOH corresponding to a freezing point of -25.6 °C, a new device was developed and equipped with more powerful three-stage Peltier elements (Figure 4.6 right; Figure 4.7 right). This variant of prototype could cool the sample from 4 ^{o}C to -40.3 ^{o}C in 6.5 minutes as shown in Figure 4.9. The sample and reference volumes remained unchanged (Figure 4.8).

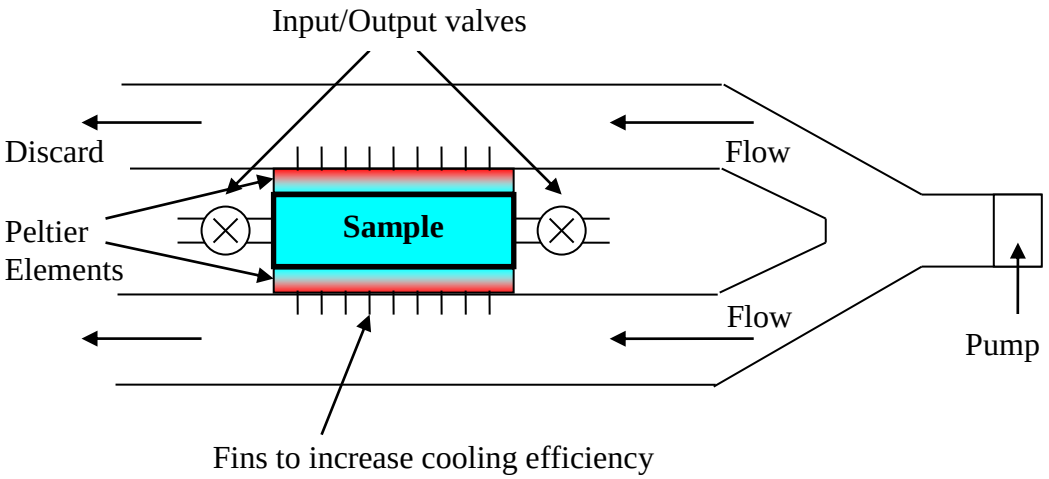

Approximate sample holder dimensions:

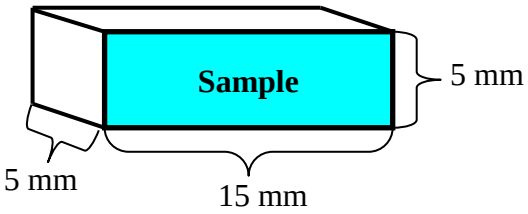

Figure 4.5 Schematic of the conceptual design of Peltier device

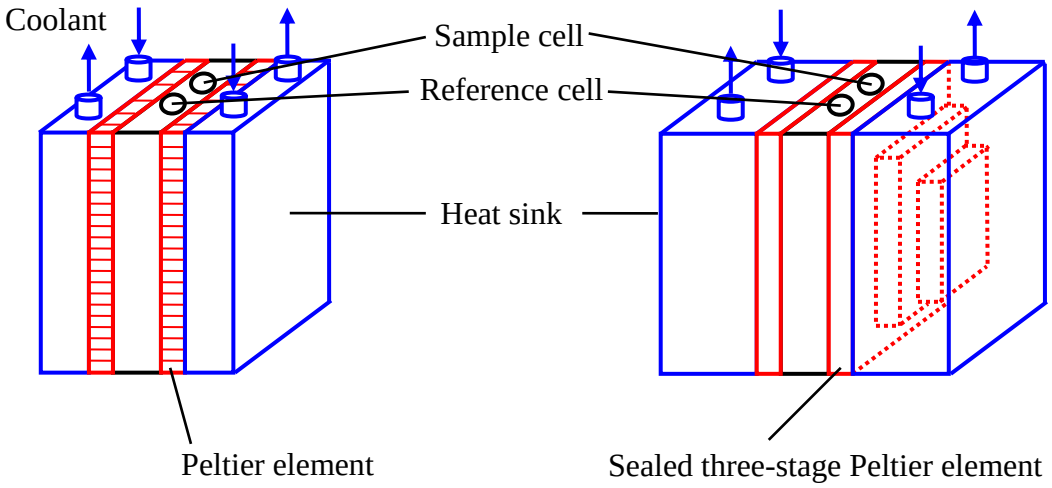

Figure 4.6 Prototype structure: left – previous device, right – modified device with three-stage Peltier elements

Figure 4.7 Picture of the prototype set-up: left – one-stage Peltier device, right – three-stage Peltier device

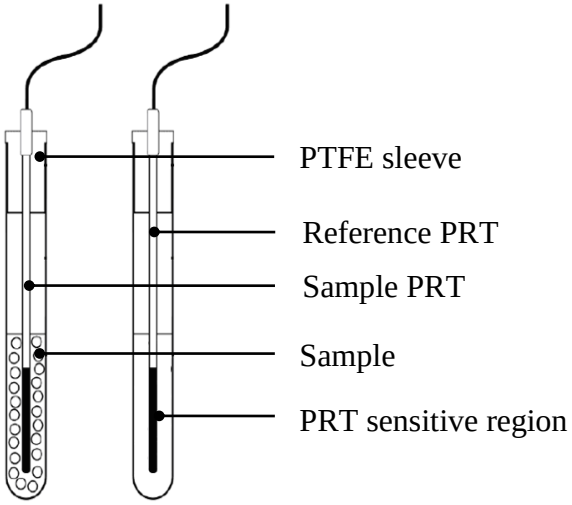

Figure 4.8 Cells of the prototype device: left – sample cell, right – reference cell

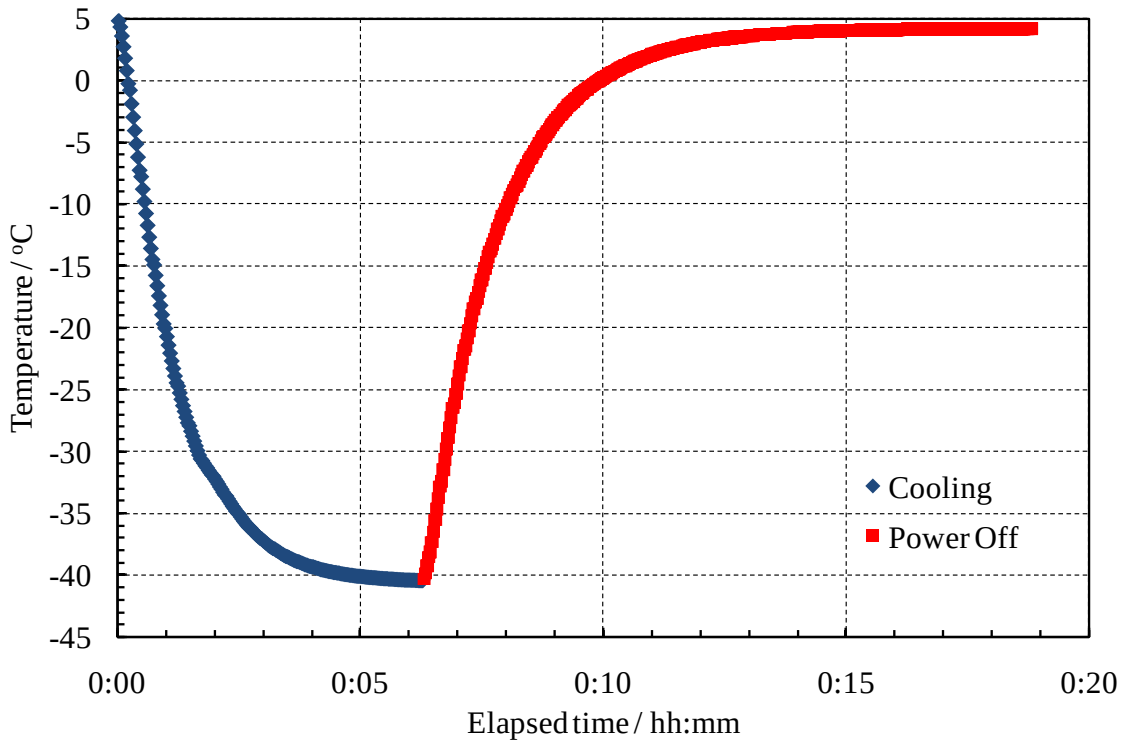

Figure 4.9 The performance of the Peltier device with three-stage Peltier elements

For example, assuming that 10 °C subcooling is needed for ice formation, it can be possible to freeze aqueous alcohol solutions with concentration up to 45 mass% EG or 35 mass% MeOH. However, it was observed that, the cooling efficiency of the prototype device was reduced after several cycles, and the device could cool the sample down to -35 °C against previous -40 °C. The reason of that effect could be in the moisture precipitation between n-p semiconductor parts (which actually transferred heat) within Peltier elements. The condensation reduced thermal insulation between hot and cool sides, because water droplets are generally more heat conductive than the air. This, consequently, reduced the whole cooling efficiency of the device. Therefore, the newest concept of the prototype was proposed which incorporates sealed three-stage Peltier elements, as well as new insulation material Polyurethane (250 W/m°C heat conductivity) applied for the whole device. Implementation of the newest concept resulted in stabilisation of cooling power of the device, so that the sample could be cooled from 4 °C to -38.5 °C in 7 minutes. The newest device is also equipped with temperature controller for linearization of heating/cooling processes, and new thermocouple sensors which are adequately small to make the whole device more transportable for the industrial application. The instructions for the application of the developed freezing point prototype are available in Appendix B.

4.3.3 Specifications of the Final Prototype

Schematic of the Peltier element device designed to measure freezing point of aqueous solutions is shown in Figure 4.10. In the centre of the aluminium block, two wells accommodate the test sample and the reference fluid which temperatures are continuously monitored. Two three-stage Peltier elements are attached to the two faces of the central block. Each of the three-stage Peltier elements has two outer sides called hot side and cold side, and contains three one-stage Peltier elements inside. The internal Peltier elements are connecting hot side to cold side in sequence. The outer cold side contacts the central block, and the outer hot side contacts the outside layer called heat sink. A thermal couplant is applied between the interfaces of the block and the Peltier element and between the heat sink and the Peltier element to ensure a good thermal contact. The heat sinks were connected to a cooling bath to remove the heat generated by the Peltier elements. Thermal probes located in each heat sink can monitor the temperature in the heat sinks. Main components of the final device are summarised in Table 4.7.

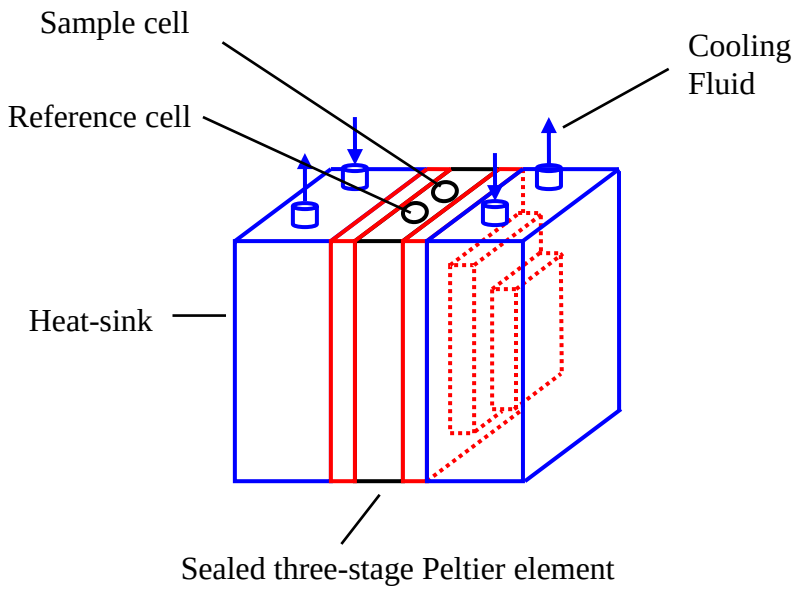

Figure 4.10 Schematic design

Table 4.7 Specification of the main elements for the final freezing prototype

Name	Quantity	Specifications
Peltier element PE	2	Company: SuperCool Model: PE3-119-20-15 I_{max} (A): 8 U_{max} (V) 8.2 Pc_{max} W 14.9 ΔT_{max} (^{o}C) 100 R_{AC} (ohm) 0.97 Ac (mm) 22 Bc (mm) 22 A (mm) 44 B (mm) 44 H (mm) 12.9 L (mm) 200
Insulation	1	Company: SuperCool Model: ISO-S45-071-V Sandwiched, white PVC coated Polyurethane 590x1200x45
Temperature sensors	2	T100 and T1000
Temperature reader	1	Company: National Instruments Model: Ni 9211
Cooling Bath	1	Company: Grant Instruments Model: R3
Power Supply	1	Company: Digimess Model: SM3040
Controller	1	Company: SuperCool Model: TC-XX-PR-59 Regulation type: PWM I max: 15 A Voltage: 10-30 V Settings ^{o}C: Sensor dependent Trim from ^{o}C: Software selectable Accuracy 1 ^{o}C: Sensor dependent Hysteresis ^{o}C: Software selectable Low Voltage Protection: Software selectable

Essential properties:

1. Device cools a solution down to -40 ^{o}C within 10 minutes;

2. Device error range is no more than ±0.1 ^{o}C;

3. Device provides a constant cooling-heating rate within the range of 0.1-0.5 ^{o}C/sec to ensure linearity of cooling and heating processes;

4. Device is suitable for laboratory and potentially field conditions (further tests are required);

5. Device is accompanied by easy-to-use software based on Windows operational system.

Possible upgrades:

1. Measure freezing/melting points under pressure (i.e., possibility of measurement of hydrate formation/dissociation);

2. Implement mixing in the cells;

3. Use high accuracy temperature sensors;

4. Use three or more wells to accommodate the test samples.

4.4 MEASUREMENT RESULTS

4.4.1 Experimental Set-up

The developed freezing point prototype (Section 4.3) was used for tests in this section.

4.4.2 Materials

Methanol, 99.9%, supplied by Aldrich. Ethylene glycol, 99.0%, supplied by Alf Aesar. Sodium Chloride, 99+%, A R grade, supplied by Aldrich

4.4.3 Procedures

The measurement cell was filled up with 1 ml of different solutions (water with alcohol and salt). The reference cell was filled up with 70 mass% aqueous methanol solution

which has low freezing point, -137 ^{o}C (Table 4.8). The circulation of bath cooling fluid through the device equalise the sample and the reference fluid temperature at 4 ^{o}C. The onset of ice formation was initiated by reduction of the system temperature from 4 ^{o}C to set temperature (e.g. -30 ^{o}C). The cooling was conducted at a constant rate of 0.2 ^{o}C/min or at maximum device power to accelerate measurements. The sample was freezing when the latent heat of ice formation had released and the sample temperature had risen compared to reference temperature, as shown schematically in Figure 4.11. The ice had been crystallized when the sample temperature was back to reference temperature. Then the heating process was activated at rate 0.2 ^{o}C/min to the target 4 ^{o}C temperature (Figure 4.12). The freezing point was identified from the plot of the delta temperature against sample temperature, as shown schematically in Figure 4.13 in which there is a small systematic drift between gauges of 0.2535 ^{o}C which can be corrected. The uncertainty of this measurement technique is within ±0.2 ^{o}C. Freezing point is the sample temperature at which measured data starts descending linear trend. The detailed measurement instruction for the developed device prototype is described in Appendix B.

Table 4.8 Freezing point of aqueous methanol and ethylene glycol solutions (Weast et al., 1989)

Concentration, mass%		0	10	20	30	40	50	60	70	80	90	100
Methanol Freezing temperature	^{o}F	32	20	0	-15	-40	-65	-95	-215	-225	-230	-145
	^{o}C	0	-7	-18	-26	-40	-54	-71	-137	-143	-146	-98
Ethylene Glycol freezing temperature	^{o}F	32	25	20	5	-10	-30	-55	-60	-50	-20	10
	^{o}C	0	-4	-7	-15	-23	-34	-48	-51	-45	-29	-12

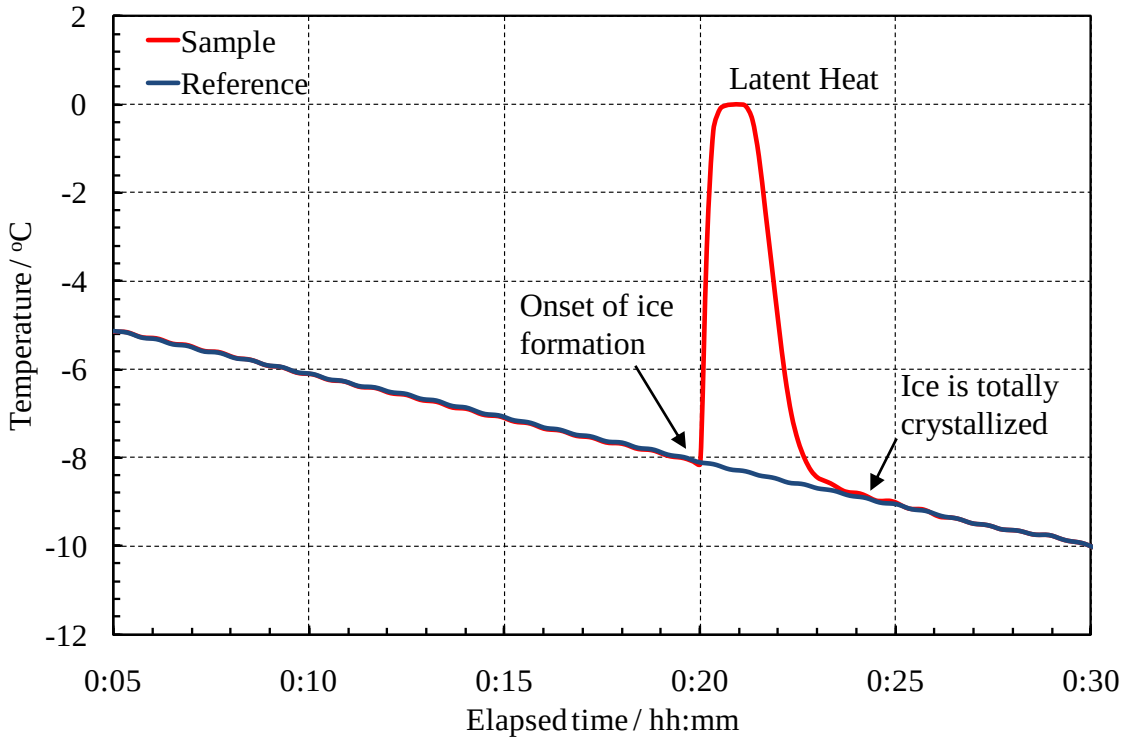

Figure 4.11 Schematics of onset of ice formation during the cooling stage

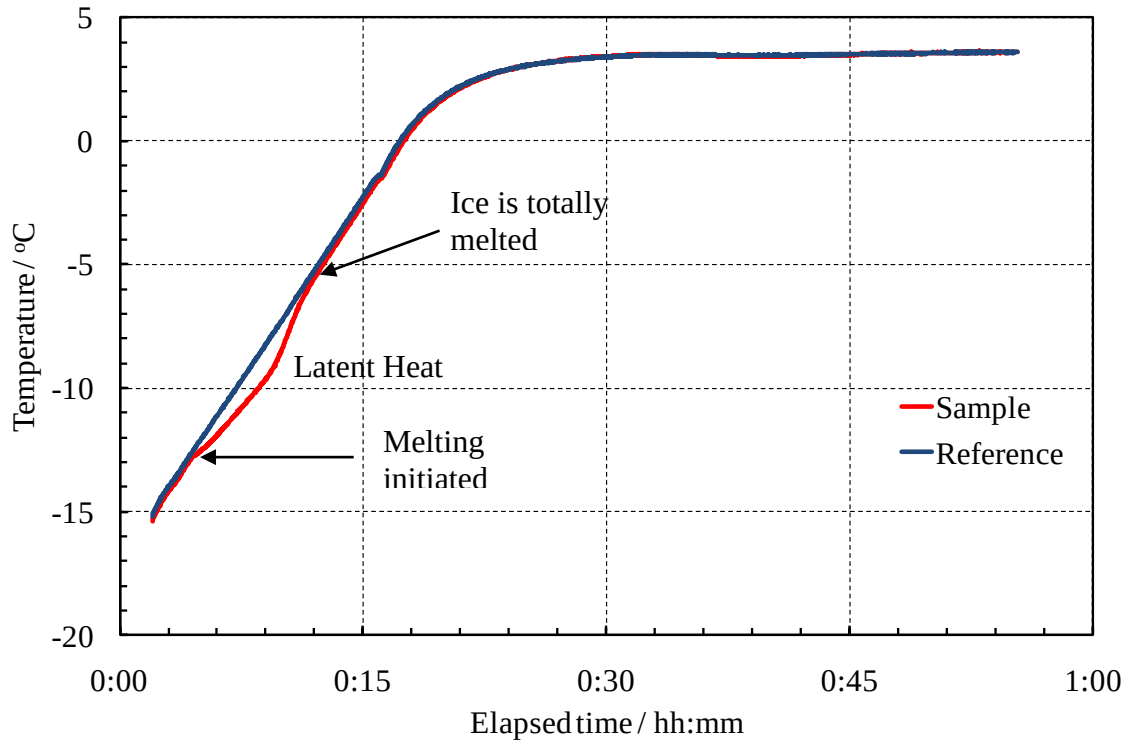

Figure 4.12 Melting during the heating stage of measurement cycle

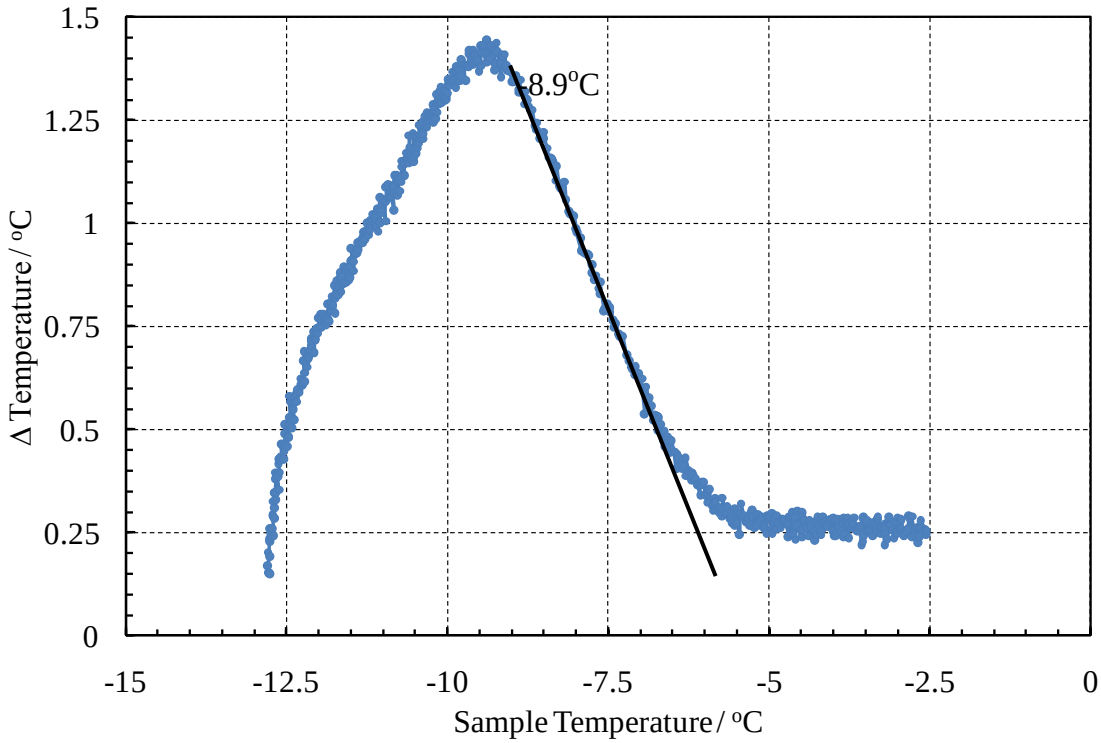

Figure 4.13 Delta temperature plotted against sample temperature used to identify freezing point. Delta temperature is the difference between reference and sample temperatures. Freezing point is the sample temperature at which measured data starts descending linear trend. In this example, the measured freezing point is -8.9 °C for 21.5 mass% aqueous methanol solutions.

4.4.4 Results of Freezing Point Depression Measurements

The freezing point depression of aqueous ethylene glycol and methanol solutions were measured to investigate the method applicability. Firstly, the freezing point depression of aqueous EG and MeOH solutions in the absence of salts were measured using the one-stage Peltier device. The maximum EG concentration was 35 mass%, and the MeOH concentration was up to 30 mass%. Both the measured and the predicted freezing point depression are tabulated in Table 4.9. In Figure 4.14, the measured freezing point depressions were compared with the thermodynamic predictions of HWHYD. The thermodynamic calculations were based on a general phase equilibrium model with a condition of uniformity of component fugacities in all coexisting phases (Appendix C).

Table 4.9 Measured and predicted freezing point depression

Alcohol mass%	Freezing Point Depression, °C			
	EG		MeOH	
	Measured	Predicted	Measured	Predicted
0.0	0.0	0.0	0.0	0.0
5.0	1.9	1.6	3.0	3.1
10.0	3.4	3.4	6.8	6.6
15.0	5.4	5.5	10.3	10.6
20.0	8.0	8.0	14.9	15.1
25.0	10.5	10.9	19.8	20.0
30.0	14.8	14.3	24.4	25.6
35.0	18.2	18.2		

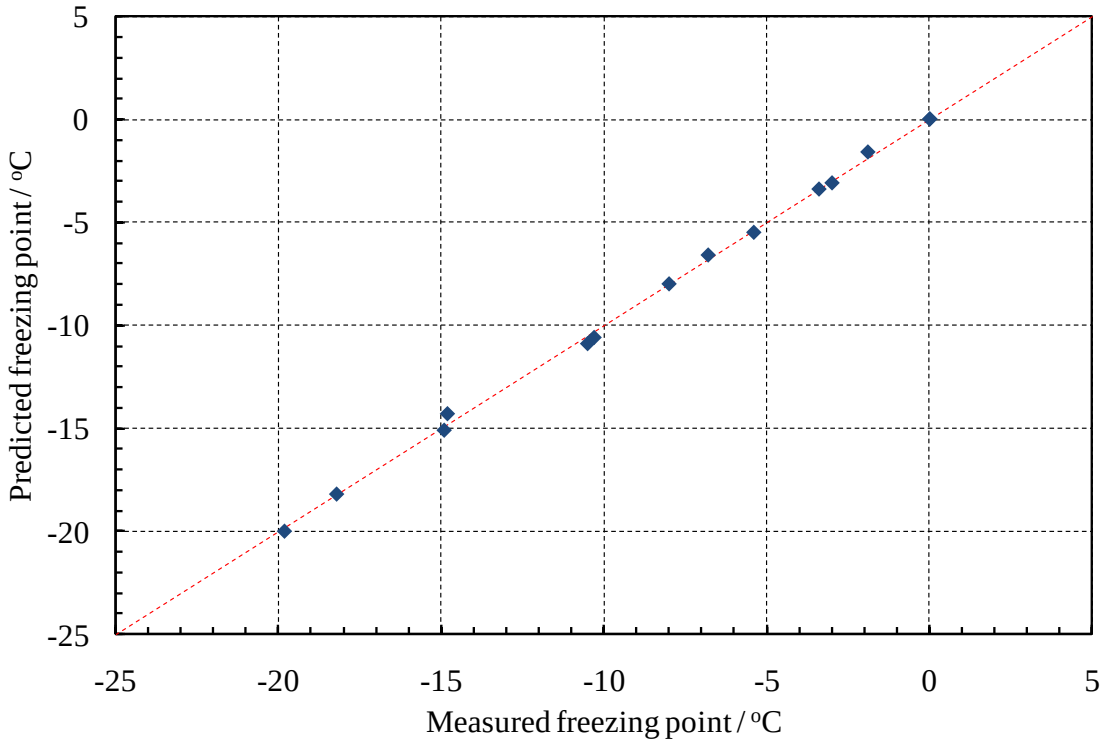

Figure 4.14 Comparison of the measured freezing point depression with the predicted for the aqueous ethylene glycol and methanol solutions without salts

Generally, the measured freezing point depressions are in agreement with the predictions. In the tests with aqueous EG solutions the deviation is within 0.5 °C, whilst in the tests with aqueous MeOH solutions the largest deviation is 1.2 °C. According to the correlation (4.3), this can lead to a deviation in the prediction of the hydrate dissociation temperature of approximately 0.3 °C for the system with EG, and 0.8 °C for the system with MeOH.

Further freezing point depression tests were conducted using the three-stage Peltier element device for aqueous alcohol solutions in the presence of salts. The EG

concentration was 25 mass%, and the MeOH concentration was 20 mass%. In both solutions the salt concentration varied from 5 to 10 mass%. Both the measured and the predicted freezing points are tabulated in Table 4.10. In Figure 4.15, the measured freezing points are compared with the prediction of the thermodynamic model.

Table 4.10 Measured and predicted freezing point depression

	Freezing Point Depression, °C					
	Salt, 5 mass%		Salt, 7.5 mass%		Salt, 10 mass%	
	Measured	Predicted	Measured	Predicted	Measured	Predicted
MeOH, 20 mass%	19.7	19.9	22.4	22.6	25.3	25.6
EG, 25 mass%	15.6	15.7	18.3	18.5	21.4	21.5

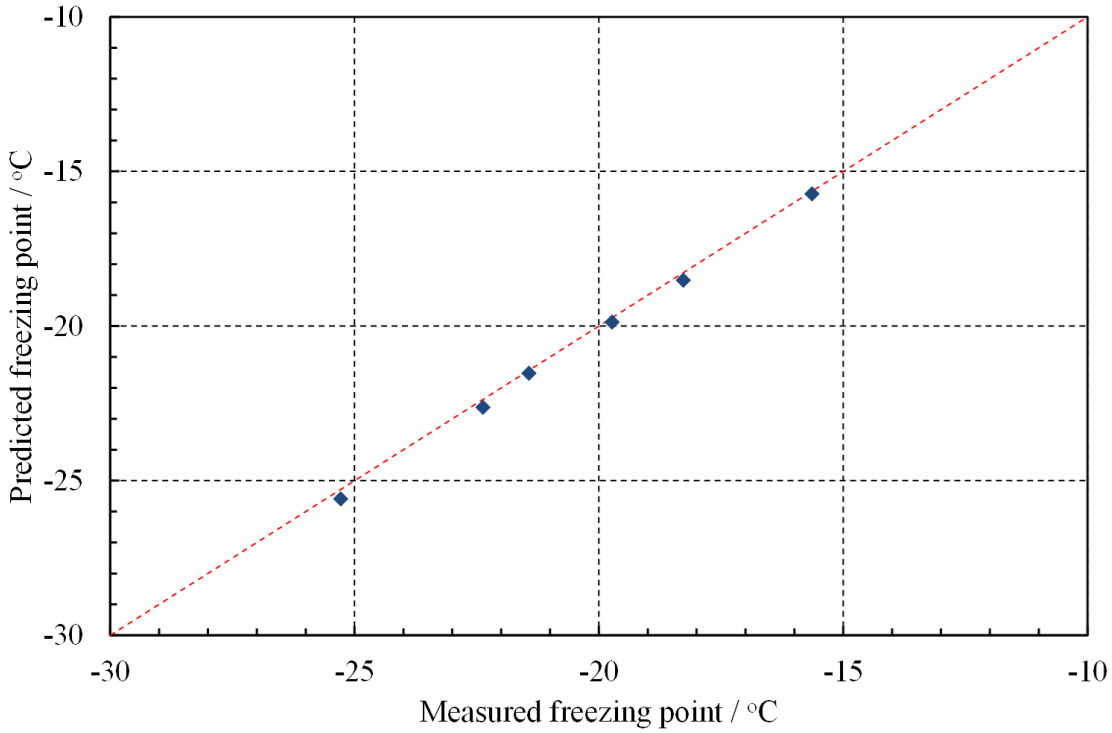

Figure 4.15 Comparison of the measured freezing point depression with the predicted for the aqueous ethylene glycol and methanol solutions in the presence of salt

As seen in Figure 4.15, the measured freezing points are in agreement with the prediction within acceptable error range of ±0.5 °C. In the tests with aqueous solutions the deviation is within 0.5 °C. According to the new correlation (4.4), this can lead to a maximum deviation in hydrate dissociation temperature, approximately, 0.4 °C for a pressure range up to 280 bar. The sensitivity of heating rate on accuracy of freezing point determination was not investigated in the context of these experiments. However, for example, hydrate dissociation temperature can be sensitive to heating rate, as it was investigated elsewhere (Gulbrandsen et al., 2008).

4.4.5 Determination of Hydrate Dissociation Temperature Using the Measured Freezing Point Depression

For easy comparison, methane was selected as a reference gas for these investigations. The methane hydrate phase boundary was predicted by HWHYD. The inhibition depression of the methane hydrate phase boundary was correlated by the previously developed correlation (4.3). The comparisons between the predicted and the correlated methane hydrate phase boundaries are shown in Figure 4.16 and Figure 4.17.

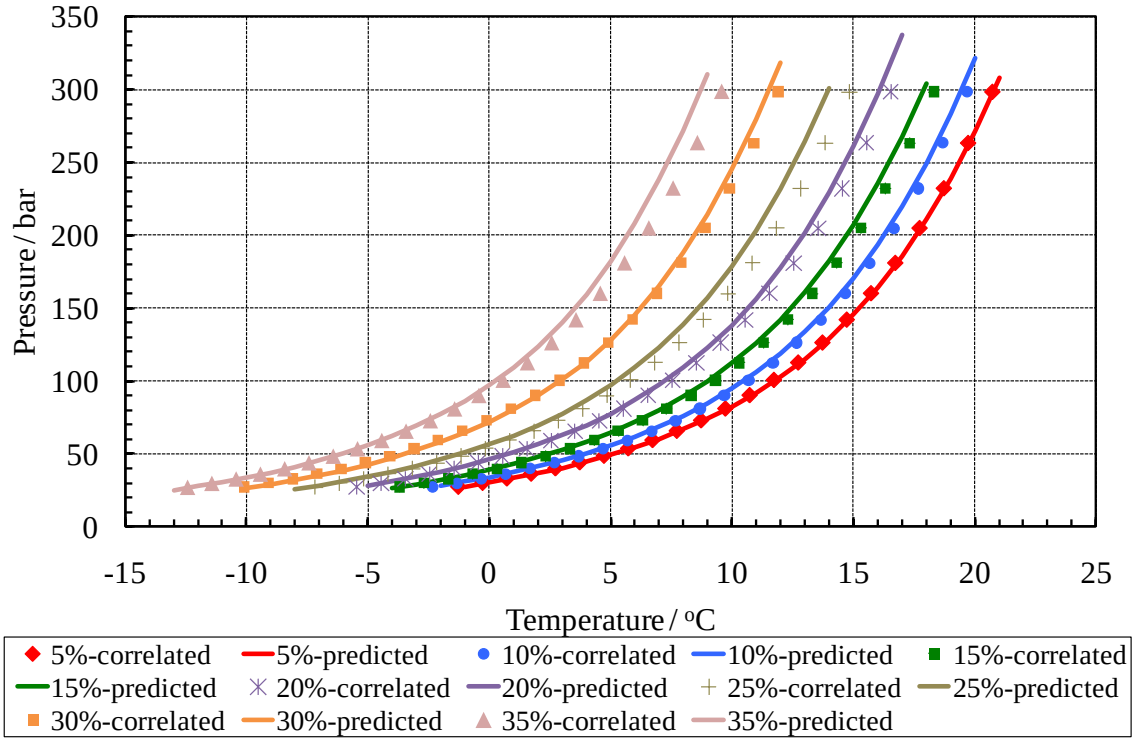

Figure 4.16 Correlated and predicted methane hydrate phase boundary for the aqueous ethylene glycol solutions without salts

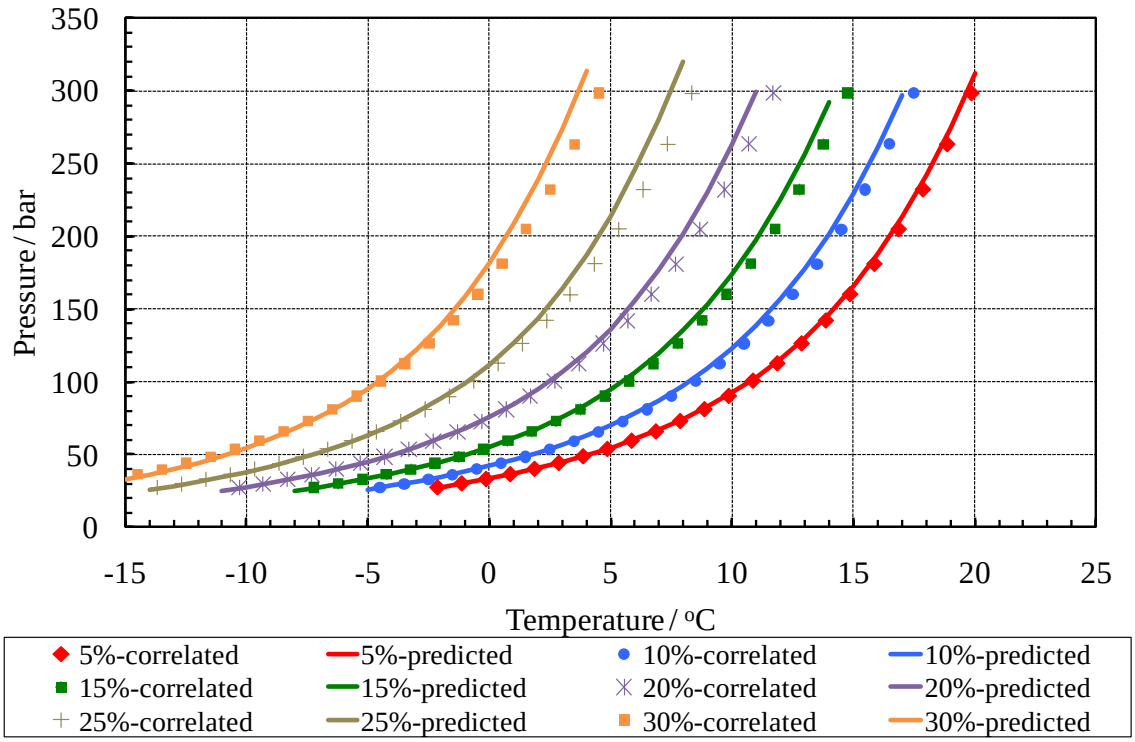

Figure 4.17 Correlated and predicted methane hydrate phase boundary for the aqueous methanol solutions without salts

In Figure 4.16 and Figure 4.17, the points represent the methane hydrate dissociation points correlated using the correlation and the solid lines represent the corresponding methane hydrate phase boundaries predicted by HWHYD. In general, the correlated dissociation points are in line with the predicted phase boundaries. For low alcohol concentrations, they match very well over a wide pressure range up to 300 bar. The temperature difference is less than 0.5 °C. For high alcohol concentrations, the deviations are small at low pressure, but gradually become larger as pressure rises. At 200 bar, for example, the temperature deviation could be around 1 °C.

It can be found that the correlated dissociation temperatures are always higher than the predicted values. These systematic errors can be from the correlation (4.3), which is not suitable for high alcohol concentrations.

Similarly, the freezing point depression data for aqueous alcohol solutions with salts, measured by the three-stage Peltier device, were used to examine the performance of the modified correlation (4.4). Figure 4.18 and Figure 4.19 present the comparison between the predicted and the correlated methane hydrate phase boundary for the aqueous MeOH and EG systems with various NaCl concentrations.

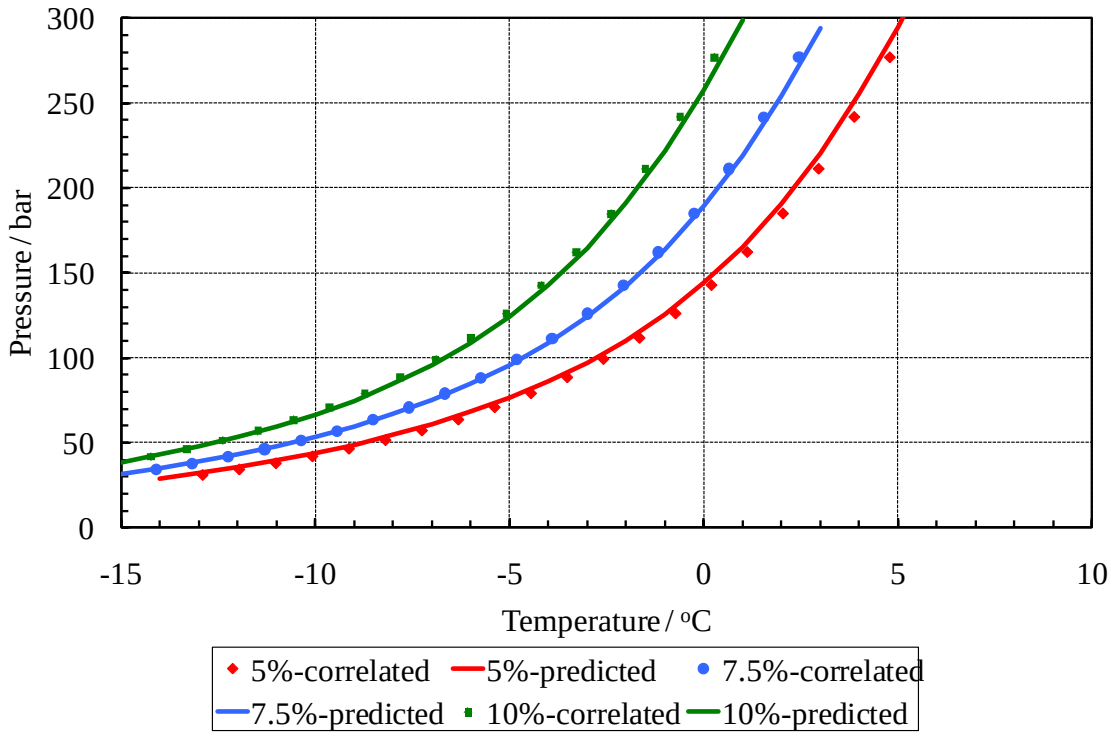

Figure 4.18 Correlated and predicted methane hydrate phase boundary for the 20 mass% aqueous methanol solutions with various sodium chloride contents

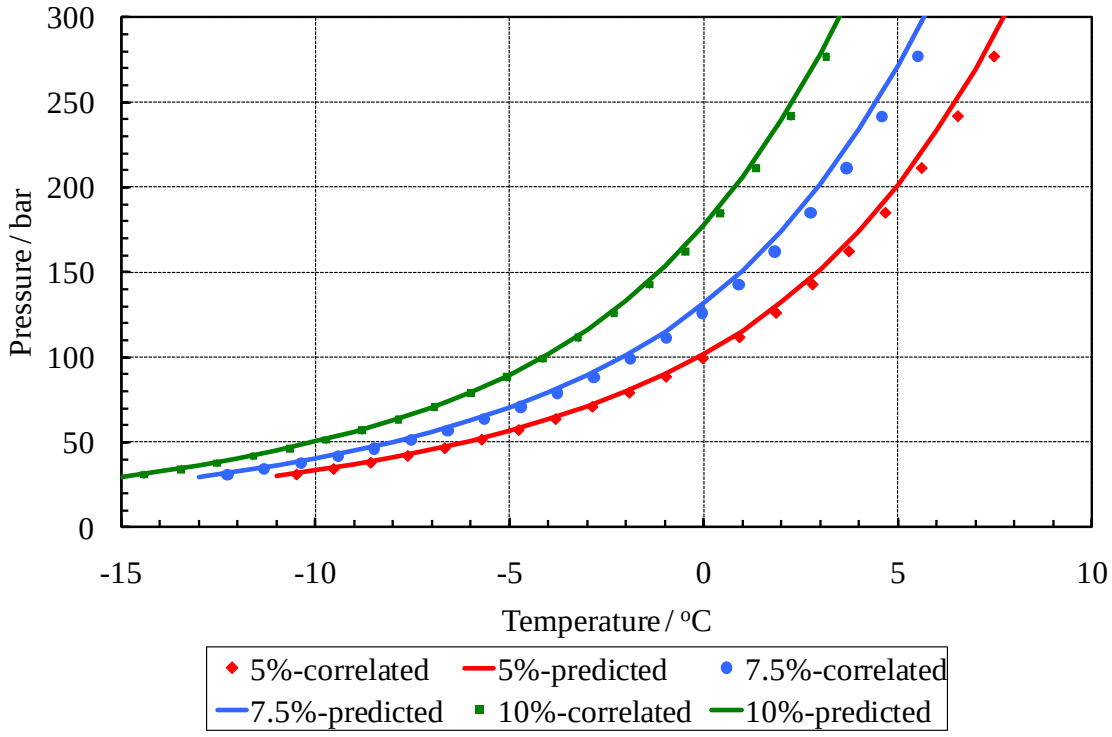

Figure 4.19 Correlated and predicted methane hydrate phase boundary for 25 mass% aqueous ethylene glycol solutions with various sodium chloride contents

In Figure 4.18 and Figure 4.19, the correlated hydrate dissociation conditions are in good agreement with HWHYD model predictions in both low and high pressure regions. Because the freezing point measurements are not sensitive to contaminations due to oil droplets and/or solid particles, the freezing point device can provide a robust technique for determining the hydrate safety margin.

4.5 PSEUDO CONCENTRATION METHOD

The developed correlation (4.4) for predicting the hydrate inhibition effect was based on the concept of water freezing point depression due to the presence of salt and/or organic inhibitor(s). In order to improve the prediction method, more physical elements can be integrated in the calculation loop. Common sense is that any additional information like the knowledge of inhibitor type(s) present in the produced fluid can improve the predictability of hydrate formation characteristic. Thermodynamic modelling which is based on equity of chemical potentials of various components in different phases can serve as the tool for incorporating external information into the prediction process. In this section, studies have been conducted to test a new approach to relate the freezing point depression of aqueous solutions to their hydrate inhibition characteristics. In this approach a pseudo inhibitor concentration is calculated based on the measured freezing point depression. Figure 4.20 shows the GUI of the FPD (freezing point device) executable programme for determining pseudo inhibitor concentration using the measured freezing point depression. Within the program, the concentrations of selected aqueous components are adjusted to match the measured freezing point, so that to match the thermodynamic response of the modelled solution. The calculated pseudo concentrations are not necessarily the real ones, but can be used to calculate the hydrate stability zone.

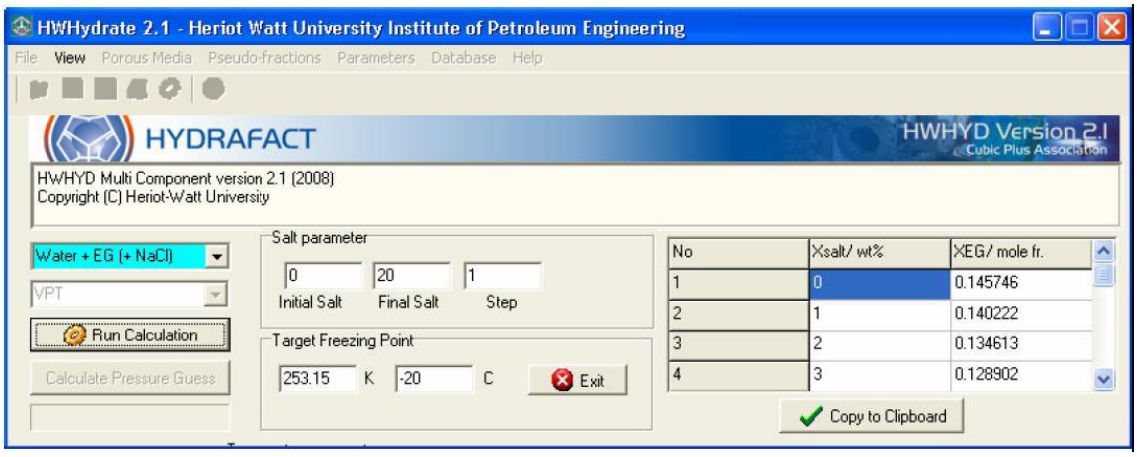

Figure 4.20 GUI of the FPD executable programme for determining pseudo inhibitor concentration using the measured freezing point depression

4.5.1 Feasibility

This idea was first tested by numerical simulation using our in-house thermodynamic model for several fluid systems, which have the same freezing point. The hydrate stability zones of these systems (HSZs) are then compared. Results show that all the HSZs lie within 0.1 ^{o}C. Further evaluation was conducted using various gaseous mixtures to examine the effect of different structures. The results show that predicted HSZs are within ±0.2 ^{o}C (independent of the hydrate structure) which implies an applicability of this method to predict phase boundary for both structures I and II gas hydrates.

Furthermore, the approach was further evaluated using various inhibitor combinations to examine the effect of selected inhibitor on the results. A gas mixture with composition given in Table 4.11 was used in all predictions. This is a representation of natural gas composition which forms hydrate of structure II. Eight aqueous phase compositions were chosen to match the measured freezing point (Table 4.12). Results are plotted in Figure 4.21 and Figure 4.22, for comparison. As shown in the figures the HSZ of all systems are very close, within ±0.2 ^{o}C and ±4 bar. The results demonstrate that the type of inhibitor does not play a major role in the final hydrate phase boundary, though it is recommended to use the actual inhibitor system to capture other phase behaviour aspects.

Table 4.11 Gas composition

Component	N_2	CO_2	C_1	C_2	C_3	iC_4	nC_4	iC_5	Total
Mole %	2.16	1.69	89.74	4.62	1.26	0.17	0.30	0.06	100

Table 4.12 Freezing points for various aqueous phase compositions

Liquid	Freezing Point, ^{o}C
2 mass% NaCl, 10 mass% MeOH	-7.98
2.98 mass% NaCl, 9 mass% MeOH	-7.98
5 mass% NaCl, 6.92 mass% MeOH	-7.98
10 mass% NaCl, 1.68 mass% MeOH	-7.97
11.54 mass% NaCl	-7.98
11.78 mass% MeOH	-7.98
19.94 mass% EG	-7.98
15.98 mass% Ethanol	-7.97

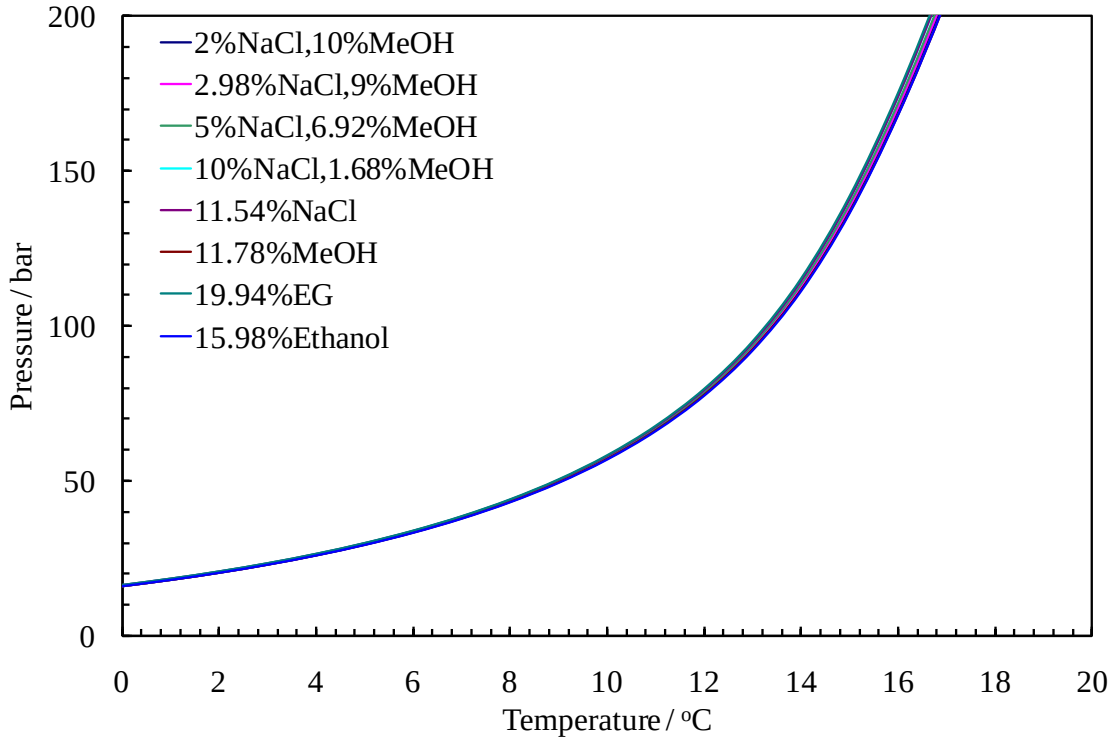

Figure 4.21 HSZs for different fluid systems having the same FP

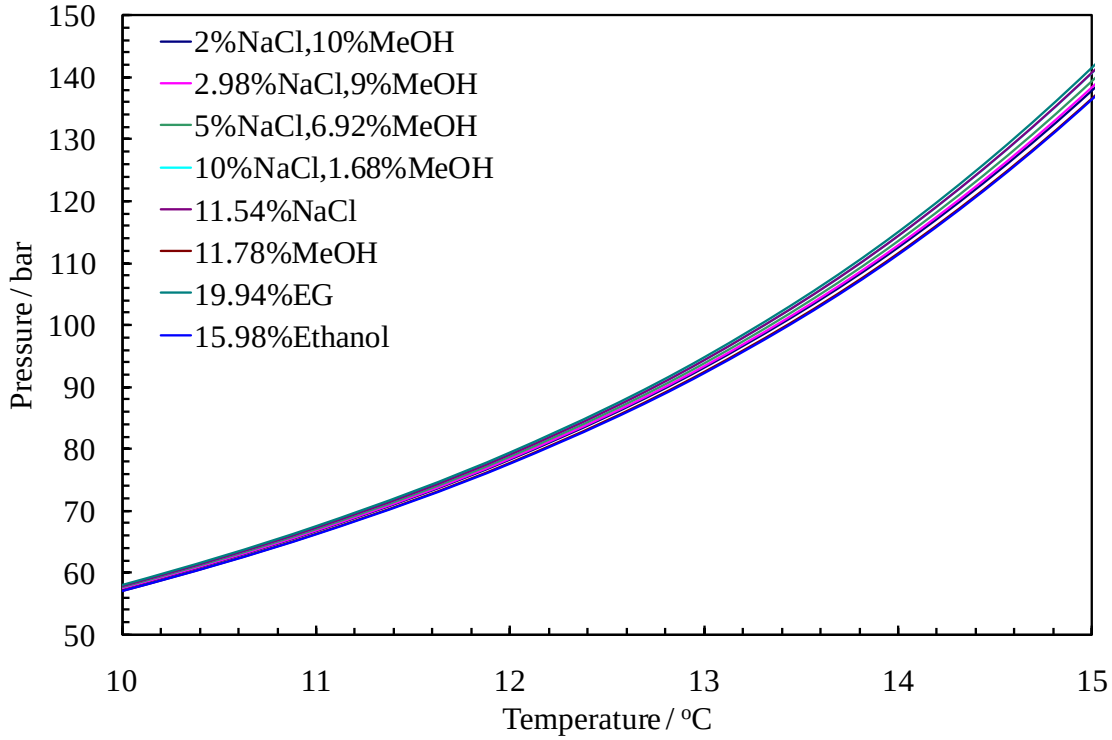

Figure 4.22 (Enlarged picture) HSZ for different fluid systems having the same FP

4.5.2 Effect of Hydrate Structure

4.5.2.1 Structure I

Tested systems: the gas composition is given in Table 4.13 and chosen to form structure I hydrate. Aqueous phase compositions are chosen to give the same freezing point (Table 4.12). HSZs (Figure 4.23; Figure 4.24) are within ±0.1 ^{o}C and ±2 bar, this method can therefore be applied to predict the hydrate phase boundary of structure I forming systems.

Table 4.13 Composition of gas forming structure I gas hydrate

Component	C_1	C_2	C_3	iC_4	nC_4	Total
Mole (%)	99.43	0.5	0.05	0.01	0.01	100

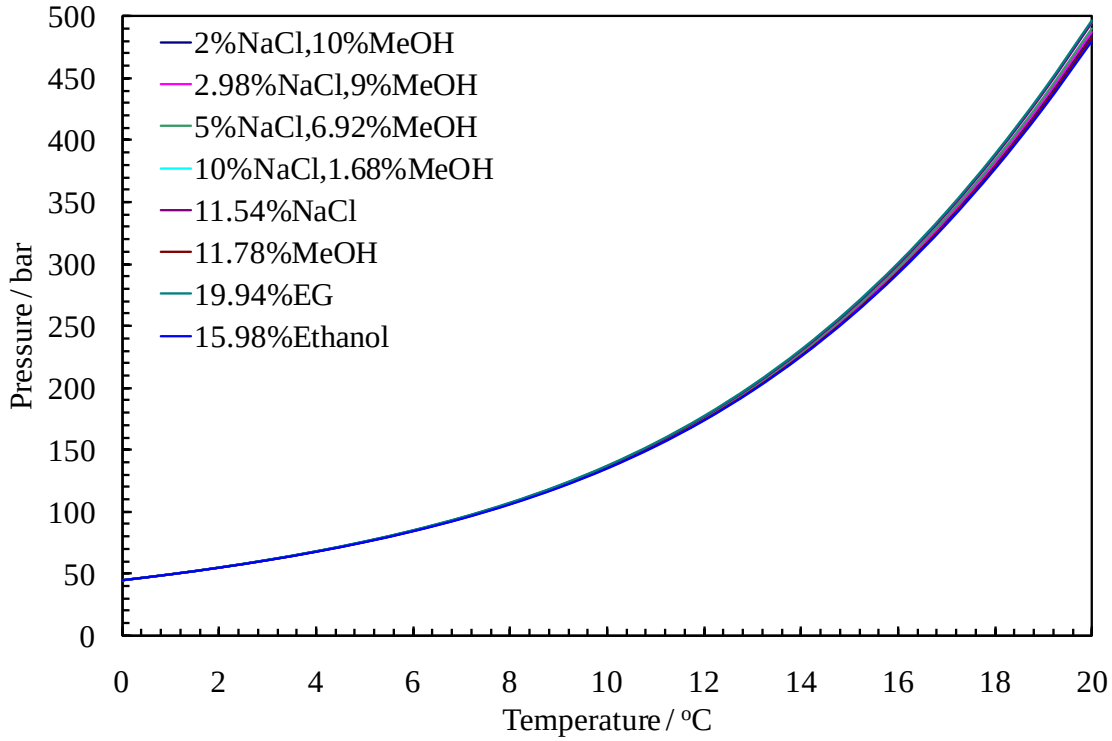

Figure 4.23 Structure I gas hydrate stability zone for fluid systems having the same FP

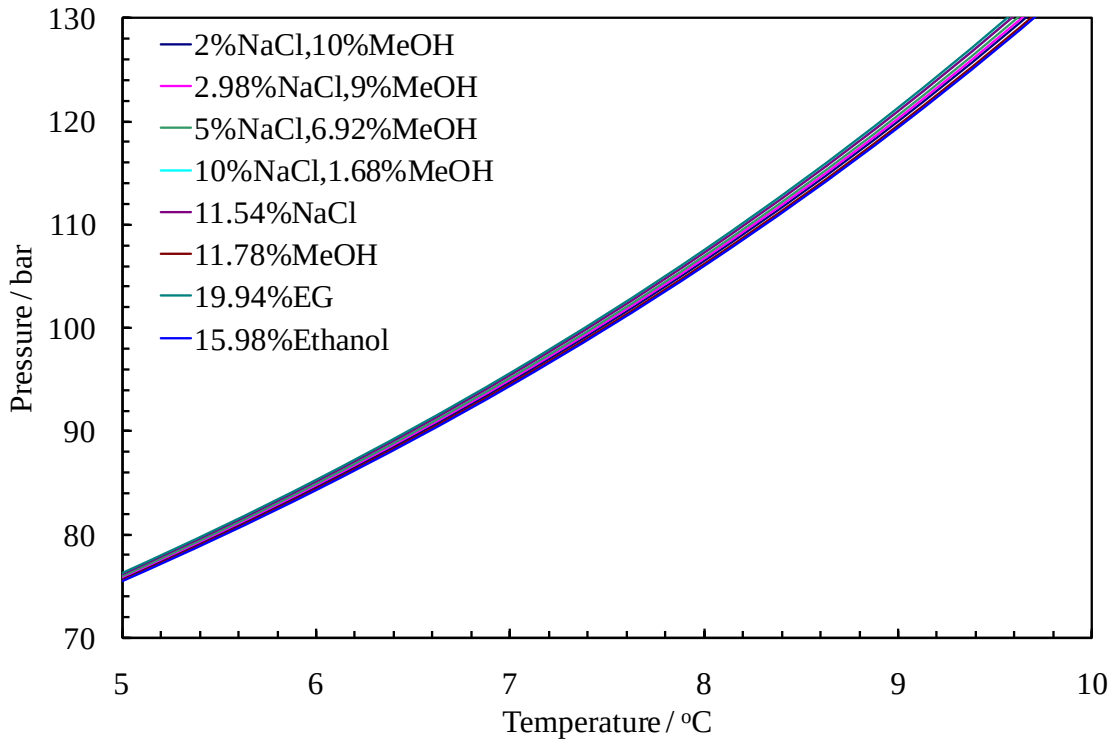

Figure 4.24 (Enlarged picture) Structure I gas hydrate stability zone for fluid systems having the same FP

4.5.2.2 Structure II

Tested systems: the gas composition is given in Table 4.14 and chosen to form structure II hydrate. Aqueous phase compositions are chosen to give the same freezing point (Table 4.12). HSZs (Figure 4.25; Figure 4.26) are within ±0.2 °C and ±4 bar, this method can therefore be applied to predict the hydrate phase boundary of structure II forming systems.

Table 4.14 Gas composition forming structure II gas hydrate

Component	C_1	C_2	C_3	iC_4	nC_4	Total
Mole (%)	83	5	8	3	1	100

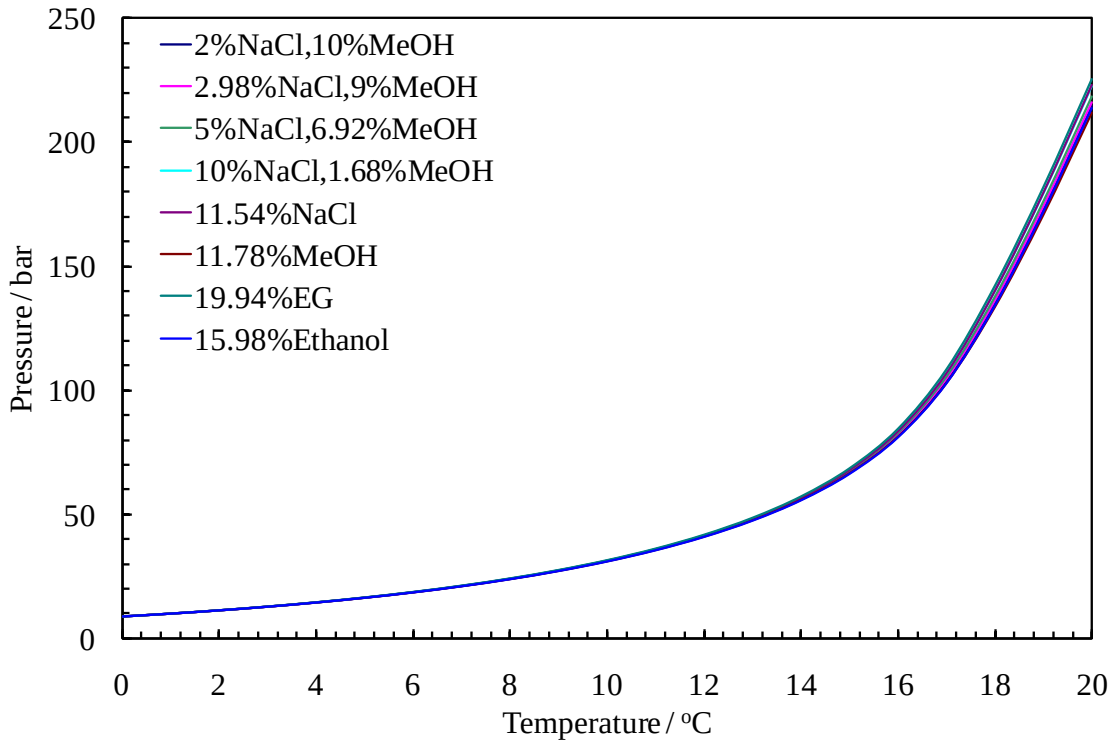

Figure 4.25 Structure II gas hydrate stability zone for fluid systems having the same FP

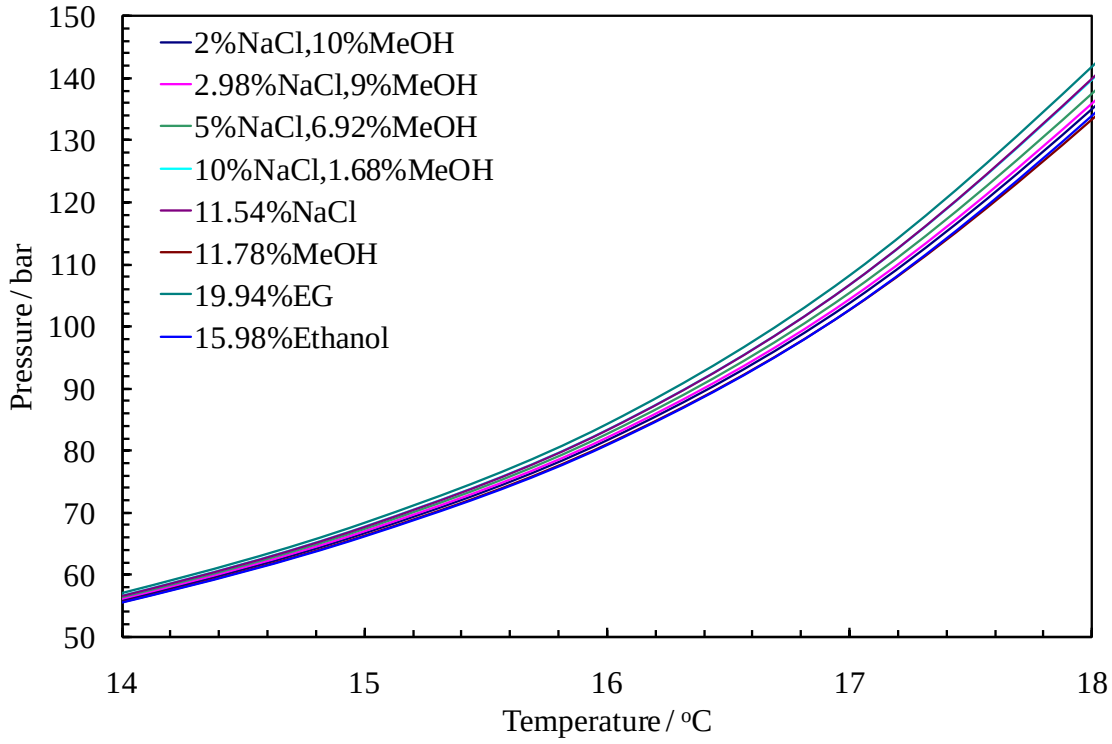

Figure 4.26 (Enlarged picture) Structure II gas hydrate stability zone for fluid systems having the same FP

4.5.3 Comparison with the Correlation

In this study, a typical gas composition was used (Table 4.11). The existing correlation (4.4) was compared with this new approach, the Pseudo Concentration Method (PCM) for low and high concentrations of hydrate inhibitors. When the concentration of inhibitors is low, the correlation and PCM method give similar results (Figure 4.27). However, when the concentration of inhibitors is high, i.e. the difference between the HSZ of the inhibited system and distilled water is high, the PCM method is much better than the correlation (Figure 4.28; Figure 4.29). In Figure 4.29, the high deviation in the HSZs is due to the high variations in NaCl concentration (5 mass% steps). Taking into account the fact that, in real systems, the salt content is not expected to vary so much, this new approach was tested every 1 mass%. Results are plotted in Figure 4.30; HSZs of the various systems are within ±0.2 ^{o}C (Figure 4.30).

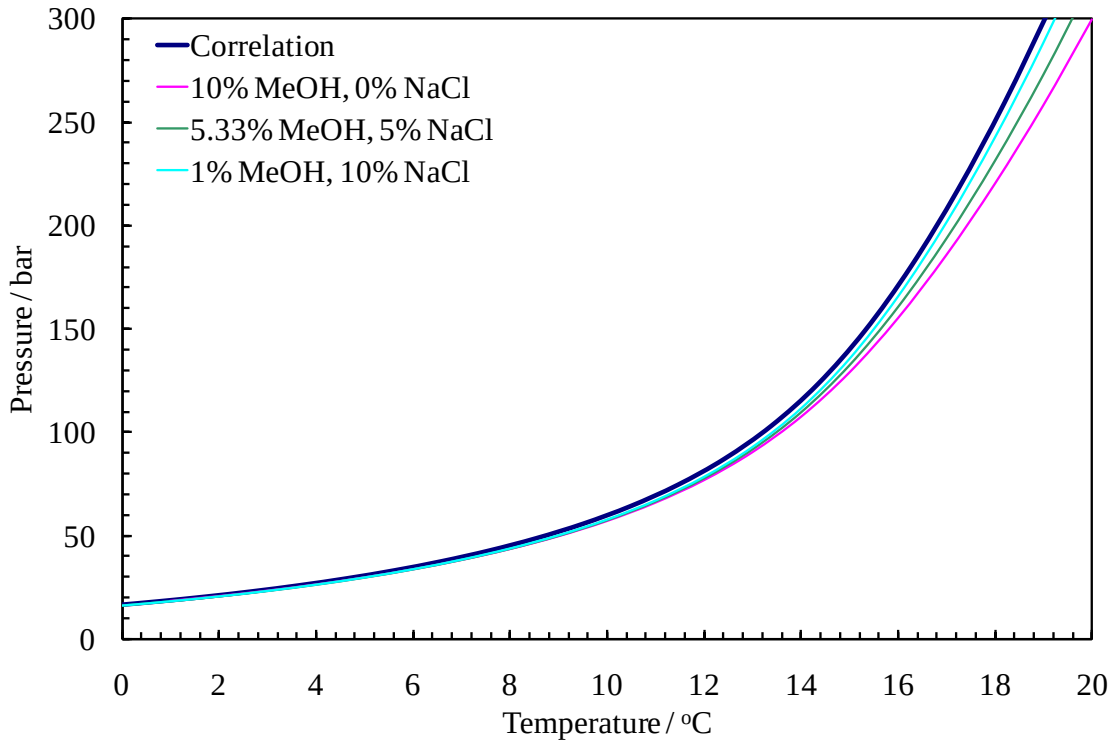

Figure 4.27 Comparison of correlation method with PCM for aqueous solutions with low MeOH-NaCl content which have the same -6.47 ^{o}C freezing point

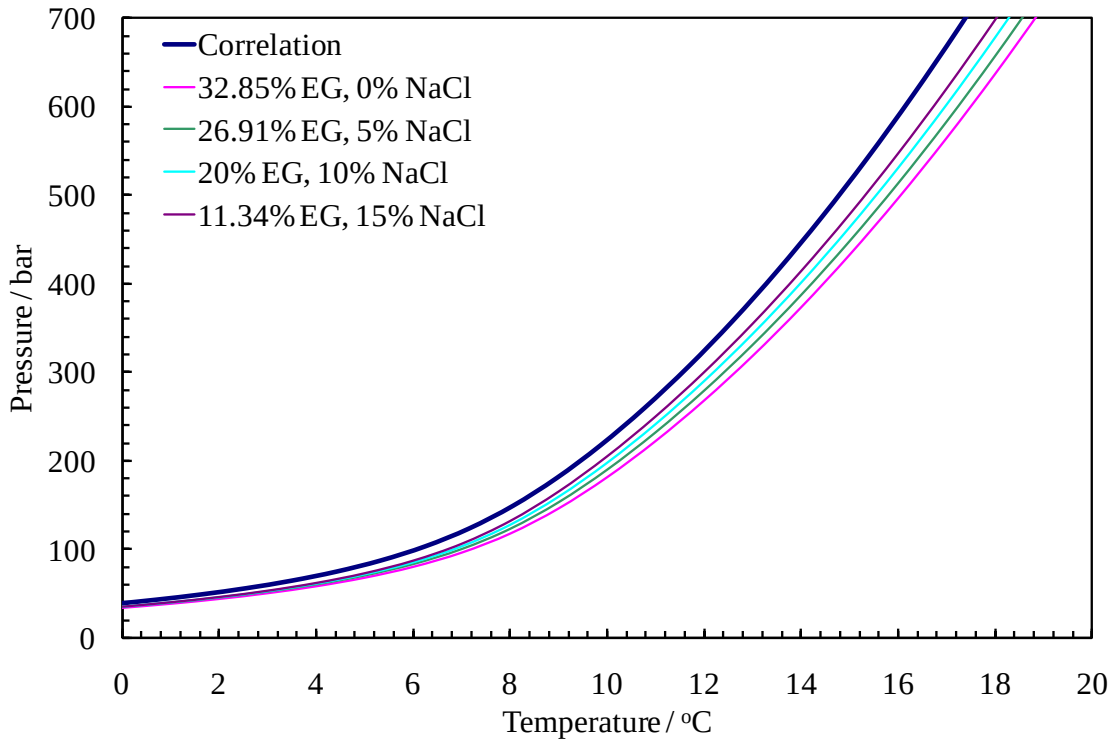

Figure 4.28 Comparison of correlation method with PCM for aqueous solutions with high EG-NaCl content which have the same -16.32 °C freezing point

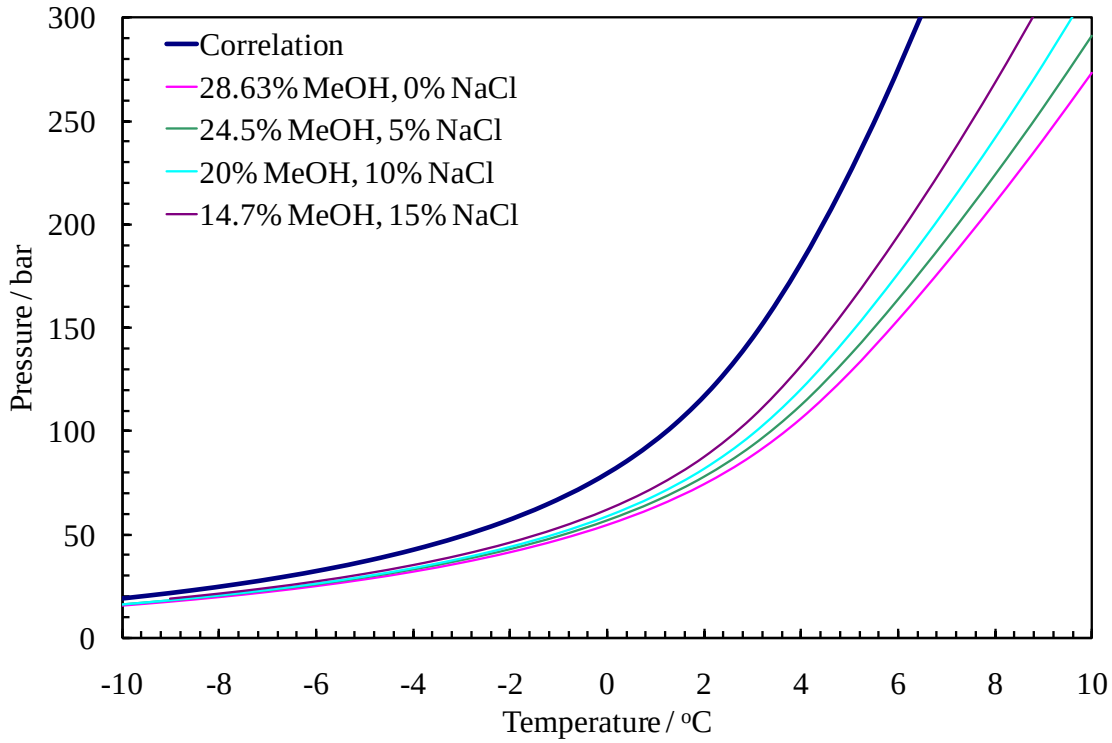

Figure 4.29 Comparison of correlation method with PCM for aqueous solutions high MeOH-NaCl content which have the same -23.25 °C freezing point

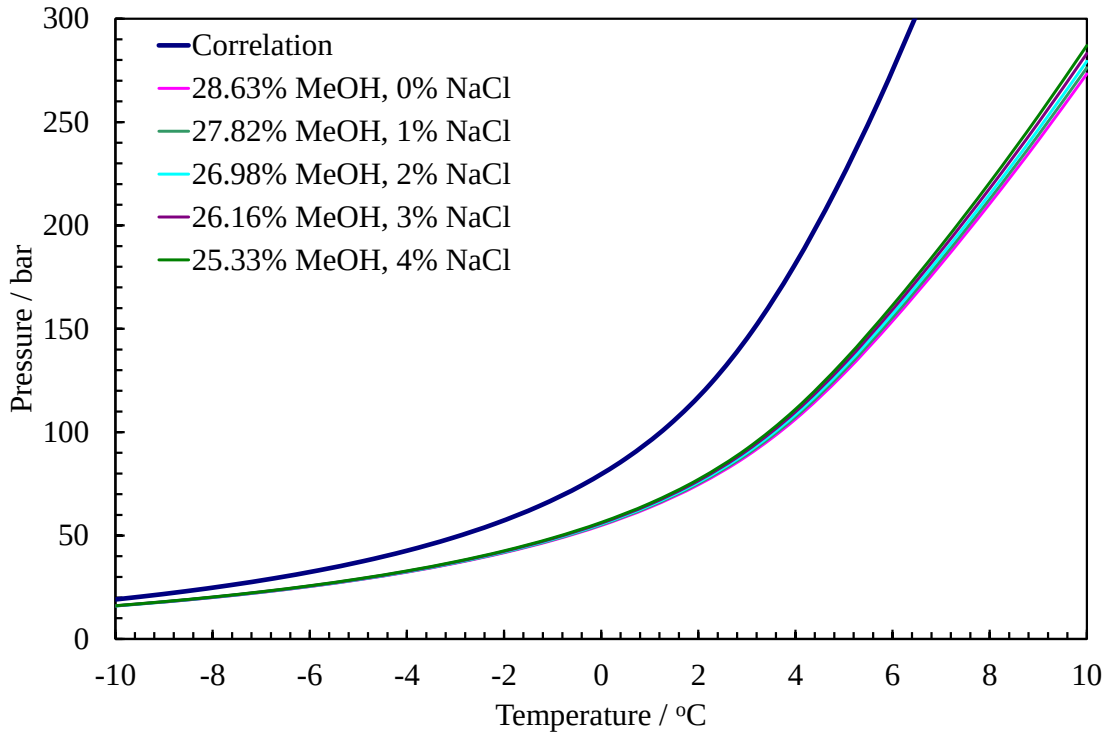

Figure 4.30 Comparison of correlation method with PCM for aqueous solutions with high methanol and ±2 mass% variation in NaCl content showing the PCM methodology robustness and reliability. Solutions have the same -23.25 °C freezing point.

This new approach is more reliable and robust than the previously developed correlation (4.4), since it takes into account the pressure, hydrate structure and inhibitor type effects.

4.6 CONCLUSIONS

To minimise the risk of hydrate formation in petroleum production/processing facilities, inhibitor injection is generally applied to force the hydrate phase boundary away from operating conditions and ensure an acceptable hydrate safety margin. In this Chapter, a technique has been developed and investigated by which the hydrate formation properties of the tested fluid can be determined providing a fast and reliable inhibition monitoring.

The technique is based on the measurement of the freezing point of the produced fluid and the calculation of the hydrate phase boundary via simple correlation. It was experimentally investigated and proven that freezing point depression of aqueous

solutions can be applied to determine the hydrate stability zone of various fluid systems in the presence of salts and/or organic inhibitors. An experimental device was designed and manufactured for measuring freezing points.

A simple correlation was developed in Centre for Gas Hydrate Research, Heriot-Watt University to determine the hydrate stability zone for various fluid systems based on freezing point depression of aqueous solutions due to the presence of salts and/or alcohols. The correlation was examined using different aqueous solutions containing salts and/or organic inhibitors over a wide range of concentration. Taking into account the effect of pressure, the correlation was further improved by Dr. Antonin Chapoy as part of Joint Industrial Project which this thesis is a part of. It was tested in the presence of various concentrations of EG, MeOH and salt. The improved correlation has better agreement with the predictions of the thermodynamic model (HWHYD) for both low and high pressure conditions.

Pseudo Concentration Method (PCM) was developed as a new approach to relate the freezing point depression of aqueous solutions to their hydrate inhibition characteristics. The concentrations of dominating dissolved components are adjusted to match the measured freezing point, so that to match the thermodynamic response of the modelled solution. This new approach was shown to be more reliable and robust than the previously developed correlations, since it takes into account the pressure, hydrate structure and inhibitor type effects.

A freezing set-up based on Peltier device was manufactured, which remarkably facilitated the freezing point measurements and made the freezing point depression technique more feasible and applicable for field laboratory conditions and potentially for online applications. Using the Peltier device prototype, freezing point depression was measured for aqueous EG and MeOH with salt (NaCl) solutions. The measured freezing point depression was used for determining the phase boundary of methane hydrates in the presence of the salts and/or alcohols. The typical deviation with experimental data was less than 0.5 ^{o}C. The correlated hydrate phase boundaries are in good agreement with the HWHYD model predictions.

In conclusion, the freezing point depression method can be used as a simple flow assurance technique for monitoring the hydrate safety margin with an acceptable accuracy. The new concept of Peltier element device presents a good potential for on-line application.

CHAPTER 5 ONSET OF ICE FORMATION

5.1 INTRODUCTION

Flow assurance is a major challenge in oil production operations. The industry is continually looking for innovative solutions not only to flow assurance issues, but also new solutions to reduce the CAPEX and OPEX, to eliminate remedial costs of removing pipeline blockages, prevent deferred production and improve the overall recovery factors. One of the innovations in this area is implementation of cost effective hydrate prevention techniques along with the early warning system which detects the moment of first hydrate crystals formation. Typically, an early alarming could be given if any hydrate water structure is identified by some techniques. In this Chapter, the hydrate water history phenomenon has been investigated as an indicator for hydrate early warning.

It has been found that at identical conditions gas hydrates could reform earlier and faster after hydrate dissociation. This has been explained by the hydrate water history effect. It is assumed that after hydrate dissociation there can still be some kind of water molecular structure remaining in liquid phase. This water structure could exist as residual clusters of water molecules. This phenomenon was previously investigated using several experimental techniques (Sloan et al., 1998; Bylov et al., 1997; Ohmura et al., 2000; Zain et al., 2005). Although it was not yet clearly theoretically understood what the water memory is in terms of molecular structure and how it can remain and behave in the liquid phase, experimentally, it was evident that hydrate water history could sustain for several hours to a few tens of hours under certain thermodynamic conditions.

Projecting the effect in to industrial systems, hydrate nuclei can form in a part of a pipeline with appropriate temperature-pressure conditions, and be transported to another

part where conditions are suitable for hydrate to dissociate. Hydrate dissociates into water and original gas leaving no obvious evidence of its past presence. However, the released water can keep the so-called hydrate structure which in turn can be detected if there were suitable temperature-time conditions at the point of sampling. Presumably, the thermodynamics of freezing process can depend on the presence of remaining hydrate cluster structure in aqueous phase. Therefore, the hypothesis was originated to measure the memory by ice crystallization. In this Chapter, the presence of memory in aqueous phase has been investigated to have an impact on freezing point. Specific equipment and procedures were designed to facilitate the study.

5.2 ONSET OF ICE FORMATION METHOD

5.2.1 Experimental Set-up and Procedures

5.2.1.1 Experimental Set-up

Water samples after hydrate dissociation and the water samples saturated with natural gas were prepared using the high pressure kinetic rig (Figure 5.1).

This rig was equipped with high-pressure cell of 300 ml volume, coolant jacket and temperature/pressure recording equipment controlled by a computer. The operating temperature range was in the range of –30 to 75 ^{o}C. Internal temperature was measured by a thermocouple in an accuracy of 0.05 ^{o}C. The cell pressure was monitored by quartzdyne pressure transducer of 0.07 bar accuracy. This rig was also equipped with magnetic stirrer.

The test cell was loaded with the required volume of water, vacuumed for 1 hour to remove any trap air from the fluid, and then charged with the natural gas to the desired pressure. To form hydrates, the system was cooled down and kept at a temperature inside the hydrate stability zone at a certain stirring rate.

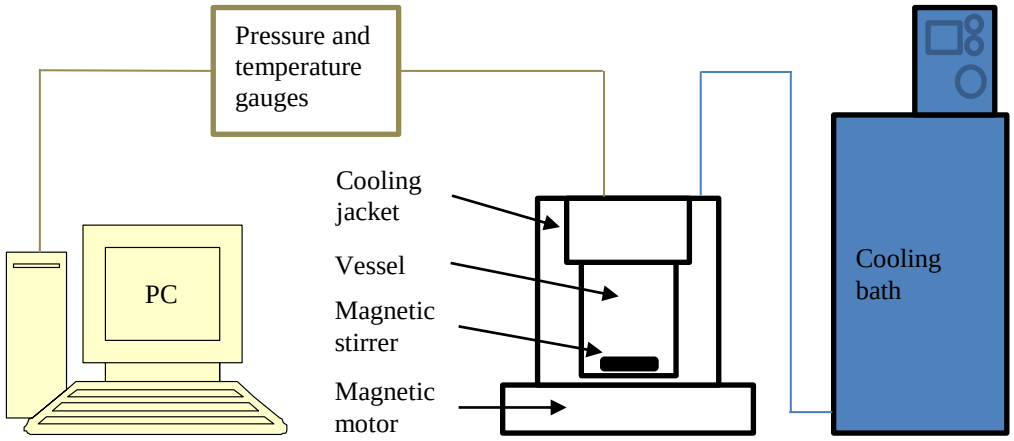

Figure 5.1 Schematic diagram of the high pressure hydrate kinetic rig

The samples were tested using new freezing point depression apparatus shown in Figure 5.2 and Figure 5.3. The apparatus consisted of 21 platinum resistance temperatures (PRT) probes, 21 stainless steel tubes, temperature reader and a temperature-controlled bath. 1 ml of the test sample was placed in each stainless steel tube for tests. Each sample tube was then equipped with PRT temperature sensor. The tubes were immersed in the bath for temperature control. One of the probes was used for recording reference temperature of the bath itself. All temperatures were recorded by feeding the analogue signal into a temperature reader block which was then transmitted digital data to computer equipped with analytical software.

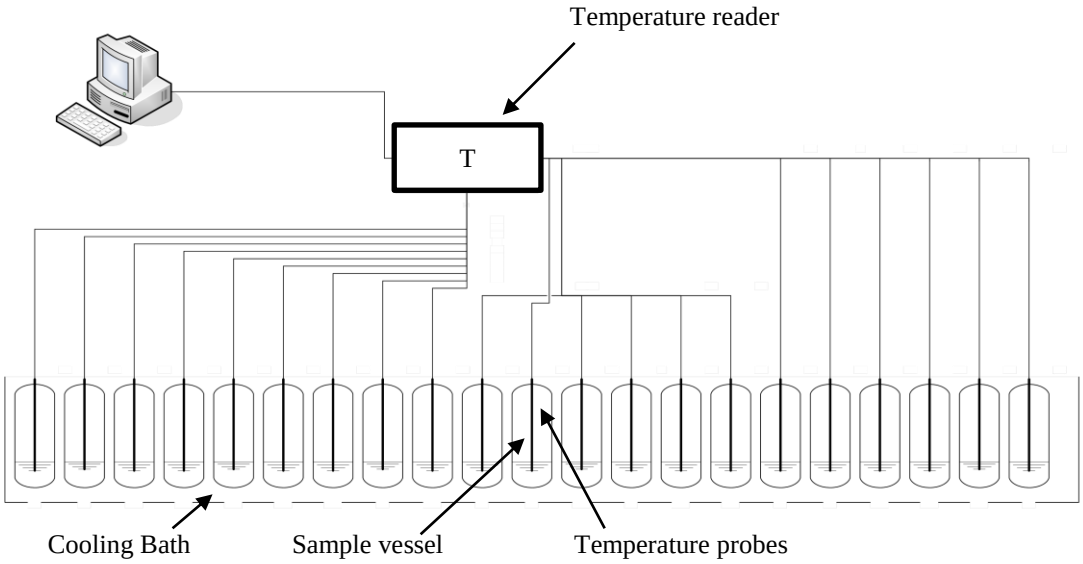

Figure 5.2 Freezing point depression apparatus (overall view)

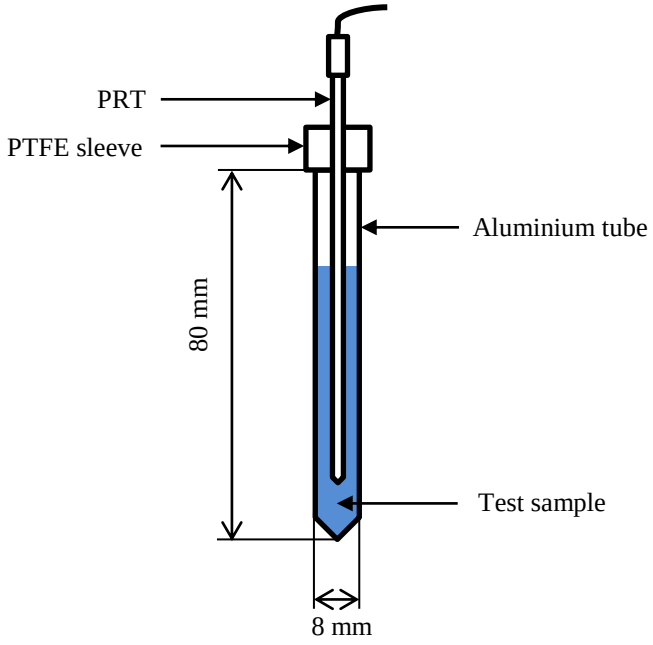

Figure 5.3 Freezing point depression apparatus (sample probe)

5.2.1.2 Materials

Deionised water. Produced water provided by BP containing 5 mass% salts. TOTAL produced water containing 23 mass% Methanol, 3 mass% salts, and an unknown corrosion inhibitor. Natural gas composition is provided in Table 2.1.

5.2.1.3 Procedures

The water samples were prepared by following a specific temperature-pressure paths in the kinetics rig (Figure 5.4). Hydrate deionised/produced water (HDW/HPW), heated hydrate deionised/produced water (HDWht/HPWht), saturated deionised/produced water (SDW/SPW), and heated saturated deionised/produced water (SDWht/SPWht) were prepared to investigate the presence of water history, and to differentiate between water with and without hydrate history (Table 5.1). The main idea was to test if the hydrate water and hydrate water heated to remove memory have different freezing statistics. Deionised water was initially used for pure experiments to depict the memory phenomenon and to analyse it in uncontaminated conditions. The produced water tests were designed to understand if the measurable phenomenon retain in the real industrial fluid.

Table 5.1 Types of samples prepared to investigate the memory phenomenon

Sample type	Abbreviation	Features
Hydrate deionised water	HDW	Hydrates formed and dissociated in deionised water. Retain hydrate clusters causing the memory effects.
Hydrate produced water	HPW	Hydrates formed and dissociated in produced water. Retain hydrate clusters causing the memory effects.
Heated hydrate deionised water	HDWht	Hydrates formed and dissociated in deionised water. Heated to a temperature that no memory clusters can be retained.
Heated hydrate produced water	HPWht	Hydrates formed and dissociated in produced water. Heated to a temperature that no memory clusters can be retained.
Saturated deionised water	SDW	Hydrates were never formed in deionised water. Followed the cooling process somewhat similar to the samples which formed hydrates.
Saturated produced water	SPW	Hydrates were never formed in produced water. Followed the cooling process somewhat similar to the samples which formed hydrates.
Heated saturated deionised water	SDWht	Hydrates were never formed in deionised water. After cooling process heated to the same temperature used to remove memory.
Heated saturated produced water	SPWht	Hydrates were never formed in produced water. After cooling process heated to the same temperature used to remove memory.

Theoretically, since hydrate water has memory of hydrate formation, it should nucleate faster than saturated water which does not possess any hydrate memory. At the same time, saturated water and heated saturated water should have similar freezing statistics, because neither of them has a memory of phase transition.

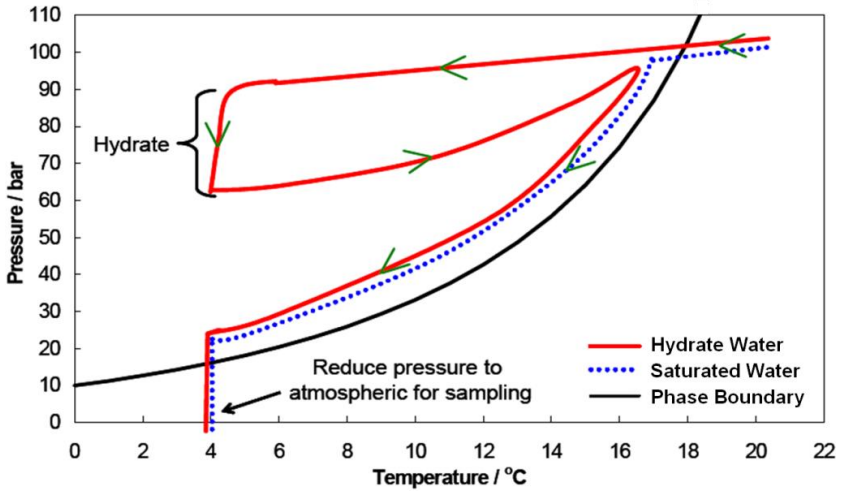

Figure 5.4 Preparation of hydrate water and saturated water samples along the paths inside the hydrate phase boundary

The HDW/HPW sample was prepared by charging approximately 250 ml of deionised/produced water into the kinetic rig at 20 ^{o}C. The kinetic rig was pressurised to 100 bar by injecting the natural gas. Water-natural gas system was directly cooled to about 4 ^{o}C to form hydrates. The hydrate formation was detected based on pressure drop. Following gas hydrate formation, the hydrate was dissociated by the thermobaric path indicated schematically in Figure 5.4. The system temperature and pressure were reduced stepwise along the paths inside the hydrate phase boundary. The system was released to atmospheric pressure at 4 ^{o}C prior to sampling. About 50 ml of the water sample was used for series of the onset of freezing point measurements.

The HDWht/HPWht sample was prepared by heating up about 50 ml of the HDW/HPW sample to ~60 ^{o}C (temperature was measured after sample taken from microwave) in the microwave for 1 minute to remove water memory.

The SDW/SPW sample was used to study the effect of gas solubility on water history. It was prepared in the high-pressure rig by saturating deionised/produced water with the natural gas at 100 bar and 20 ^{o}C (just inside the hydrate phase boundary but no hydrate formation) for several hours. Similarly, the system temperature and pressure were reduced stepwise along a path just inside the hydrate phase boundary. The system was released to atmospheric pressure at 4 ^{o}C for sampling. About 50 ml of the water sample was used for the measurements.

The SDWht/SPWht sample was prepared by heating up about 50 ml of the SDW/SPW sample in the microwave for 1 minute. Then sample was taken at 4 ^{o}C for the onset of freezing point measurements.

All water samples were kept at constant temperature of 4 ^{o}C in the bath and atmospheric pressure. The onset of ice formation from various types of water samples was determined using the freezing point apparatus. The temperature of the system was reduced from 4 ^{o}C to -17 ^{o}C at a constant rate of 0.2 ^{o}C/min. The onset of ice formation was identified based on a rise in sample temperature as the latent heat of ice formation was released which is shown schematically in Chapter 4 Figure 4.11. The onset temperature and corresponding induction time were recorded as the point at which ice started crystallizing. Trapezoidal numerical integration was used to calculate divergence area between probe and bath temperatures which is proportional to the amount of heat release during crystallization. Due to stochastic nature of ice nucleation,

a set of experimental data were gathered to determine the distribution of onset of ice formation for these water samples.

5.2.2 Nucleation Probability Distribution

The number of nuclei forming in a supersaturated medium within a given time interval is a random quantity. The kinetics theory of nucleation considers the average number of nuclei and relates it to the macroscopic parameters and properties of the system including time (Toschev et al., 1972). Investigating the stochastic nature of CO_2 hydrate nucleation, it was reported that the nucleation rates significantly increased when the water had previously frozen as ice and melted (freezing-memory effect), except when the meltwater was heated to 298 K before nucleation. The nucleation rates also increased with O_2-saturated meltwater, but decreased with degassed water. These experimental results were explained by: 1) the meltwater contains longlived metastable water clusters encaging O_2 molecule that were transferred from the ice; or 2) a clathrate-like structure remains in solution with a long lifetime after ice melts (Takeya et al., 2000). Performing statistical study of hydrate nucleation in a water/CH_3CCl_2F system with prior hydrate formation/dissociation, it was concluded that the rate of nucleation was dependant on the thermal history of the system (Ohmura et al., 2003).

Based on the nucleation theory, the nucleation probability distribution P(t) can be expressed by a nucleation rate J (s^{-1}) in a given volume of liquid as:

$$P(t) = 1 - e^{-J(t-\tau_0)} \qquad 5.1$$

where τ_0 is the onset time of nucleation in seconds (i.e. the shortest induction time for the measurements using the same sample).

The nucleation probability distribution for each water samples was obtained by repeating measurement of induction time 12 times under the same experimental conditions. The measurement was done using a fresh sample each time. The nucleation probability distribution $P(t)$ that nucleation occurred on or before time t_m (i.e., the m^{th} shortest induction time among 12 measurements) is given by $P(t_m) = \frac{\mathrm{m}}{12}$. The nucleation probability distribution for various water samples was plotted against time. The nucleation rates J and the onset time of nucleation τ_0 were determined by best-fit to the equation (5.1) with the observed nucleation probability distributions for various types of aqueous samples.

5.2.3 Results and Discussion

5.2.3.1 Investigation with Applied Nucleation Theory

In this section 5.2.3.1 of Chapter 5, experimental and analytical work was performed together with another PhD student Ms. Zahidah Zain who is gratefully acknowledged.

The nucleation rate was used as an indicator to distinguish the presence of hydrate water history. In the experiments, the onset of ice formation for water with hydrate history (HDW) and deionised water saturated with natural gas (SDW) at static condition were compared. Two different paths for samples preparation were studied: inside and outside hydrate phase boundary (Figure 5.5 and Figure 5.7 respectively). The result for the sample prepared inside phase boundary showed the water with hydrate history was freezing earlier due to the presence of remnant hydrate like water structure (Figure 5.6). Similar trend was observed for the sample path outside the hydrate phase boundary as shown in Figure 5.8. The nucleation rates for all measurements were tabulated in Table 5.2. The analysis validated that samples with hydrate formation history (i.e., water history) tend to freeze earlier and to nucleate faster than that without hydrate history regardless of the sample preparation paths inside (Figure 5.5) or outside the hydrate stability zone (Figure 5.7). In general, the distribution of onset of ice formation for both type of water was very distinct and had a potential to be further explored as a simple technique for early warning system.

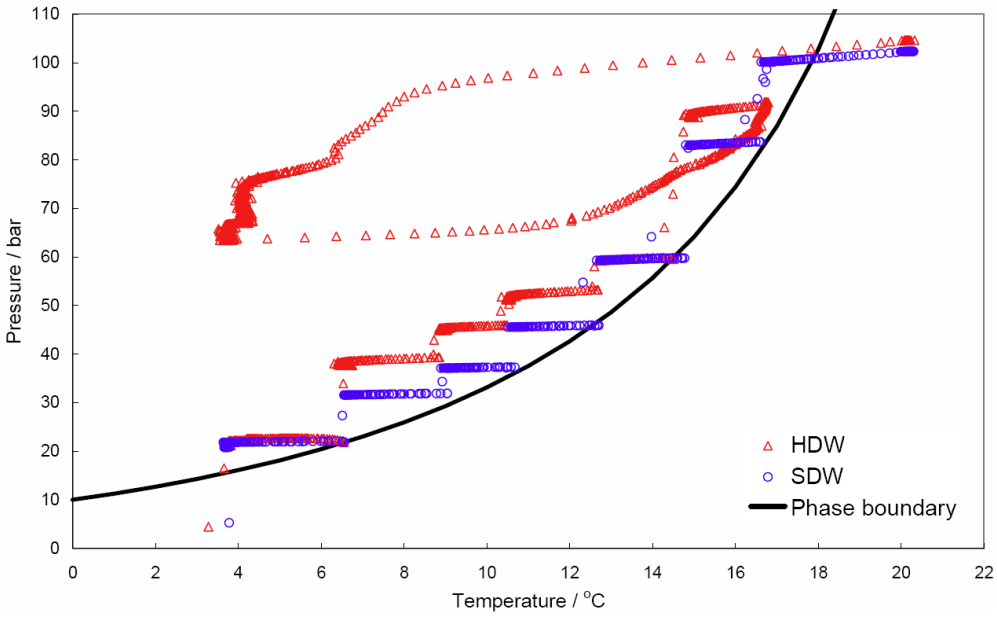

Figure 5.5 Sample preparation paths inside hydrate phase boundary

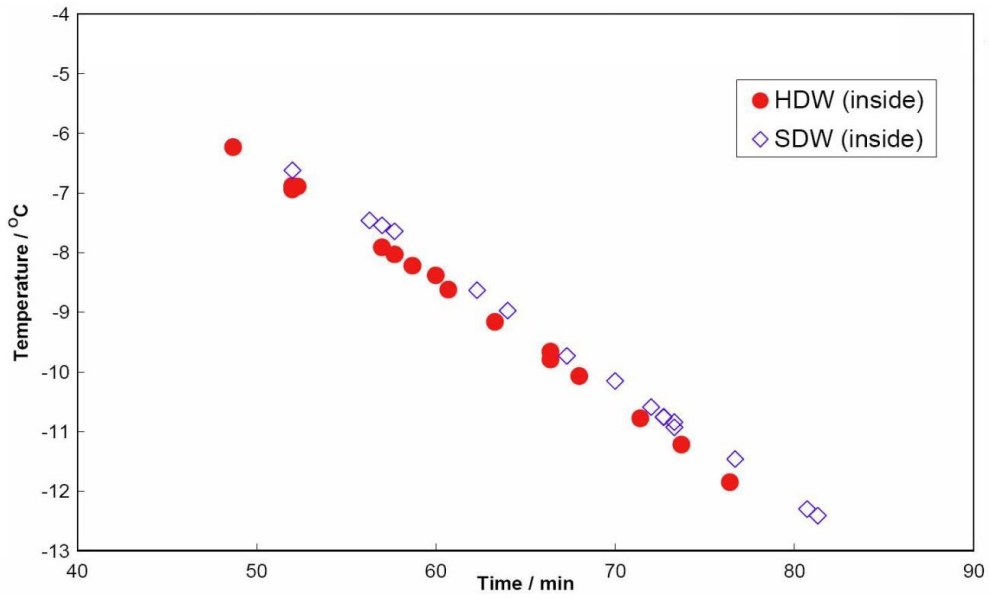

Figure 5.6 Onset of ice formation for sample preparation paths inside hydrate phase boundary

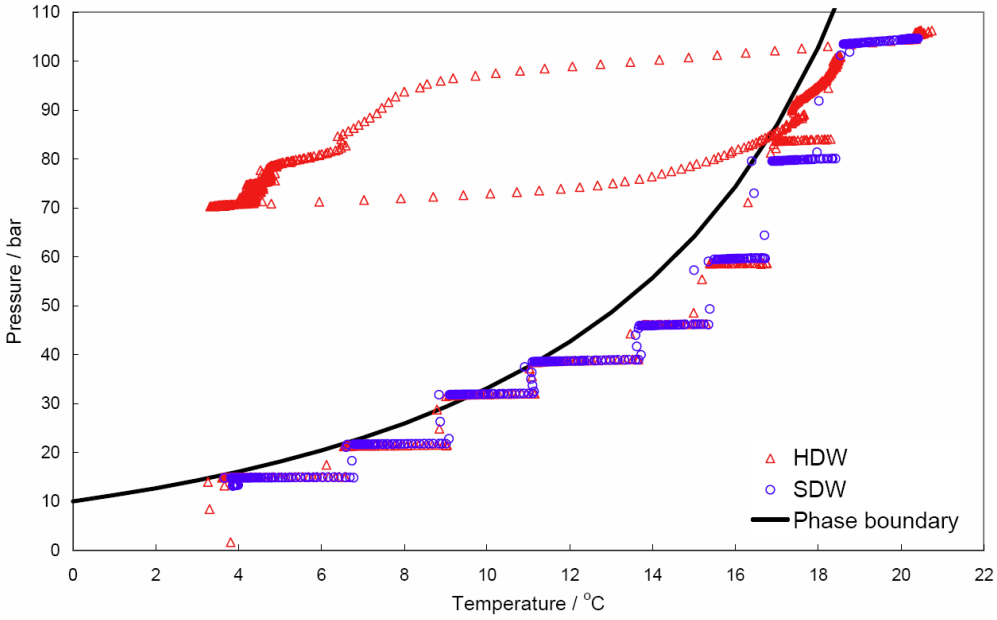

Figure 5.7 Sample preparation paths outside hydrate phase boundary

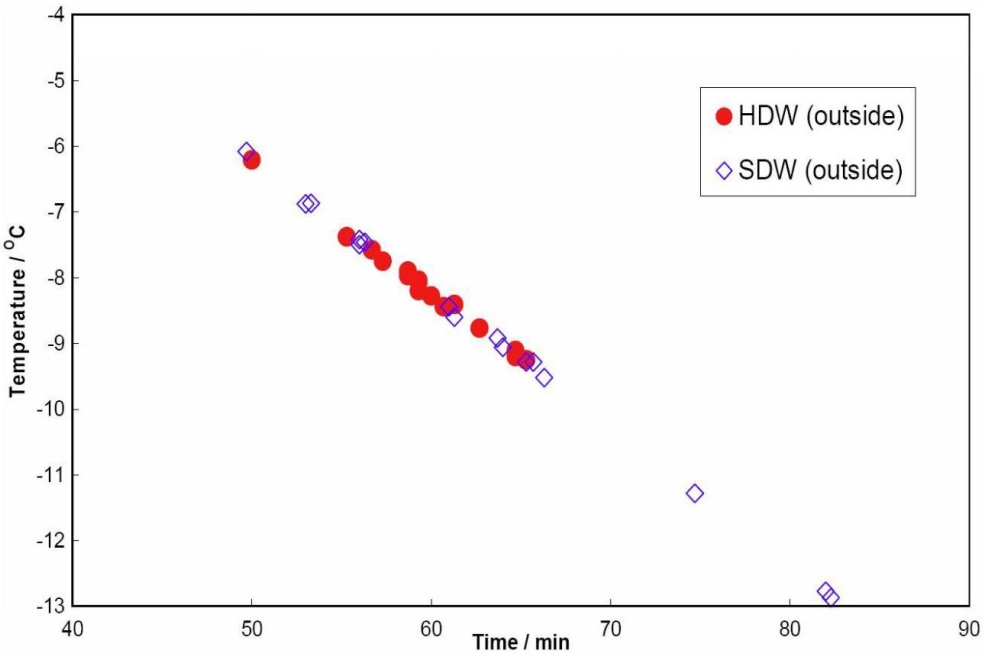

Figure 5.8 Onset of ice formation for sample preparation paths outside hydrate phase boundary

By preserving the hydrate memory within the water structure, there can be a considerable amount of natural gas micro bubbles or excessive gas molecules remaining in the aqueous phase. Sensitivity to dissolved gas was also investigated. The excess of dissolved gas was removed by vacuum pump. The prepared sample was vacuumed for an hour prior to any freezing measurements. As it can be seen from Table 5.2, the results suggested that removing dissolved gas could significantly eliminate the effect of water structure on ice nucleation, but the presence of hydrate history was still measurable based on the observed effect on ice nucleation rate.

Table 5.2 Nucleation rates for various water samples

Sample	J (x 10^{-2}) / min^{-1}	τ_0 / min	Error $\Sigma (P(t)_{exp.} - P(t)_{pred.})^2$
HDW (inside)	8.60	47.1	0.013
SDW (inside)	6.98	52.0	0.055
HDW (outside)	19.48	49.8	0.014
SDW (outside)	8.75	48.1	0.015
HDW (inside)*	12.40	63.0	0.023
SDW (outside)#	9.62	49.5	0.008
HDWV	10.88	52.5	0.058
SDWV	9.16	48.2	0.056

*Note: * depressurised to atmospheric pressure to dissociate hydrate at 4 °C*
 # depressurised and reduced temperature with limited steps to reach 4 °C

5.2.3.2 Investigation with Applied Statistical Analysis

These experiments were performed using 20 probes set-up. Freezing of deionised water samples was investigated by means of classical nucleation theory and advanced statistics. The nucleation rate was determined by best-fitted curve to the relevant experimental data using the nucleation probability distribution equation (5.1). Divergence area related to latent heat was also used for differentiation of samples. To calculate divergence area between probe and bath temperatures, the trapezoidal numerical integration program written in Matlab language was used (Appendix D). To distinguish between water with and without hydrate memory, three statistical tests were applied to freezing points and divergence areas obtained in the tests: t-test (Student test) which gives the probability that means of two data sets are equal; f-test (Fisher test) which gives the probability that variance of two data sets are equal; ks-test (Kolmogorov-Smirnov test) which gives the probability that the distribution of two data sets are equal. Microwave was used for removing hydrate memory. Applied statistical tests were also calculated in the Matlab mathematical environment (Appendix D). The mean freezing point, the mean divergence area, nucleation rates, and t-, f- , ks- tests for all samples measured in this study are summarised and tabulated in Table 5.3.

Table 5.3 Mean freezing temperatures, divergence area, nucleation rates and t-, f-, ks-tests for 4 tests on deionised water

Test	Water	Mean		J ($*10^{-2}$)	Tests for FP			Tests for Integral		
		FP, ^{o}C	Area, ^{o}C*min	/min^{-1}	T	F	KS	T	F	KS
4	HDW	-12.08	14.52	20.8	0.10	0.34	0.12	0.49	0.94	0.96
	HDWht	-10.43	13.93	21.9						
	SDW	-11.46	13.49	17.0	0.12	0.73	0.12	0.85	0.90	1.00
	SDWht	-12.80	13.30	18.2						
3	HDW	-11.48	14.63	24.9	0.08	0.17	0.46	0.89	0.53	0.96
	HDWht	-12.64	14.74	59.2						
	SDW	-10.92	11.28	30.6	0.91	0.69	0.96	0.01	0.22	0.12
	SDWht	-10.84	12.80	35.8						
2	HDW	-10.62	13.00	37.4	0.34	0.87	0.46	0.28	0.78	0.74
	HDWht	-11.28	12.33	32.9						
1	HDW	-9.96	11.21	28.0	0.54	0.56	0.25	0.12	0.36	0.46
	HDWht	-10.47	11.95	42.4						

The initial expectation was that statistical tests for water with hydrate formation history (HDW) and HDW with memory removed by heating the sample in a microwave oven (HDWht) should have given lower values than that for saturated water which followed the same path as HDW but without hydrate formation history (SDW) and SDW with memory removed by heating in a microwave oven (SDWht). However, it was noted

that the difference was negligible in the 4th test. Another noticeable element was that nucleation rate was expected to be higher for HDW comparing to SDW, whereas, in Test 3, it was opposite.

There can be two reasons to explain the results above. As the treatment in the microwave oven was originally used as a new approach to remove hydrate memory, it could potentially cause overheating of the water samples or impact water physical properties by exposure to electromagnetic radiation. Another explanation could be attributed to the stochastic nature of ice crystallisation process which was depicted by standard deviation parameter in Table 5.5. Due to the presence of strong stochastic element of ice crystallisation, it takes considerable time to build meaningful freezing statistics used to distinguish water samples. That was the main reason to pay more attention to the alternative method described in Chapter 6.

5.2.3.3 Trends Observed in Produced Water

BP produced water

The HPW and SPW samples preparation actually followed the path shown in Figure 5.9. The measurements on all samples were repeated 12 times to establish the statistical distribution of onset of ice formation/nucleation. The distribution of temperature for onset of ice formation is plotted against time for all measured points as shown in Figure 5.10 (a). These data were converted to the probability of nucleation in a time interval of 1 minute. The nucleation rate was determined by best-fitted curve to the relevant experimental data using the nucleation probability distribution equation (5.1), as shown in Figure 5.10 (b). The nucleation rate and the mean freezing temperature were used as an indicator for determining the presence of hydrate water history. A similar step was taken for the measurements on TOTAL produced water. In Figure 5.10 b, one can note that equation 5.1 does not fit very well the experimental data. This can be explained by the fact that the nucleation probability equation was developed for the static temperature/subcooling conditions in which the induction time is the primary parameter indicating the nucleation. During these experiments, because of the continuous cooling imposed on the sample, the driving force for ice crystallization continuously increases. The uncertainty on the J values determined from the fit is probably high enough not to allow a valuable comparison of the systems and to draw definite conclusions based on nucleation rate only. Therefore, statistical analysis accompanied statements in this Chapter.

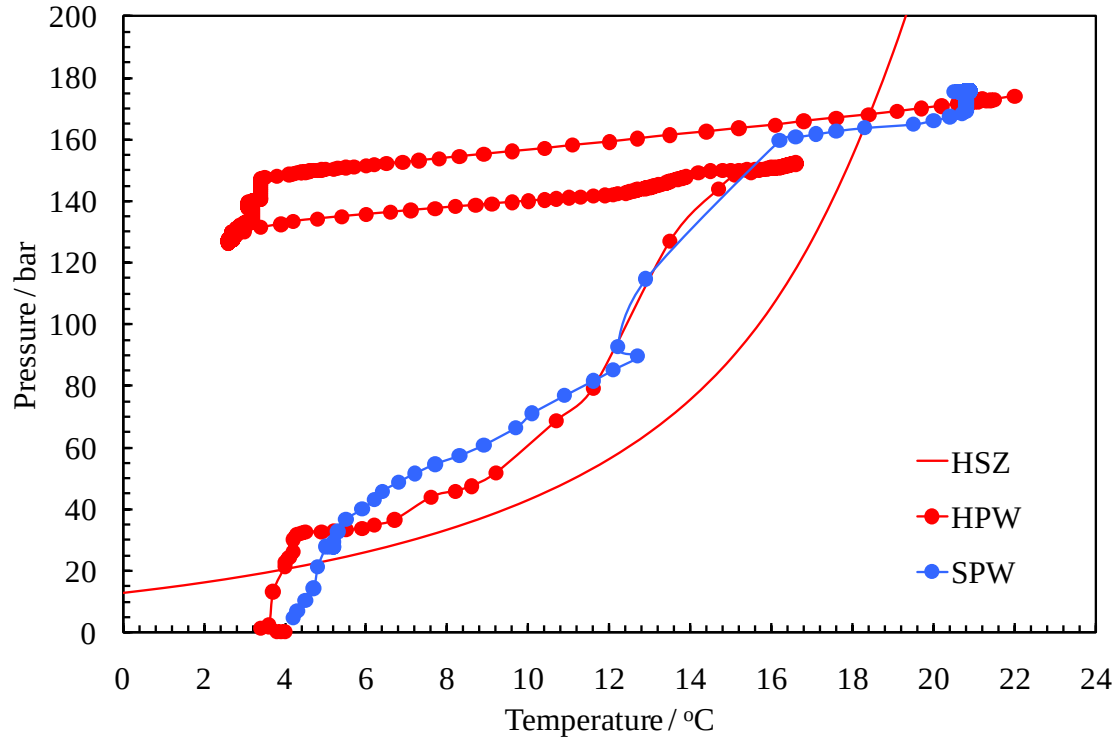

Figure 5.9 Sample preparation path for BP produced water

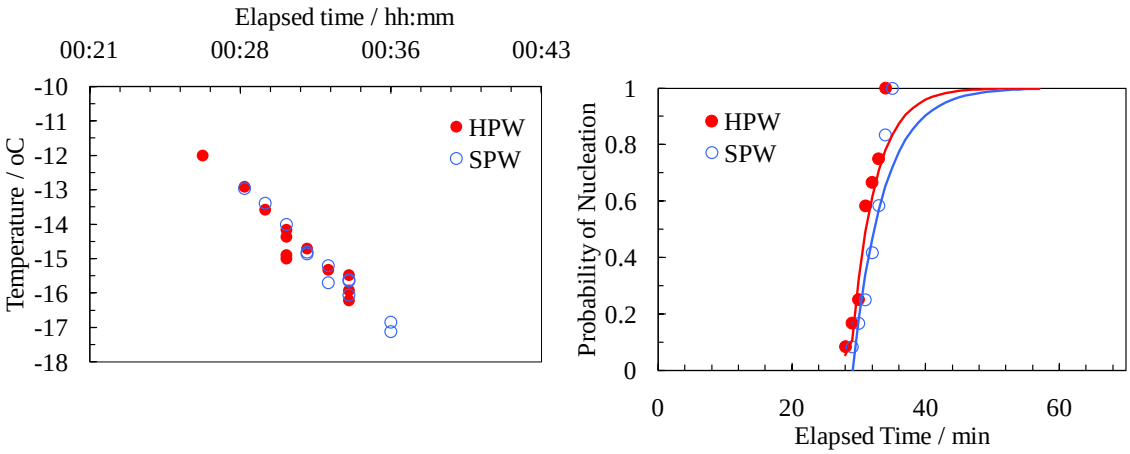

(a) Distribution of Onset Ice formation (b) Probability of ice nucleation

Figure 5.10 Onset of ice formations for BP produced water

The result for this case shows that the ice nucleation for HPW distributed within 27 – 34 minutes (Figure 5.10 (b)). However, the distribution for SPW appeared to be more scattered with the highest density within 29-36 minutes. The ice nucleation rate for HPW was higher than that for SPW (Table 5.4 and Figure 5.10 (b)), suggesting that the samples with water history nucleate faster due to the presence of remnant water structure created by prior hydrate formation.

Table 5.4 Freezing points and nucleation rates for BP produced water samples

Sample	Average of Freezing point, °C	STD of Freezing point, °C	J (x10^{-2}) /min^{-1}	τ_0 /min	Sum Squared Error
HPW	-14.5	1.3	28	28.1	0.045
SPW	-15.2	1.3	21	28.5	0.084

TOTAL produced water

The samples preparation path and the hydrate phase boundary for TOTAL produced water are shown in Figure 5.11. As it was indicated, TOTAL produced water contained 23 mass% Methanol and 3 mass% salt which inhibited hydrate formation and shifted phase boundary to the lower temperatures. Therefore, HPW path was designed to reach target -12.5 °C to promote hydrate formation. As it can be seen in Figure 5.12 (a), the distribution of ice nucleation for the HPW was clustered within 51 – 75 minutes indicating higher scattering of data comparing to tests with BP water. For the SPW, the distribution was within 55 – 71 minutes. The ice nucleation rate was higher for HPW than that for the SPW (Table 5.5 and Figure 5.12 (b)) implying the hydrate water history does have a noticeable effect on the ice nucleation.

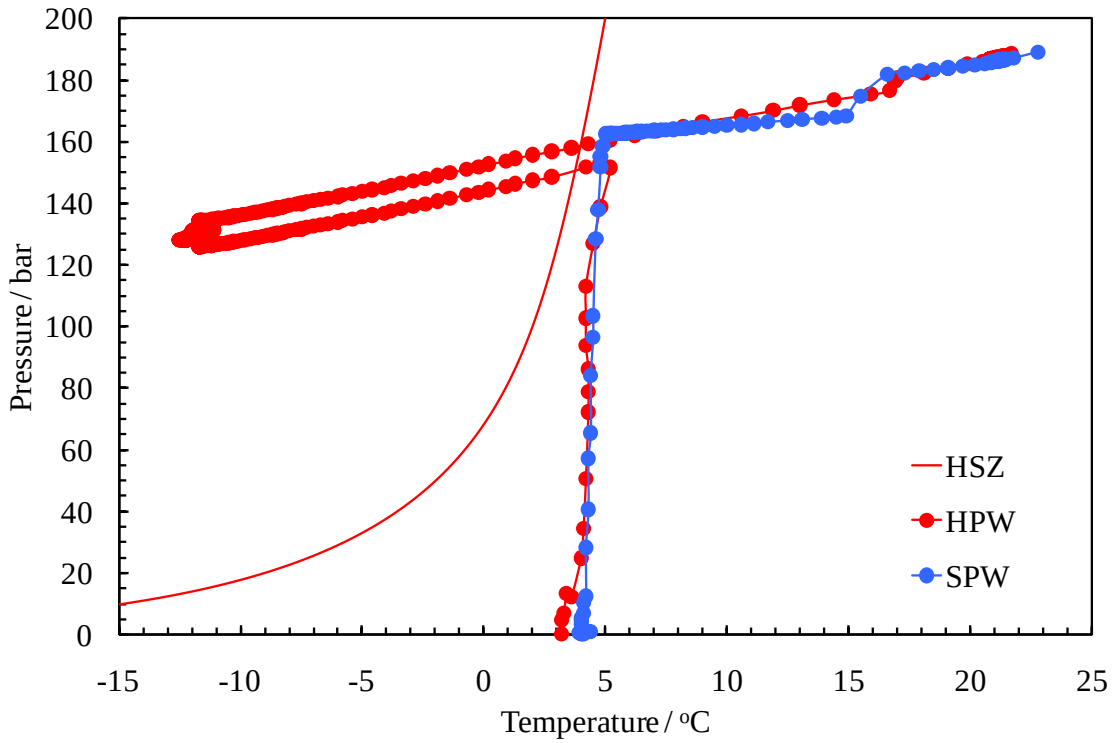

Figure 5.11 Sample preparation path for TOTAL produced water

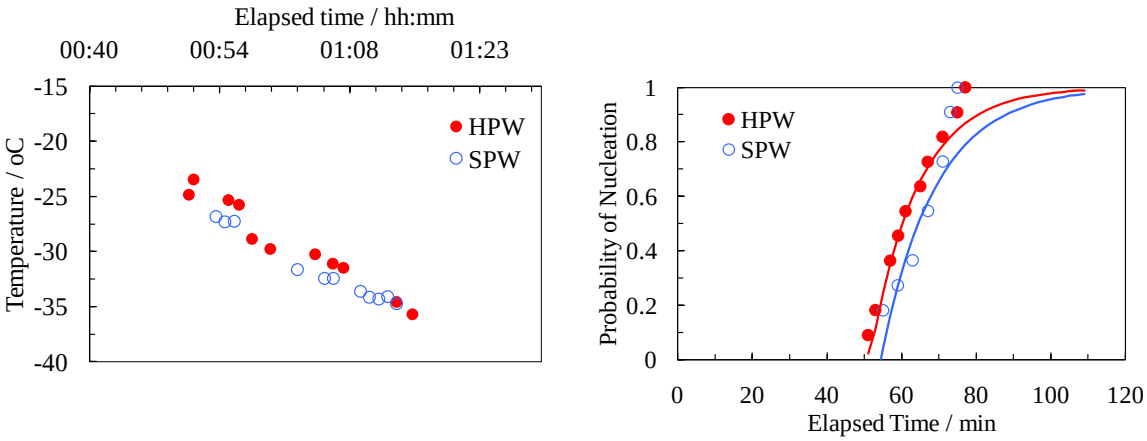

(a) Distribution of Onset Ice formation

(b) Probability of ice nucleation

Figure 5.12 Onset of ice formations for TOTAL produced water

Table 5.5 Freezing points and nucleation rates for TOTAL produced water samples

Sample	Average of Freezing point, ^{o}C	STD of Freezing point, ^{o}C	J (x10^{-2}) /min^{-1}	τ_0 /min	Sum Squared Error
HPW	-29.2	4.0	7.9	50.4	0.011
SPW	-31.7	3.1	6.8	53.4	0.056

The results on both produced water samples implied that the samples with hydrate water history tend to freeze earlier and to nucleate faster than those without hydrate water history. These results suggested the effectiveness of the onset of ice formation technique for the produced water. However, due to time requirement for gathering statistical data it does not seem to be a practical technique for field application.

5.3 CONCLUSIONS

In surface facilities, produced gas normally coexists with water creating a risk of hydrate formation and blockage. In a typical flow assurance problem where the hydrate can potentially crystallize due to favourable pressure-temperature conditions, the main question remains to be whether it has started to form or phases can further flow under existing steady state. In this Chapter, the technique based on water memory was studied to answer this question as part of early warning systems.

After hydrate dissociation, it is believed that there can still be some kind of water molecular structure remaining in liquid phase which causes the memory effect. As this effect appears after crystal generation and disintegration, the hypothesis was argued that it can be reflected in the ice formation. In this Chapter, the onset of ice formation method was investigated to depict the presence of memory in aqueous phase.

The effect of different sample preparation paths on water history was investigated. Generally, the results suggest that aqueous samples with hydrate formation history tend to freeze earlier and to nucleate faster than that without hydrate history regardless of the sample preparation paths are inside or outside the hydrate stability zone. The role of dissolved gas in the sustainability of water structure was studied by removing excess dissolved gas. The results suggest that removing dissolved gas could significantly eliminate the effect of water structure on ice nucleation, but the presence of hydrate history is still measurable based on the observed effect on ice nucleation rate.

The onset of ice formation technique for detecting hydrate water history was tested using the produced water samples supplied by BP and Total. The nucleation probability distribution based on classical nucleation theory was applied to describe the stochastic nature of the nucleation data. The results on both produced water samples imply that the samples with hydrate water history tend to freeze earlier and to nucleate faster than those without hydrate water history. These result confirmed the effectiveness of the onset of ice formation technique for the produced water.

In general, the results suggest that changes in water structure due to hydrate formation could be detected using freezing method. The element of stochasticity/randomness in the measured data cannot be negligible, as it was shown with three statistical tests and the nucleation probability distribution based on classical nucleation theory. To develop this technique further, it can be beneficial to introduce procedures and experimental framework in order to have better control over the freezing statistical parameters. However, this technique due to a time requirement to generate necessary statistical data cannot be recommended for field application.

CHAPTER 6 ONSET OF HYDRATE FORMATION

6.1 INTRODUCTION

As it was shown in the previous Chapter, the onset of ice formation method can be a challenge to develop further as a hydrate early warning techniques due to stochastic nature of ice crystallization. To provide signals of initial hydrate formation in the pipeline and/or processing facilities, alternative method is suggested. The method presented in this Chapter is based on subcooling temperature measurements of fluid samples which are then used to determine whether the initial hydrate formation took place in the system. The signals are designed to give the operator adequate time to initiate remedial steps prior to massive hydrate formation/build up which could result in pipeline/facilities blockage.

The technique principle states that hydrate forms easier from a solution which experienced hydrate formation than from a fresh solution. This has been explained by the hydrate water memory effect, which has gained researchers' interest over the past decade. The effect and its mechanism have been considered and discussed from various aspects (Lederhos et al., 1996; Parent et al., 1996; Bylov et al., 1997; Ohmura et al., 2000; Roger et al., 2000; Takeya et al., 2000; Ohmura et al, 2003; Zain et al., 2005; Thompson et al., 2006; Zeng et al., 2006). The onset of gas hydrate formation of water with hydrate memory was found to be much less stochastic (Ohmura et al., 2003). Recently, the heterogeneous nucleation of THF water mixtures was statistically studied using an automatic lag-time apparatus which possessed the capability to crystallize and melt samples 300 times in succession. From the obtained "survival curves", the authors concluded that the freezing point temperature could be fairly good probabilistic parameter (Wilson et al., 2005). Another recent research work showed better repeatability of KHI tests using re-cooling of samples (Villanoa et al., 2011).

The approach has been proposed to identify hydrate history by measuring the required subcooling/induction time for the aqueous sample under examination. As a result of investigations, it was found that the measurements of subcooling temperature of hydrate formation can serve as a reliable technique for detection of hydrate water memory. However, there can be challenges in applying the technique in field conditions.

Investigations of this technique were conducted for a number of aqueous solutions containing alcohol (methanol or ethylene glycol) and salt (sodium chloride), and for produced water system. Effect of temperature and time, effect of depressurisation and effect of mixing were studied. In the apparatus side of the technique, two mini-rig designs were tested: tall-narrow, and short-wide. The short and wide design showed better applicability for onset of hydrate formation method.

6.2 EXPERIMENTAL SET-UP AND PROCEDURES

6.2.1 Experimental Set-up

To investigate the memory effect, the onset temperatures of hydrate formation for indicated aqueous solutions were measured in a high pressure kinetic rig (Figure 6.1).

The phase equilibrium was achieved in a cylindrical cell made of hastelloy, the cell volume was ~80 ml and it could be operated up to 400 bar between -40 and 100 ^{o}C. The cell was immersed in a constant–temperature liquid bath that controls and maintains the desired temperature. In order to perform accurate temperature measurements of the tested sample, platinum resistance thermometer (PTR) was used to directly take readings inside the cell with an accuracy of ± 0.05 ^{o}C. Pressure was measured by means of a Druck pressure transducer. The pressure transducer was calibrated against a dead weight pressure tester which provided measurement accuracy of ± 0.1 bar in 2 to 400 bar range. To achieve a fast thermodynamic equilibrium and to provide a good mixing of the fluids, a stirrer driven by a magnetic motor was used to agitate the test sample.

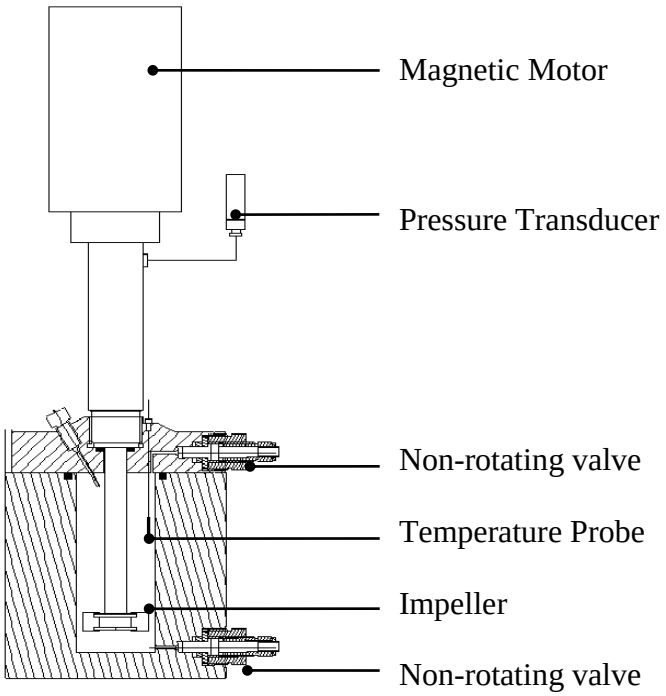

Figure 6.1 Schematic diagram of the high pressure hydrate kinetic rig

6.2.2 Materials

Fluid samples used in the experiments were deionised water, methanol of 99.9% certified purity (Aldrich), Ethylene glycol and n-propanol (99.0%, supplied by Alf Aesar) and sodium chloride of 99 mol% certified purity (Aldrich). Produced water was provided by one of the project sponsors (BP) and contains 5 mass% of unknown salts/solids. Natural gas composition is provided in Table 2.1.

6.2.3 Procedures

The experimental procedures consist of several steps. Prior to the tests the equilibrium cell was cleaned and evacuated. The sample of aqueous liquid solution was loaded into the cell and then natural gas was injected into the cell to achieve the desired starting pressure (100 bar). Once the cell had been charged with the desired components the mixing was started and the temperature lowered 14 ^{o}C inside the hydrate stability zone (HSZ) at constant 500 rpm and at 0.2 ^{o}C/min cooling rate. The subcooling temperature at which hydrate started to form was measured. The system was then left for 4 hours at 18 ^{o}C subcooling to make sure sufficient amount of hydrates had formed. Then hydrates were dissociated by heating up the cell to 2, 7, 12, 17, 22 and 32 ^{o}C outside the hydrate stability zone and left for either 1 or 12 hours to study time-temperature effect.

The system was then cooled the second time down to 14 ^{o}C subcooling at the same cooling rate to form hydrates again. The subcooling temperature at which hydrates started to form was measured and compared to the initial one. The heating/cooling cycles were repeated several times to test the repeatability of the measurements and to investigate the effect of heating to different temperatures and times on the memory detection. In particular, the cycle for initial hydrate formation measurement was repeated three times. Cycles which were designed to test the memory effect (after the initial formation) were repeated two times.

6.2.4 Definitions

Figure 6.2 illustrates the main definitions used throughout this chapter. Subcooling temperature is the difference between the current point inside HSZ and the projection of that point on HSZ curve at a given pressure. The subcooling is a representation the driving force for the hydrate formation in a system. Temperature outside HSZ means the difference between the current point outside HSZ and its projection to HSZ curve at a given pressure. It therefore represents the driving force for the formed hydrate to dissociate.

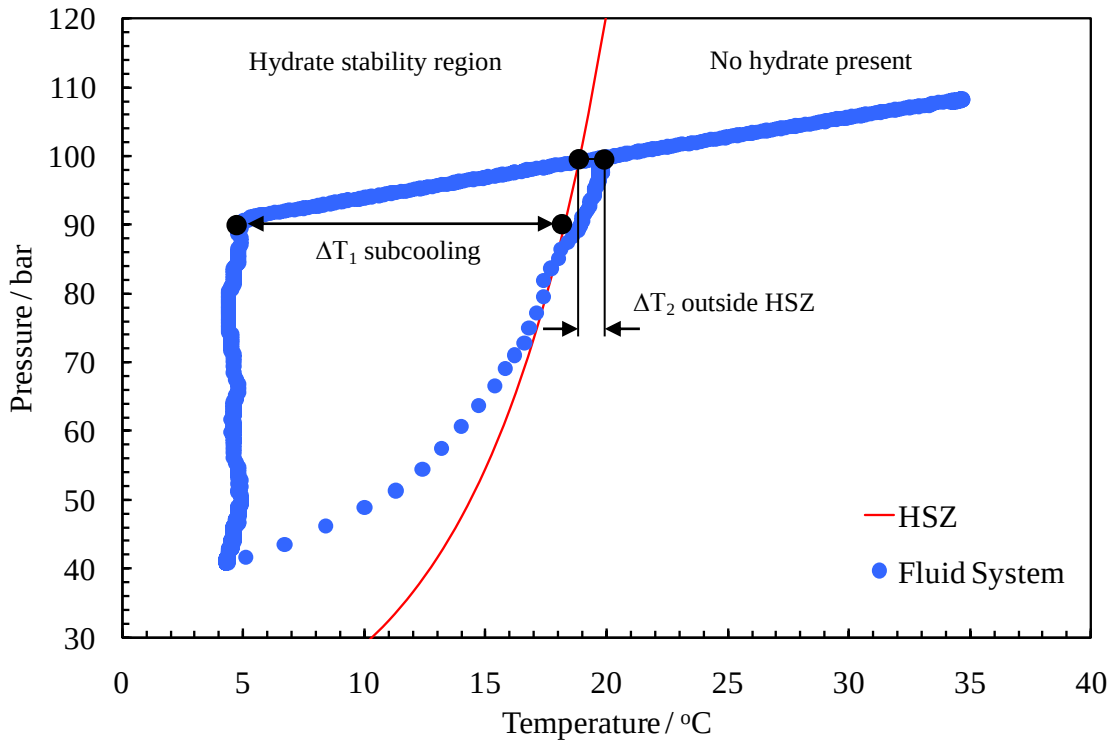

Figure 6.2 Pressure-Temperature diagram for a typical gas hydrate (Natural gas and water) to illustrate main definitions used throughout Chapter 6

6.3 RESULTS

The water memory phenomenon was investigated for aqueous solutions containing various percentages of alcohol and/or salt. Samples were prepared as explained in section 6.2.3 above.

6.3.1 Natural Gas - Deionised Water Systems

The investigated fluid system was distilled water and natural gas at initial conditions of 100 bar and 20 ^{o}C.

6.3.1.1 Effect of Temperature and Time

Several cooling/heating cycles were repeated to investigate the hydrate water memory effect. Typical results are presented in Figure 6.3 where the system pressure is plotted against system temperature. The hydrate stability zone is also presented to give an indicator where the system is within or out of the hydrate stability region.

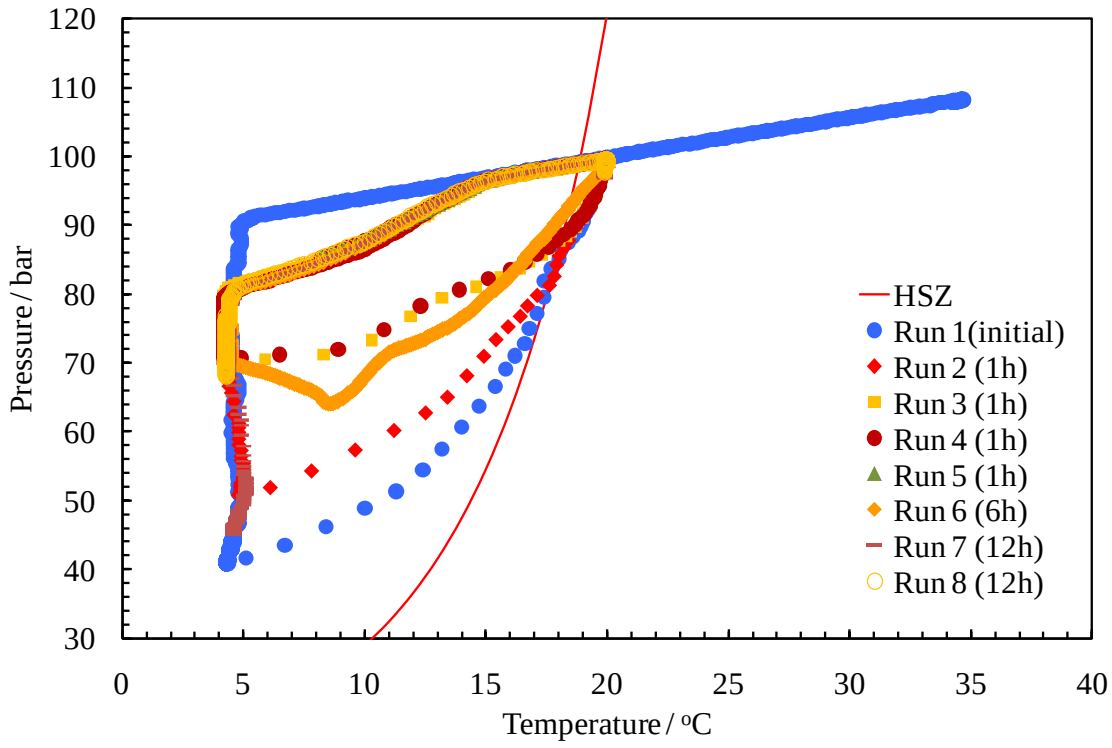

Figure 6.3 Cooling/heating cycles repeated for the distilled water-natural gas system

As seen in Figure 6.3, initial hydrate formation (blue line) appeared at 12.3 ^{o}C subcooling, and system was then left at 4 ^{o}C for 4 hours to form sufficient amount of hydrate. Then the cell was heated up to 20 ^{o}C (2 ^{o}C outside the hydrate stability zone)

and the hydrate was dissociating for 1 hour prior to the second time cooling to 4 ^{o}C at the same cooling rate (0.2 ^{o}C/min). The second time hydrate formation was initiated at 3.4 ^{o}C subcooling which is 8.8 ^{o}C lower than the initial formation. This result gave a clear indication of hydrate water memory. Experiments were repeated with heating to different temperatures and waiting for different time outside hydrate stability zone as summarized in Table 6.1. The obtained numbers were consistent and repeatable which gave a good confidence in the measurements. The memory effect disappears when the subcooling temperature becomes independent (flat line) on the heating temperature outside the hydrate stability zone. The memory disappears after heating to between 25 and 30 ^{o}C which is between 7 and 12 ^{o}C outside HSZ correspondingly. Another finding was that the subcooling of repeated hydrate formation was independent of the amount of hydrate formed at the cooling stage. In Figure 6.3, the pressure drop during hydrate formation is proportional to the mass of hydrate formed.

Table 6.1 Subcooling temperature of hydrate formation measured in the repeated cooling- heating cycles for distilled water-natural gas system

Dissociation temperature outside HSZ, °C	Subcooling (°C) observed after keeping the system at dissociation temperature for 1 and 12 hrs	
	1 hr	12 hrs
Initial formation	12.3	
2	3.4	3.4
7	10.2	10.1
12	11.7	10.1
17	10.4	
22	11.8	
32	12	

Results of experiments of heating to various temperatures and waiting for either 1 or 12 hours outside the hydrate stability zone are presented in Figure 6.4 where T_{sub} is the subcooling temperature of hydrate formation and T_{out} is the temperature of hydrate dissociation outside the hydrate stability zone (see section 6.2.4). As it can be seen from Figure 6.4, the memory effect is more dependent on the heating temperature rather than on the time of being outside the hydrate stability zone. Again, one can note that hydrate memory is not detectable after heating to around 10 ^{o}C outside HSZ (between 7 and 12 ^{o}C outside HSZ).

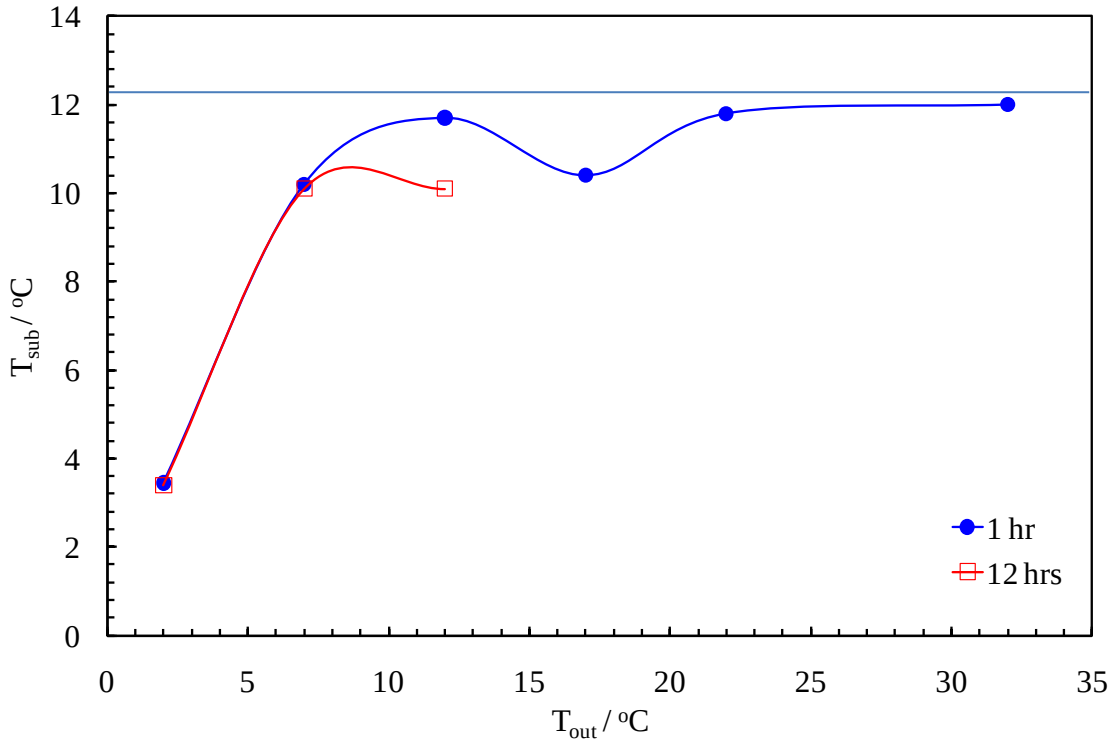

Figure 6.4 Evolution of subcooling temperature for distilled water-natural gas system

6.3.1.2 Effect of depressurisation

In these tests, after hydrate dissociation, the cell was depressurised to atmospheric conditions, and, then, charged to the initial pressure by injecting the same natural gas. The system was then cooled to 4 °C at 2 °C/min cooling rate to form hydrates again. Results summarised in Table 6.2 show that the effect of depressurisation did not influence the hydrate water memory for the system at 20 °C, since the subcooling of secondary hydrate formation was lower than that in initial cycle. Additionally, these tests modelled the industrial sampling from the production pipeline when the water is depressurised to atmospheric pressure and then transported to the laboratory for testing. However, the effect of time was not investigated here. It can be concluded that industrial type of sampling at certain temperature will not influence the representatively of the solution taken for the hydrate memory tests.

Table 6.2 Subcooling temperature of hydrate formation after heating to various temperatures in the depressurisation tests

Conditions	Subcooling, °C
Initial formation	12.3
Depressurised at 20 °C for 4 hours	7.7
Depressurised at 50 °C for 4 hours	12.3

6.3.1.3 Effect of Mixing

In these tests, no mixing was applied during cooling phase (2 ^{o}C/min rate) of the measurement cycles. To accelerate hydrate formation, mixing was switched on when the system reached the target temperature of 1 ^{o}C (above freezing point to prevent any ice crystallization). At the dissociation stage, the cylindrical cell was heated up with the mixing applied. The temperature imposed to dissociate hydrates was 20 ^{o}C. The heating-cooling cycle was repeated to see if the memory effect could be captured by the secondary hydrate formation. The results (Figure 6.5) showed that the hydrate memory remained in water after initial cycle was not strong enough to initiate early hydrate formation during secondary cooling phase. Therefore, the water memory can only be measured by hydrate formation in a well-mixed environment. The reason of this is that the mixing considerably increases the macroscopic interface between the two fluid phases (by creating a vortex for example), the diffusion of water and/or gas molecules across the interface (leading to an increased gas saturation in water), and the heat transfer of hydrate formation away from the interface. Moreover, when hydrate grows, mixing will further improve the exchange of water/gas molecules across the interface and already formed hydrate particles to maintain the phase contact area and to sustain further grow.

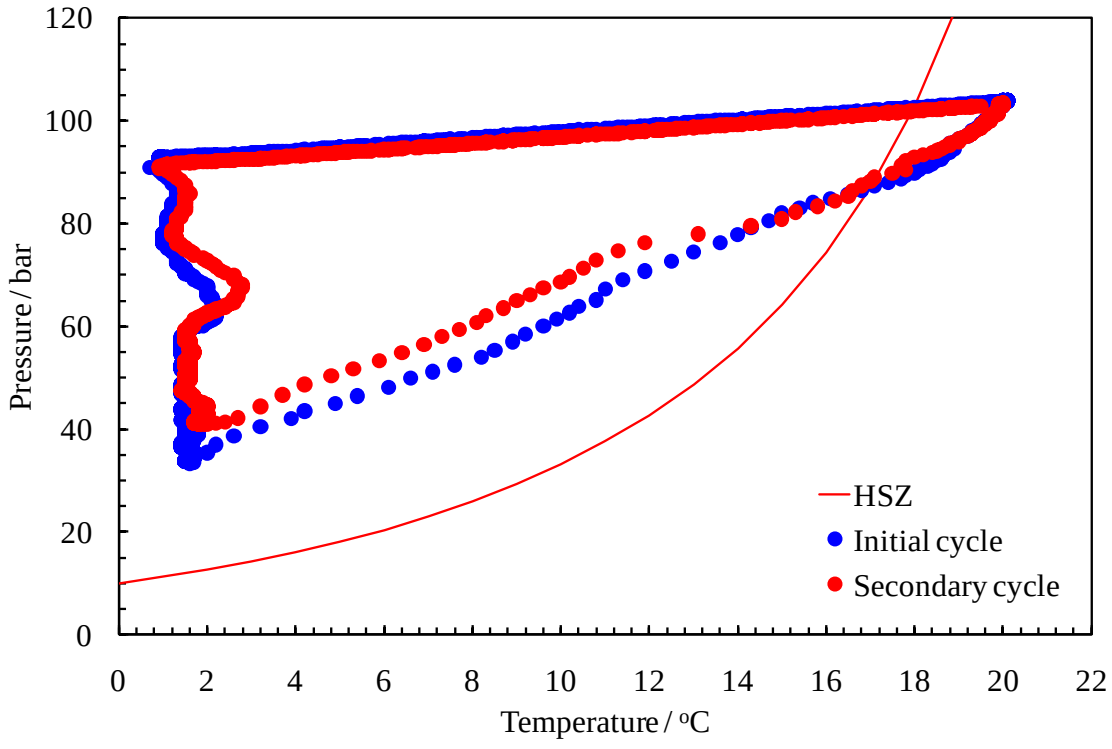

Figure 6.5 Initial and secondary hydrate formation without mixing

6.3.2 Natural Gas - Deionised Water Systems with 3 mass% Salt

To prepare the brine solution, 3 mass% of NaCl was added to distilled water. The same test procedure was conducted to investigate the heating temperature-time effect on hydrate water memory. The results are summarised in Table 6.3 and presented in Figure 6.6. The initial formation of gas hydrates appeared at 11.5 ^{o}C subcooling. The memory disappears between 35 and 40 ^{o}C (19 and 24 ^{o}C outside HSZ). The results show that the memory effect for water with salt was longer than that for pure water (Figure 6.4).

Table 6.3 Subcooling temperature of hydrate formation measured in the repeated cooling- heating cycles for 3 mass% aqueous NaCl solution

Dissociation temperature outside HSZ / °C	Subcooling / °C	
	1 hr	12 hrs
Initial formation	11.5	
3.8	4.5	6.5
8.7	6.4	9.1
13.9	6.1	9.3
18.9	6.7	8.2
23.9	10.4	9.7
29	9.7	12.0
33.9	12.8	14.6

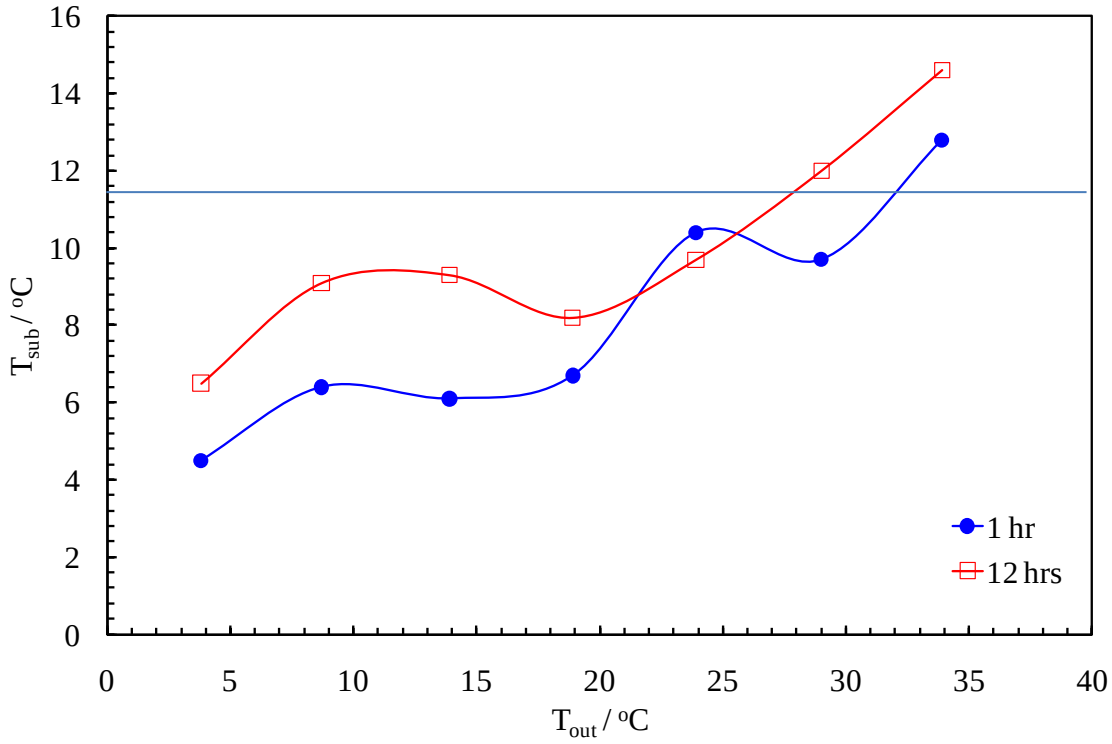

Figure 6.6 Evolution of subcooling temperature for 3 mass% aqueous NaCl solution

6.3.3 Natural Gas - Deionised Water Systems with 5 mass% Salt

For synthetic brine with 5 mass% of NaCl, the initial hydrate formation appeared at 12.7 ^{o}C subcooling. The results of tests are summarised in Table 6.4 and presented in Figure 6.7. The memory disappears between 22.6 and 27.4 ^{o}C (6.9 and 11.7 ^{o}C outside HSZ). The memory effect for water with salt seemed to be slightly longer than that for pure water (Figure 6.4).

Table 6.4 Subcooling temperature of hydrate formation measured in the repeated cooling- heating cycles for 5 mass% aqueous NaCl solution

Dissociation temperature outside HSZ / °C	Subcooling / °C	
	1 hr	12 hrs
Initial formation	12.7	
2	3.1	3.1
6.9	13.3	10.6
11.7	12.3	17.1
16.4	13.6	14.7
21.5	13.6	14.5

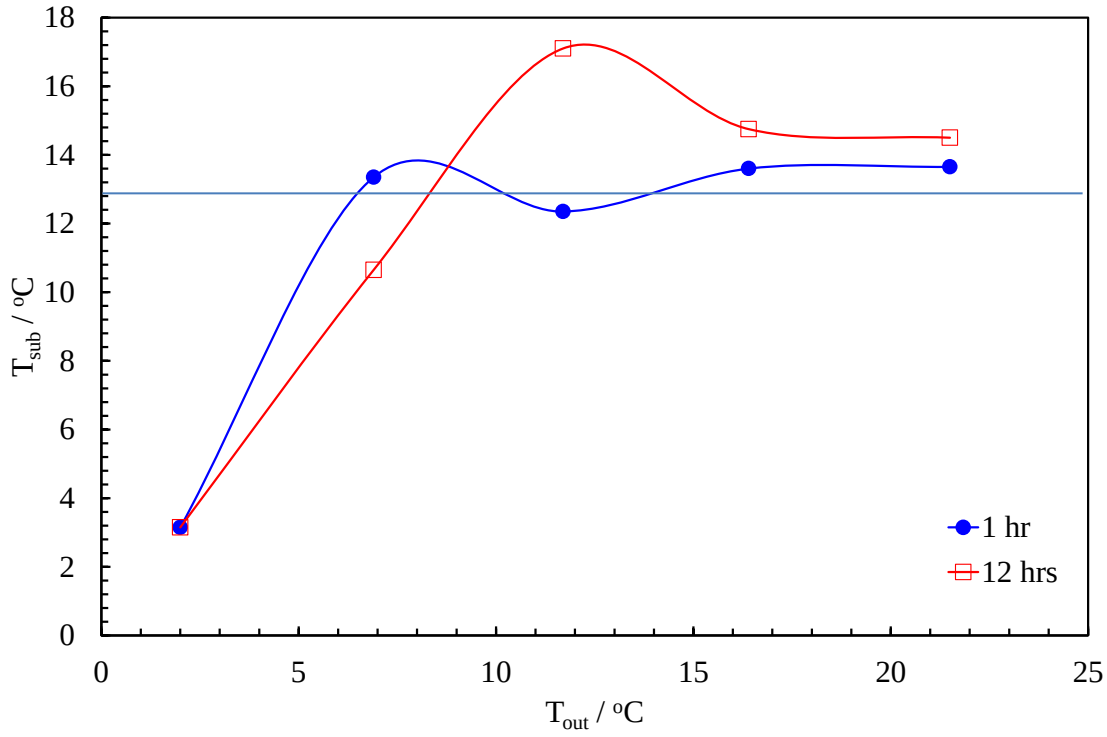

Figure 6.7 Evolution of subcooling temperature for 5 mass% aqueous NaCl solution

6.3.4 Natural Gas - Deionised Water Systems with 10 mass% Salt

For synthetic brine with 10 mass% of NaCl, the initial hydrate formation appeared at 14 ^{o}C subcooling. The results of tests are summarised in Table 6.5 and presented in Figure 6.8. The memory disappears right between 22.3 and 27.3 ^{o}C (7 to 12 ^{o}C outside the HSZ). The memory effect for water with high concentration of salt was slightly longer when compared with pure water tests (Figure 6.4), but shorter when compared with 3 mass% aqueous NaCl solution (Figure 6.6). It was therefore concluded that salt nonlinearly prolongs water memory. However, this finding lies within the uncertainty of measurements and is most likely apparatus dependent. Further experiments are required to refine the nonlinearity around 3 mass% with smaller concentration steps.

Table 6.5 Subcooling temperature of hydrate formation measured in the repeated cooling- heating cycles for 10 mass% aqueous NaCl solution

Dissociation temperature outside HSZ / °C	Subcooling / °C	
	1 hr	12 hrs
Initial formation	14	
2.2	1.7	4.2
7	6.9	11.1
12	15.5	14.4
16.8	14.4	14.6
21.8	14.1	

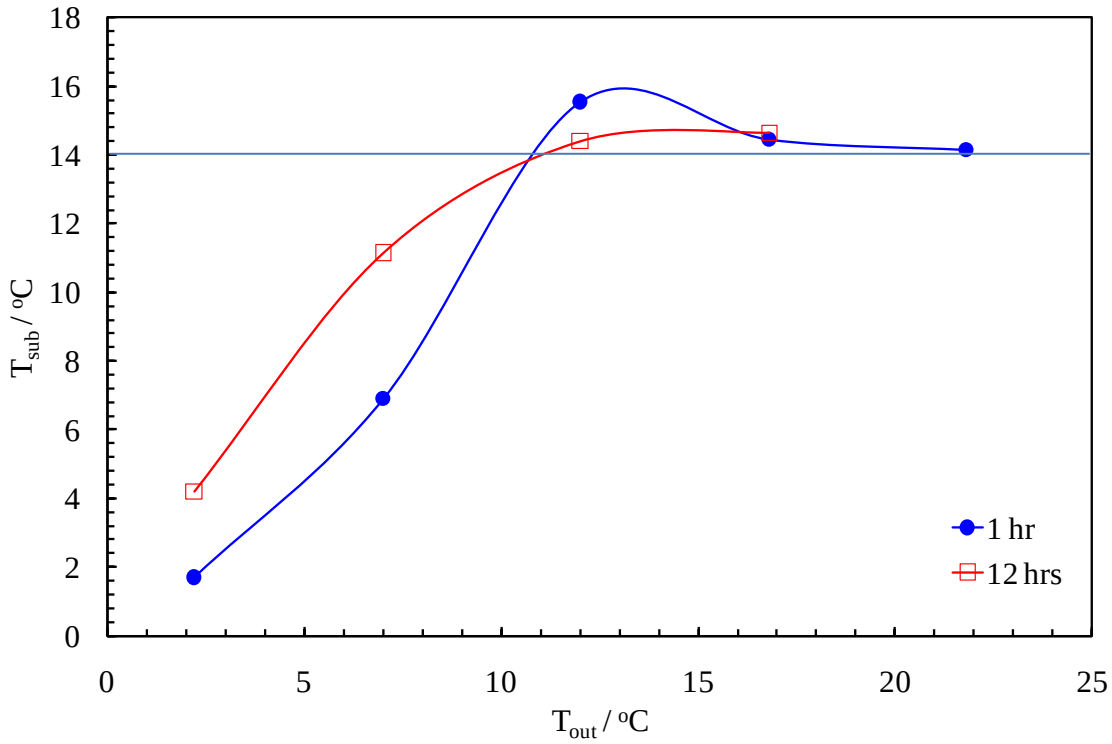

Figure 6.8 Evolution of subcooling temperature for 10 mass% aqueous NaCl solution

6.3.5 Natural Gas - Deionised Water Systems with 15 mass% Methanol

For the natural gas-deionised water systems with 15 mass% methanol, the initial hydrate formation occurred at 15.2 ^{o}C subcooling. The results (Table 6.6, Figure 6.9) implied that the memory effect for water with methanol is slightly shorter than that for deionised water (Figure 6.4). The memory disappears between 18 and 23 ^{o}C (7 and 12 ^{o}C outside HSZ).

Table 6.6 Subcooling temperature of hydrate formation measured in the repeated cooling- heating cycles for 15 mass% aqueous MeOH solution

Dissociation temperature outside HSZ / °C	Subcooling / °C	
	1 hr	12 hrs
Initial formation	15.2	
2.1	4.0	6.0
7.1	9.7	13.6
12.1	14.1	15.2
17.1	14.8	15.0
22.1	14.8	14.8
27.1	14.0	14.7

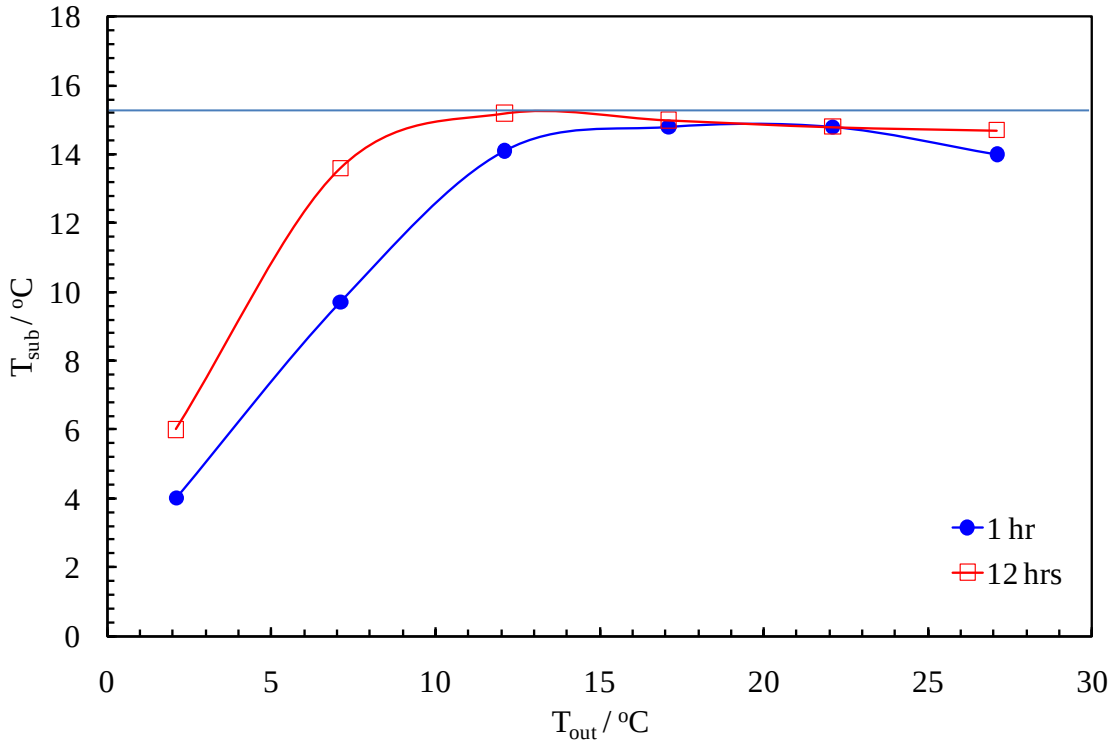

Figure 6.9 Evolution of subcooling temperature for 15 mass% aqueous MeOH solution

6.3.6 Natural Gas - Deionised Water Systems with 3 mass% Salt and 15 mass% Methanol

The initial hydrate formation occurred at 15.2 ^{o}C subcooling for the natural gas-deionised water systems in the presence of 15 mass% of MeOH and 3 mass% NaCl. The results of these tests are summarised in Table 6.7 and presented in Figure 6.10. As it can be seen, the memory effect for water with methanol and salt was longer than that for water with methanol alone (Figure 6.9). In the presence of salt, the memory could be detected up to 20 ^{o}C (i.e. 12 ^{o}C outside the HSZ), since 1.5 ^{o}C difference in subcooling temperature was still observed. It could therefore be again concluded that salt can extend the water memory.

Table 6.7 Subcooling temperature of hydrate formation measured in the repeated cooling- heating cycles for solution containing 3 mass% NaCl and 15 mass% MeOH

Dissociation temperature outside HSZ / °C	Subcooling / °C	
	1 hr	12 hrs
Initial formation	15.2	
2	3.2	4.2
7	9.4	10.3
12	10.8	12.8
17	15.6	15.5
22	13.3	15.3
27	15.6	

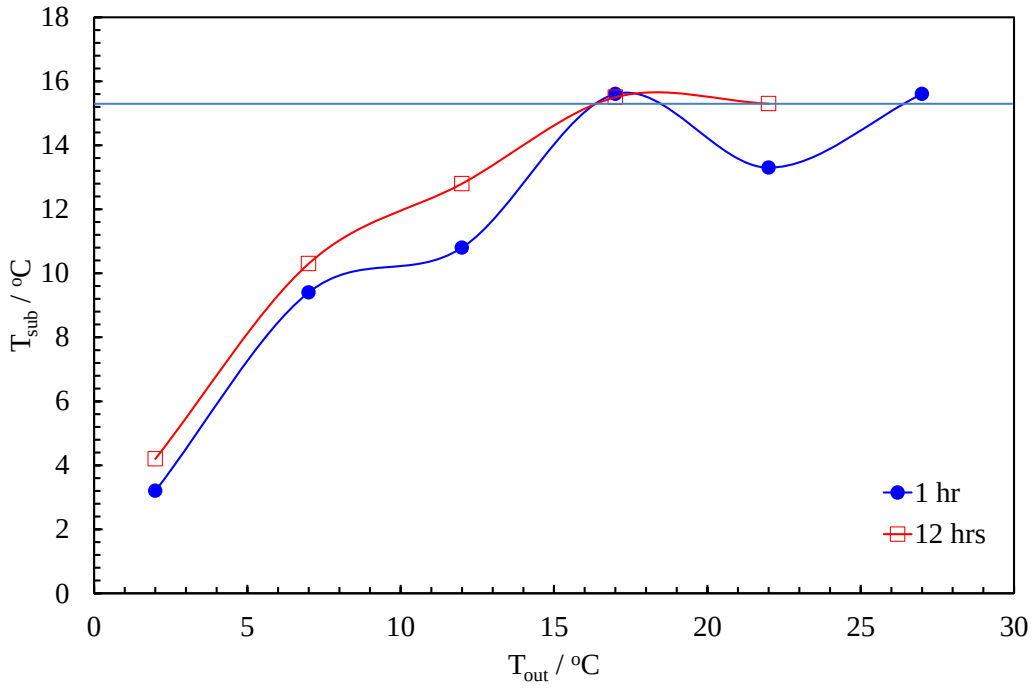

Figure 6.10 Evolution of subcooling temperature for aqueous solution containing 3 mass% NaCl and 15 mass% MeOH

6.3.7 Natural Gas - Deionised Water Systems with 30 mass% Methanol

For the aqueous methanol solution with 30 mass% methanol, the initial hydrate formation occurred at 8.7 ^{o}C subcooling. The results of tests are summarised in Table 6.8 and presented in Figure 6.11. The memory effect for water with high concentration of methanol was almost negligible when compared with pure water tests (Figure 6.4). It was not possible to detect the memory right at 3.9 ^{o}C (2.6 ^{o}C outside the HSZ) after 12 hours heating. It could therefore be concluded that methanol shorten water memory. Again, this finding lies within the uncertainty of measurements and is most likely apparatus dependent. Further experiments are necessary to refine the effect.

Table 6.8 Subcooling temperature of hydrate formation measured in the repeated cooling- heating cycles for 30 mass% aqueous MeOH solution

Dissociation temperature outside HSZ / °C	Subcooling / °C	
	1 hr	12 hrs
Initial formation	8.7	
2.6	4.2	8.6
7.4	8.6	8.3
12	7.9	8.1
17	9.5	11.4

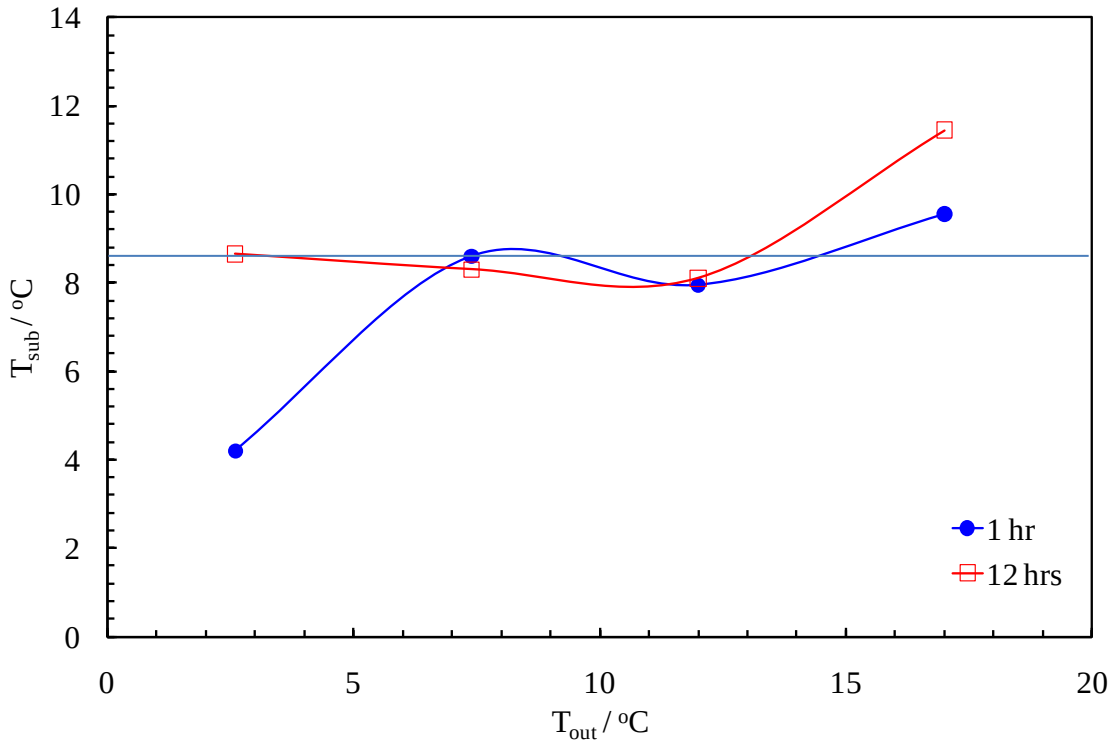

Figure 6.11 Evolution of the onset of hydrate formation temperature for 30 mass% aqueous MeOH solution

6.3.8 Natural Gas - Deionised Water Systems with 15 mass% Ethylene Glycol

To examine the effect of ethylene glycol on the sustainability of hydrate memory, an aqueous solution was prepared by adding 15 mass% of EG into deionised water. The initial hydrate formation is at 13.4 ^{o}C subcooling. The results of tests are summarised in Table 6.9 and presented in Figure 6.12. The memory effect for water with ethylene glycol was similar to pure water (Figure 6.4). The memory can be detected up to 20.8 ^{o}C (7.3 ^{o}C outside HSZ), since a 2 ^{o}C difference in subcooling temperature is still observed. It could therefore be concluded that ethylene glycol has a limited effect on water memory.

Table 6.9 Onset of hydrate formation temperature measured in the repeated cooling-heating cycles for 15 mass% aqueous EG solution

Dissociation temperature outside HSZ / °C	Subcooling / °C	
	1hr	12hrs
Initial formation	13.4	
2.2	1.7	4.2
7	6.9	11.1
12	15.5	14.4
16.8	14.4	14.6
21.8	14.1	

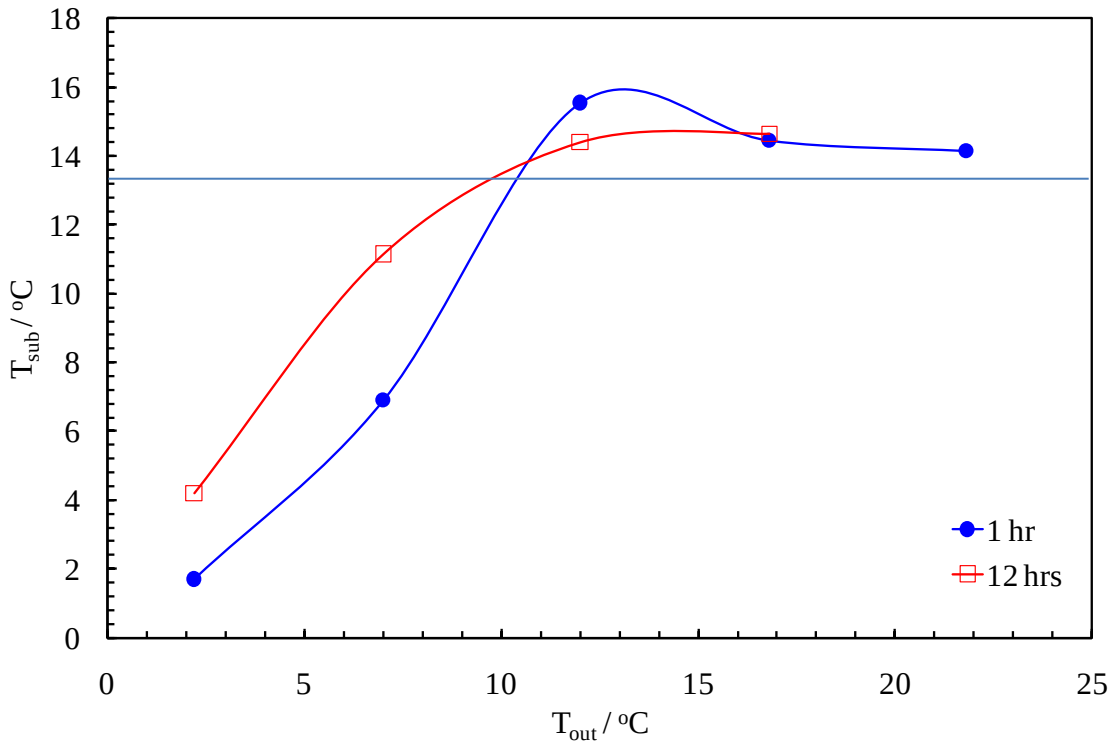

Figure 6.12 Evolution of subcooling temperature for 15 mass% aqueous EG solution

6.3.9 Natural Gas - Deionised Water Systems with 3 mass% Salt and 15 mass% Ethylene Glycol

For the solution with 15 mass% of EG and 3 mass% NaCl, the initial hydrate formation appeared at 14.5 ^{o}C subcooling. The results of tests are summarised in Table 6.10 and presented in Figure 6.13. The memory effect for water with ethylene glycol and salt was kept longer when compared to water with ethylene glycol alone (Table 6.9 and Figure 6.12). The memory can be detected up to 19.9 ^{o}C (7.3 ^{o}C outside the HSZ), since a 4.8 ^{o}C difference in subcooling temperature was still observed. It could therefore be again concluded that salt can prolong the effect of water memory.

Table 6.10 Subcooling temperature of hydrate formation measured in the repeated cooling- heating cycles for aqueous solution containing 3 mass% NaCl and 15 mass% EG

Dissociation temperature outside HSZ / °C	Subcooling / °C	
	1hr	12 hrs
Initial formation	14.5	
2.3	3.8	4.1
7.3	4.9	9.7
12	14.2	14.9
16.8	14.7	15
21.9	14.8	

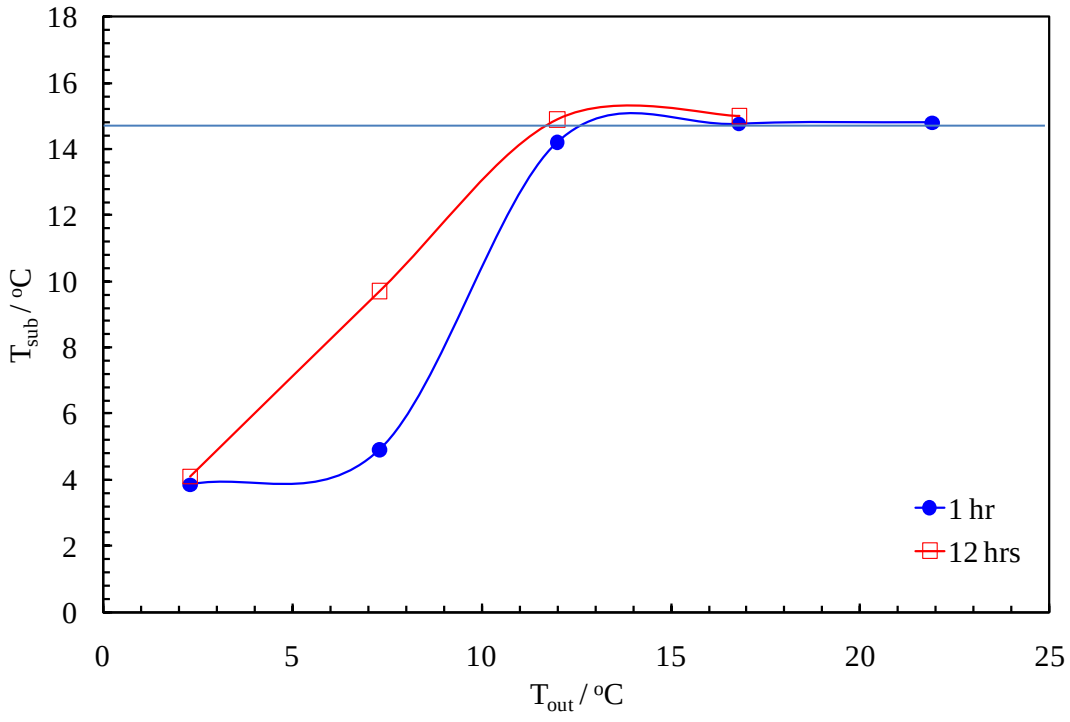

Figure 6.13 Evolution of subcooling temperature for aqueous solution containing 3 mass% NaCl and 15 mass% EG

6.3.10 Natural Gas - Deionised Water Systems with 30 mass% Ethylene Glycol

For the aqueous solution with 30 mass% of EG, the initial hydrate formation appeared at 12.5°C subcooling. The results of tests are summarised in Table 6.11 and presented in Figure 6.14. The memory effect for water with high concentration of ethylene glycol was longer when compared to distilled water (Figure 6.4). The memory can be detected up to 20.2 °C (12.2 °C outside the HSZ). It could therefore be concluded that high concentrations of EG can prolong the effect of water memory.

Table 6.11 Subcooling temperature of hydrate formation measured in the repeated cooling- heating cycles for 30 mass% aqueous EG solution

Dissociation temperature outside HSZ / °C	Subcooling / °C	
	1 hr	12 hrs
Initial formation	12.5	
2.3	3.9	4.6
7.3	5.6	7.2
12.2	10.8	14.6
16.9	11.2	12.9
21.9	14.0	

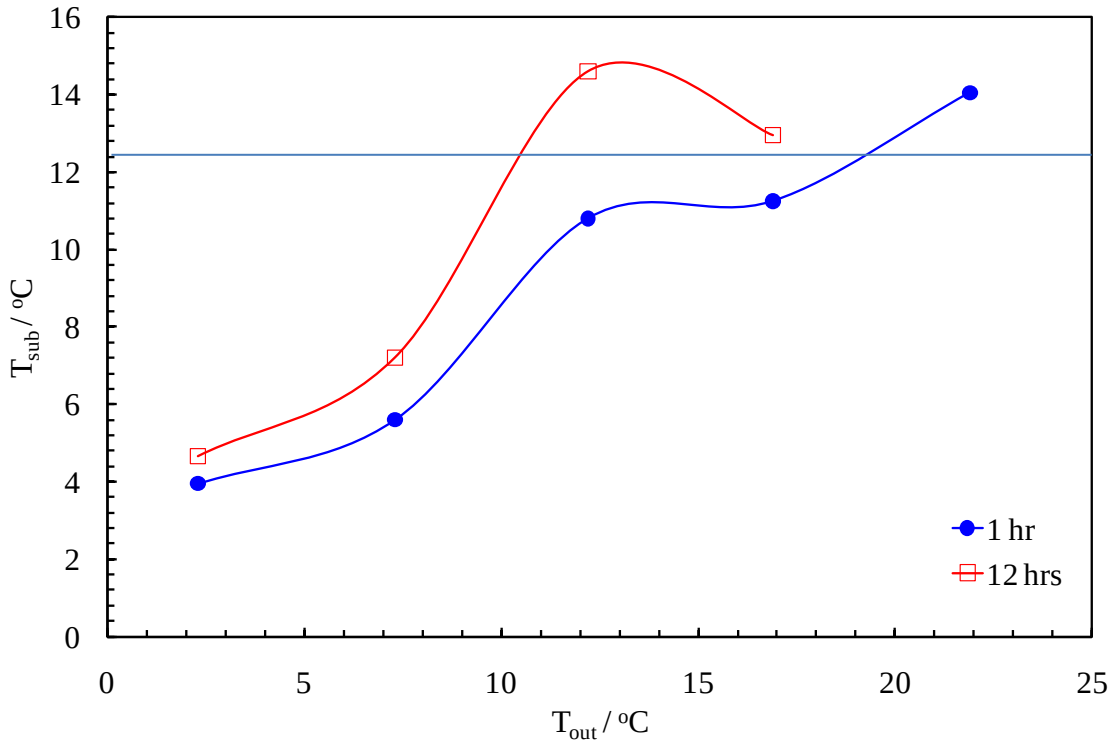

Figure 6.14 Evolution of subcooling temperature for 30 mass% aqueous EG solution

6.3.11 Produced Water

The produced water (provided by one of the project sponsors, BP) containing 5 mass% salts/solids was used in the experiments. The initial hydrate formation was observed at 12.5 ^{o}C subcooling. The results of tests are summarised in Table 6.12 and presented in Figure 6.15. As it was expected, the memory effect for produced water is similar to 5 mass % aqueous NaCl solution (Figure 6.7). The memory is observed up to 33.5 ^{o}C (16.4 ^{o}C outside HSZ). It can therefore be concluded that water memory is detectable in the industrial produced water. Time spent by produced water outside HSZ is generally short to have an effect on memory. The next level of development would be to transfer the technique from laboratory to production installations. Further experiments are required as it is discussed in recommendations for future work (section 7.2).

Table 6.12 Onset of hydrate formation temperature measured in the repeated cooling-heating cycles for water with 15 mass% EG systems

Dissociation temperature outside HSZ / °C	Subcooling / °C	
	1 hr	12 hrs
Initial formation	12.5	
1.8	6.9	7
6.7	10.1	11.0
16.4	12.9	12.7
21.5	12.5	

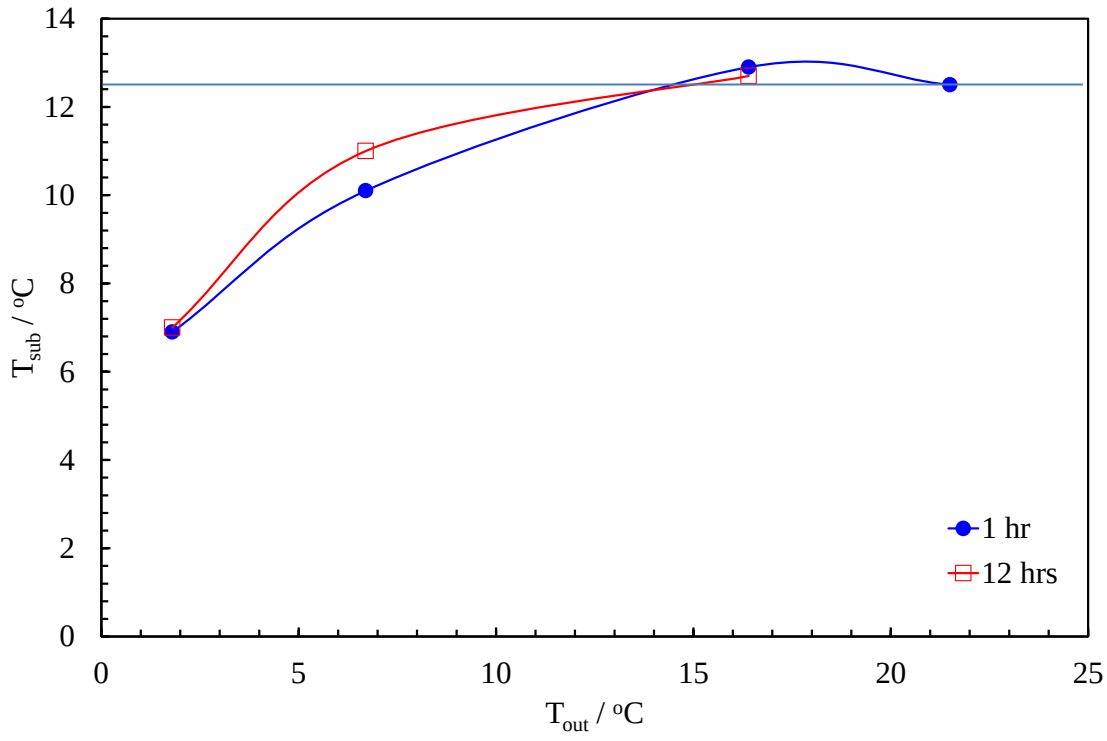

Figure 6.15 Evolution of subcooling temperature for water with 15 mass% EG systems

6.4 SUMMARY

The key findings are summarized below:

- The memory effect is more dependent on the heating temperature rather than on the time of being outside hydrate stability zone.
- The effect of depressurisation is not strong enough to destroy the hydrate water memory.
- The water memory is not strong enough to initiate early hydrate formation in static conditions. The water memory can have an effect on hydrate formation only in a well-mixed environment.
- Presence of salt in aqueous solution can prolong/enhance the memory effect. However, salt nonlinearly prolong water memory.
- Presence of methanol in aqueous solution can slightly shorten/suppress the memory effect.
- The presence of ethylene glycol has a limited effect on water memory. However, high concentrations of EG can prolong/enhance the effect.
- The water memory was detectable in the produced water.

Comparisons of various solutions tested in this section are presented in Figure 6.16 and Figure 6.17, and the summary Table 6.13.

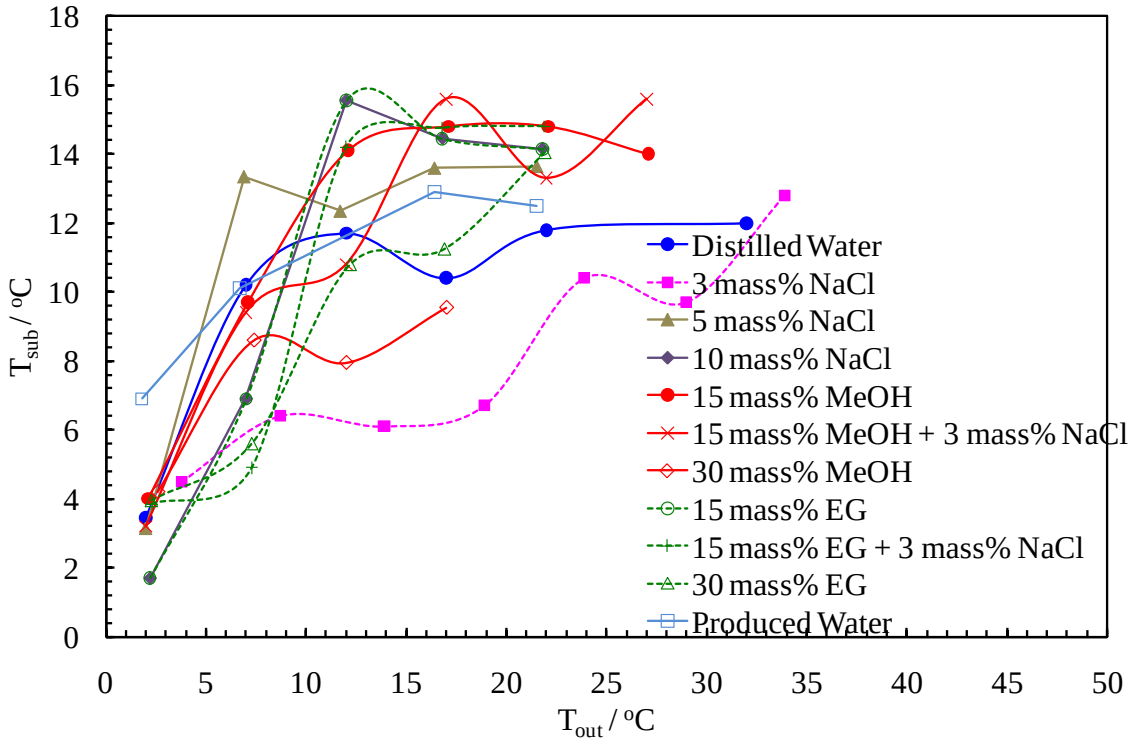

Figure 6.16 Summary of various aqueous solutions tests with 1 hour dissociation

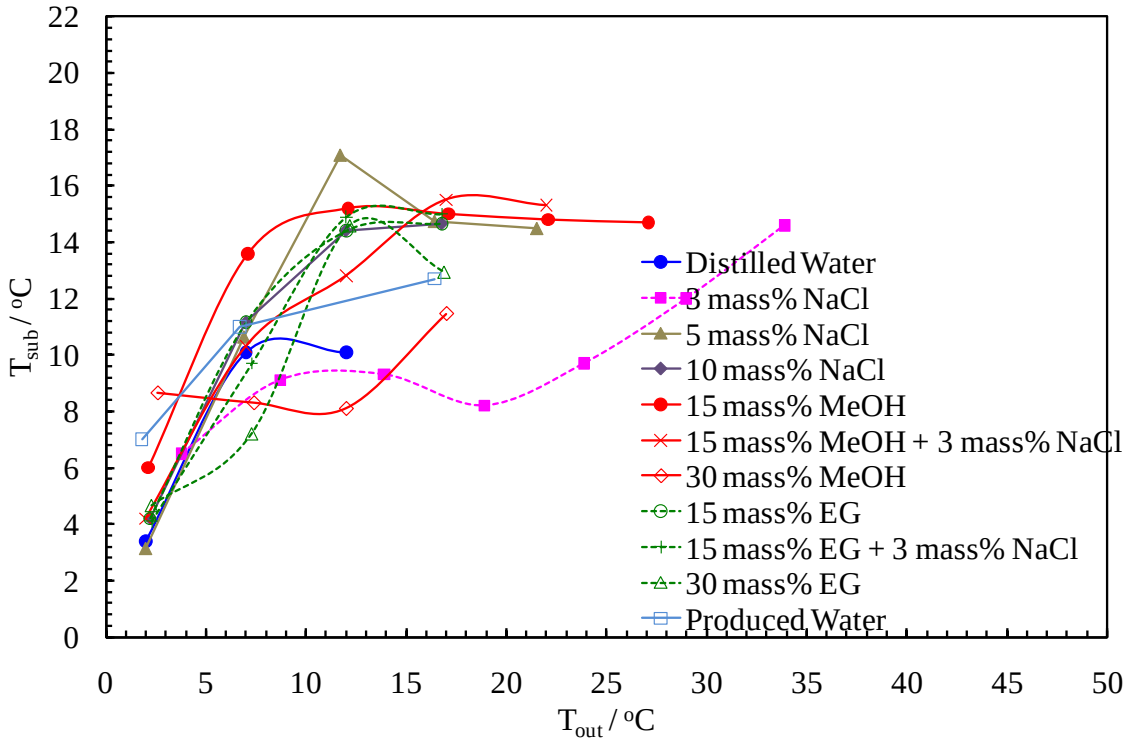

Figure 6.17 Summary of various aqueous solutions tests with 12 hours dissociation

Table 6.13 Summary of various aqueous solutions tests

Dissociation temperature outside HSZ / °C	Subcooling / °C	
	1 h	12 hrs
Distilled Water		
2	3.4	3.4
7	10.2	10.1
12	11.7	10.1
17	10.4	
22	11.8	
32	12.0	
3 mass% NaCl		
3.8	4.5	6.5
8.7	6.4	9.1
13.9	6.1	9.3
18.9	6.7	8.2
23.9	10.4	9.7
29	9.7	12.0
33.9	12.8	14.6
5 mass% NaCl		
2	3.15	3.15
6.9	13.3	10.6
11.7	12.3	17.1
16.4	13.6	14.7
21.5	13.6	14.
10 mass% NaCl		
2.2	1.7	4.2
7	6.9	11.1
12	15.5	14.4
16.8	14.4	14.6
21.8	14.1	
15 mass% MeOH		
2.1	4.0	6.0
7.1	9.7	13.6
12.1	14.1	15.2
17.1	14.8	15.0
22.1	14.8	14.8
27.1	14.0	14.7
15 mass% MeOH + 3 mass% NaCl		
2	3.2	4.2
7	9.4	10.3
12	10.8	12.8
17	15.6	15.5
22	13.3	15.3
27	15.6	
30 mass% MeOH		
2.6	4.2	8.6
7.4	8.6	8.3
12	7.9	8.1
17	9.5	11.4

Dissociation temperature outside HSZ / °C	Subcooling / °C	
	1 h	12 hrs
15 mass% EG		
2.2	1.7	4.2
7	6.9	11.1
12	15.5	14.4
16.8	14.4	14.6
21.8	14.1	
15 mass% EG + 3 mass% NaCl		
2.3	3.85	4.1
7.3	4.9	9.7
12	14.2	14.9
16.8	14.7	15
21.9	14.8	
30 mass% EG		
2.3	3.9	4.6
7.3	5.6	7.2
12.2	10.8	14.6
16.9	11.2	12.9
21.9	14.0	
Produced Water		
1.8	6.9	7
6.7	10.1	11.0
16.4	12.9	12.7
21.5	12.5	

6.5 HYDRATE MINI RIGS

In the light of the successful investigations showing that the onset of gas hydrate formation in the water with hydrate memory was consistent and reliable, the hydrate mini-rigs were designed and developed. The purpose of those miniature rigs was to provide fast response on detection of hydrate water memory by measuring the required subcooling/induction time for small quantities of aqueous sample. Additional benefit of such an instrument was the ease of its deployment in the industry. Some of the mini rig designs mentioned elsewhere (Oskarsson et al., 2005) were tested with limited success for evaluation of anti-agglomerants (AA). In this section, two novel designs, tall-narrow and short-wide, were developed and tested. The evaluation criteria were based on the ability to form hydrates in a short time at sufficient pressure and temperature inside the hydrate stability zone.

6.5.1 Tall-Narrow Design

The first approach for reducing the volume of tested fluid (by reducing the size of the instrument) led to creating a tall-narrow mini-rig (Figure 6.18). This mini-rig had 4 ml sample container, could be pressurised up to a maximum of 103.5 bar, and heated/cooled within the temperature range of -30 ^{o}C to 50 ^{o}C.

Figure 6.18 Picture of the tall-narrow hydrate mini-rig set-up

The rig was experimentally investigated against the evaluation criteria. 2 ml volume of water was loaded into the container and charged with natural gas to 100 bar pressure. To form hydrates, the sample was then cooled down to 18 ^{o}C inside the hydrate stability zone at 0.2 ^{o}C/min cooling rate with applied magnetic stirrer mixing. The system was then kept cooled for 4 hours to make sure sufficient time was given for hydrates to form. The miniature cell was than heated to 2 ^{o}C outside the hydrate stability zone and kept for 5 hours. In the test, it was found that the hydrate did not form. As the width of the sample cell was too narrow, the mixing efficiency was highly dependent on the

stirrer size. Giving the reason for the result in the efficiency of mixing, the cooling-heating cycles were repeated with a shorter magnetic stirrer bar which was able to freely rotate at the bottom of container. The temperature-pressure profile during the test (Figure 6.19) again confirmed no evidence of hydrate formation.

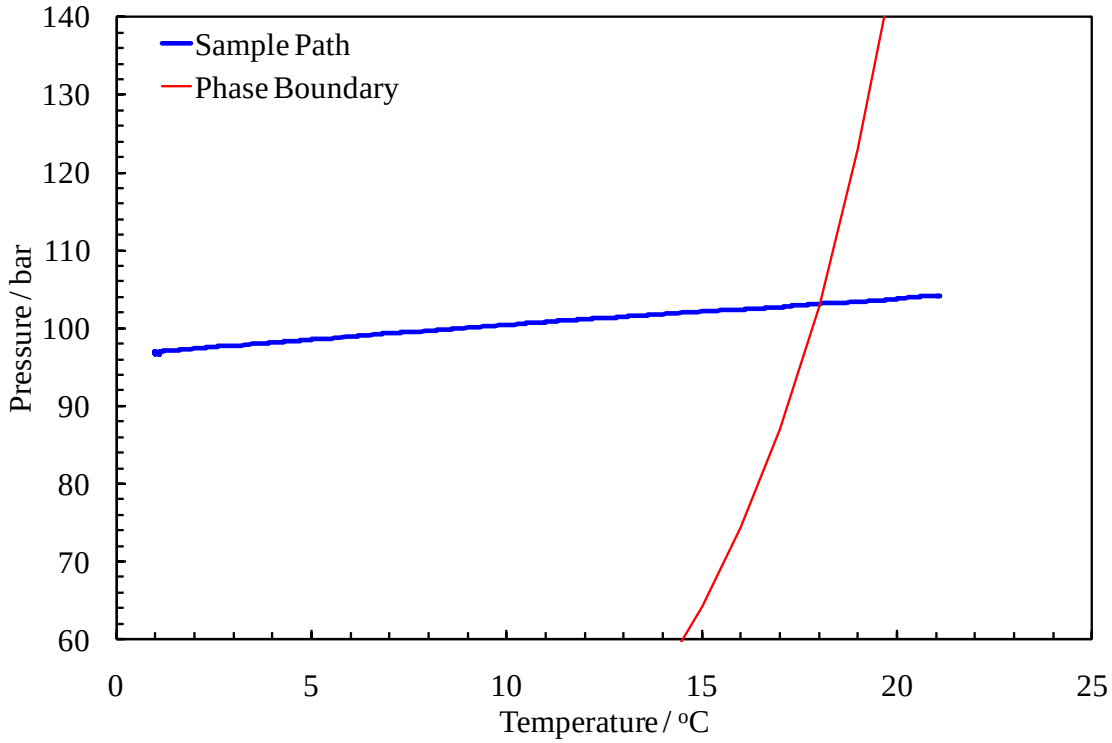

Figure 6.19 Sample temperature-pressure path showing no sign of hydrate formation

6.5.2 Short-Wide Design

As the methodology of this technique involves hydrate crystallisation from the most of/whole volume of aqueous sample, the form of mini-rig was redesigned to adopt mixing in the maximum volume. The created short-wide mini-rig with a 12 ml container cell, could be operated at maximum pressure of 275 bar, and temperature of -30 °C to 50 °C. The rig accommodated a magnetic stirrer mixer at the centre of container. The picture of modified set up is presented in Figure 6.20.

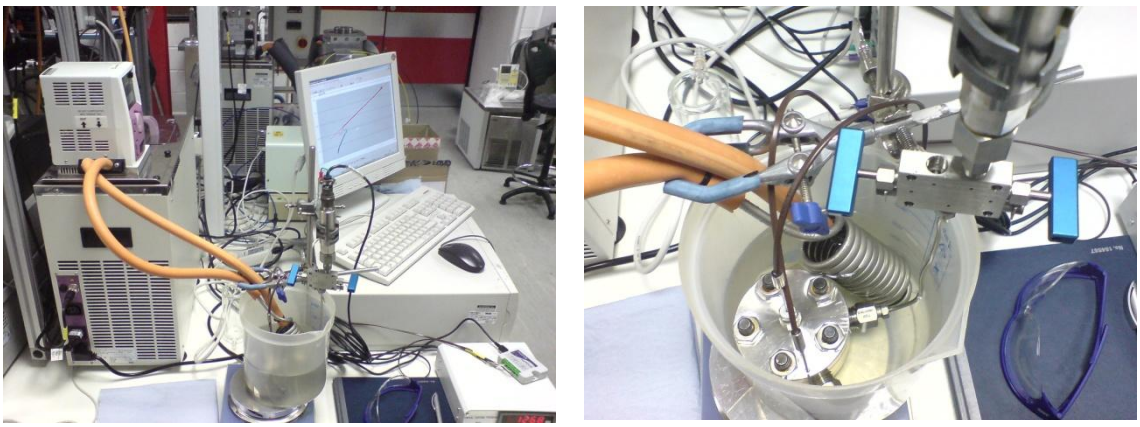

Figure 6.20 Picture of the short-wide hydrate mini-rig set-up

To test the developed set-up, 6 ml of water was loaded into the container which was then charged with natural gas up to 100 bar pressure. The system was cooled down to 15 ^{o}C inside the hydrate stability zone at 0.2 ^{o}C/min cooling rate under applied magnetic stirrer mixing. As it can be seen from the temperature-pressure profile (Figure 6.21), the hydrate formation appeared at 7.2 ^{o}C (10.8 ^{o}C subcooling).

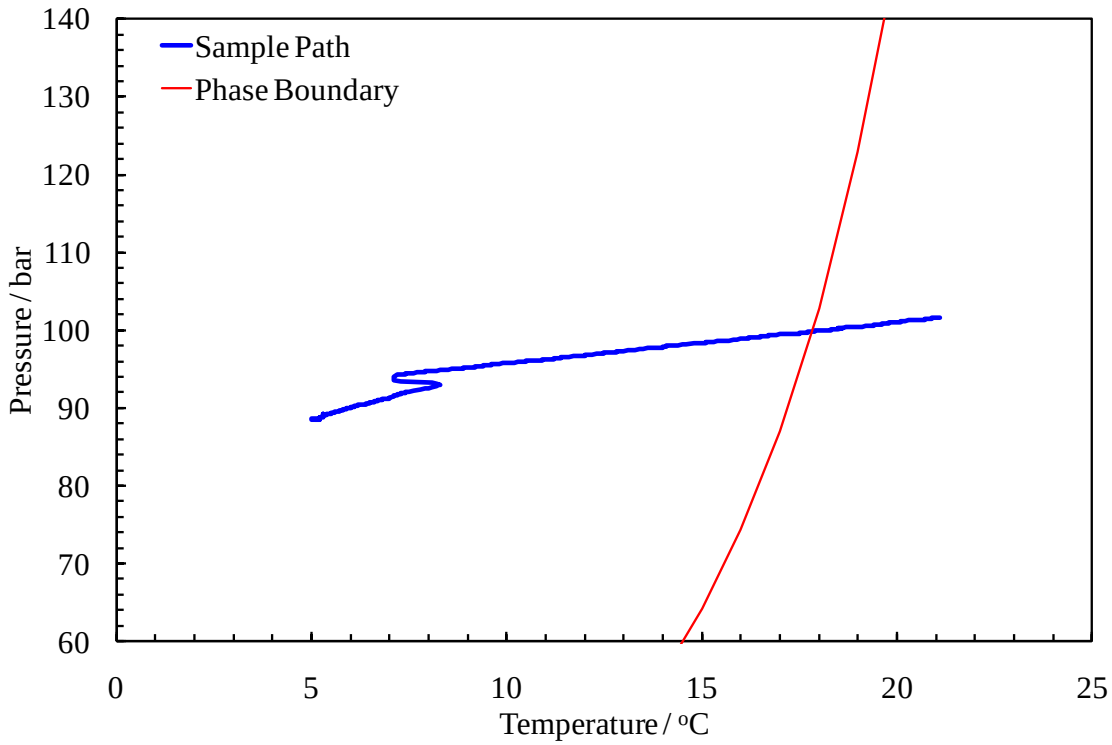

Figure 6.21 Sample temperature-pressure path showing notable hydrate quantities formed

Inspired by the above result, improved hydrate mini rig design was recommended which utilises ideology of initial (Figure 6.18) and modified (Figure 6.20) set-ups. Wider plastic cap was suggested to increase the maximum pressure. Shorter and wider container was proposed to allow magnetic bar to rotate and mix sample in the whole volume. Those are summarised in recommendations section 7.2. The construction of proposed mini rig was intended being completed in the JIP project based on recommendations discussed in this thesis.

6.6 CONCLUSIONS

Prior to a massive agglomeration and blockage, hydrate nucleus are sporadically crystallizing and disintegrating in a region of production facilities with subcooled conditions. Experienced hydrate crystallisation, aqueous phase can preserve and deliver the memory to the sampling point. Being detected, hydrate memory can serve as an indicator for the operating body to alter the production condition and assure the flow. In this Chapter, the method for investigation of hydrate water memory was developed. Using the developed approach, the onset of gas hydrate formation was investigated as one of the early warning techniques.

The required subcooling/induction time was measured for different aqueous solutions with alcohol and salt. The preliminary results showed that the onset of hydrate formation is much less stochastic than the onset of ice formation investigated in the previous chapter (Chapter 5). The onset difference between the water samples with preserved hydrate history and those without it was measurable even after heating the system to several degrees Celsius outside the hydrate stability zone for 12 hours. The measurements were performed in a well-mixed environment, since it was shown that it is critical for the detection of water memory by hydrate formation.

It was found that the presence of additives in pure water can alter the memory response. Salt component could nonlinearly prolong/enhance water memory with a maximum influence at around 3 mass%, whereas methanol slightly shortened/suppressed it. It was shown that the presence of ethylene glycol has a limited effect, unless its concentration is high in which case the memory could be prolonged/enhanced. Produced water containing 5 mass% unknown salts showed similar behaviour as distilled water with 5 mass% NaCl. Water memory is detectable in the produced water.

Two types of mini-rigs were designed and tested for the applicability to serve as apparatus part of the technique providing fast response on detection of hydrate water memory by measuring the required subcooling/induction time for small quantities of aqueous sample. The short and wide design showed better parameters for onset of hydrate formation.

CHAPTER 7 CONCLUSIONS AND RECOMMENDATIONS

7.1 CONCLUSIONS

The current industry practice for hydrate prevention is injecting hydrate inhibitors at the upstream end of pipelines based on the calculated/measured hydrate phase boundary, water cut, worst pressure and temperature conditions, and the amount of inhibitor lost to non-aqueous phases. In general, systematic ways of controlling and monitoring along the pipeline and/or downstream to examine the degree of inhibition are very limited. This thesis presents the research work performed for Hydrate Monitoring and Early Warning Systems which aim to reduce the risk of gas hydrate blockage in oil and gas pipelines and processing facilities. Several physical hypotheses were generated and examined for the purpose of this thesis. Some of them showed a high potential to be further employed in the industry (Table 7.1).

Table 7.1 Techniques categorised by their applicability in laboratory and industrial conditions

	Technique	Laboratory	Industry
Hydrate Monitoring Techniques	Freezing point depression	Yes	Yes
	Concentration monitoring by Spectroscopy	Yes	No
	Concentration monitoring by Dielectric Permittivity	Further work	Further work
Hydrate Early Warning Techniques	Spectroscopy	Yes	Further work
	Onset of Ice Formation	No	No
	Onset of Hydrate Formation	Yes	Yes

In Chapter 2, the spectroscopy technique (commonly used in analytical chemistry and physics) was investigated to figure out if hydrates formation and dissociation can influence light properties. The results imply that hydrates nucleation can be detected through reduction in light intensity prior to seeing pressure drop in Pressure-Temperature profile. The results suggest that hydrate water memory could be detected

using UV/VIS/NIR spectroscopy. It was demonstrated that water memory can exist for 24 hours after hydrate dissociation at 2 °C outside the HSZ. A preliminary investigation on inhibitor concentration monitoring was conducted with promising results. For this purpose, the technique was further tested in Chapter 3.

Monitoring techniques based on measurement of the concentrations of chemical inhibitors in the aqueous solutions were studied in Chapter 3. Two electromagnetic methods were examined to provide valuable data on concentrations of hydrate inhibitors which then can be used to predict hydrate stability zone for industrial application. Spectroscopy technique showed possibility to quantitatively measure methanol or ethylene glycol concentration from light spectrum with acceptable sensitivity ~0.6 $mW.m^{-2}$/mass%. NaCl concentration analysis indicated that salt has limited effect on light properties in 320-1100 nm spectrum region. PVCap concentration in EG solution can be measured by spectroscopy in the UV range (300-550 nm) with tolerance to salt (NaCl) component. Therefore this technique can be applied to define both EG and PVCap concentrations from one measurement, since they influence separate spectrum regions.

The effect of impurities (oil and sand) indicates that the method is tolerant to oil presence in the fluid system. However, it is significantly affected by the presence of particles (sand) which stochastically alters the spectrum reducing it in UV and increasing it in NIR parts. Provided that the water is fines free, the method can be applied. Produced water tests validated the statement, since particles free BP water test results showed that alcohol concentration was detectable. The technique is showing to be viable and can provide a quick and reliable response on the inhibitor concentration change in pipeline flow.

Applicability of dielectric permittivity technique for monitoring alcohol-salt concentrations in aqueous phase has been also investigated. The effect of impurities on dielectric response of solutions was also studied. Alcohols and salts concentrations can potentially be monitored in separate spectrum regions, since their polarization mechanisms are different. The screening of dielectric permittivity technique as concentration monitoring element of the system showed a potential for practical application, further experimental work was suggested.

Another hydrate monitoring method based on measurements of freezing point of aqueous phase was studied in Chapter 4. A freezing device set-up based on Peltier

elements was designed and manufactured, which remarkably facilitated freezing point measurements and made the freezing point depression technique more feasible and applicable for field laboratory conditions and potentially for online applications. The prototype was used to employ the empirical correlation linking the freezing point depression with the hydrate stability zone for various fluid systems in the presence of salts and/or organic inhibitors. As part of the JIP, the correlation was developed by Dr. Hesam Najibi et al. (2006) and improved by Dr. Antonin Chapoy, Centre for Gas Hydrate Research, Heriot-Watt University.

Pseudo Concentration Method (PCM) was developed as a new approach to relate the freezing point depression of aqueous solutions to their hydrate inhibition characteristics. This new approach was shown to be more reliable and robust than the previously developed correlations, since it takes into account the pressure, hydrate structure and inhibitor type effects.

The second main objective of this thesis work was to develop a number of techniques for early warning system against initial hydrate formation. The aim was to give the operator adequate time to initiate remedial steps prior to massive hydrate formation/build up which could result in pipeline blockage. In Chapter 5, the onset of ice formation by freezing method was investigated as a potential technique for hydrate early warning systems based on detection of the hydrate memory in water. The results on both deionised and produced water samples show that the samples with hydrate water history tend to freeze earlier and to nucleate faster than those without hydrate water history. The effect of different sample preparation paths on water history was investigated suggesting no influence. The role of dissolved gas in the sustainability of water structure was studied by removing excess dissolved gas. The results suggest that removing dissolved gas could significantly eliminate the effect of water structure on ice nucleation, but the presence of hydrate history is still measurable based on the observed effect on ice nucleation rate. In general, the results suggest that changes in water structure due to hydrate formation could be detected using freezing method. The element of stochasticity/randomness in the measured data cannot be negligible, as it was shown with three statistical tests and the nucleation probability distribution. Based on the above results, the onset of hydrate formation presented in Chapter 6 was suggested as an interesting alternative to the ice formation method.

The principle of hydrate formation technique is that hydrate forms more easily from a solution which has experienced hydrate solid state in the past than from a freshly prepared gas-water mixture. The required subcooling/induction time for the aqueous sample was measured for different aqueous solution with alcohol and salt additives in Chapter 6. The onset difference between the water samples with preserved hydrate history and those without it was measurable even after heating the system to several degrees Celsius outside the hydrate stability zone for 12 hours. It was found that the presence of additives in pure water can alter the memory response. Salt component could nonlinearly prolong/enhance water memory with a maximum influence at around 3 mass%, whereas methanol slightly shortened/suppressed it. It was shown that the presence of ethylene glycol has a limited effect, unless its concentration is high. Water memory was detectable in the produced water containing 5 mass% of unknown salts. Two types of mini-rigs were designed and tested for the applicability to serve as apparatus part of the technique providing fast response on detection of hydrate water memory by measuring the required subcooling/induction time for small quantities of aqueous sample.

7.2 RECOMMENDATIONS FOR FUTURE WORK

The spectroscopy memory experiments, in Chapter 2, were encouraging; however, only pure water was investigated. The suggestion can be to test the contaminated systems that can realistically replicate the aqueous phase of produced oilfield fluids.

For the spectroscopy technique (Chapter 3), it was shown that salt (NaCl) component has minor effect on light properties in 320-1100 nm spectrum region. Expansion of the experiments in to further IR range of 1100-3000 nm is suggested. ATR technique is suggested in that range, since it avoids strong attenuation of the IR signal in highly absorbing media, such as aqueous solutions. Moreover, according to the results presented in Chapter 3, particles/fines can bock the transmitted light hindering any useful spectral signal. The idea can be to try to purify the produced fluid to the maximum achievable purity prior to any memory test commenced. However, a new process of purification in the whole memory measurement cycle introduces additional error/uncertainty term which has to be analytically taken into account and corrected. That means that the effect of purification on the quality of memory measurements has to be additionally examined.

For the dielectric permittivity technique as part of hydrate monitoring systems, further experimental work is suggested. Further investigation is proposed for the effect of corrosion inhibitors, KHI, and Anti-aglomerants. The technique was found to be sensitive to calibration. It is suggested to make the necessary arrangements to ensure the calibration of the device is stable and repeatable against standard materials including air, water, EG, MeOH, and conductive metal. The effect of contamination by sand and oil has been studied and resulted in a new set-up proposal. Modifications in the design aim to ensure measurement of dielectric properties in the whole fluid volume. In order to do that, the entire solution has to be placed between two electrodes to form a capacitor which properties, e.g. capacitance, conductance, resistance and reactance, have to be measured over the desirable frequency range, and then converted in a dielectric spectrogram. This whole set-up has to be calibrated against etalon materials of known dielectric permittivity to make sure reasonable accuracy and reliability can be achieved. Additional work is recommended to be done to utilise the experience of service companies (e.g. ROXAR AS) in multiphase flow meters mainly based on dielectric properties measurement.

Generally, Chapter 5 showed that onset of ice formation has a physical background for detection of a memory phenomenon, since the results implied the hydrate water history does have a noticeable effect on the ice nucleation. However, due to a time and number of probes limitation for gathering statistical data, it did not seem to be a practical technique for further field application as a part of early warning systems. The recommendation here can be to try building a set-up which can test a large number of aqueous phase samples in a relatively short time period similar to existing apparatus built elsewhere (Wilson et al., 2005). There is no requirement on a volume of sample; therefore, it can be as small as a droplet. The reduced size of the sample will reduce the time needed for it to be cooled and frozen. However, the freezing time has to be as short as possible on one side, and enough to provide a reasonable sensitivity for the freezing temperature on another. That means there should be a good balance between the speed of cooling and the accuracy of freezing point measurement.

For the onset of hydrate formation technique (Chapter 6), further investigations are suggested to test the effect of the amount of hydrates formed during the hydrate formation stage. The amount of hydrates formed can affect the number of structural elements remaining in the entire aqueous phase after hydrate is dissociated. Water memory detection can most likely have a minimum hydrate formed threshold which will most likely be apparatus dependent. Another point for this technique is to continue experiments and further study synthetic produced water systems containing oil, sand and other contaminants. Furthermore, the presence of KHI can slow down the kinetics of hydrate dissociation and/or shift the hydrate phase boundary towards higher temperatures, further tests are recommended to see the effect of KHI inhibitors. Based on investigations presented in Chapter 6, new design of hydrate mini-rig has been proposed and remained under construction as part of the research plan for the JIP project. Further laboratory tests are necessary to evaluate the workability of that set-up and define the design elements that can be further improved.

REFERENCES

Aasberg-Petersen K., Stenby E. and Fredenslund A. (1991) Prediction of high-pressure gas solubilities in aqueous mixtures of electrolytes, Ind. Eng. Chem. Res., 30, 2180-2185.

Akerlof G. (1932) Dielectric constants of some organic solvent–water mixtures at various temperatures, J. Am. Chem. Soc., 54, pp. 4125–4139.

Amy T.K., Gongmin F., Malene A.W. and Mason B. T. (2002) Effect of hydrate inhibitors on oilfield scale formation and inhibition, SPE Oilfield Scale Symposium, Aberdeen, SPE 74657.

Anderson F.E. and Prausnitz J.M. (1986) Inhibition of gas hydrates by methanol, AIChE J., 32, 1321-1333.

Application Note 1217-1 (1992) Basics of measuring the dielectric properties of materials, Hewlett Packard literature number 5091-3300E.

Asaf U., Hechel D. and Felner I. (1995). Magnetic Properties of Cooper Chloride Hydroxide Hydrate CU3Cl4(OH) 2·2H2O, J. Solid State Communications, 98, 571-573.

Avlonitis D. (1992) Thermodynamics of Gas Hydrate Equilibria, Ph.D. Thesis, Heriot-Watt University.

Avlonitis D. A. (1992) Thermodynamics of gas hydrate equilibria, Ph.D. Thesis, Heriot-Watt University.

Avlonitis D., Danesh A. and Todd A.C. (1994) Prediction of VL and VLL equilibria of mixtures containing petroleum reservoir fluids and methanol with a cubic EoS, Fluid Phase Equilibr., 94, 181-216.

Avlonitis D., Varotsis N. (1996) Modelling gas hydrate thermodynamic behaviour: theoretical basis and computational methods, Fluid Phase Equilibria, 123, 107-130.

Bailey D. and Wright E. (2003) Practical SCADA for Industry, 1-10.

Berner D. (2003) Hydrates for Transport of Stranded Natural Gas, paper SPE 84255 presented at the 2003 SPE annual Technical Conference and Exhibition, Denver, Oct. 5-8.

Betancourt S., Dubost F. and Mullins O. (2007) Predicting Downhole Fluid Analysis Logs to Investigate Reservoir Connectivity, IPTC 11488.

BP Statistical Review of World Energy, June 2008.

BP Statistical Review of World Energy, June 2010.

Brost D., Rexach F., and Winslow G. (1991). Optical Methods for Monitoring Treating Chemicals in Oilfield water Systems, SPE 22781.

Buchanan P., Soper A. and Thompson H. (2005). Search for memory effects in methane hydrate: Structure of water before hydrate formation and after hydrate decomposition, J. Chem. Phys., 123, 164507.

Bursulaya B. D., Zichi D. A. and Kim H. J. (1996) Molecular Dynamics Simulation Study of Polarizable Solute Solvation in Water. 1. Equilibrium Solvent Structure and Solute Rotational Dynamics, J. Phys. Chem., 100, 1392-1405.

Bylov M. and Rasmussen P. (1997). Experimental Determination of Refractive Index of Gas Hydrates," Chemical Engineering Science 52, 3295-3301.

Clarke G., Reynders D. and Wright E. (2003) Practical Modern SCADA Protocols, 12-62.

Colic M., Morse D. (1999) The elusive mechanism of the magnetic ‘memory’ of water, Elsevier Colloids and Surfaces A, 154, 167-174.

Dirk W. Lachenmeier (2007). Rapid quality control of spirit drinks and beer using multivariate data analysis of Fourier transform infrared spectra, Food Chemistry, 101, 825-832.

Eisenberg D. and Kauzmann W. (1969) The Structure and Properties of Water, Oxford University Press, Oxford.

Evdokimov I. N., Eliseev and Akhmetov B. R. (2003) Assembly of asphaltene molecular aggregates as studied by near-UV/visible spectroscopy: I. Structure of the absorbance spectrum, Journal of Petroleum Science and Engineering, Volume 37, Issues 3-4, pp. 135-143.

Feldman Y., Kozlovich N., and Nit I. (1997) Dielectric spectroscopy of microemulsions, Physicochemical and Engineering Aspects, 128, 47-61.

Feldman Y., Kozlovich N., and Nit I. (1997) Dielectric spectroscopy of microemulsions, Physicochemical and Engineering Aspects, 128, 47-61.

Felizardo P., Baptista P., Menezes J.C., and Correia M.J.N|. (2007). Multivariate near infrared spectroscopy models for predicting methanol and water content in biodiesel, Analytica Chimica Acta, 595, 107-113.

Foot J., Webster M., Trueman D., Yusti G. and Grose T. (2006) ISIS – A real-time information pipeline, SPE 99850.

Franks F. (1972) Water, A Comprehensive Treatise The Physics and Physical Chemistry of Water, vol. I, Plenum, New York.

Fröhlich H. (1958) Theory of dielectrics. Oxford: Clarendon Press, pp. 137-187.

Gallignani M., Brunetto M. (2004) Infrared detection in flow analysis—developments and trends (review), Talanta, 64, 1127-1146

Gbaruko B., Igwe J., Gbaruko P., and Nwokeoma R. (2007) Gas hydrates and clathrates: Flow assurance, environmental and economic perspectives and the Nigerian liquefied natural gas project, J. Petroleum Science and Engineering, 56, 192–198.

Guardiaa E., Martia J., Padrob J. A., Saizc L. and Komolkind A. V. (2002) Dynamics in hydrogen bonded liquids: water and alcohols, J. Mol. Liq., 96, 3.

Gudmundsson J. S., Andersson V., and Parlaktuna M., "Hydrate Concept for Capturing Associated Gas", paper SPE 50598 was preaented at the 1998 SPE European Petroleum Conferenceheld in The Hague, The Netherlands, 20-22 October 1998.

Gulbrandsen A.C. and Svartaas T.M. (2008) Influence of Melting Rate on the Dissociation of Gas Hydrates with the Kinetic Inhibitor PVCap Present, Proceedings of the 6th International Conference on Gas Hydrates, Vancouver, British Columbia, CANADA.

Haghighi H., Chapoy A., and Tohidi B. (2008) Freezing point depression of common electrolyte solutions: experimental and prediction using the CPA equation of state, J. Ind. Eng. Chem. Res., 47, 3983-3989.

Haghighi, H., Azarinezhad, R., Chapoy, A., Anderson, R., and Tohidi, B.: "Hydraflow: Avoiding Gas Hydrate Problems", paper SPE 107335 presented at SPE Europec/EAGE Annual Conference and Exhibition, London, United Kingdom, 11–14 June (2007).

Halim A., Orban P. and N., Haryanto E. and C. Ayan (2007) Reservoir Fluid Characterization using Downhole Fluid Analysis In Northern Kalimantan, Indonesia, IPTC 11239.

Hammerschmidt E.G. (1939) Gas hydrate formation, Gas, 15(5) 30-34, 94.

Hammerschmidt EG. (1934) Formation of gas hydrates in natural gas transmission lines. Ind. Eng. Chem. 26:851.

Hasani M., Moloudi M., and Emami F. (2007) Spectrophotometric resolution of ternary mixtures of tryptophan, tyrosine, and histidine with the aid of principal component–artificial neural network models, Analytical Biochemistry, 370, 68-76

Havre T.E. (2004) Near-IR spectroscopy as a method for studying the formation of calcium naphthenate, J. Colloid & Polymer Science, Volume 282, Number 3, pp. 270-279.

Holder G.D. and Hand J.H. (1982) Multiple-phase equilibria in hydrates from methane, ethane, propane, and water mixtures, AIChE J., 28, 440-447.

Hydrafact Ltd., Predictive Software – HWHYD (2008) Available from: http://www.hydrafact.com/Predictive_Software.html [Accessed on 15 Apr 2009].

Kelland M. A., Svartaas T. M. and Dybvik L. (1995) A new generation of gas hydrate inhibitors, SPE 30695-MS.

Kihara T. (1953) Virial Coefficient and Models of Molecules in Gases, Reviews of Modern Physics, 25(4), 831-843.

Landau L.D., Lifshitz E.M. and Pitaevskii L.P. (1984) Course of Theoretical Physics Volume 8: Electrodynamics of Continuous Media, Butterworth-Heinemann, pp. 182-195.

Lederhos J. P., Long J. P., Sum A., Christiansen R. L. and Sloan E. D. (1996) Effective kinetic inhibitors for natural gas hydrates, Chem. Eng. Sci., 51, pp. 1221-1229.

Loveday J. S., Nelmes R. J., Guthrie M., Belmonte S. A., Allan D. R., Klug D. D., Tse J. S. and Handa Y. P. (2001) Stable methane hydrate above 2 GPa and the source of Titan's atmospheric methane, Nature, 410, 661–663.

Makogon Y.F., Holditch S.A. and Makogon T.Y. (2007) Natural gas-hydrates – A potential energy source for the 21st Century, J. Petroleum Science and Engineering, 56, 14–31.

Makogon Y.F., Holditch S.A. and Makogon T.Y. (2004) Proven Reserves and Basics for Development of Gas Hydrate Deposits, AAPG, Vankouver.

Makogon Y.F., Makogon T.Y. and Holditch S.A. (1999) Gas Hydrate Formation and Dissociation with Thermodynamic and Kinetic Inhibitors, SPE 56568.

Mao W.L., Mao H.K., Goncharov A.F., Struzhkin V.V., Guo Q., Hu J., Shu J., Hemley R.J., Somayazulu M. and Zhao Y. (2002) Hydrogen Clusters in Clathrate Hydrate, Science, 297, pp. 2247-2249.

Mathews P. N., Subramanian S. and Creek, J. (2002) High Impact, Poorly Understood Issues with Hydrates In Flow Assurance, 4th International Conference on Gas Hydrates, Yokohama, 899-905.

Max J., Chapados C. (2000) IR spectroscopy of aqueous alkali halide solutions: Pure salt-solvated water spectra and hydration numbers, Journal of chemical physics, 115, 6.

Mei D.H., Liao J., Yang J.T. and Guo T.M. (1998) Hydrate Formation of a Synthetic Natural Gas Mixture in Aqueous Solutions Containing Electrolyte, Methanol, and (Electrolyte + Methanol), J. Chem. Eng. Data, 43, 178-182.

Menten, P.D., Parrish W.R. and Sloan E.D. (1981) Effect of inhibitors on hydrate formation, Ind. Eng. Chem. Proc. Des. Dev., 20, 399-401.

Mohammadi A. H. and Tohidi B. (2005) A Novel Predictive Technique for Estimating the Hydrate Inhibition Effects of Single and Mixed Thermodynamic Inhibitors, The Canadian Journal of Chemical Engineering, 83, pp. 951-961.

Muller N., Elshahawi H., Dong C. and Mullins O. (2006) Quantification of carbon dioxide using downhole Wireline formation tester measurements, SPE 100739.

Mullins O. and Schroer J. (2000) Real-Time Determination of Filtrate Contamination During Openhole Wireline Sampling by Optical Spectroscopy, SPE 63071.

Najibi H., Mohammadi A.H. and Tohidi B. (2006) Estimating the Hydrate Safety Margin in the Presence of Salt and/or Organic Inhibitor Using Freezing Point Depression Data of Aqueous Solutions, Ind. Eng. Chem. Res., 45 (12), pp. 4441-4446.

Ng H.-J., Chen C.-J. and Saeterstad T. (1987) Hydrate formation and inhibition in gas condensate and hydrocarbon liquid systems, Fluid Phase Equilibria, 36, 99-106.

Nielsen, R. B. and Bucklin R. W. (1983) Why not use methanol for hydrate control? Hydrocarbon Processing, 62(4), 71-78.

Ning F., Zhang L., Jiang G.,Tu Y., Wu X. and Yu Y. (2011) Comparison and application of different empirical correlations for estimating the hydrate safety margin of oil-based drilling fluids containing ethylene glycol, Journal of Natural Gas Chemistry, 20 (1), pp. 25-33.

Nordlund D., Odelius M., Bluhm H., Ogasawara H., Pettersson L.G.M. and Nilsson A. (2008) Electronic structure effects in liquid water studied by photoelectron spectroscopy and density functional theory, Chemical Physics Letters 460, 86–92.

Ohmura R., Ogawa M. Yasuoka K. and Mori Y.H. (2003). Statistical Study of Clathrate-Hydrate Nucleation in a Water/Hydrochlorofluorocarbon System: Search for the Nature of the Memory Effect, J. Phys. Chem. B, 107, 5289-5293.

Ohmura R., Shigetomi T. and Mori Y.H. (2000) Mechanical Properties of Water/Hydrate-Former Phase Boundaries and Phase Separating Hydrate Films, Annals of the New York Academy of Sciences, The New York Academy of Sciences, NY 912, 958.

Ohmura R., Shigetomi T. and Mori Y.H. (2000) Mechanical Properties of Water/Hydrate-Former Phase Boundaries and Phase Separating Hydrate Films, Annals of the New York Academy of Sciences, The New York Academy of Sciences, NY 912, 958.

Ohmura R., Shigetomi T. and Mori Y.H. (2000). Mechanical Properties of Water/Hydrate-Former Phase Boundaries and Phase Separating Hydrate Films, Annals of the New York Academy of Sciences, The New York Academy of Sciences, NY 912, 958.

Oskarsson H., Nobel A., Lund A. and Hjarbo K. (2005) New Technique for Evaluating Antiagglomerate Gas-Hydrate Inhibitors, SPE 93075.

Ostergaard K.K., Masoudi R., Tohidi B., Danesh A. and Todd A.C. (2005) A general correlation for predicting the suppression of hydrate dissociation temperature in the presence of thermodynamic inhibitors, J. of Petroleum Sc. and Eng., 48. 70– 80.

Palese S., Mukamel S., Miller R. J. D. and Lotshaw W. T. (1996) Interrogation of Vibrational Structure and Line Broadening of Liquid Water by Raman-Induced Kerr Effect Measurements within the Multimode Brownian Oscillator Model, J. Phys. Chem., 100, 10380-10388.

Parent J.S. and Bishnoi P.R. (1996) Investigations into the Nucleation Behaviour of Natural Gas Hydrates, Chemical Engineering Communications, 144, pp. 51-64.

Parka S., Kang K., and Yoonc W.-S. (2006). Magnetic spin glass properties of the bi-layer hydrate Na0.3NiO2·1.3H2O, J. Solid State Communications, 139, 60-63.

Parka S., Yoonc W.-S., and Vogta T. (2007). Structure and magnetism of the mono-layer hydrate Na0.3NiO2·0.7H2O, J. Solid State Communications, 142, 75-79.

Parrish W.R. and Prausnitz J.M. (1972) Dissociation pressure of gas hydrates formed by gas mixtures, Industrial and Engineering Chemistry Proc. Des. Dev., 11, 26-35.

Plyler E. (1952) Infrared Spectra of Methanol, Ethanol, and n-Propanol, Journal of Research of the National Bureau of Standards, Vol. 48, No. 4.

Priestly J. (1790) Experiments and Observations on Different Kinds of Air and Other Branches of Natural Philosophy Connected with the Subject. In Vol. 3, T. Pearson.

Ratajska-Gadomska B., Białkowski B., Gadomski W. and Radzewicz Cz. (2006) Ultrashort memory of the quasicrystalline order in water by optical Kerr effect spectroscopy, Chemical Physics Letters, 429, 575–580.

Ripmeester J.A., Tse J.S., Ratcliffe C.I. and Powell B.M. (1987) A new clathrate hydrate structure, Nature. Vol. 325, pp. 135–136.

Roger P.M. (2000) Methane Hydrate Melting and Memory, Annals of the New York

Roger P.M. (2000) Methane Hydrate Melting and Memory, Annals of the New York

Sassen R. and MacDonald I.R. (1994) Evidence of structure H hydrate, Gulf of Mexico continental slope, Organic Geochemistry, Volume 22, Issue 6, pp. 1029-1032.

Schanke T., Kjolberg S., and Vogel F. (2001). Oil in Water Monitoring for Subsea and Downhole Separators, SPE 66538.

Seth G., Zope D., Deka B. and Ghosh B. (2007) Downhole Fluid Analysis and Sampling Establishes Compositional Gradient in A Deep Water Gas-Condensate Reservoir, SPE 109204.

Skoog D. A. and Leary J. J. (2008) Principles of instrumental analysis, Saunders college Publishing, 6th edition, pp. 256- 275.

Sloan E. D. (1990) Clathrate Hydrates of Natural Gases, 1st edition, Marcel Dekker Inc., PP. 46-50.

Sloan E. D. (1998) Clathrate hydrates of natural gases. Second edition, Marcel Dekker Inc.:New York.

Sloan E. D. (1998) Clathrate hydrates of natural gases. Second edition, Marcel Dekker Inc.:New York.

Sloan E. D. and Bloys J. B. (2005) Hydrate Engineering, SPE Henry L. Doherty series, 21, pp. 1-4.

Sloan E. D. (2005) A changing hydrate paradigm – from apprehension to avoidance to risk management, Fluid Phase Equilibria, 228–229, pp. 67–74.

Sloan E. D., and Koh C.A. (2008) Clathrate Hydrates of Natural Gases, 3rd edition, CRC Press, pp. 11-13, pp. 53-72, p. 85.

Sloan E. D., Subramanian S., Matthews P. N., Lederhos J. P. and Khokhar A. A. (1998) Quantifying Hydrate Formation and Kinetic Inhibition, Ind. Eng. Chem. Res., 37, 3124-3132.

Smith J. M. and Van Ness H. C. (1987) Introduction to Chemical Engineering Thermodynamics, McGraw-Hill Inc., New York.

Smith R., Lee S., and Komori H.(1998) Relative permittivity and dielectric relaxation in aqueous alcohol solutions, Fluid Phase Equilibria, 144, 315-322.

Smith R., Lee S., and Komori H.(1998) Relative permittivity and dielectric relaxation in aqueous alcohol solutions, Fluid Phase Equilibria, 144, 315-322.

Szymczak S., Sanders K., Pakulski M. and Higgins T. (2006) Chemical Compromise: A Thermodynamic and Low-Dose Hydrate-Inhibitor Solution for Hydrate Control in the Gulf of Mexico, SPE 96418.

Takeya S., Hori A. and Hondoh T., and Uchida T. (2000). Freezing-Memory Effect of Water on Nucleation of CO2 Hydrate Crystals, J. Phys. Chem., 104, 4164-4168.

Tellurex Corporation (2007) C1-1.4-127-1.14 Module Specifications.

Thomas M. J. K. and Denney R.C. (1996) Ultraviolet and Visible Spectroscopy, John Wiley and sons, New York, pp. 215-232.

Thomas S. and Dawe R. A. (2003) Review of ways to transport natural gas energy from countries which do not need the gas for domestic use, Energy 28, 1461.

Thompson H., Soper A. and Buchanan P. (2006). Methane hydrate formation and decomposition: Structural studies via neutron diffraction and empirical potential structure refinement, J. Chem. Phys., 124, 164508.

Tohidi B, Burgass R.W., Danesh A. and Todd A.C. (1993) Hydrate inhibition effect of produced water, Part 1. Ethane and propane simple gas hydrates. In: Proceedings of the SPE Offshore Europe 93 Conference, Aberdeen.

Tohidi B., Burgass R.W., Danesh A. and Todd A.C (1993) Gas Hydrates, Problem or Source of Energy, International Non-Renewable Energy Sources Congress, Tehran, Iran.

Tohidi B., Burgass R.W., Danesh A. and Todd A.C. (1993) Hydrate inhibition effect of produced water, Part 1. Ethane and propane simple gas hydrates, In: Proceedings of the SPE Offshore Europe 93 Conference, Aberdeen.

Tohidi B., Burgass R.W., Danesh A. and Todd A.C. (1993) Hydrate Inhibition Effect of Produced Water: Part 1 – Ethane and Propane Simple Gas Hydrates, SPE Offshore European Conference, SPE 26701.

Tohidi B., Chapoy A., Yang J., Ahmadloo F., Valko I. and Zain Z. (2008) Developing Hydrate Monitoring and Early Warning Systems, OTC 19247.

Tohidi B., Danesh A., and Todd A.C. (1997) On the mechanism of gas hydrate formation in subsea sediments, American Chemical Society, 213, 37-Fuel.

Tohidi-Kalorazi B. (1995) Gas hydrate equilibria in the presence of electrolyte solutions, Ph.D. Theses, Heriot-Watt University.

Toschev S., Milchev A. and Stoyanov S. (1972). On Some Probabilistic Aspects of The Nucleation Process, Journal of Crystal Growth 13/14, 123-127.

Trench C. (2001) How Pipelines Make the Oil Market Work – Their Networks, Operation and Regulation, A Memorandum Prepared for the Association of Oil Pipe

Lines And the American Petroleum Institute's Pipeline Committee, Allegro Energy Group.

Udachin K. A., Ratcliffe C. I. and Ripmeester J. A. (2001) A Dense and Efficient Clathrate Hydrate Structure with Unusual Cages, Angew. Chem. Int. Ed., 40 (7), 1303–1305.

Uematsu M. and Frank E. U. (1980) Static Dielectric Constant of Water and Steam, J. Phys. Chem. Ref. Data, vol. 9, no. 4, pp. 1291-1306.

Valderrama J.O. (1990) A generalized Patel-Teja equation of state for polar and non-polar fluids and their mixtures, J. Chem. Eng. Jpn., 23, 87-91.

Van der Waals J. H. and Platteeuw J.C. (1959) Clathrate Solutions, Advances in Chemical Physics, 2, 1-57.

Venkataramanan L., Elshahawi H., McKinney D. and Flannery M. (2006) Downhole Fluid Analysis and Fluid Comparison Algorithm as an Aid to Reservoir Characterization, SPE 100937.

Villanoa L.D. and Kelland M.A. (2011) An investigation into the laboratory method for the evaluation of the performance of kinetic hydrate inhibitors using superheated gas hydrates, Chemical Engineering Science, Volume 66, Issue 9, pp. 1973-1985.

von Stackelberg M., (1949) Feste Gashydrate, Naturwissenschaften 36, No. 11, 327-359.

von Stackelberg M. and Müller H.R. (1954) Feste Gashydrate II, Zeitschrift für Elektrochemie 58, Nr. 1, 104.

Weast R.C., Lide D.R., Astle M.J. and Beyer W.H. (1989) Handbook of chemistry and physics, 70th edition, CRC Press, pp. D-221-271.

Welling and Associates, (2000) N., Flow Assurance Still Leading Concern Among Producers, Offshore, 1999 Survey, cited by Macintosh.

William T., Harrison and Shiao C. (1994). Synthesis, Structure, and Magnetism of a New Barium Vanadium Phosphate Hydrate, J. Solid State Chem. , 113, 444-447.

Wilson P.W., , Lester D. and Haymet A.D.J. (2005) Heterogeneous nucleation of clathrates from supercooled tetrahydrofuran (THF)/water mixtures, and the effect of an added catalyst, Chemical Engineering Science, Volume 60, Issue 11, pp. 2937-2941.

Wu M., Wang S. and Liu H. (2007) A Study on Inhibitors for the Prevention of Hydrate Formation in Gas Transmission Pipeline, J. of Natural Gas Chemistry, 16, 81-85.

Yousif M. H. and Young D. B. (1993) A simple correlation to predict hydrate point suppression in drilling fluids, SPE 25705, SPE/IADC Drilling Conference, Amsterdam, Netherlands.

Zain Z.M, Yang J., Tohidi B., Cripps A. and Hunt A. (2005) Hydrate Monitoring and Warning System: A New Approach for Reducing Gas Hydrate Risks, SPE 94340, presented at EAGE/SPE International Conference and Exhibition, Madrid, Spain, 13-16 June.

Zain Z.M, Yang J., Tohidi B., Cripps A. and Hunt A. (2005) Hydrate Monitoring and Warning System: A New Approach for Reducing Gas Hydrate Risks, SPE 94340, presented at EAGE/SPE International Conference and Exhibition, Madrid, Spain, 13-16 June.

Zain Z.M, Yang J., Tohidi B., Cripps A. and Hunt A. (2005). Hydrate Monitoring and Warning System: A New Approach for Reducing Gas Hydrate Risks, SPE 94340, presented at EAGE/SPE International Conference and Exhibition, Madrid, Spain, 13-16 June.

Zeng H., Moudrakovski I. L. and Ripmeester J. A. (2006). Effect of Antifreeze Protein on Nucleation, Growth and Memory of Gas Hydrates, AIChE Journal, 52, No 9.

APPENDIX A

INTRODUCTION

The following system design was completed as part of Hydrate Monitoring and Early Warning Systems introduced in Chapter 1. The system consists of three main parts:

1. User;
2. Pipeline sensors;
3. Surface sensors.

SYSTEM DESIGN AND ALGORITHMS

Design of information acquisition and control systems in the petroleum industry has been comprehensively described by a number of authors (Bailey et al. 2003; Clarke et al., 2003; Foot et al., 2006). In the system developed in this work, the user part is operated by the cyclic algorithm presented in Figure A.1. The operator can read, analyse and manipulate measured data through a sophisticated Graphical User Interface (Figure A.2). This so called Human-Machine Interface (HMI) is developed to give user necessary analytical instruments for pipeline hydrate flow assurance analysis, e.g. artificial intelligence techniques such as neural networks and fuzzy logic. The pipeline and surface sides of the system are controlled and operated by network linked electronic microcontrollers which are governed by algorithms presented in Figure A.3 and Figure A.4. The main functions of those algorithms are to receive commands, conduct measurements and transmit data to the database centre.

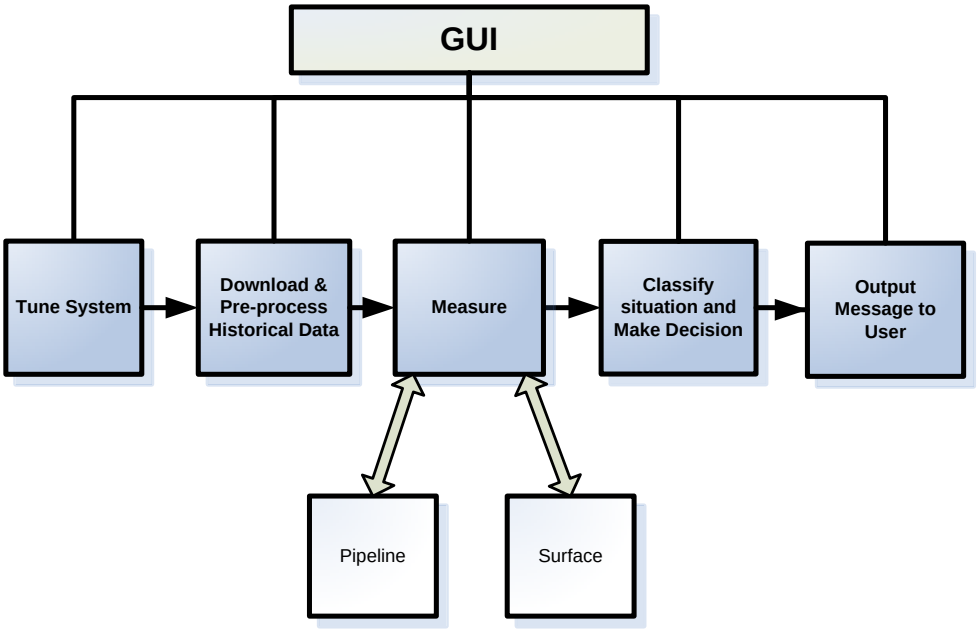

Figure A.1 Block diagram for User side of the system

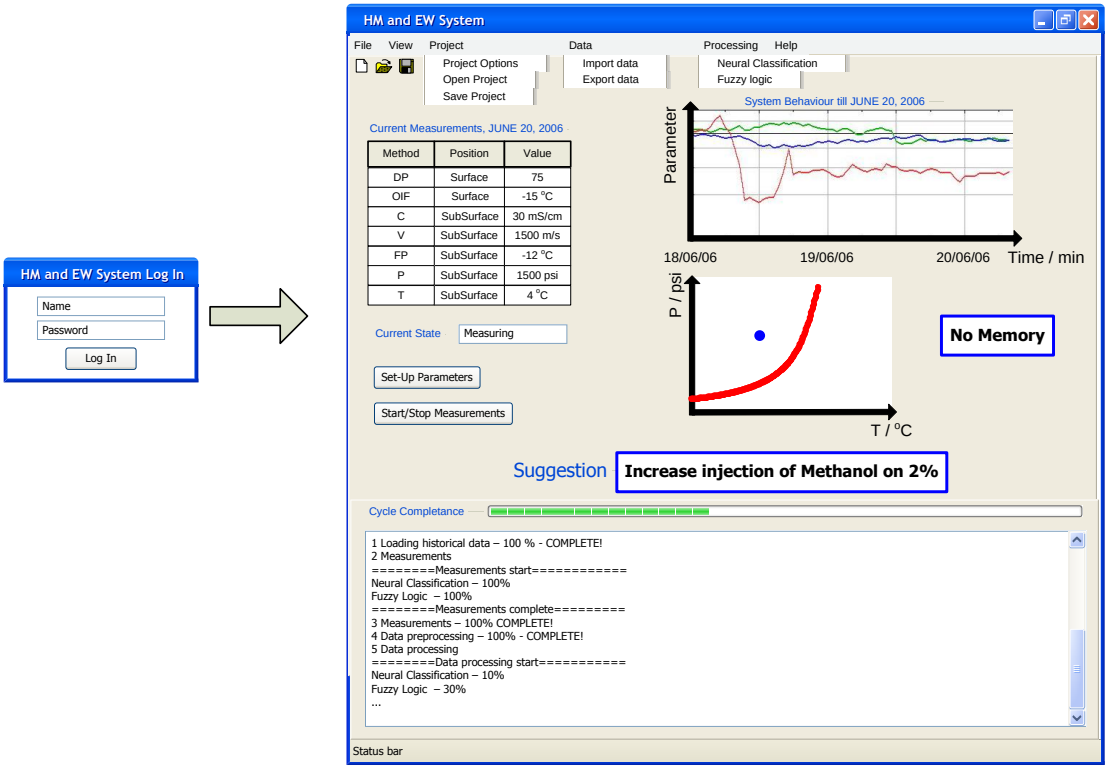

Figure A.2 Graphical User Interface

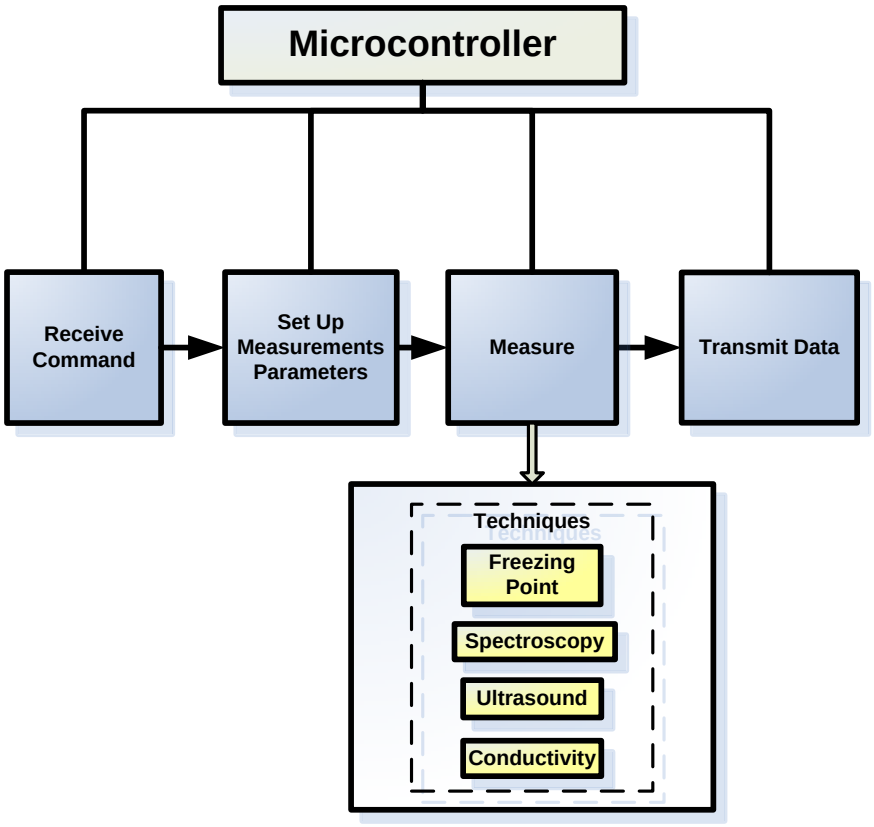

Figure A.3 Block diagram for Pipeline side of the system

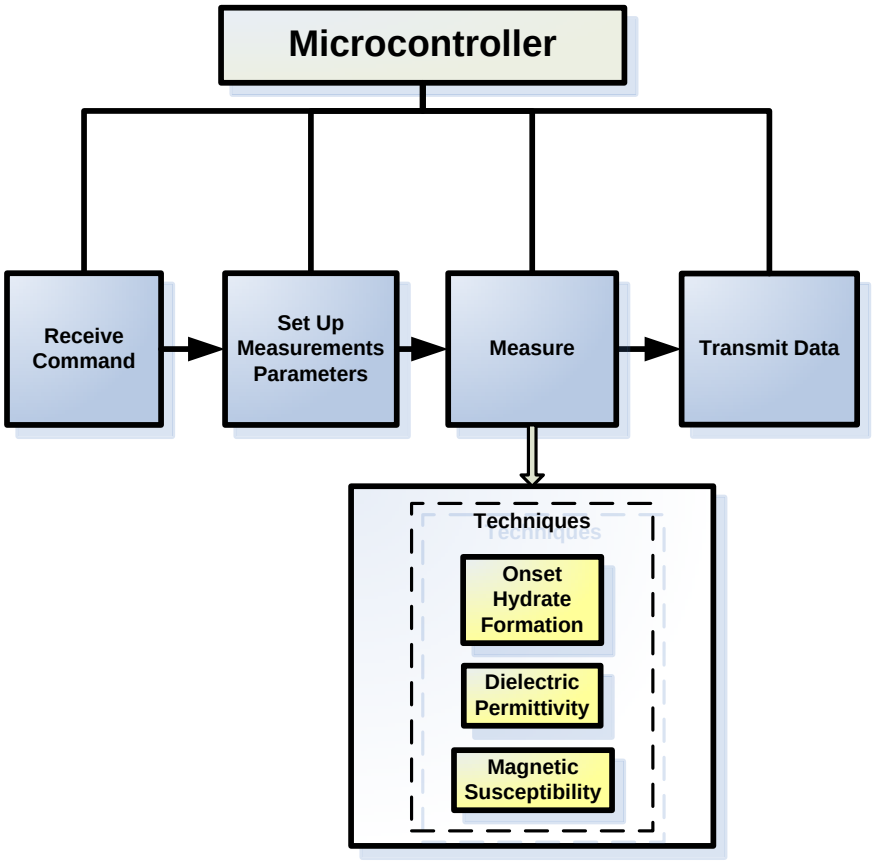

Figure A.4 Block diagram for Surface side of the system

APPENDIX B

PELTIER DEVICE SET-UP PROCEDURE

1. Hardware Connections
2. Software Installation
3. Measurement
4. Precautions

HARDWARE CONNECTIONS

The instrument elements should be connected together by a stepwise manner to get to the final set up shown in Figure B.1.

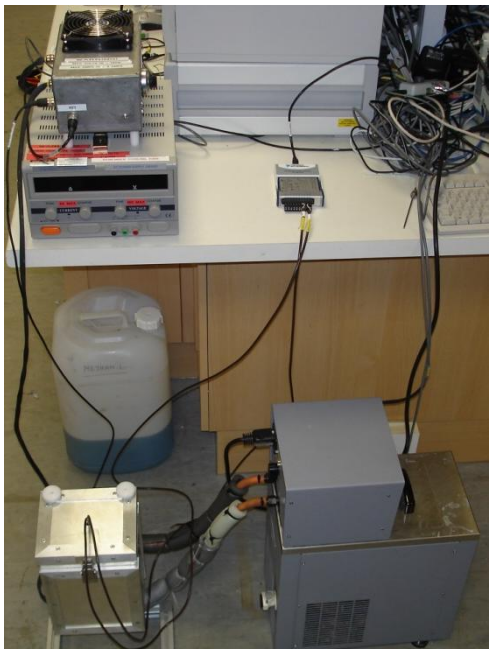

Figure B.1 Overview of prototype

Figure B.2 Power Supply

STEP 1. Connect a power cable to power supply (Figure B.2).

STEP 2. Controller (Figure B.3). To connect the controller to power supply use the wire labelled “to power supply” solidly connected to controller shown in Figure B.4. Red end connects to red output (+), blue end connects to black output (-).

STEP 3. To connect the controller to Peltier elements, use the connection picture in Figure B.5, and the connection scheme (wiring) shown in Figure B.7.

STEP 4. To connect the controller to the computer, use the wire shown in Figure B.6 (left end connects to controller, right end connects to computer). To help connection process, each wire and each port was labelled.

Figure B.3 Controller

Figure B.4 Controller power cable to power supply (DCV output; 0~40A)

Figure B.5 Peltier elements wiring

Figure B.6 Controller to computer wire (right end – to controller; left end – to computer COM port)

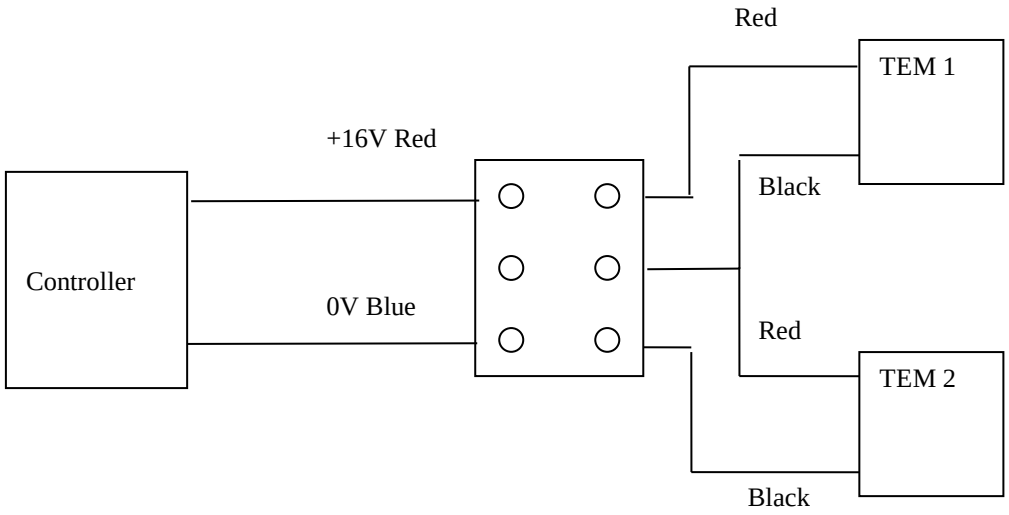

Figure B.7 Peltier elements wiring (schematic diagram)

Figure B.8 Temperature reader

STEP 5. Temperature reader (Figure B.8). NI 9211 device (temperature reader) should be connected to computer through USB interface. Thermocouples should be passed through cap of the prototype and connected to NI 9211 as shown in Figure B.8.

STEP 6. Bath. Connect yellow tubes from the measurement block of the device to the bath and carefully tighten the connections to avoid any leakage.

STEP 7. Connect temperature sensor “Control PRT 1000” from measurement block to controller port “Temp. Sensor 1”.

SOFTWARE

For freezing point measurements, two pieces of software are necessary: NI-DAQmx which is logging the temperature from NI 9211 device; Matlab Runtime Component

which makes it possible to run temperature controlling program (Measure.exe) for cooling and heating cycles.

a) Installation of NI-DAQmx Software

Insert installation CD. When 'autorun' shows the installation start up menu, press "Install NI-DAQmx / VI Logger" to install the program. When the product information appears on the screen, press Next button. Select the folder for installation. Usually it is "C:\Program Files\National Instruments\". Leave features in the next menu as they are and press Next. When product information again appears on the screen, press Next button. Accept the license agreement, and press Next. At the start installation menu, press Next, and the installation process will start. At the end of the installation, the system should be restarted.

b) Setting up the parameters for NI-DAQmx Software

After system reboot, go to start -> all programs -> national instruments -> VI logger -> VI Logger (NI-DAQmx) to lunch NI-DAQmx software.

In the program window, go to configuration VI Logger tasks, click right mouse button and press "Create New …" as shown in Figure B.9.

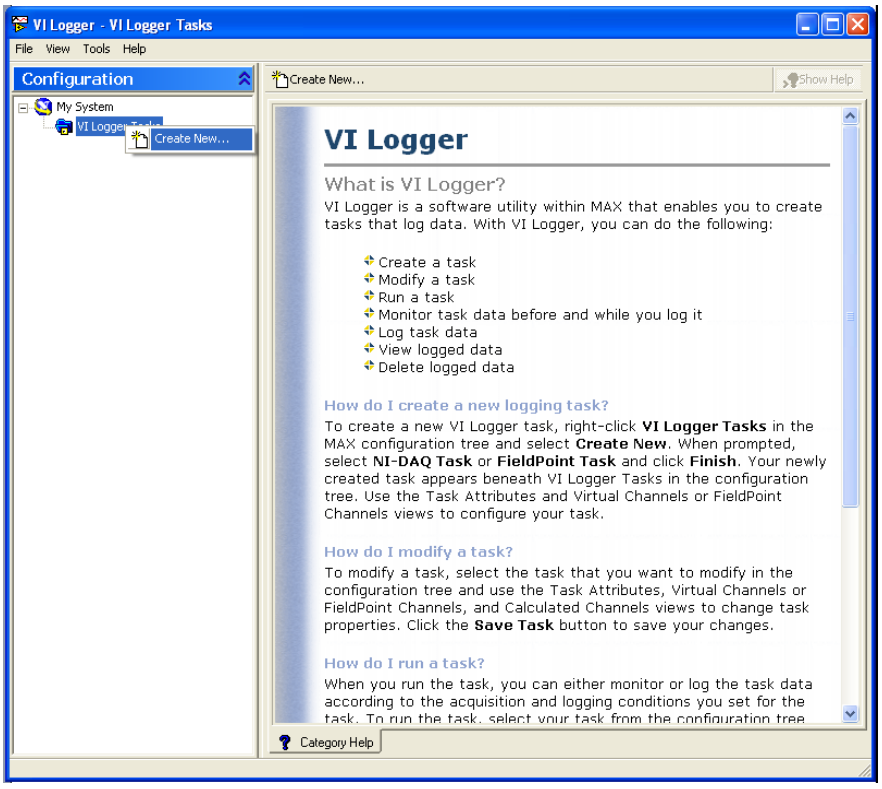

Figure B.9 VI logger main window

In Measurement and Automation explorer select “Using NI-DAQmx” and press Finish button, as it is shown in Figure B.10.

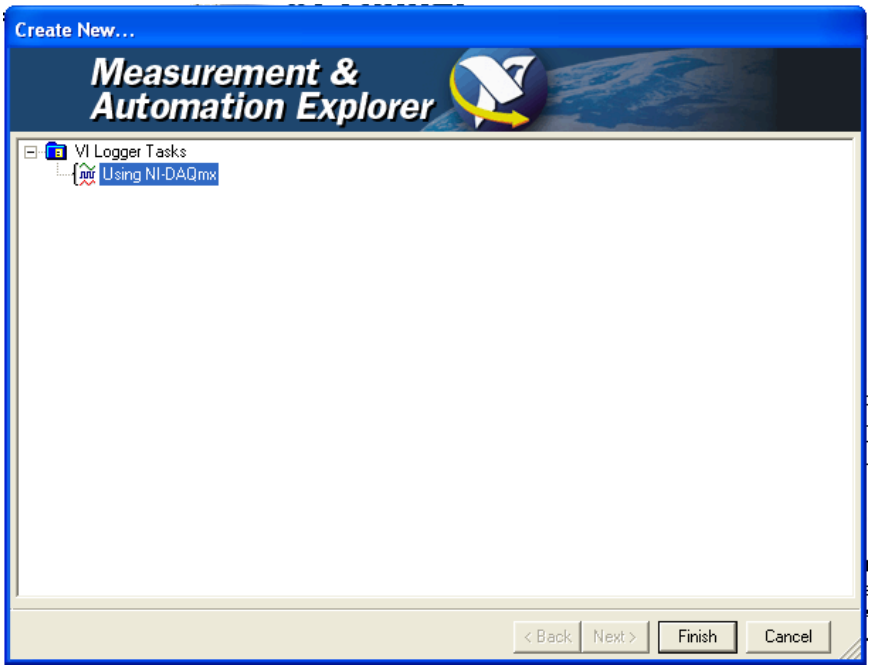

Figure B.10 Measurement and Automation explorer

Then new task appeared, tick “View in Excel when tack stops” in Data Export, and press Create New in the Acquisition Settings box, as it is shown in Figure B.11.

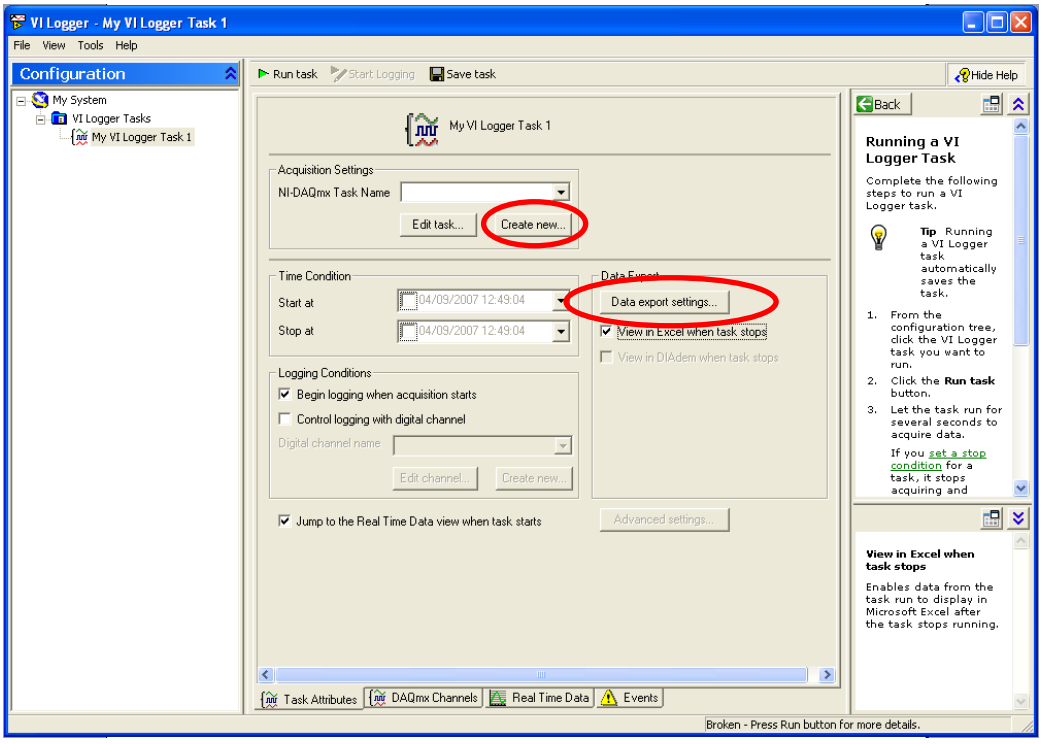

Figure B.11 VI logger: New task

At this stage, disconnect the NI 9211 device from the computer and connect again through USB port. Install device driver using the hardware installation wizard. First choose "No action" and press next. Select install software automatically, and press next. If attention message will appear on the screen, press Continue anyway. If the second driver installation will be asked, repeat the procedure.

Go to VI Logger, in the Create New window, select Analogue Input -> Temperature -> Thermocouple as it is shown in Figure B.12. Then select two first channels which are used for temperature measurements as shown in Figure B.13.

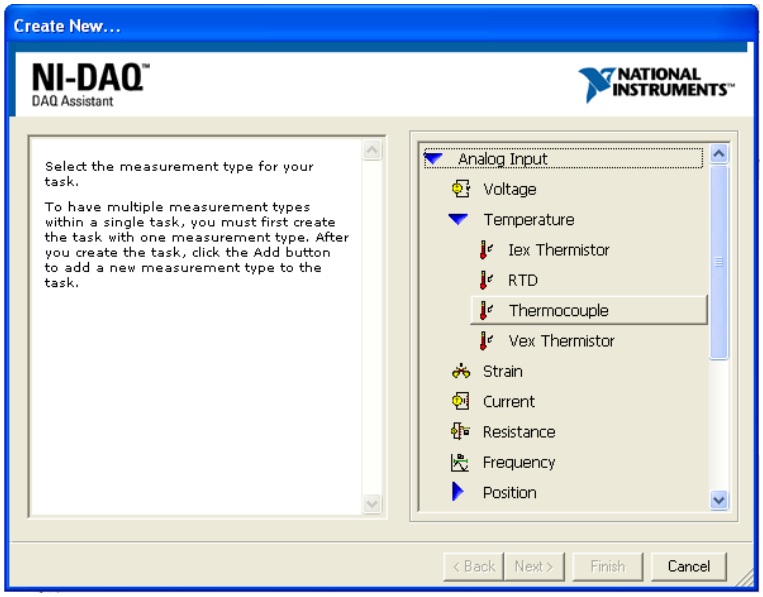

Figure B.12 Create New window

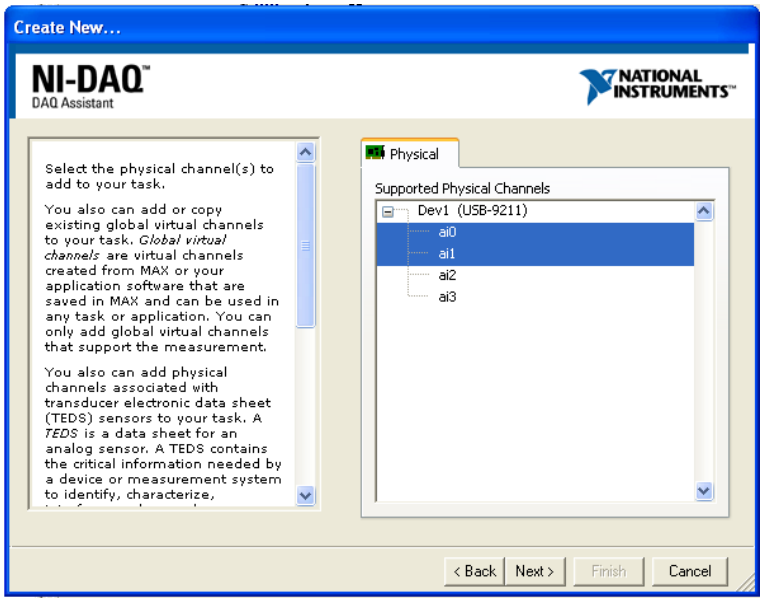

Figure B.13 Create New window

Enter the name for created tack (MyTemperatureTask by default), and press Finish button. In the appeared DAQ Assistant, for both temperature channels (Temperature0 and Temperature1) select min and max temperature range from 50 ^{o}C to -50 ^{o}C, thermocouple type to T type, and Acquisition mode to Continuous with Samples to Read equal to 1, and Rate equal to 2 Hz (2 times per second), as shown in Figure B.14.

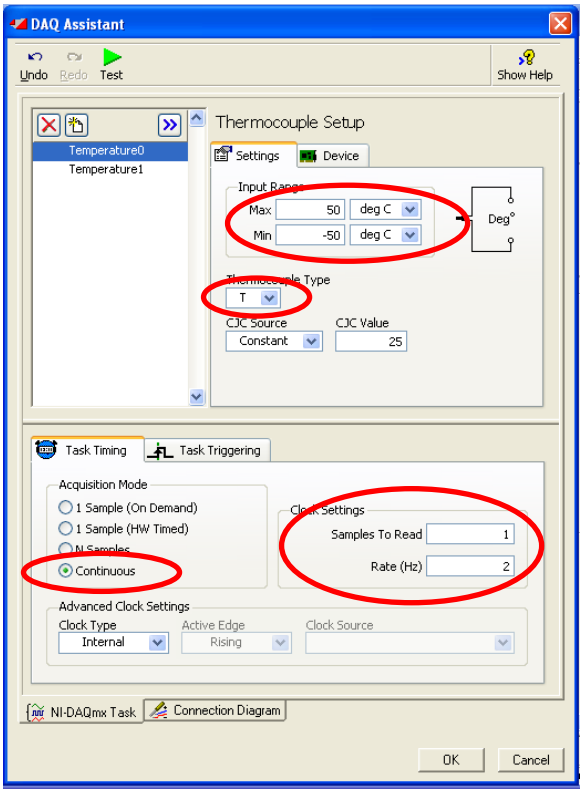

Figure B.14 DAQ Assistant

All settings are done. Go to Real Time Data tab, and press "Run task" to start temperature measurement logging as shown in Figure B.15.

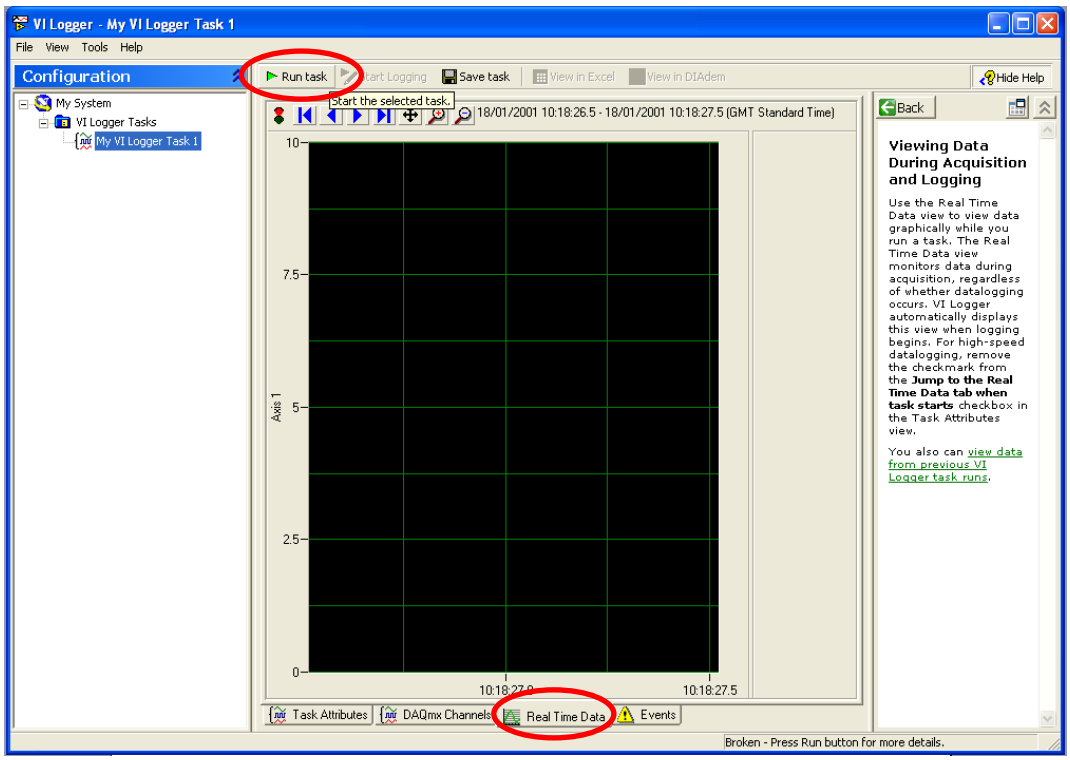

Figure B.15 Real Time Data tab

When stop button is pressed, the data will be automatically exported to Excel.

c) Install Matlab Runtime Component (MRCinstall.exe)

Insert the CD labelled “Measure”.

Open the CD, and copy 3 files MCRInstaller.exe, Measure.exe, and Measure.ctf into your computer hard drive. Lunch MCRInstall.exe to install “Matlab Component Runtime” on your computer. In the installation guide, pres next to select the installation directory (C:\Program Files\MathWorks\MATLAB Component Runtime\, by default). Then the installation is completed, press Close button.

d) Lunch Measure.exe, to start running the measurement program

Lunch Measure and set up Port, cooling/heating parameters. Refer to Measurement section for measurement process description.

MEASUREMENT

1. Prepare sample. Insert the sample probe into the sample container. Put thermo gel to reference probe and insert it to reference container in the measurement block.

2. Switch on cooling bath, and set the target temperature to 4 ^{o}C.

3. Switch on power supply, and set up voltage to 16 V, and current to 0 A.

4. Before measurements, open two programs installed in advance: 'VI logger', and 'Measure'.

5. In 'VI logger', press Run Task to start recording temperature data.

6. In 'Measure'. Prior to initiating the measurements, parameters should be set up in the menu of program "Measure":

7. Cooling Rate = rate of sample temperature decline in ^{o}C per minute. In this version of the program, infinity cooling rate is only available.

8. ColdT = lowest temperature to which the probe will be cooled down (-15 ^{o}C by default)

9. Heating Rate = rate of sample temperature increase in ^{o}C per minute

10. HotT = highest temperature to which the probe will be heated up after cooling (10 ^{o}C by default)

11. Port = COM port to which the device is connected

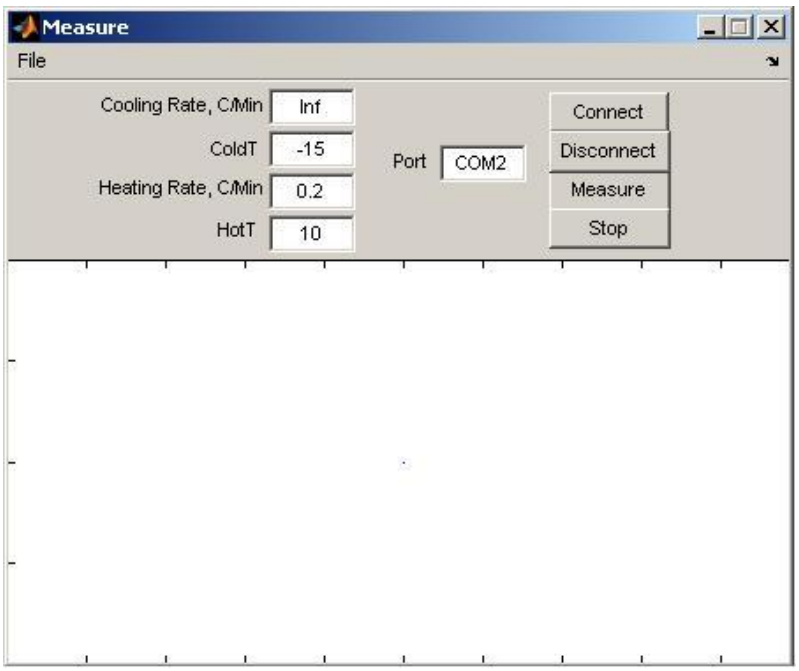

Figure B.16 Program Measure for controlling temperature

When the parameters have been set up, the device should be connected by pressing "Connect" button. To initiate measurements, press "Measure" button. If there is a need to stop the measurement, press "Stop" button. When all the measurements are finished, press "Disconnect" button, and close the program.

12. In VI logger, to save the measured data, press 'Stop task' button. The data will be automatically exported to Excel (Figure B.17). After data appeared in the Excel worksheet, it may be manually treated and calibrated.

	A	B	C	D	E	F	G
1	NI VI Logger						
2	Created: 11/09/2007 16:28:52.699 GMT Daylight Time						
3	Number of scans: 4234						
4	Scan rate: 0.5 seconds						
5							
6	Row	Time	Temperatu	Temperature1(Temperature:Thermocouple)			
7	1	53:33.0	-0.99807	-6.76122			
8	2	53:33.5	-1.04513	-6.75023			
9	3	53:34.0	-1.05306	-6.75198			
10	4	53:34.5	-1.05553	-6.71851			
11	5	53:35.0	-1.08501	-6.73			
12	6	53:35.5	-1.07832	-6.74799			
13	7	53:36.0	-1.06593	-6.68329			
14	8	53:36.5	-0.95647	-6.6808			

Figure B.17 Exported temperature data

13. In Excel, the exported data needs to be analysed as it is shown in Figure B.18. Calculate additional column: Reference temperature (channel 1) – Sample Temperature (channel 0). Plot T1-T0 versus T0 in the heating region (Figure B.18). In the constructed plot of difference between reference and sample temperatures versus sample temperature (Figure B.19), find the start of the declining slope which indicates the freezing point temperature. As a final stage, add 0.8°C the obtained freezing point to receive calibrated measured freezing point. In this example, the solution was 20 mass% Ethylene glycol which freezing point is -8.08 °C.

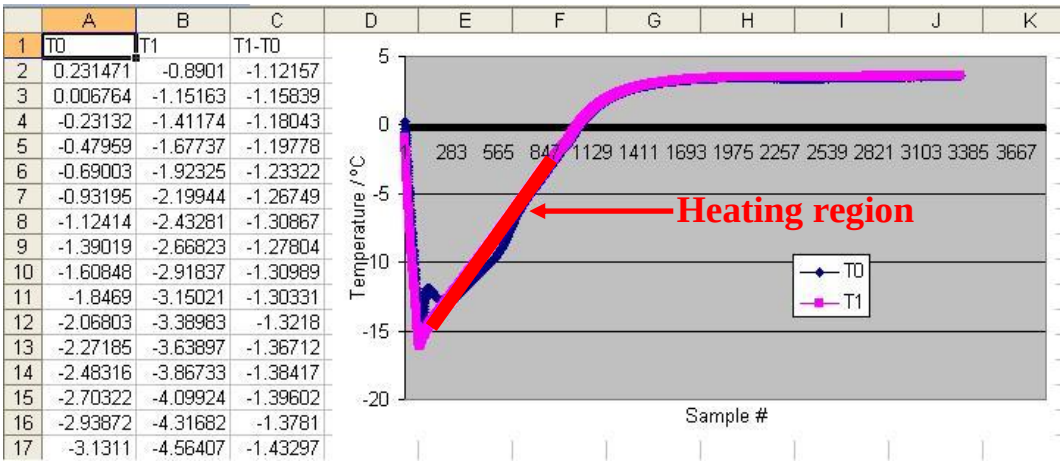

	A	B	C
1	T0	T1	T1-T0
2	0.231471	-0.8901	-1.12157
3	0.006764	-1.15163	-1.15839
4	-0.23132	-1.41174	-1.18043
5	-0.47959	-1.67737	-1.19778
6	-0.69003	-1.92325	-1.23322
7	-0.93195	-2.19944	-1.26749
8	-1.12414	-2.43281	-1.30867
9	-1.39019	-2.66823	-1.27804
10	-1.60848	-2.91837	-1.30989
11	-1.8469	-3.15021	-1.30331
12	-2.06803	-3.38983	-1.3218
13	-2.27185	-3.63897	-1.36712
14	-2.48316	-3.86733	-1.38417
15	-2.70322	-4.09924	-1.39602
16	-2.93872	-4.31682	-1.3781
17	-3.1311	-4.56407	-1.43297

Figure B.18 Temperature data analysis (T0 – channel 0, or sample temperature; T1 – channel 1, or reference temperature; T1-T0 – difference between reference and sample temperatures)

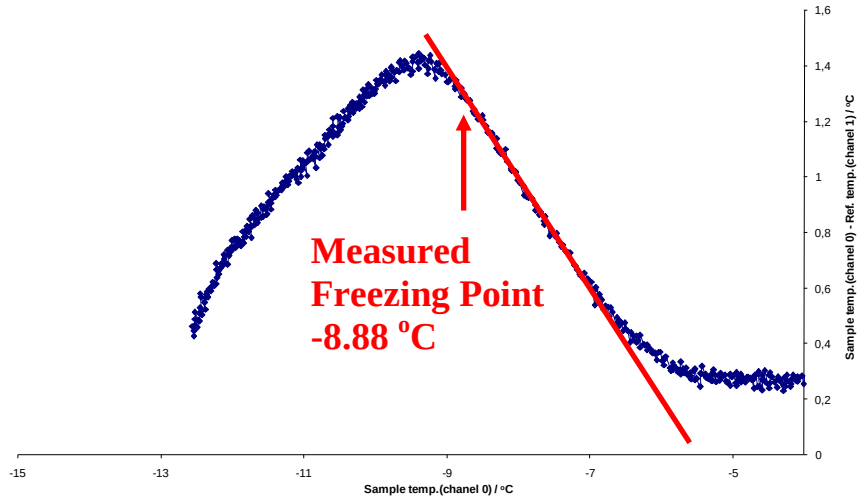

Figure B.19 Difference between reference and sample temperatures versus sample temperature

PRECAUTIONS

1. Keep voltage below 17 V. This is the maximum value at which Peltier elements can work.

2. Make sure that main Power supply is 230 V 50 Hz 1 phase.

3. Turn off current and voltage when switching on power supply.

4. If the sample and reference temperature goes up after start of measurement, the connection of controller to Peltier elements should be changed as mentioned in section “Hardware connections”.

If the program “Measure” will crash, copy its files from the CD to your Computer in to another folder once again, and start the program.

APPENDIX C

HWHYD THERMODYNAMIC MODELLING

In this study, a general phase equilibrium model based on the uniformity of component fugacities in all coexisting phases has been used for thermodynamic modelling (Avlonitis, 1992; Tohidi et al., 1993). In summary, The Valderrama modification of the Patel-Teja (VPT) equation of state (Valderrama et al., 1990) combined with non-density-dependent (NDD) mixing rules (Avlonitis et al., 1994) is used to determine component fugacities in fluid phases. The VPT – EoS is given by:

$$P = \frac{RT}{v-b} - \frac{a}{v(v+b)+c(v-b)} \qquad \text{C.1}$$

This combination has proven to be a strong tool in modelling systems with polar as well as non-polar compounds (Avlonitis et al., 1994; Tohidi-Kalorazi, 1995).

For ice phase modelling, the fugacity of a pure solid has (as for a supersaturated pure liquid) been calculated using the Poynting correction, i.e., assuming that the volume of the supersaturated phase is constant at the volume for the saturated phase (Smith et al., 1987; Anderson et al., 1986). For ice the expression becomes:

$$f_w^I = \phi_w^{sat} P_I^{sat} \exp\left(\frac{v_I\left(P - P_I^{sat}\right)}{RT}\right) \qquad \text{C.2}$$

where f_w^I is the fugacity of water in the ice phase (Pa), ϕ_w^{sat} is the water fugacity coefficient in the vapour phase at pressure equal to the ice vapour pressure (dimensionless), P_I^{sat} is the ice vapour pressure (Pa), v_I is the ice molar volume

(m^3/mol), *R* is the universal gas constant (R = 8.314 $J.mol^{-1}.K^{-1}$), and *P* and *T* is the system pressure (Pa) and temperature (K), respectively.

When salt is present, the fugacities of non-electrolyte components in the aqueous phase are calculated by combining an EoS with the Debye-Hückel electrostatic term to take into account the effect of electrolyte (Aasberg-Petersen et al., 1991):

$$\ln \phi_i = \ln \phi_i^{EoS} + \ln \gamma_i^{EL} \qquad i = 1, 2, ..., N \qquad \text{C.3}$$

where *N* is the number of non-electrolyte components (dimensionless), ϕ_i is the fugacity coefficient of component *i* (dimensionless), ϕ_i^{EoS} is the fugacity coefficient of component *i* calculated by an EoS (dimensionless), neglecting the electrostatic effect, and γ_i^{EL} is the contribution of the electrostatic term (dimensionless). A detailed description of the modelling of ice phase and electrolyte solution can be found elsewhere (Haghighi et al., 2008).

The hydrate phase is modelled using the solid solution theory of van der Waals and Platteeuw (Van der Waals, 1959), as developed by Parrish and Prausnitz (Parrish et al., 1972). The equation recommended by Holder (Holder et al., 1982) is used to calculate the heat capacity difference between the empty hydrate lattice and pure liquid water. The Kihara model for spherical molecules is applied to calculate the potential function for compounds forming hydrate phases (Kihara, 1953). The Kihara potential parameters for methane are taken from Tohidi-Kalorazi (Tohidi-Kalorazi, 1995).

APPENDIX D

MATLAB CODE

The following Matlab code was developed as part of research work presented in this thesis. The MATLAB® is a high-performance language for technical computing which integrates computation, visualization, and programming in an easy-to-use environment where problems and solutions are expressed in familiar mathematical notation. The code written in Matlab aimed to compute the freezing time, temperature and integral (divergence area between probe and bath temperatures), as well as statistical tests used to distinguish sample with and without hydrate memory (Chapter 5).

```
% Program Finds: Freezing time/point and integral
% Calculates: t-, f-, ks- statistical tests

clc;
clear;
warning off MATLAB:xlswrite:AddSheet;

%% Load data
level = 0.7;
freezing_flag = 1;
melting_flag = 0;
step = 1; % minutes for Nucleation function
letter1 = { 'B', 'H', 'N', 'T', 'Z', 'AF'  'AL' 'AR' 'AX' 'BD' 'BJ'
'BP'};
letter2 = { 'C', 'I', 'O', 'U', 'AA', 'AG' 'AM' 'AS' 'AY' 'BE' 'BK'
'BQ'};
letter3 = { 'D', 'J', 'P', 'V', 'AB', 'AH' 'AN' 'AT' 'AZ' 'BF' 'BL'
'BR'};
%OutputFile = 'Results-test1-HW.xls';
%InputFile = 'data\test4-Cross.xls';
InputFile =  'data\Test2_HW_HWrm_1.xls';
% sheet = { 'HW2' 'HW1' 'HWrm' };
sheet = { 'HW' 'HWrm' };
% sheet = { 'SW' 'SWrm' };
% sheet = { 'HW' 'HWrm' 'SW' 'SWrm' };
% sheet = { 'run1' 'run2' 'run3' 'run4' 'run5' 'run6' 'run7' 'run8'
'run9' 'run10'};
```

```
% sheet = { 'run1' 'run2' 'run3' 'run4' 'run5' 'run6' };

%% Calculation loop
for q=1:length(sheet)
data = xlsread( InputFile, sheet{q}, 'A2:U50000' );
Time = data(:,1);
Ref  = data(:,2);
Samp = data(:,3:end);

if freezing_flag
%% Compute freezing time, point and integral
start_point_m1 = [];
% Find freezing point start position
for k=1:size(Samp,2)
    for j=1:length(Time)
        if Samp(j,k) < 0
             start_point1(k) = j;
             break;
        end
    end
end

% find start point of freezing
start_point = [];
for k=1:size(Samp,2)
    Ref1 = Ref - (Ref(start_point1(k))-Samp(start_point1(k),k));
    start_point(k) = start_point1(k);
    for i=start_point1(k):length(Time)    % Might have mistake!!!
        if Samp(i,k)-Ref1(i) > level
            start_point(k) = i;
            break;
        end
    end
end

end_point = [];
% find end point of freezing
for k=1:size(Samp,2)
    Ref1 = Ref - (Ref(10)-Samp(10,k));
        for j=start_point(k):length(Time)
            if Samp(j,k)-Ref1(j) < level
                end_point(k) = j;
                break;
            end
        end
end

start_point = start_point - 1;
end_point = end_point + 7;

% Calculate new time and difference between integrals of sample and
reference
for k=1:size(Samp,2)
    if ~isempty(start_point(k))
        result.Freezing{q,k}.Time = Time( start_point(k):end_point(k)
) - Time(start_point1(k)); % calibrate data
        result.Freezing{q,k}.Samp = Samp(
start_point(k):end_point(k),k );
        result.Freezing{q,k}.Ref  = Ref ( start_point(k):end_point(k)
);
    else
        result.Freezing{q,k}.Time = [];
        result.Freezing{q,k}.Samp = [];
```

```
        result.Freezing{q,k}.Ref  = [];
    end
end

% Compute integral
for k=1:size(Samp,2)
    if ~isempty(start_point(k))
        result.Freezing_Time(q,k)     = result.Freezing{q,k}.Time(1);
        result.Freezing_Point(q,k)    = result.Freezing{q,k}.Samp(1);
        result.Freezing_Integral(q,k) =
trapz(result.Freezing{k}.Time,result.Freezing{k}.Samp) -
trapz(result.Freezing{k}.Time,result.Freezing{k}.Ref);
    else
        result.Freezing_Time(q,k)     = [];
        result.Freezing_Point(q,k)    = [];
        result.Freezing_Integral(q,k) = [];
    end
end

Freezing_Time     = result.Freezing_Time(q,:)' ;
Freezing_Point    = result.Freezing_Point(q,:)';
Freezing_Integral = result.Freezing_Integral(q,:)';
Freezing_Time_full     = [Freezing_Time; mean(Freezing_Time);
std(Freezing_Time)];
Freezing_Point_full    = [Freezing_Point; mean(Freezing_Point);
std(Freezing_Point)];
Freezing_Integral_full = [Freezing_Integral; mean(Freezing_Integral);
std(Freezing_Integral)];

end

if melting_flag
start_point_m1 = [];
% Find melting point start position
for k=1:size(Samp,2)
    for j=end_point(k)+1:length(Time)
        if Samp(j,k) - Samp( end_point(k),k ) > 0
             start_point_m1(k) = j;
             break;
        end
    end
end
start_point_m1 = start_point_m1+10;

start_point_m = [];
% find start point of melting
for k=1:size(Samp,2)
    Ref1 = Ref - (Ref(start_point_m1(k)) - Samp(start_point_m1(k),k));
    for i=start_point_m1(k):length(Time)    % Might have mistake!!!
        if Ref1(i) - Samp(i,k) > level
            start_point_m(k) = i;
            break;
        end
    end
end

end_point_m = [];
% find end point of melting
for k=1:size(Samp,2)
    Ref1 = Ref - (Ref(start_point_m1(k)) - Samp(start_point_m1(k),k));
    for j=start_point_m(k):length(Time)
            if Ref1(j) - Samp(j,k) < level
                end_point_m(k) = j;
```

```
                break;
            end
    end
end

for k=1:size(Samp,2)
    if end_point_m(k) == 0
        end_point_m(k)   = length(Time);
    end
end

if end_point_m + 7 - length(Time) <= 0
    end_point_m   = end_point_m + 7;
end

% Calculate new time and difference between integrals of sample and
reference
for k=1:size(Samp,2)
        result.Melting{q,k}.Time = Time(
start_point_m(k):end_point_m(k) ) - Time( start_point1(k) );
        result.Melting{q,k}.Samp = Samp(
start_point_m(k):end_point_m(k),k );
        result.Melting{q,k}.Ref  = Ref (
start_point_m(k):end_point_m(k) );
end

% Compute integral
for k=1:size(Samp,2)
        result.Melting_Time(q,k)     = result.Melting{q,k}.Time(1);
        result.Melting_Point(q,k)    = result.Melting{q,k}.Samp(1);
        result.Melting_Integral(q,k) =
trapz(result.Melting{k}.Time,result.Melting{k}.Ref -
trapz(result.Melting{k}.Time,result.Melting{k}.Samp));
end

Melting_Time      = result.Melting_Time(q,:)' ;
Melting_Point     = result.Melting_Point(q,:)';
Melting_Integral  = result.Melting_Integral(q,:)';
Melting_Time_full      = [Melting_Time; mean(Melting_Time);
std(Melting_Time)];
Melting_Point_full     = [Melting_Point; mean(Melting_Point);
std(Melting_Point)];
Melting_Integral_full  = [Melting_Integral; mean(Melting_Integral);
std(Melting_Integral)];

else

Melting_Time      = result.Freezing_Time(q,:)' ;
Melting_Point     = result.Freezing_Time(q,:)' ;
Melting_Integral  = result.Freezing_Time(q,:)' ;
Melting_Time_full      = [Melting_Time; mean(Melting_Time);
std(Melting_Time)];
Melting_Point_full     = [Melting_Point; mean(Melting_Point);
std(Melting_Point)];
Melting_Integral_full  = [Melting_Integral; mean(Melting_Integral);
std(Melting_Integral)];

end

% Process data
[ x, y, y_calc, j, t ] = probab( Freezing_Time, step );
```

```
% Save Results
start_position = letter1{q};
xlswrite( InputFile, sheet(q), 'Results', strcat(start_position,'1'));
xlswrite( InputFile, {'F Time' 'F Point' 'F Integral' 'M Time' 'M
Point' 'M Integral'}, 'Results', strcat(start_position,'2'));
xlswrite( InputFile, [ Freezing_Time_full   Freezing_Point_full
Freezing_Integral_full...
                       Melting_Time_full    Melting_Point_full
Melting_Integral_full...
                     ], 'Results', strcat(start_position,'3'));
xlswrite( InputFile, [ j; t ],       'Results',
strcat(start_position,num2str(10+length(Freezing_Time))));
xlswrite( InputFile, [ x' y' y_calc' ], 'Results',
strcat(start_position,num2str(12+length(Freezing_Time))));

end

xlswrite( InputFile, {'mean'; 'std'; ''; 'ttest'; 'ftest'; 'kstest';
''; 'J'; 'tau0';}, 'Results',
strcat('A',num2str(3+length(result.Freezing_Time(1,:)))));

% Add ttest, ftest, kstest for F Time
for i=1:length(sheet)-1
    [ h_t,p_t   ] =
ttest2(result.Freezing_Time(i,:)',result.Freezing_Time(i+1,:)');
    [ h_f,p_f   ] =
vartest2(result.Freezing_Time(i,:)',result.Freezing_Time(i+1,:)');
    [ h_ks,p_ks ] =
kstest2(result.Freezing_Time(i,:)',result.Freezing_Time(i+1,:)');
    xlswrite( InputFile, [ p_t; p_f; p_ks ], 'Results',
strcat(letter1{i},num2str(6+length(result.Freezing_Time(1,:)))));
end

% Add ttest, ftest, kstest for FP
for i=1:length(sheet)-1
    [ h_t,p_t   ] =
ttest2(result.Freezing_Point(i,:)',result.Freezing_Point(i+1,:)');
    [ h_f,p_f   ] =
vartest2(result.Freezing_Point(i,:)',result.Freezing_Point(i+1,:)');
    [ h_ks,p_ks ] =
kstest2(result.Freezing_Point(i,:)',result.Freezing_Point(i+1,:)');
    xlswrite( InputFile, [ p_t; p_f; p_ks ], 'Results',
strcat(letter2{i},num2str(6+length(result.Freezing_Time(1,:)))));
end
% Add ttest, ftest, kstest for Integral
for i=1:length(sheet)-1
    [ h_t,p_t   ] =
ttest2(result.Freezing_Integral(i,:)',result.Freezing_Integral(i+1,:)'
);
    [ h_f,p_f   ] =
vartest2(result.Freezing_Integral(i,:)',result.Freezing_Integral(i+1,:
)');
    [ h_ks,p_ks ] =
kstest2(result.Freezing_Integral(i,:)',result.Freezing_Integral(i+1,:)
');
    xlswrite( InputFile, [ p_t; p_f; p_ks ], 'Results',
strcat(letter3{i},num2str(6+length(result.Freezing_Time(1,:)))));
end
```